Observation of metastable states in a superconducting Josephson circuit using an Andreev interferometer

Andrea Iagallo

Royal Holloway College
University of London

Supervisors:

Prof. V. T. Petrashov Dr. J. T. Nicholls

Dissertation submitted for the degree
of Doctor of Philosophy

July 18, 2011

Declaration of Authorship

I Andrea Iagallo hereby declare that this thesis and the work presented in it is entirely my own. Where I have consulted the work of others, this is always clearly stated.

Signed:

Date: 18/07/2011

Abstract

We report on measurements of macroscopic quantum states in superconducting Josephson circuits using a highly sensitive hybrid quantum interferometer as the readout probe. The investigated Josephson circuit is one of the leading candidates as solid-state qubits (persistent current qubit), which are known to exhibit macroscopic quantum states with atomic-like properties. The readout device is a modified Andreev interferometer with semi-metallic normal segment in a "folded" geometry, and is designed to reduce the back action during measurement, as well as minimising the electromagnetic coupling between the circuit and the environment.

A pulsed lock-in technique has been developed to perform continuous readout of the superconductor phase difference using pulse lengths down to 10 ns. The technique enables to control the energy of the probing quasiparticles in the normal segment of the interferometer, which in turn allows to control of the supercurrent flowing in the SNS junction and prevents electron heating of the normal segment.

An experimental set-up was designed and installed in a dilution fridge consisting of shielded wiring, magnetic screens, RF tight sample holder and printed circuit board to allow the injection of high frequency excitation signals, while minimising the environment effect on the qubit through careful electrical filtering. The effect of strong RF irradiation on Andreev interferometers allowed us to estimate the response time of the readout device to be less than 40 ps.

The measurements show that two macroscopically distinct metastable states exist when the device is biased at the qubit degeneracy point, between which the system makes transitions that can be continuously monitored. Real time kinetics of the system has been investigated at different magnetic fluxes, pulse parameters, temperature and RF radiation. Based on statistical analysis of the transitions, we argue that the metastability is connected with macroscopic quantum tunnelling effects rather than thermal excitation. The experimental data support the hypothesis of a large low frequency noise causing low transition rates.

Acknowledgments

First of all, I would like to thank both my supervisors Prof. Victor Petrashov and Dr. James Nicholls for their help and support. They lead me through my PhD with their expertise and precious advice, while allowing me to carry an independent work. Among the many reasons, a special thank goes to Prof. Petrashov for finding extra economic support in the final year, while I am indebted to Dr. Nicholls for his constant help while writing my thesis.

My thanks go to all the technicians working in the workshop, who helped me in many occasion. In particular, I am very grateful to Mr. Massimo Venti, whose skills and expertise have been essential for this project, and from whom I have learned many useful things.

I would like to thank Dr. Chris Checkley for teaching me how to use the clean room facilities, and for being always available to help me during the sample fabrication.

I am grateful to Dr. Gregoire Ithier for his advice in building a cryogenic setup, which has been essential to understand the role played by noise and the need to reduce it.

My sincere thanks go to Dr. Giovanna Tancredi and Dr. Michele Faucci Giannelli, with whom I shared many happy moments, and who were a constant source of encouragement and help.

I wish to thank my friends Alessandra, Elio, Marco and Simona, who have always been present though the distance, because time seems to pause when we are apart, and then to restart when we meet again.

Of course my parents and brothers deserve one of the biggest thanks, for their support and encouragement which allowed me to pursuit my interests.

Finally, a special place is held by my girlfriend Giorgia, because she always stands patiently my mood swings and gives me her endless support and encouragement.

Contents

Chapter 1

Introduction

1.1 Overview

Since the proposal of R. Feynman in 1982 [1] of a universal quantum simulator, great interest aroused in the scientific community. The reasons for studying it go beyond constructing a quantum computer, and involve the possibility of realising artificially fabricated structures showing quantum-mechanical coherence.

In a quantum computer, the elementary unit is called a quantum bit (or qubit). The simplest qubit is a two-state quantum system which, as a classical bit, can be found in two distinct states, but has the additional important property that it can also be found in a linear superposition of such states. Computation is performed by the manipulation of the qubit state, which involves the creation and the readout of this superposition states. The construction of a quantum computer seems a long-time prospect, as it would require the realisation of quantum memory registers containing at least $\sim 10^4$ qubits, while so far interaction between only a limited number (≤ 10) of qubit has been achieved [2]-[4]. On the other hand, this aspect put in evidence one of the main features of a quantum bit, which is the scalability.

Several systems have been proposed in the past, including among the many, cavity quantum electrodynamics systems [5], ion traps [6], and nuclear spins [7], all of which are promising candidates for single qubits. However, interaction between a large number of these systems is still a difficult task. On the other hand, solid state circuits can be integrated into standard large-scale fabrication technology, which makes them scalable. Thus, in principle, no limit exists to the number of qubits which can be put in interaction.

Many solid-state qubits are based on superconducting technology and make use of mesoscopic Josephson junctions as main element. Several im-

plementations of Josephson devices has been proposed, which show macroscopic quantum effects when the coupling to external degrees of freedom is sufficiently reduced. Josephson qubits are conventionally grouped into three major categories depending on the quantum variable used to store the information: charge in confined superconducting islands ("charge" qubit or Cooper-pair box [8]), phase difference across Josephson junctions ("flux" or "persistent current" qubits [9, 10], and "phase" qubits [11]), and phase-charge ("quantronium" circuit [12]).

Microscopic systems (e.g., atoms, photons, spins...) can be easily isolated from the environment, Josephson devices however are subject to more severe interactions due to their integration in a solid-state environment. Coupling to external degrees of freedom is undesirable as it leads to the phenomenon of "decoherence", which causes the loss of quantum coherence and thus leads to an irreversible collapse of the qubit into a classical state. Quantum superposition of states and coherent oscillations has been observed in all three Josephson qubits. Currently, coherence times in the microsecond range [13] has been achieved, and coupling between three qubits has been established using different coupling methods (see Ref. [14] and references therein). Nevertheless, the use of these elements in a practical quantum computer is still far from being realised, and great efforts, both theoretical and experimental, are continuously undertaken to further decrease decoherence.

Typically, carefully designed cryogenic experimental setups are used, aimed at attenuating external electrical and magnetic noise from the laboratory. One of the major decoherence source is the local electromagnetic environment, defined by the leads that are coupled to the read-out device or are used to apply control signals. These leads provide great flexibility in control of the system, but are also a source of considerable coupling to the environment.

Particular attention has been paid to the readout method used to recover the information of the quantum state of the qubit. A suitable device needs to be implemented, which entangles with the qubit to collect the information on its state, and transfers this information to a macroscopic variable which can then be detected by an experimental measurement setup. From this point of view, maximum coupling between the readout device and the qubit is desirable. However, the same coupling is also responsible for the exposure of the qubit to environmental noise, as the detector connects the output ports of the circuit, subject to noise from the experimental setup, to the qubit location. Moreover, the detector is a mesoscopic device permanently coupled to the qubit, and can act itself as a source of decoherence. These aspects determine the backaction of the readout device, which is of central importance for implementing an efficient measurement scheme.

1.2 This project

This thesis investigates the use of a novel readout method of the state of superconducting "persistent current" (or "flux") qubits. A hybrid superconductor/normal metal device, known as an Andreev interferometer, was first proposed in Ref. [15], and its attractive properties made it a promising candidate as an efficient and low-backaction readout device. In that work, measurements of the ground state of a flux qubit were performed exploiting the sensitivity of the interferometer resistance to the Josephson phase difference across the qubit.

Flux qubits are mesoscopic loops of superconducting metal containing one [9], three [10] or four [16] Josephson junctions, whose parameters can be suitably engineered to create a device with atomic-like properties. For certain values of magnetic flux through the loop, two classically degenerate states exist, corresponding to persistent currents flowing in opposite directions, whose coherent superpositions form the qubit states. The existence of these superposition states, as well as their coherent evolution, has already been demonstrated [10], and the decoherence mechanisms has been extensively studied. Most experiments employ measurement methods based on Superconducting Quantum Interference Devices (SQUIDs), used as magnetometers to detect the magnetic moment associated with the persistent currents. This requires the SQUID to be switched to the voltage state, and the information on the qubit state is inferred from a statistical analysis of $\sim 10^4$ switching events.

The readout method investigated in this thesis aims to detect the qubit state via a simple measurement of the interferometer resistance, which can be achieved using standard lock-in techniques. Previous work by Dr. Kok Gnee Chua [17] and Dr. Kevin Marshhall [18] concentrated on the feasibility of this approach, and identified designs parameters necessary to maximise the read-out efficiency. More recently Dr. Chris Checkley [19] perfected the fabrication technology which allows unprecedented control over small size structures, and reported the first evidence of spectroscopy of a qubit probed by an Andreev interferometer.

In this thesis, two novel features has been introduced into the interferometer design: an Antimony normal conductor was used to increase the resistance of the interferometer, thus decreasing its backaction on the qubit; a "folded" geometry for contacting the electrical leads to the interferometer, thus reducing the electromagnetic coupling between the device and the en-

vironment.

A lock-in technique has been developed to measure the interferometer resistance with pulsed signals with frequencies up to 1 MHz and pulse lengths down to 10 ns. This method allows continuous monitoring of the superconductor phase difference, while enabling control of the energy of the probing quasiparticles in the normal segment of the interferometer. This aspect is important as it prevents electron heating in the normal segment.

An experimental set-up was designed and installed in a dilution fridge to perform measurement on interferometer-qubit devices in a low-noise environment. This required the installation of shielded wiring, magnetic screens, RF tight sample holder and printed circuit board to allow the injection of high frequency excitation signals, while minimising the environmental effect on the qubit through careful electrical filtering. The properties of this modified interferometer-qubit devices required a deep investigation with respect to temperature and pulse parameters, and were complemented by the investigation of the effect of RF radiation on an Andreev interferometer.

The measurements show that two macroscopically distinct metastable states exist when the device is biased at the qubit degeneracy point, between which the system makes transitions with typical rates of 0.01-10 s^{-1}. These transitions were continuously monitored and their real time kinetics has been investigated at different magnetic fluxes, pulse parameters, temperature and RF radiation. The statistical analysis of the transitions gives evidence that the metastability is connected with quantum macroscopic tunnelling of the phase between the persistent current states of the qubit. We argue that the small transition rates are caused by a large low-frequency noise whose origin has not yet been identified.

Chapter 2

Josephson circuits as superconducting qubits

2.1 Josephson junctions

2.1.1 Fundamental equations

The basic building block of superconducting Josephson elements is the so called "Josephson junction", which is formed when two superconducting electrodes are separated by a thin ($\sim 2-3$ nm) insulating layer. The behaviour of this system was studied by B. D. Josephson in 1962 [20], who predicted two phenomena, known as DC and AC Josephson effects, described respectively by the equations

$$I = I_0 \sin(\varphi), \tag{2.1}$$

$$\frac{d\varphi}{dt} = \frac{2eV}{\hbar}, \tag{2.2}$$

which link the current I flowing through the tunnel junction and the voltage V across it. In these equations, I_0 is a characteristic constant of the junction, called "critical current", and $\varphi = \varphi_2 - \varphi_1$ is the difference between the phases φ_2 and φ_1 of the order parameters of the superconducting electrodes. A simple derivation of these equations can be found in [21]. Equation (2.1), which describe the so called "DC" Josephson effect, states that a dissipationless current can flow through the junction even when no voltage is applied across it, and its amplitude is determined by the superconductor phase difference. Upon integrating Eq. (2.2) and inserting the result into Eq. (2.1), one finds that, if a voltage V is applied, the current I is an alternating current, oscillating at the frequency $\nu = 2eV/h$, hence the name "AC" Josephson effect given to this effect.

An alternative representation of a Josephson junction as a non-linear phase-dependent inductor is often used. By derivating Eq. (2.1) with respect to time and making use of Eq. (2.2), one easily finds a relation of the form $V = L_{JJ}\frac{dI}{dt}$, where

$$L_{JJ} = \frac{L_J}{\cos(\varphi)}, \tag{2.3}$$

and $L_J = \frac{\hbar}{2eI_0}$ is the Josephson inductance.

2.1.2 The RCSJ model

A Josephson junction is usually described by the circuit representation shown in Fig. 2.1(a), known as Resistively-Capacitively Shunted Junction (RCSJ) model. In this model, the junction is described as the parallel combinations of three lumped elements: an ideal current source described by Eq. (2.1), a resistor R and a capacitor C. The resistor accounts for the current dissipation in the finite voltage regime ($I > I_0$), while C is the geometric capacitance between the electrodes. With reference to Fig. 2.1(a), the total current trough the junction can be written as

$$I = I_0 \sin(\varphi) + \frac{V}{R} + C\frac{dV}{dt}. \tag{2.4}$$

This equation can be rewritten in the form

$$\gamma M\frac{d\varphi}{dt} + M\frac{d^2\varphi}{dt^2} = E_J\left[\alpha - \sin(\varphi)\right], \tag{2.5}$$

by making use of Eq. 2.2, and defining the quantities

$$M = \left(\frac{\Phi_0}{2\pi}\right)^2 C, \qquad \gamma = \frac{1}{RC}, \tag{2.6}$$

$$\alpha = \frac{I}{I_0}, \qquad E_J = \frac{\Phi_0}{2\pi}I_0, \tag{2.7}$$

where the flux quantum $\Phi_0 = \frac{h}{2e} \approx 2.06\times10^{-15}$ Wb has been introduced. Eq. 2.5 allows to draw the analogy between the classical dynamics of a Josephson junction and that of a particle of mass M moving along the coordinate φ while subject to the damping γ, in a potential $U(\varphi,\alpha) = -E_J\left[\alpha\varphi + \cos(\varphi)\right]$. The potential $U(\varphi,\alpha)$ assumes the form of a "tilted washboard", and is plotted in Fig. 2.1(b) for different values of the parameter α. For α=0, the particle is localised at one of the potential minima, say at φ=0, where, ignoring thermal

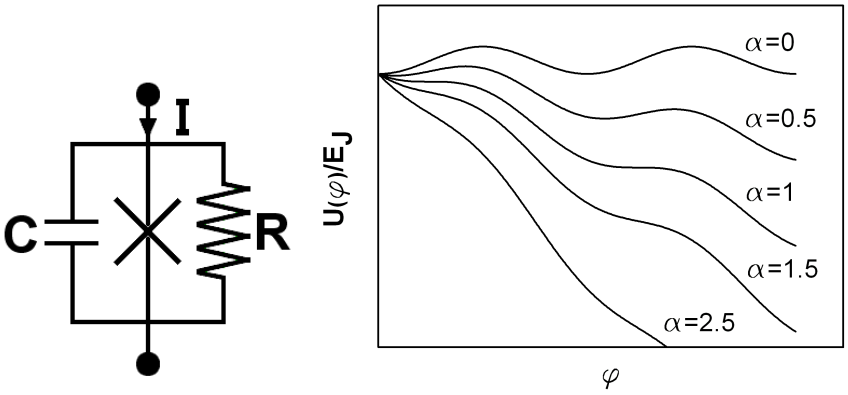

(a) (b)

Figure 2.1: *(a) RCSJ equivalent circuit of a Josephson junction, comprising a resistor R, a capacitor C, and the non linear current source ("×" symbol) described by Eq. 2.1. (b) Tilted washboard potential $U(\varphi)/E_J$ for different value of α.*

or quantum activation processes, it is trapped by the two large barriers at each side. As α is increased, the tilting of the potential will increase, and the minimum position move to larger φ. Thus, a dissipationless current flows per Eq. (2.2), but no voltage drop exists across the junction. When α=1, the barrier height on one side disappears. Further increase of α will cause the particle to move from the minimum position and roll down the potential. This situation corresponds to the finite-voltage state of the junction, where the change in φ produces a voltage across the junction via the relation in Eq. 2.2. When $\alpha \gg 1$, the junctions shows an Ohmic behaviour ($\frac{\hbar}{2e}\frac{d\varphi}{dt} \approx RI$).

2.1.3 Relevant energy scales

The Josephson coupling energy E_J, already used to define Eq. (2.5), measures the coupling strength between the two superconducting electrodes, and arises when calculating the electrical work W_J necessary to produce a change of the Junction phase. By integrating in time the electrical power $P = VI$, where V and I are given by Eqs. 2.2 and 2.1, respectively, one finds (up to a constant)

$$W_J = -\frac{\hbar I_0}{2e}\cos(\varphi) = -E_J\cos(\varphi), \tag{2.8}$$

which was the phase dependent term entering the potential $U(\varphi)$ calculated above.

Analogously, the energy associated to the tunnelling of one Cooper pair through the junction can be calculated as the work needed to move a charge $2e$ from one plate to the other of the capacitor C, which gives the so called charging energy

$$E_C = \frac{(2e)^2}{2C}. \tag{2.9}$$

The two energies defined above play an important role in designing superconducting qubits. The two quantities associated with each energy, the phase φ and charge Q, are quantum conjugate variables, and thus obey to Heisemberg's uncertainty relation [22]. If $E_J \gg E_C$, the phase φ is a well defined quantity while Q is subject to large fluctuation. This regime is used in phase or flux qubits [9, 10, 11], where the phase φ (or the associated magnetic flux Φ) is the control variable used to manipulate and readout the quantum state. On the other hand, if $E_J \ll E_C$, the charge Q is the suitable quantity to be manipulated, as it is exploited in charge qubits [8].

A further important parameter characterising a Josephson junction is the plasma frequency ω_p. In the classical representation of a junction given above, ω_p is the characteristic frequency of small oscillations at the bottom of the potential well when α=0, and is given by

$$\omega_p \equiv \left[\sqrt{\frac{d^2U(\varphi)}{d\varphi^2}}\right]_{\alpha=0} = \frac{1}{\hbar}\sqrt{2E_J E_C}. \tag{2.10}$$

The plasma frequency coincides with the "attempt" frequency, i.e., the frequency at which the particle "knocks" against the potential barrier, and is an important parameter in defining the tunnelling probability in a flux qubit [23].

The two energies are characteristic properties of a junction, depending on the geometry and the insulating barrier, and can be tuned during the fabrication process.

2.2 The persistent current qubit

The persistent current qubits are mesoscopic loops of superconducting metal containing one [9], three [10] or four [16] Josephson junctions. Here, to describe the main properties of these devices, we focus on the three-junction design, which has been more deeply investigated. The qualitative description of this design extends also to the four-junction design used in this thesis, for which an analytical representation of the potential energy can not be

obtained.

The three junction flux qubit was first proposed in Ref. [24]. In this device, two junctions are fabricated to have the same nominal critical current I_0, while the critical current of the third is smaller by a factor α=0.5-0.8. The high value of the energy ratio E_J/E_C =10-100 provides well defined phases across the junctions. The superconducting loop is designed to have a small geometric inductance, and the phases across the junctions are bound by the fluxoid quantisation condition to the externally applied flux Φ through the relation

$$\sum_{i=1}^{3} \varphi_i = \frac{2\pi\Phi}{\Phi_0}. \tag{2.11}$$

where φ_i is the phase of the i^{th} junction. This condition allows to write the system potential energy in the bidimensional form [23]

$$U(\varphi_1, \varphi_2) = E_J \left[2 + \alpha - \cos(\varphi_1) - \cos(\varphi_2) - \alpha \cos(2\pi \frac{\Phi}{\Phi_0} + \varphi_1 - \varphi_2) \right], \tag{2.12}$$

shown in Fig. 2.2(a) for $\Phi = 0.5\Phi_0$. At this value of magnetic flux, the potential forms a symmetric double well as a function of the phase coordinate φ_m defined along the direction $\varphi_1 = -\varphi_2$, allowing for two classically stable positions located at $\varphi_m = \pm\varphi_m^*$ and separated by a barrier. The two degenerate minima correspond to classical persistent currents of amplitude I_p flowing around the superconducting loop in opposite directions. In a quantum mechanical picture, these currents are associated to the ground states $|0\rangle$ and $|1\rangle$ of the discrete set of quantum levels localised in each well of the double well potential.

For suitable heights of the barrier, quantum tunnelling between the persistent current states occurs, and the system is described by a symmetric and an antisymmetric superposition of the states $|0\rangle$ and $|1\rangle$, shown in Fig. 2.2(b), given by

$$|g\rangle = \alpha\,|0\rangle + \beta\,|1\rangle\,, \tag{2.13}$$

$$|e\rangle = \alpha\,|0\rangle - \beta\,|1\rangle\,, \tag{2.14}$$

where, for a symmetric double well, $\alpha = \beta = 1/\sqrt{2}$. As effect of the tunnelling, this states are separated in energy by an amount Δ, hence the labels "g" (ground) and "e" (excited) used above. More generally, the tunnelling occurs in a narrow region around $\Phi = 0.5\Phi_0$, and the energy splitting between these states is

$$\nu = \sqrt{\Delta^2 + \epsilon^2}, \tag{2.15}$$

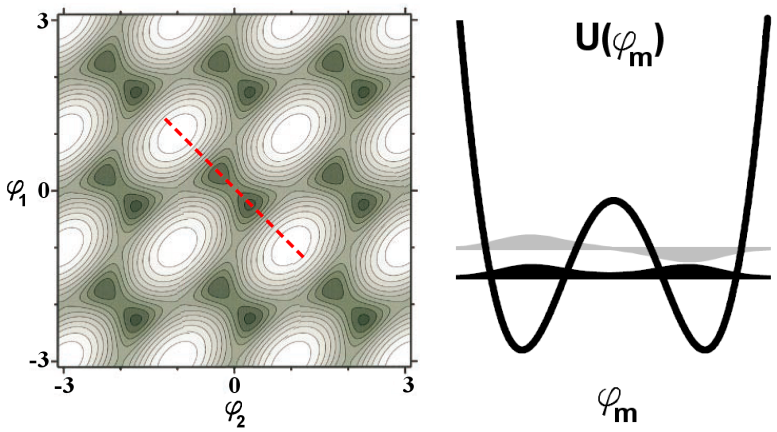

(a) (b)

Figure 2.2: *(a) Contour plot of the potential* $U(\varphi_1, \varphi_2$ *for* $\Phi = 0.5\Phi_0$*. The direction* $\varphi_1 = -\varphi_2$ *is indicated by the red dashed line. Adapted from Ref. [24] (b) Double well potential and wavefunctions of the symmetric (black) and antisymmetric (grey) superposition of the states* $|0\rangle$ *and* $|1\rangle$ *localised in each well.*

where $\epsilon = 2I_p\,(\Phi - 0.5\Phi_0)$. The energy spectrum of the ground and excited states as a function of magnetic flux Φ is shown in Fig. 2.3, together with the energies of the classical persistent current states $|0\rangle$ and $|1\rangle$. As the quantum tunnelling lifts the degeneracy between the classical states at $\Phi = 0.5\Phi_0$, the shape of this spectrum is often referred to as "anti-crossing". The corresponding quantum mechanical expectation value $\langle I_p \rangle$ of the persistent current associated with the states $|g\rangle$ and $|e\rangle$ is shown in the lower panel of Fig. 2.3.

2.3 Readout methods for flux qubits

The readout method for flux qubits proposed in Ref. [24] uses a two-junction Superconducting Quantum Interference Device (DC SQUID) as magnetometer to detect the magnetic flux associated with the persistent currents. In this design, shown in Fig. 2.4(a), the DC SQUID surrounds the qubit loop and thus couples inductively to it. A second design, where the coupling is further increased by direct contact between the SQUID and the qubit, as shown in Fig. 2.4(b), was also proposed [26]. In these systems, the detection of the qubit state is performed by measuring the SQUID switching

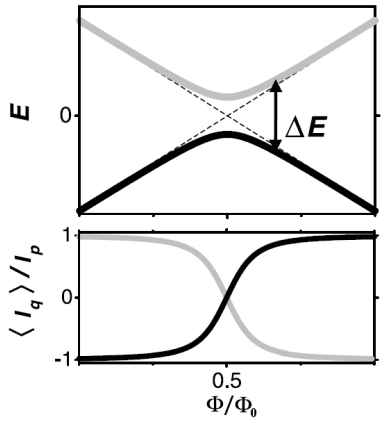

Figure 2.3: *Upper: Energy spectrum of a persistent current qubit as a function of magnetic flux* Φ*. The dashed lines are the energies of the classical states* $|0\rangle$ *and* $|1\rangle$*, which are degenerate at* $\Phi = 0.5\Phi_0$*. Also shown is the energy splitting* ν*. Lower: Quantum mechanical expectation value* $\langle I_p \rangle$ *of the persistent current, normalised to the amplitude* I_p *of the classical current. Figure adapted from Ref. [10]*

current I_{SW} which, being dependent on the flux threading the its loop, is sensitive to the changes of flux induced by the variations of $\langle I_p \rangle$. Typically, the SQUID is biased with a current pulse of amplitude $I < I_{SW}$, and the measurement consists in determining if a switching to the voltage-state has occurred in a certain time interval. The detection of the qubit state is obtained by performing repeated (typically $\sim 10^3 - 10^4$) measurements of this kind, thus obtaining the information on the qubit state from the probability of switching of the SQUID.

With a SQUID readout, spectroscopic measurements on single persistent current qubits were successfully performed by applying pulses of microwave radiation at the qubit resonant frequency [10], which produced the energy spectrum, as shown in Fig. 2.5(a). The implementation of more complex pulse sequences based on NMR techniques (for a review, see Ref. [27]) allowed to obtain the manipulation of the qubit state [26, 28], such as the coherent Rabi oscillations shown in Fig. 2.5(b). Currently, relaxation and decoherence times of the order of microseconds can be achieved [13].

Spectroscopic measurements on coupled flux qubits were also performed [29] and where able to resolve the multilevel spectrum arising from the qubit interaction. Recently, operation of a C-NOT logic gate in a two qubit system was demonstrated [30].

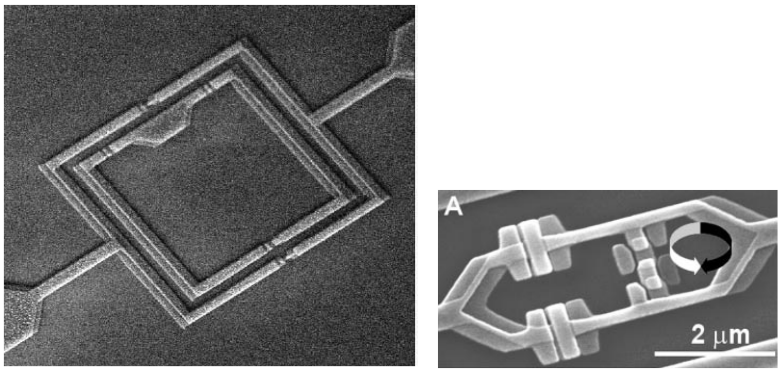

(a) (b)

Figure 2.4: *SEM images of flux qubit employing where the SQUID is (a) coupled inductively and (b) directly attached to the qubit. Images from Refs. [25] and [26].*

Despite the success of this readout method, it has two major disadvantages. The first is related to the intrinsic stochastic nature of the switching event, which requires that a large number of readings are acquired to infer the qubit state. A second drawback is due to dissipation of energy occurring when the SQUID switches to the finite-voltage state, which requires long waiting times between the readings. Moreover, the qubit state is perturbed during the switchings. Alternative readout methods have been proposed to overcome this problems. Dispersive readout methods involving the measurement of the impedance of linear resonators were successfully implemented. These methods use lumped elements circuits with high quality factors ($\sim 10^4$) inductively coupled to the qubits, where the detection of the qubit state is inferred by measurement of the effective impedance. With these method, coherent evolution of single flux qubits [31] was measured and spectroscopy on a two qubit system was performed [32]. Recently, also different approaches based on non-linear resonators were implemented [33, 34, 35].

2.4 The Andreev interferometer readout

The readout method investigated in this thesis is based on the use of an Andreev interferometer to readout the state of a device designed to work as a persistent current qubit. Compared to the methods described in the previous sections, the proposed method is believed to have some advantages.

The simple relation between the phase across the qubit loop and the

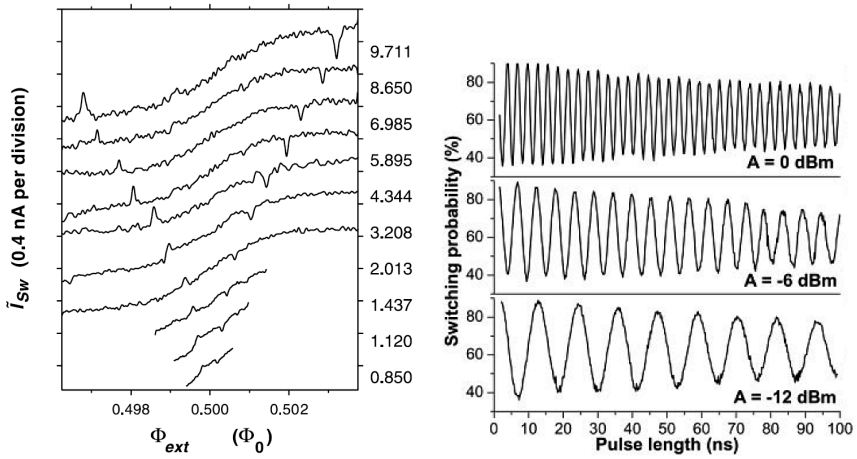

(a) (b)

Figure 2.5: *(a) Spectroscopic measurement using a DC SQUID. From Ref. [10]. (b) Coherent oscillations of the qubit state measured in Ref. [26].*

interferometer resistance, described in detail in Sec. 4.1.3, promises to reduce the problem of the detection of the qubit state to a more simple measurement of resistance, which can be achieved using standard lock-in technique. This technique would also guarantee continuous monitoring of the qubit state. Moreover, the direct coupling achievable with the design used in this thesis would allow to readout the state of each single qubit in an array comprising several qubits.

The backaction mechanisms of our method on the qubit are still not completely understood. In particular, the problem of noise induced by the readout SNS junction deserve a more deep investigation. As shown in this thesis (see Sec. 8.2.3), thermal noise due to the normal metal section of the interferometer, which was thought to be the main contribution to decoherence in our readout method, is a minor issue. Experimental data show that the coupling to a quantum mechanical environment with strong low frequency component seems the main cause of decoherence.

Chapter 3

The proximity effect and Andreev interferometers

3.1 The superconducting proximity effect

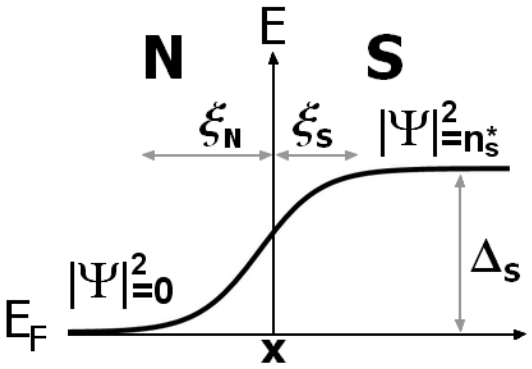

Figure 3.1: *Schematic of N/S interface. The contact between a normal conductor (N) and superconductor (S) causes a modification of the properties at the N/S interfaces in a region of width given by the coherence lengths ξ_N and ξ_S.*

On a mesoscopic length scale, the contact between a superconductor (S) and a normal conductor (N) produces a series of interesting phenomena collectively known as proximity effect. The composite system can be described qualitatively within the Ginzburg Landau theory [36] by means of a space-dependent order parameter $\Psi(x)$, whose square modulus $|\Psi(x)|^2$ gives the local density of superconducting electrons $n_s(x)$. When a normal conductor

is put in electrical contact with a superconductor, pairing correlations are induced into the N side by the proximity with S, resulting in a "leakage" of the order parameter into N, as schematically shown in Fig. 3.1. Conversely, the effect of the N conductor on the superconductor is a reduction of the order parameter in the latter in a narrow region near the interface.

The order parameter changes continuously across the interface, with a smooth variation from $|\Psi(x)|^2$=0 (deep into N) to its maximum $|\Psi(x)|^2 = n_s^*$ in S, and has a finite amplitude in the intermediate region across the N/S interface. The transition occurs within length scales of the order of the coherence lengths ξ_S and ξ_N in S and N, respectively [37]. For temperatures well below the superconductor critical temperature, the coherence length ξ_S in S depends on the Fermi velocity v_F and the zero temperature superconducting gap $\Delta_S(0)$, and is given by [38]

$$\xi_S = \frac{\hbar v_F}{\pi \Delta_S(0)}, \tag{3.1}$$

For a normal conductor at thermal equilibrium and in the diffusive regime, i.e., when the dimensions of the N sections are much larger than its mean free path ℓ, the coherence length ξ_N is given by the thermal coherence length [37]

$$\xi_T = \sqrt{\frac{\hbar D}{2\pi k_B T}}, \tag{3.2}$$

where $D = \frac{1}{3} v_F \ell$ is the diffusion coefficient of the normal conductor.

3.2 Andreev reflection

The transport properties at an N/S interface show interesting features arising from the different electronic structure in the two N and S electrodes, as shown in Fig. 3.2. At equilibrium, the electrons in N responsible for charge transfer have energies $\sim k_B T$ around the Fermi energy E_F; when the electron energy is smaller than the superconductor energy gap Δ_S, i.e. $k_B T < \Delta_S$, no single particle states are available in the superconductor at the other side of the interface, where the energy gap Δ_S prevents a direct charge transfer from N to S. An electron having such an energy and moving toward the N/S interface should then be reflected at the N/S boundary. If one considers the "ordinary" reflection represented in Fig. 3.3(a), this mechanism implies that the wavevector component $k_{||}$ parallel to the interface remains constant, while the perpendicular component $k_\perp$ is reversed. The reversal of $k_\perp$ would

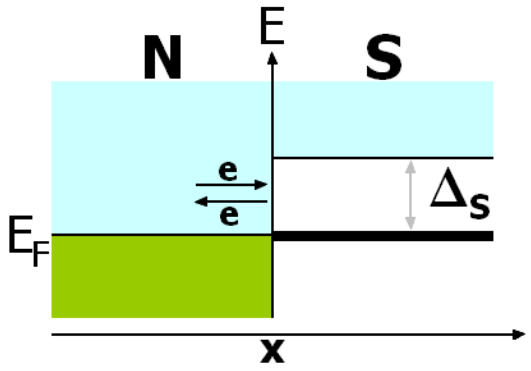

Figure 3.2: *Schematic of the band structure at a N/S interface.*

require a total change $\Delta k_\perp \approx 2k_F$, where k_F is the Fermi wavevector which has typical values $k_F \sim 10^{10}\ m^{-1}$ [39]. Such wavevector change can not be provided by the smooth potential variation across the interface, and the reflection of the incoming electron, as well as its transmission, is forbidden.

In 1964, Andreev [40] suggested a mechanism of charge transport through a N/S interface, named "Andreev reflection", which allows the transfer of charge through a N/S interface at energies $E < \Delta_S$ by involving the retro-reflection of a quasiparticle and the simultaneous creation of a Cooper pair in the superconductor. Andreev reflection is central to the proximity effect because it provides a microscopic mechanism for the penetration of the superconductor correlations into the normal conductor.

The mechanism can be explained with the aid of Fig. 3.3(b) considering an electron approaching the N/S interface from the N side. Due to interaction with the pairing potential in the interface region, the electron gradually loses its electron-like character and acquires a hole-like character. During the process, both the electron charge e and velocity v_e change their sign, thus producing the reflection of the initial electron as a hole. During the process, the total charge q_N in N undergoes a change $\Delta q_N = -2e$, due to the loss of charge of the incoming electron $(-e)$ and the appearing of the reflected hole $(-e)$. Charge conservation imposes that a total charge $\Delta q_N = -2e$ must enter the S side, which occurs with the creation of a Cooper pair. The Andreev reflection mechanism can be straightforwardly inverted to account for the transfer of charge from the superconductor to the normal conductor, in which case a Cooper pair from S diffuses into N as an electron moving away from the interface and a hole moving toward it.

Compared to the "ordinary" reflection, where the momentum and velocity components parallel to the interface are conserved while the perpendicular

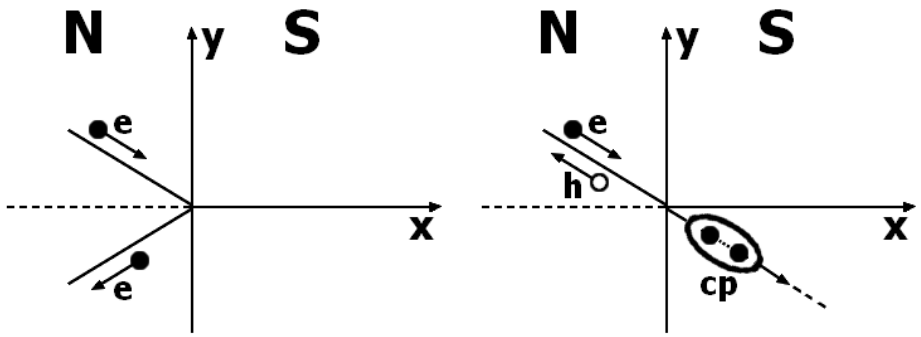

Figure 3.3: *Reflection mechanisms for quasiparticles of energies $E < \Delta_S$ at a N/S interface: (a) Ordinary reflection and (b) Andreev reflection. An ordinarily reflected electron* ***e*** *follows a specular trajectory with respect to the incoming electron. During Andreev reflection, the incoming electron* ***e*** *is transformed into a hole* ***h****, which retraces the original trajectory, and a Cooper pair* ***cp*** *is created in the process.*

ones are reversed, during Andreev reflection all the momentum components do not change their direction while all the velocity components are reversed. The Andreev reflected particle is said to be retro-reflected, and retraces the trajectory of the initial quasiparticle.

Perfect retro-reflection occurs only when the initial quasiparticle has an energy $E = E_F$, because in such case its wavevector k_e and the one of the Andreev reflected particle, k_h, will be equal. If the electron energy is $E = E_F + \delta E$ (and thus the wavevector is $k_e = k_F + \delta k/2$), the Andreev reflected particle will have energy $E_h = E_F - \delta E$ (and wavevector $k_h = k_F - \delta k/2$), with an overall energy difference $\Delta E = 2\delta E$ and wavevector mismatch $\Delta k = \delta k$. For small energies δE, one finds $\delta k \approx k_F 2\delta E/E_F$, which is an increasing function of δE.

A further property of Andreev reflection is the sensitivity of the correlated pair to the phase χ of the pair potential in the superconductor bank. The transformation of the initial quasielectron into the retro-reflected quasihole is accompanied by a total phase change [41]

$$\delta\vartheta = \chi + \arccos(\frac{\delta E}{\Delta_S}), \tag{3.3}$$

where the second term on the right hand side gives $\pi/2$ when $E = E_F$.

The coherence properties of the quasiparticle pair created by Andreev

reflection can be obtained using a simple model of travelling waves to describe the single electrons in N. In this picture, the phase difference between the two paired quasiparticles is a function of their energy difference ΔE given by $\Delta\varphi \approx \frac{\Delta E}{\hbar}t$, where the phase term due to the wavevector has been ignored. In diffusive regime, the time τ_d needed for a particle to cover the distance x is $\tau_d \approx x^2/D$, which gives the phase difference

$$\Delta\varphi = \frac{x^2}{\xi_E^2}, \tag{3.4}$$

where the quantity

$$\xi_E = \sqrt{\frac{\hbar D}{\Delta E}}, \tag{3.5}$$

is the energy-dependent coherence length in N, and sets the length scale for the maximum distance x from the N/S interface below which the two particles maintain their coherence. When the electrons in N are at equilibrium at $E = K_B T$, ξ_E coincides with the thermal coherence length given in Eq. (3.2). Equation 3.5 produces a further important parameter, the Thouless energy E_{TH}, which sets the energy scale below which correlated electron pairs maintain their coherence over the entire length of the normal conductor. For a conductor of length L, the Thouless energy is found by setting $L = \xi_E$ in Eq. 3.5, which gives

$$E_{TH} = \frac{\hbar D}{L^2}. \tag{3.6}$$

Considering the energy dependence of ξ_E given in Eq. 3.5, one finds that if the electron energy is $E = E_F$, an infinite coherence length is obtained. Such unrealistic result is overcome by taking into account single particle phase-breaking events, that has been ignored so far. These events are due to inelastic scattering processes causing random disruption of the particle phase, and occur over a typical length scale L_φ called phase-breaking length. At sub-Kelvin temperature, this length can reach several microns [42], compared to typical values of ξ_T of the order of hundreds of nanometers. Thus, L_φ is the ultimate upper limit to ξ_E, which allows to observe the long-range phenomena discussed in Sec. 3.4.

In the following we will consider interference phenomena occurring in normal conductors coupled to superconducting banks. Thus, we will make the implicit assumption that the sizes of the N metal are always smaller than the phase breaking length, so that the relevant length scale in these systems is the coherence length ξ_E.

3.3 SNS weak links

Interesting physical systems are created when two superconductors are connected by a region of "weak" superconductivity. These systems, generally known as "weak links" [43], can be created by a variety of physical implementations, such as using thin insulating layers or normal metal sections where the proximity effect induces a weak superconducting state. If the length L of the weak link is $L < 2\xi_T$, then the order parameters induced in N by the proximity effect from both S sides will overlap, and coupling of the superconductors is established. With the aid of Eq. 3.6, one can see the importance of the Thouless energy as energy scale for defining two regimes for SNS junction: $E < E_{TH}$, when the induced correlations extend to the whole length L of the N wire, and $E > E_{TH}$, in which case the order parameter in N decays within a length shorter than L.

In SNS systems, Andreev reflection at two interfaces gives rise to interference phenomena that modify the quasiparticle density of state (DOS) in N. A structured DOS appears, comprising an energy gap and a spectrum of current-carrying energy levels responsible for the flow of a dissipationless current. Both features are described in Secs. 3.3.1 and 3.3.2. The effect of proximity induced correlations on the conductance will be discussed instead in Sec. 3.4, where, due to the close relation of this property with superconductor phase, a review of Andreev interferometers is also reported.

3.3.1 Proximity induced mini-gap

The correlations induced into a normal metal by the proximity effect cause a modification of the quasiparticle density of states (DOS) at energy around the Fermi energy E_F. The spectrum of quasiparticle states presents an energy gap similar to the that in a bulk superconductor, but with smaller amplitude, hence the term "mini-gap" usually found in literature.

The presence of such a structured DOS in N/S systems was experimentally observed by Guéron *et al.* [44] as a function of the distance from the interface by tunnelling spectroscopy , and their results were later explained within the quasi-classical Green's function formalism in Ref. [45]. In these works, the dependence of the characteristic energy scale describing the induced gap on the distance x from the interface was confirmed to follow the expected $E \sim \hbar D/x$ form, arising from the diffusion time $\tau \sim x^2/D$.

In a diffusive SNS junction where the length $L \approx \xi_N$, an energy gap $E_g \sim E_{TH}$ is formed in the DOS as a result of Andreev reflections occurring at both interfaces. The sensitivity of correlated pairs in N to the phases χ_1 and χ_2 of the order parameters in the S electrodes causes the amplitude of

the gap to depend on the phase difference $\Delta\chi = \chi_2 - \chi_1$ [46], with maximum amplitude at $\Delta\chi = 0$ and complete suppression at $\Delta\chi = \pi$, as shown in Fig. 3.4(a).

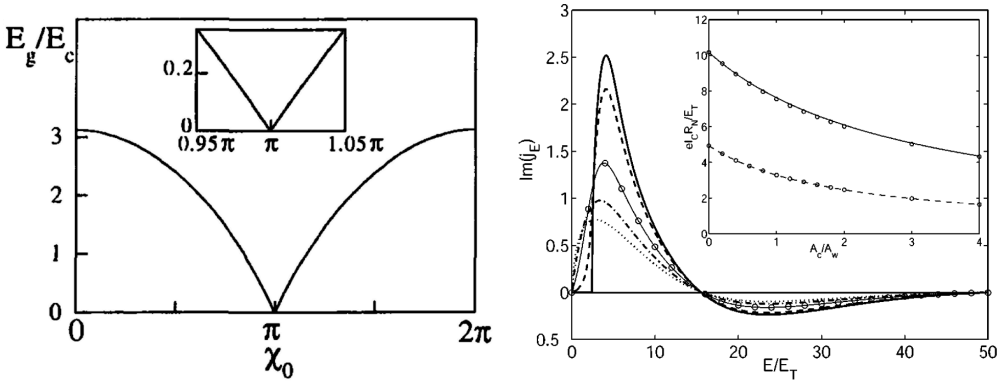

(a) (b)

Figure 3.4: *(a) Induced mini-gap amplitude as a function of superconductor phase difference in an SNS junction of length $L \approx \xi_N$, reproduced from Ref. [46]. (b) Spectral current density as a function of quasiparticle energy E normalised to the Thouless energy E_T, in a cross-shaped SNS junction with different cross section of the control probes A_c. Inset: Junction critical current as a function of A_c/A_w, where A_w is the width of the N wire. Reproduced from Ref. [57].*

3.3.2 Supercurrent transport

In a SNS weak link, the supercurrent is carried by a spectrum of bound states created in the normal metal by the quasiparticles Andreev reflected at both N/S interfaces. The formation of such states can be explained with simple arguments considering an SNS system in the ballistic regimes, that is, when the dimensions of the normal conductor are smaller than the elastic mean free path. In this regime, the Andreev reflected quasiparticles travel between the interfaces without their trajectories being deflected by scattering events. In these systems, a bound state is formed when the phase change acquired by a quasiparticle after reflection at both N/S interfaces is a multiple of 2π. As this double reflection results in the transfer of a Cooper pair from one superconducting contact to the other, the bound state carries a supercurrent. A whole discrete spectrum of bound states is thus formed, composed by two subsets carrying current in opposite direction [47], which,

if not equally populated, give a net phase-dependent supercurrent.

If a diffusive N conductor is considered, the broad distribution of electron trajectories due to elastic scattering causes a smearing of the energy spectrum, and the supercurrent is thus a continuous function of quasiparticle energy. The discrete density of states is substituted by a continuous spectral current density J_S, see Fig. 3.4(b), which can be calculated using the quasiclassical Green's function theory [48, 49] for a given SNS geometry. The observable supercurrent is then calculated as [50, 51]

$$I_S(\Delta\chi) = \frac{1}{eR_N}\int_0^{+\infty} Im[J_S(\epsilon,\Delta\chi)](1-2f(\epsilon))d\epsilon, \tag{3.7}$$

where R_N is the normal-state resistance of N, and $f(E)$ is the electron-hole distribution function. As in the case of the ballistic system, the spectral density J_S depends on the superconductor phase difference $\Delta\chi$, and produces a phase-dependent supercurrent.

The current-phase relation is predicted to be a periodic function of $\Delta\chi$, with strongly non-sinusoidal shape for lengths $L \ll \xi_N$ [50], as shown in Fig. 3.5(a) for different temperatures. For $k_BT \gg E_{TH}$ or $L \gg \xi_N$ the coupling between the superconducting banks is reduced, and $I_S(\Delta\chi)$ is predicted to have the form [43]

$$I_S(\Delta\chi) \approx I_c \sin(\Delta\chi), \tag{3.8}$$

where I_c is the critical current, i.e., the maximum current which can flow in the weak link without dissipation. Equation (3.8) is the famous Josephson relation valid for SIS (I=insulator) tunnel junctions. A direct measurement of the current-phase relation in a Nb/Ag/Nb junction in the regime $k_BT \geq E_{TH}$ was obtained in Ref. [52] by measuring the screening magnetism with a GaAs/AlGaAs Hall probe. Their results, shown in Fig. 3.5(b), show that $I_S(\Delta\chi)$ recovers the sinusoidal form at around $k_BT \approx 2-3E_{TH}$.

For an SNS junction in the diffusive limit, the temperature dependence of the critical current is expected to be determined by the thermal coherence length ξ_T, as this is the length scale defining the penetration of the correlations into the normal conductor. A functional dependence $I_c \propto e^{-L/\xi_T} = e^{-\sqrt{k_BT/E_{TH}}}$ [53, 43] would then be expected. Experimental investigation on long ($L > \xi_T$) diffusive SNS junctions by Courtois *et al.* [54] reported a functional dependence $I_c \propto e^{k_BT/E_{TH}}$, typical of a ballistic system. The system was later analysed theoretically and calculations performed within the quasiclassical Green's function formalism [55, 56] successfully explained the measured temperature dependence. In the long junction limit

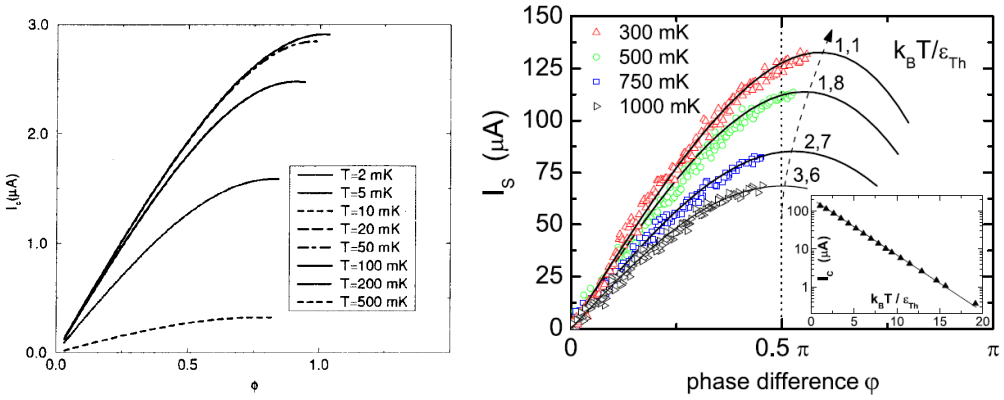

(a) (b)

Figure 3.5: *(a) Current-phase dependence at different temperature calculated in Ref. [55]. (b) Current phase relation of an* ≈ 500 *nm long Nb/Ag/Nb junction at different temperatures. The inset shows the critical current as a function of temperature. Figure from Ref. [52].*

$k_BT > E_{TH}$ (or equivalently $L > \xi_T$), the dependence was found to be

$$I_c \propto T^{\frac{3}{2}} e^{-\sqrt{k_BT/E_{TH}}}, \tag{3.9}$$

which, in the temperature interval investigated in Ref. [54], gives a result numerically very close to the ballistic regime. These results confirmed the exponential suppression of the supercurrent as a function of the quasiparticle energy.

An SNS junction with cross shaped N section was theoretically analysed in Ref. [57], and the effect of the extra terminals on the spectral current density J_S was determined, as shown in Fig. 3.4(b). In such systems, the control probes allow for the existence of states with energies below E_{TH}, and the mini-gap is thus lifted. The effect was calculated for different cross section A_c of the control probes, and showed that J_S is finite even for A_c much smaller than the cross section of the weak link.

The supercurrent through the junction can be altered by inducing a non equilibrium distribution function in the weak link. This effect can be achieved applying a voltage through extra control leads connected to N, as experimentally obtained in Ref. [58]. In this work, fine tuning of the critical current in a cross-shaped SNS junction, shown in Fig. 3.6(a), was obtained by applying a voltage perpendicularly to the junction. The distribution function in the N metal was modified by the injection of "hot" electrons, i.e., electrons

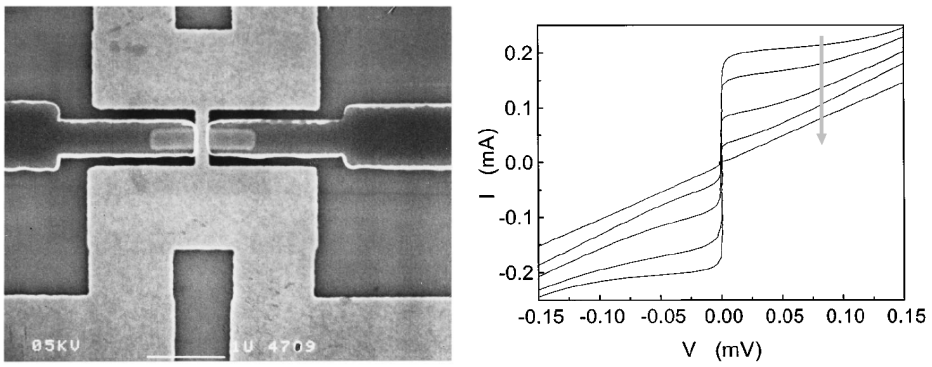

(a) (b)

Figure 3.6: *(a) SNS system measured in Ref. [58] and (b) measured I-V curve at different voltage 0-440 μA across the control line, increasing in the direction of the harrow.*

at a higher energy than those at equilibrium in the weak link, resulting in a reduction of the supercurrent amplitude, as shown in Fig. 3.6(b). In the experiments of Refs. [59, 60] on similar structures , the induced non-equilibrium was observed to produce a change of sign of the supercurrent (π-state).

3.4 Long-range interference effect

Interference phenomena in diffusive SNS junctions were investigated in physical systems known as Andreev interferometers, where the S electrodes are closed in a continuous superconducting loop and their phase difference $\Delta\chi$ can be precisely controlled by changing the magnetic flux through the loop (see Sec. 4.1.1). In these systems, the conductance of the normal conductor shows two remarkable features: phase coherent magneto-conductance oscillations and non-monotonic temperature dependence.

3.5 Phase-dependent conductance

The electrical conductance of SNS systems was predicted to be an oscillatory function of the phase difference long before fabrication technology allowed experimental realisations [61]. In this and later theoretical works considering the different temperature ranges $k_BT \gg E_{TH}$ [62, 63]

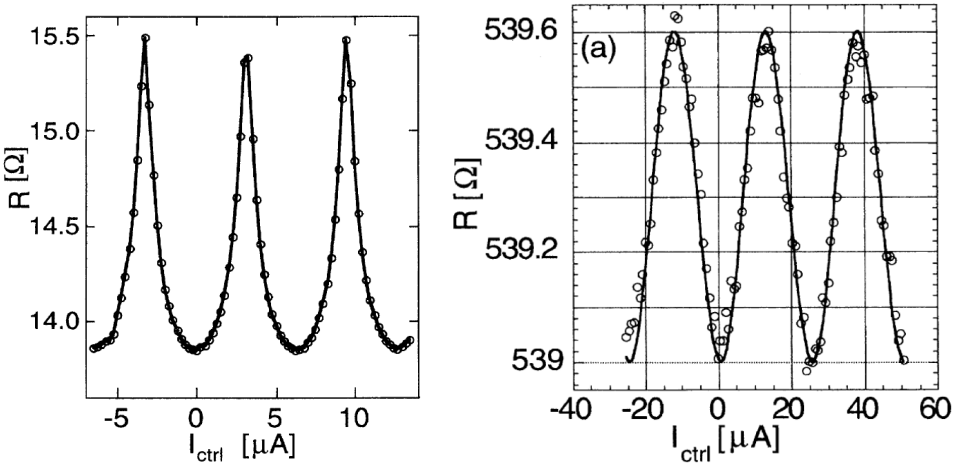

Figure 3.7: *Magneto-resistance of (a) an Ag/Al and (b) an Sb/Al interferometer as a function of current through the superconducting loop, measured in Ref. [69].*

and $k_BT \ll E_{TH}$ [64], oscillation amplitudes less than or of order of $(2e^2/h)$ were predicted, with a 2π-periodicitiy.

The first experimental evidence of interference effects in a SNS structure was provided by Petrashov *et al.* in 1993 [65], where mesoscopic N rings in contact with S islands were measured. In that design, however, the superconductor phase difference could not be controlled. In an experiment by de Vegvar *et al.* [66] on a Nb-Au-Nb SNS junction shunted by a series of SIS tunnel junctions, oscillations of amplitude $\delta G \approx 10^{-3}(2e^2/h)$ were measured. In this experiment, the superconductor phase was changed by driving a current through the SIS array, and clearly showed the 2π-periodicity of oscillations. Similar results were obtained by Pothier *et al.* [67] using an interferometer containing two SIN interfaces, which showed oscillation with amplitude of order $\delta G \approx 10^{-2}(2e^2/h)$.

The first experimental works showing oscillation with amplitude greater than $(2e^2/h)$ were carried out by Petrashov *et al.*. in 1994 [68] using silver rings and, in 1995 [69], using silver and antimony wires in the shape of a cross. In their 1995 experiment, the superconductor phase difference was equivalently controlled either by changing the magnetic flux through the superconducting loop and by passing a supercurrent through a section of the superconductor. Oscillation of amplitude up to $\delta G \approx 100(2e^2/h)$ and $\delta G \approx 3{\times}10^{-2}(2e^2/h)$ were measured for Ag and Sb, respectively, exhibiting

a periodicity of 2π, as shown in Figs. 3.7(a) and (b). In these experiments, as suggested later by van Wees *et al.*. [70], a significant screening effect was produced by the supercurrent flowing through the Al loop and caused "cusp-like" oscillations for the Ag/Al sample.

3.6 "Reentrant" effect

The conductance of metallic NS systems is known to exhibit a non-monotonic temperature and voltage dependence with a maximum when k_BT or $eV \approx E_{TH}$ [51]. This so-called "reentrance" was observed in a variety of SNS systems, and is in strict relation with the phase-coherent magneto-conductance oscillations discussed above.

A physical explanation of the reentrant effect in SNS systems was given by Volkov [71], who identified two contributions to the total correction of the phase-coherent conductance $\delta\sigma(E)$ induced in an N wire by the proximity effect, which is given by [72]

$$\delta\sigma(E) = \delta\sigma_{DOS}(E) + \delta\sigma_{an}(E). \tag{3.10}$$

The term $\delta\sigma_{DOS}$ is the change produced by the modification of the density of states in the normal metal, and decreases as the temperature is decreased. The contribution $\delta\sigma_{an}$, called "anomalous" or Maki-Thompson, is due to the penetration of Cooper pairs in the N section, and gives an increase of the conductance as the temperature is decreased. The behaviour of the two terms is shown in Fig. 3.8(a), together with the resulting total conductance correction $\delta\sigma(E)$, which displays a maximum at $E \approx E_{TH}$ arising from the different functional forms of σ_{DOS} and $\delta\sigma_{an}$. Most remarkably, the two contributions coincide either for $E \gg E_{TH}$ and $E \approx 0$, producing the reentrance of the conductance to its normal state value. For $E \gg E_{TH}$, the "anomalous" term was found too decay linearly with E_{TH}/k_BT [72].

The experiment by Petrashov *et al.* [69], where large amplitude oscillations were obtained at very low temperatures, were in clear contrast with the predicted temperature dependence, as in this regime reentrance to the normal state conductance should occur. A detailed analysis of their structure, carried out by Nazarov and Stoof [73] using quasi-classical methods, explained the results in terms of "thermal effect", where the finite temperature and voltage drop across the normal conductor cause the conductance to have a maximum at $E \sim E_{TH}$. A similar dependence was predicted by Volkov, Allsopp and Lambert [49] as a function of the voltage across the SNS junction, where a maximum was reached for $eV \approx E_{TH}$. Further experiments by Petrashov *et al.* [74, 75] indeed confirmed the prediction of Ref.

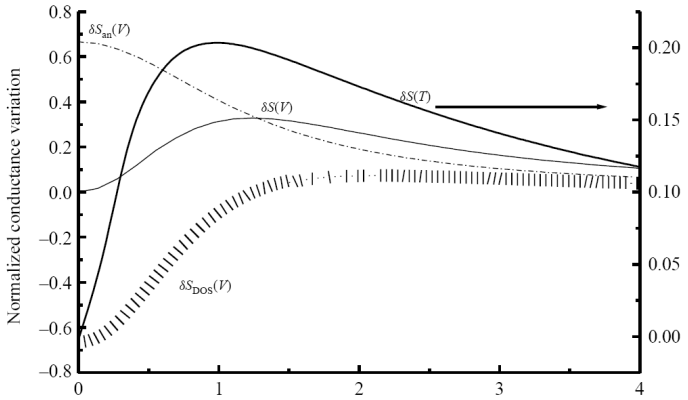

(a)

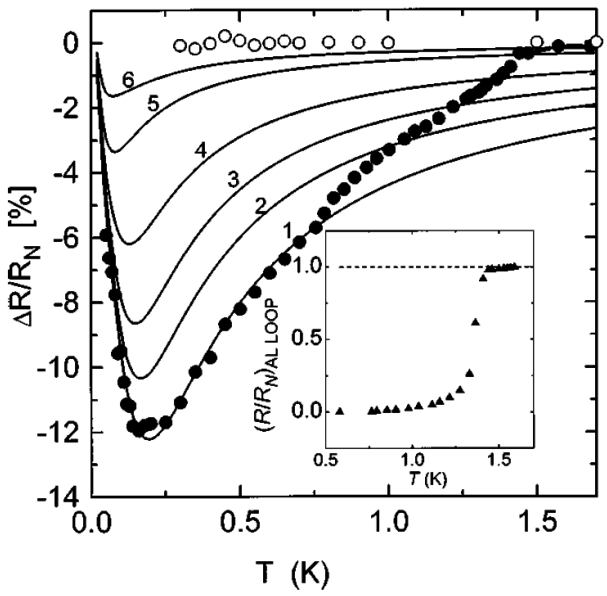

(b)

Figure 3.8: *(a) Normalized conductance contributions* $\delta S_{DOS}(V) = \delta\sigma_{DOS}/\sigma_N$ *and* $\delta S_{an}(V) = \delta\sigma_{an}/\sigma_N$*, and normalised total conductance* $\delta S(V) = \delta\sigma/\sigma_N$ *as a function of normalised voltage* eV/E_{TH} *(left vertical axis). The normalised total conductance* $\delta S(T)$ *as a function of temperature is also shown (right vertical axis). From Ref. [72]. (b) Zero bias resistance of a cross-shaped Andreev interferometer as a function of temperature for superconductor phase difference* $\Delta\chi$*=0 (filled circles) and* $\Delta\chi = \pi$ *(open circles). Reproduced from Ref. [75].*

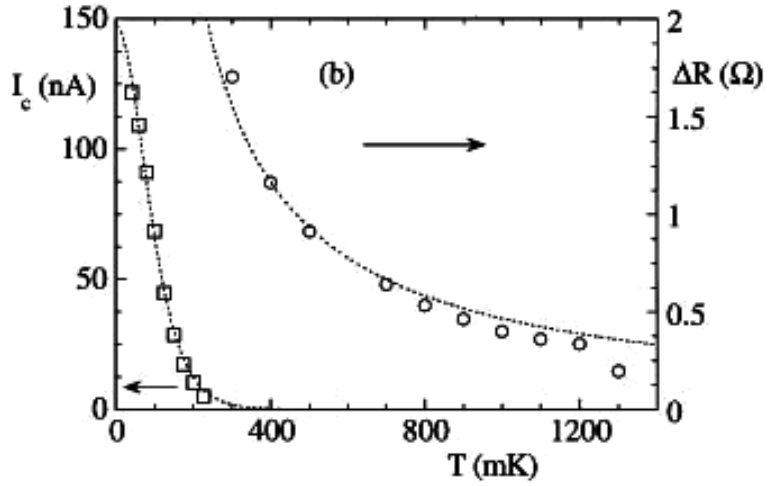

Figure 3.9: *Temperature dependence of critical current I_c (square, left axis) and resistance correction ΔR (circles, right axis) measured in Ref. [76]. The dashed line for I_c is a guide to the eye, the dashed line for ΔR is a $1/T$ fit.*

[73] and showed reentrant behaviour of the resistance, shown in Fig. 3.8(b), with maximum amplitude for $k_B T \approx E_{TH}$.

The effect of superconducting proximity on the conductance has a long-range character, i.e., the induced change of the conductivity in N persists even at distances from the N/S interfaces much greater than the thermal coherence length ξ_T. This behaviour is in clear contrast with the dependence of the Josephson current, which decays exponentially with x/ξ_T. Among other experimental works, these different dependences were clearly identified by Courtois *et al.* [76] using Cu rings in contact with one Al island, where the crossover from short ($L \ll \xi_T$) to long ($L \gg \xi_T$) junction regimes was investigated. For $L \gg \xi_T$, the amplitude of the magneto-conductance oscillations was found to decay slowly with a $1/T$ power law. Their results on the different behaviour of the critical current I_c and resistance correction $\Delta R = 1/\delta G$ are summarised in Fig. 3.9, which clearly shows the different dependencies.

A detailed theory of the long-range phase-coherent conductance in SNS interferometers was carried out in Ref. [77], where the dependence on temperature, voltage, superconductor phase and phase breaking length L_φ was determined.

Chapter 4

Probing a qubit with an Andreev interferometer

In this chapter the use of an Andreev interferometer as a readout probe of the quantum state of a Josephson superconducting circuit is described, and it is shown how the information about the state can be obtained from the measurement of the interferometer resistance. First, the functioning of an Andreev interferometer is described, and the main features of the device are outlined in Sec. 4.1.1. Second, the investigated Josephson circuit is presented and then described by an empirical model in Sec. 4.1.2. Then the combined interferometer-qubit system is considered in Sec. 4.1.3, where the possibility of using it as phase detector is investigated. Finally, the backaction of the interferometer readout junction and the contributions to decoherence due to the setup are calculated in Sec. 4.2. The results provide guidelines for designing an efficient probing scheme with low backaction.

4.1 Device models

4.1.1 Andreev interferometer

An Andreev interferometer consists of a normal (N) metal wire in contact with two superconducting (S) electrodes which are connected to form a continuous loop, as schematically depicted in Fig. 4.1. The resistance of the normal section is an oscillatory function of the phase difference φ_I between the superconductors and, in the long-junction limit, it can be described by [75]

$$R = R_N - \Delta R = R_N - \gamma \left(1 + \cos(\varphi_I)\right), \tag{4.1}$$

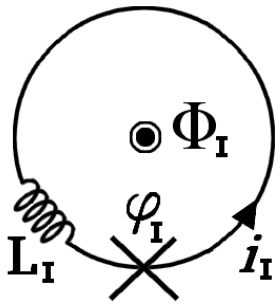

Figure 4.1: *Schematic of an Andreev interferometer, where the × sign represent the SNS junction. The superconducting loop of geometric inductance L_I is threaded by a magnetic flux Φ_I, which produces a phase difference φ_I across the junction.*

where R_N is the resistance of the N section in the normal state and ΔR is the resistance change due to the proximity effect. The latter is a periodic function of the phase φ_I, and has an amplitude γ that depends on the quality of the NS interfaces, the length and diffusion properties of the normal metal, and the temperature. The fluxoid quantisation condition around the interferometer loop links the phase φ_I to the externally applied flux through the interferometer loop Φ_{xI} via the relation

$$\varphi_I = 2\pi \frac{\Phi_{xI}}{\Phi_0}, \tag{4.2}$$

where $\Phi_0 = h/2e$ is the flux quantum. In the general case, the screening current induced in the loop must also be taken into account; this produces a magnetic field which opposes the externally applied one, with the result that the actual flux Φ_I threading the loop is decreased and becomes

$$\Phi_I = \Phi_{xI} - L_I i_I, \tag{4.3}$$

where L_I is the geometrical inductance of the loop and i_I is the induced screening current. As discussed in Sec. 3.3.2, in the long-junction regime the supercurrent i_I through the SNS junction is given, to a first approximation, by the first Josephson relation

$$i_I = I_{0I} \sin(\varphi_I), \tag{4.4}$$

where I_{0I} is the junction critical current. Inserting Eq. (4.3) into Eq. (4.2) and making use of Eq. (4.4) produces an equation which must be numerically

solved for the phase φ_I across the SNS junction as a function of the external flux Φ_{xI}. Figure 4.2(a) shows the phase φ_I as a function of flux for values of the parameter $\beta \equiv 2\pi L_I I_{0I}/\Phi_0$=0, 0.1$\pi$, 0.2$\pi$ and 0.3π. The dependence of the phase φ_I on external flux, which for β=0 is a straight line, is modified when a finite screening current is present, and becomes increasingly non-linear for larger β. The effect of the screening current on the interferometer resistance is shown in Fig. 4.2(b), which shows the resistance oscillations calculated using Eq. (4.2) and the same values of β. The non-linearity of the screening current causes the sinusoidal oscillations at β=0 to become more "cusp-like" as β is increased. In the limit β=1, φ_I is no longer a single-valued function of the externally applied magnetic flux Φ_{xI}, and an hysteretic behaviour is expected, as shown in Fig. 4.3. When β >1 and the magnetic flux is increased from Φ_{xI}=0, φ_I is a single-valued function of Φ_{xI} until point (a) is reached, where it jumps to the upper branch of the $\varphi_I - \Phi_{xI}$ curve. If Φ_{xI} is now decreased, φ_I follows the upper branch until the point (c) is reached, when it will switch to the lower branch. As a result, when β >1, there is a phase interval $\Delta\varphi_I$ between the points (a) and (c) which is not scanned by the external flux. This regime is not desirable in an Andreev interferometer used as a phase detector, in which case the condition β <1 is a constraint that must be satisfied in designing the device.

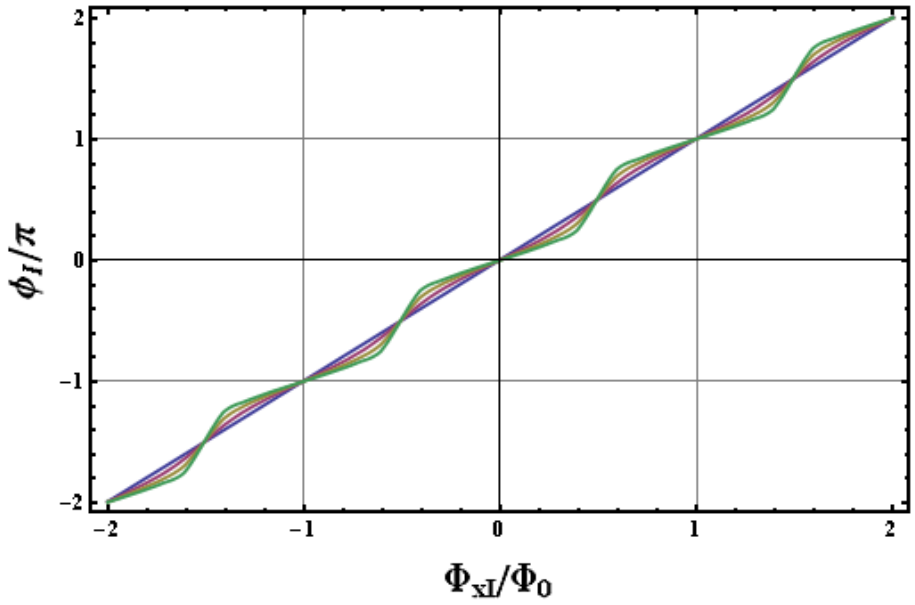

(a)

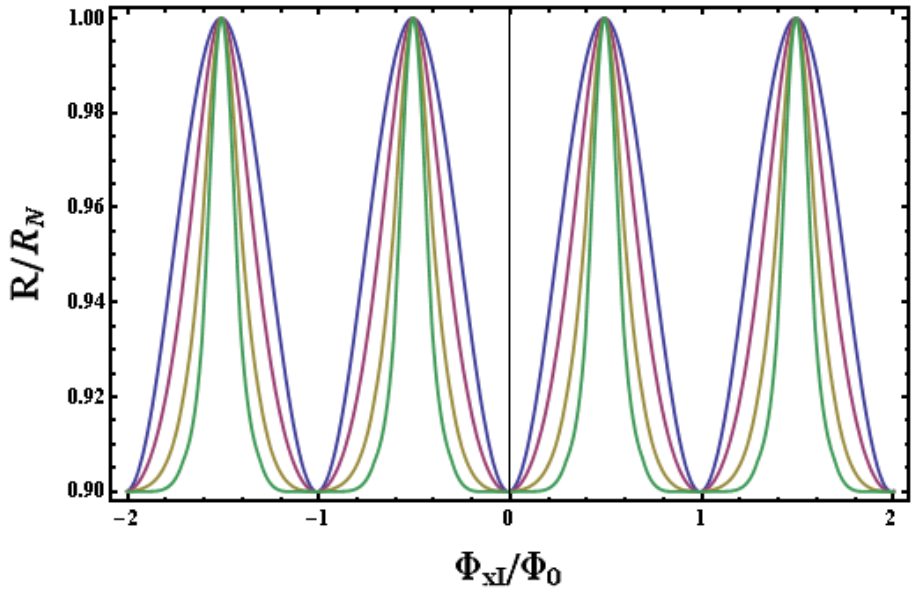

(b)

Figure 4.2: *Calculated (a) phase and (b) normalised resistance of an interferometer as a function of magnetic flux, for* $\gamma/(2R_N)$*=0.10, and* $\beta=(2\pi L_I i_{0I})/\Phi_0$*=0 (blue),* 0.1π *(magenta),* 0.2π *(yellow) and* 0.3π *(green).*

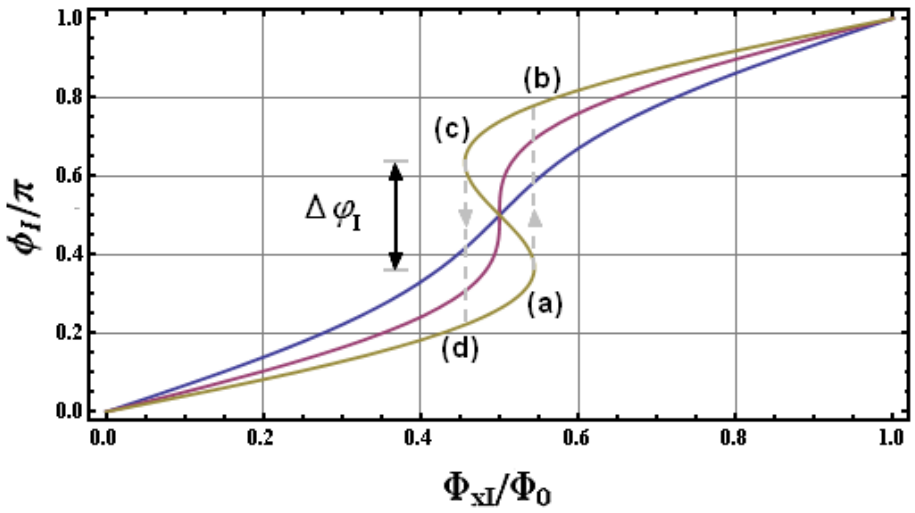

Figure 4.3: *Calculated interferometer phase as a function of magnetic flux for* $\beta=(2\pi L_I i_{0I})/\Phi_0=0.5$ *(blue), 1 (magenta), 1.5 (yellow). For* $\beta>1$*, the* $\varphi-\Phi_{xI}$ *relation is hysteretic, with a hysteresis loop defined by the points labelled in the Figure. The phase interval* $\Delta\varphi_I$ *is not scanned while sweeping* Φ_{xI}*.*

4.1.2 Four-junction superconducting loop

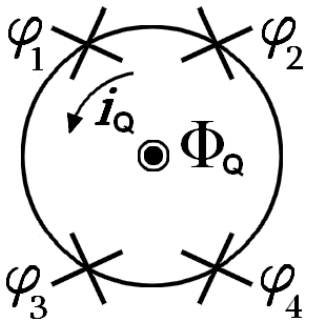

Figure 4.4: *Schematic of a four-junction persistent current qubit.*

The Josephson circuit investigated in this thesis is known as a persistent current qubit [24] and is schematically shown in Fig. 4.4. The device is a small superconducting loop interrupted by four Josephson junctions, three of which are fabricated with the same junction area A_J, while the area of the fourth is smaller by a factor $\alpha \geq 0.5$. The resulting junction critical currents I_{0i} (i=1, 2, 3, 4) are such that $I_{01} = I_{02} = I_{04} = I_0$, while $I_{03} = \alpha I_0$. The asymmetry in the Josephson energies produces the double well potential when the flux through the loop is $\Phi_Q \approx \Phi_0/2$ [23]. The dependence of the qubit variables, i.e., the phases across the Josephson junctions and the persistent current circulating in the loop, can be described by the generic energy spectrum proposed in Ref. [15], valid for $E_J \gg E_C$, as it is the case for our system:

$$E_{\pm}(\Phi_Q) = \frac{\epsilon(\Phi_Q) + \epsilon(\Phi_Q - \Phi_0)}{2} \pm \sqrt{\left(\frac{\epsilon(\Phi_Q) + \epsilon(\Phi_Q - \Phi_0)}{2}\right)^2 + \Delta^2}, \quad (4.5)$$

where 2Δ is the energy gap of the qubit at $\Phi_Q = \Phi_0/2$, $\epsilon(\Phi_Q) = E_J[1 - \cos(\pi\frac{\Phi_Q}{\Phi_0})]$ is the two junction energy, and $E_J = \hbar I_0/(2e)$ is the Josephson coupling energy of the large junctions. From the energy spectrum, the persistent current circulating in the qubit loop can be calculated from

$$i_Q = \frac{\partial E_{\pm}}{\partial \Phi_Q}. \quad (4.6)$$

The spectrum given in Eq. (4.5) describes the main features of the qubit: the splitting of the energy levels occurring at $\Phi_Q \approx n\Phi_0/2$ (n integer) and the flux dependence of the persistent current flowing in the qubit loop. Figures 4.5(a)

and (b) show the energy spectrum (in units of E_J) and the persistent current (normalised to I_0) obtained from Eqs. (4.5) and (4.6) with $\Delta = 0.1E_J$.

The phase φ_j across the jth Josephson junction can be obtained by inverting the first Josephson relation, which gives

$$\varphi_j = \arcsin\left(\frac{I_j}{I_{0j}}\right) \quad j = 1, 2, 3, 4, \tag{4.7}$$

where I_j is the current flowing through the junction and I_{0j} is its critical current. In our devices, the interferometer resistance is sensitive to the total phase in the bottom arm which, for small inductance of the qubit loop, is simply $\varphi_B = \varphi_3 + \varphi_4$. Figure 4.6 shows the total phase φ_B as a function of flux calculated using Eqs. (4.7) and (4.6), and the spectrum of Eq. (4.5).

It is worth noting some features that will be used in the next section when the combined interferometer-qubit system will be considered. The phase φ_B has a flux periodicity of $\Delta\Phi_Q = \Phi_0$, and φ_B=0 at Φ_Q=$n\Phi_0/2$ (n=0, 1, 2,...), because at these fluxes the persistent current i_Q in the qubit is zero. The fact that i_Q=0 at $\Phi_Q = \Phi_0/2$ is a distinctive feature of the quantum tunnelling between the persistent current states, and it is due to the flattening of the energy levels at the anti-crossing. On the contrary, when no tunnelling occurs, the classical energy levels have a finite slope at Φ_Q=$\Phi_0/2$, resulting in a finite persistent current i_Q.

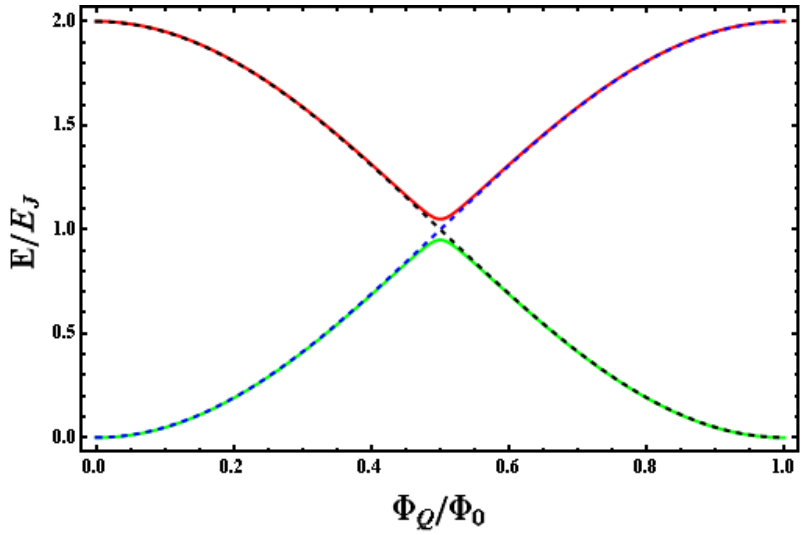

(a)

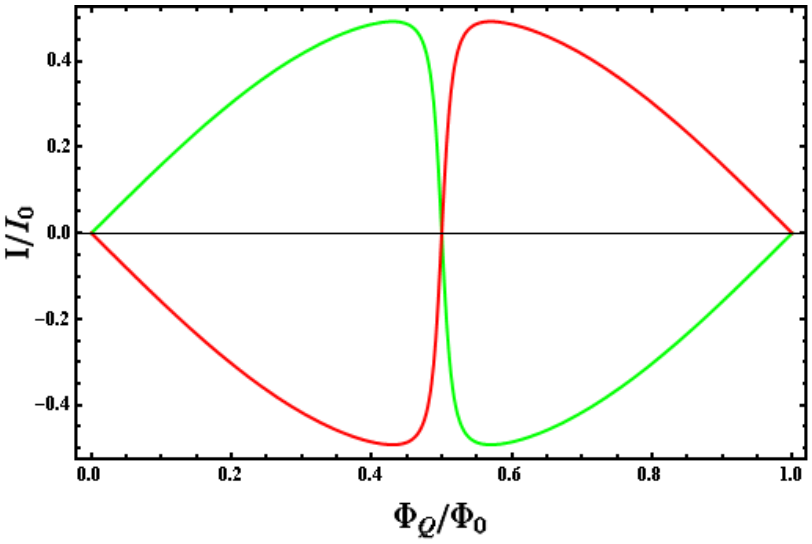

(b)

Figure 4.5: *(a) Energy spectrum calculated using Eq. (4.5) with* $\Delta = 0.1E_J$*. Green and red solid lines are the ground and first excited states, respectively, whereas the classical energy levels are shown with dashed lines. (b) Persistent currents calculated using Eq. (4.6) and the spectrum in (a).*

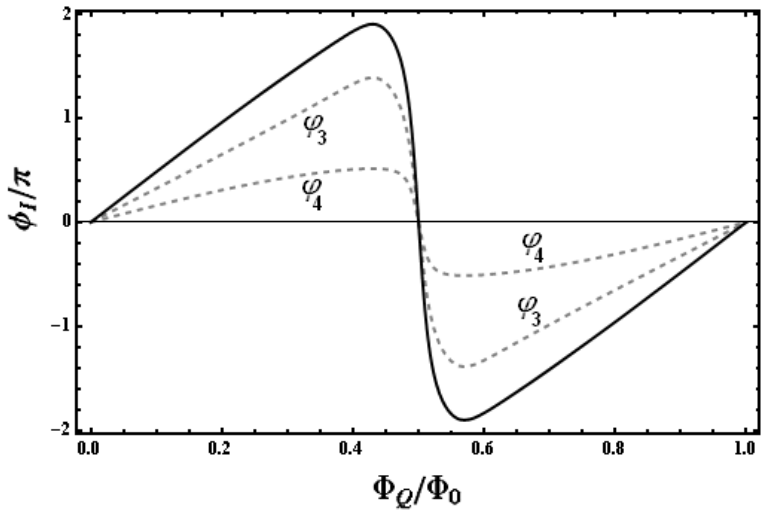

Figure 4.6: *Phases across the bottom junctions (dashed lines) and total phase* φ_B *across the bottom arm of the qubit (solid line) as a function of the flux* Φ_Q.

4.1.3 Interferometer-Qubit device

A schematic of the combined interferometer-qubit device is shown in Fig. 4.7. The device is made up of a small superconducting loop ("qubit loop") containing four Josephson junctions (φ_i, $i = 1, 2, 3, 4$), which is threaded by the externally applied magnetic flux Φ_{xQ}. The loop is divided into top and bottom branches, with geometrical inductances L_T and L_B, in which the currents i_T and i_B flow. A larger loop (the "interferometer loop") is composed of two superconducting leads of total geometric inductance L_I and the bottom branch of the qubit loop, and contains the SNS readout junction (φ_I). The externally applied magnetic flux Φ_{xI} through the interferometer loop causes a current i_I to flow, and is linked to Φ_{xQ} by $\Phi_{xI} = f\Phi_{xQ}$, where the parameter $f = A_I/A_Q$ is the ratio of the areas A_I and A_Q of the interferometer and qubit loops, respectively. Using Kirchoff's laws, the currents in the qubit branches are

$$i_T = \frac{L_B}{L_T + L_B} i_I + i_Q = \frac{L_B}{L_Q} i_I + i_Q, \tag{4.8}$$

$$i_B = \frac{L_T}{L_T + L_B} i_I - i_Q = \frac{L_T}{L_Q} i_I - i_Q, \tag{4.9}$$

where $L_Q = L_B + L_T$ and i_Q are the total qubit inductance and the persistent current flowing in the qubit loop, respectively. The flux Φ_I through the interferometer loop is bound by the conditions

$$\Phi_I = n\Phi_0 + \frac{\Phi_0}{2\pi}\left(\varphi_I + \varphi_3 + \varphi_4\right), \tag{4.10}$$

$$\Phi_I = \Phi_{xI} - L_I i_I - L_B i_B, \tag{4.11}$$

where Eq. (4.10) expresses the fluxoid quantisation, and Eq. (4.11) accounts for the self-inducted flux produced by the screening current i_I circulating in the interferometer loop. Inserting Eq. (4.11) into Eq. (4.10), and making use of Eq. (4.9) gives

$$\begin{aligned}\varphi_I &= \frac{\Phi_{xI}}{\Phi_*} - \frac{i_I}{\Phi_*}\left(L_I + L_{eQ}\right) + \frac{i_Q}{\Phi_*} L_B - \varphi_3 - \varphi_4 \\ &= \frac{\Phi_{xI}}{\Phi_*} - \frac{i_I}{\Phi_*}\left(L_I + L_{eQ}\right) + \Delta\varphi_Q,\end{aligned} \tag{4.12}$$

where $L_{eQ} = \frac{L_B L_T}{L_B + L_T}$ is the equivalent inductance of the qubit loop and $\Phi_* = \Phi_0/(2\pi)$. The phase difference across the interferometer is given by the sum of two contributions: the terms due to the flux and the screening in the interferometer, and the contribution $\Delta\varphi_Q$ of the qubit, which contains the total phase across the bottom branch and the screening term due to the

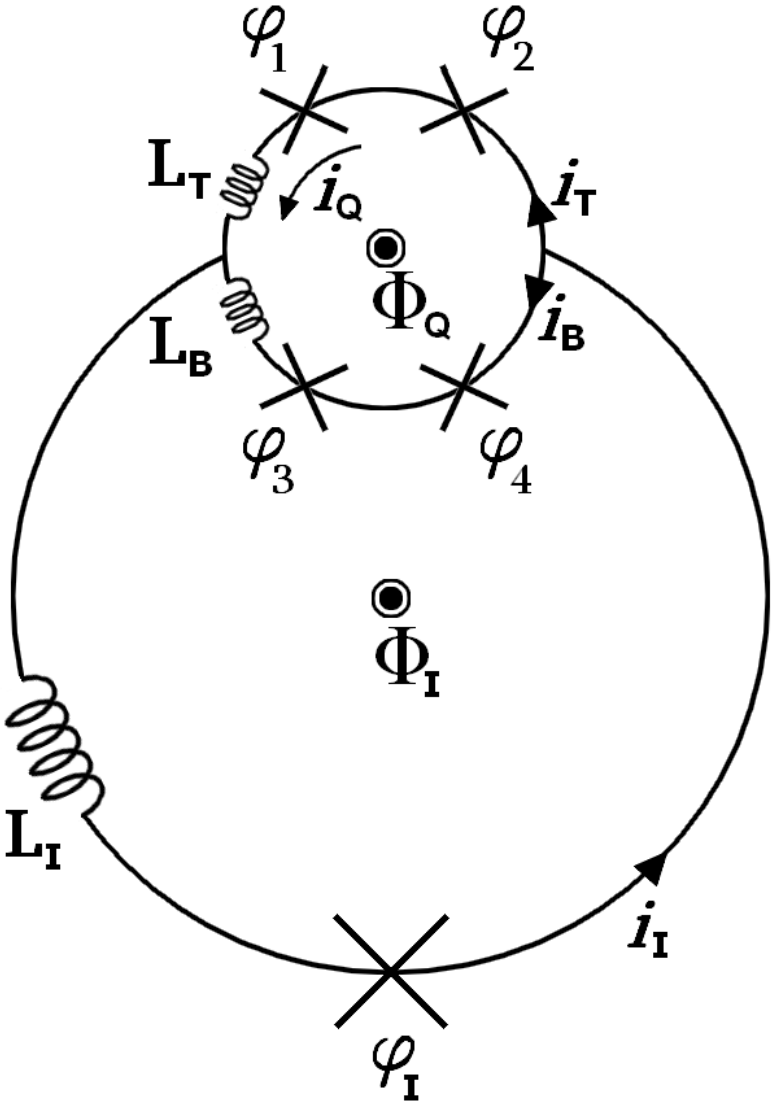

Figure 4.7: *Schematic of the combined interferometer-qubit device, showing the meaning of the symbols used in the text and the convention chosen for the direction of the currents.*

persistent current i_Q. As will be shown in Sec. 5.2, the latter contribution is much smaller than the other terms and can be safely ignored. The phases across each Josephson junction can be obtained from the inverted Josephson relation in Eq. (4.7). In our devices, $I_3 = I_4 = i_B$ due to current conservation, and $I_{03} = \alpha I_0$ and $I_{04} = I_0$ are set by fabrication. Using these values and Eq. (4.7), the qubit contribution becomes

$$\begin{aligned}\Delta\varphi_Q = &- \arcsin\left[\left(\frac{L_T}{L_Q} i_I - i_Q\right)\frac{1}{\alpha I_0}\right] \\ &- \arcsin\left[\left(\frac{L_T}{L_Q} i_I - i_Q\right)\frac{1}{I_0}\right].\end{aligned} \tag{4.13}$$

Inserting Eq. (4.13) into Eq. (4.12) produces a non-linear equation which must be numerically solved to find the phase φ_I across the SNS junction as a function of the external flux Φ_{xI}. The only unknowns in Eq. (4.12) are the currents i_I and i_Q circulating in the interferometer and qubit loops.

The current flowing through the readout SNS junction is to a first approximation given by the first Josephson relation given in Eq. (4.4), which provides an accurate description for an SNS junction in the limit $E \gg E_{TH}$. In our experiments, the temperature and current ranges correspond to $E \approx E_{TH}$, nevertheless Eq. (4.4) produces a good agreement with the experimental results, as shown in Sec. 7.1. Using Eqs. (4.4) and (4.13), Eq. (4.12) becomes

$$\begin{aligned}\varphi_I = &\frac{\Phi_{xI}}{\Phi_*} - \frac{I_{0I}}{\Phi_*}\left(L_I + L_{eQ}\right)\sin(\varphi_I) + \frac{i_Q}{\Phi_*} L_B \\ &- \arcsin\left[\left(\frac{L_T}{L_Q} I_{0I}\sin(\varphi_I) - i_Q\right)\frac{1}{\alpha I_0}\right] \\ &- \arcsin\left[\left(\frac{L_T}{L_Q} I_{0I}\sin(\varphi_I) - i_Q\right)\frac{1}{I_0}\right].\end{aligned} \tag{4.14}$$

The expected behaviour of i_Q as a function of external flux can be obtained using Eq. (4.6) and the spectrum from Eq. (4.5), using the fact that $\Phi_Q = f\Phi_{xI}$.

Figures 4.8(a-c) show plots of the phase φ_I as a function of the flux Φ_Q calculated using Eq. (4.14) using values $\beta = i_{0I}(L_I + L_{eQ})/\Phi^*$=0.5, I_0=500 nA and Δ=0.001E_J. From the figure it is evident that if the interferometer loop area is significantly larger than the qubit area, then φ_I is a linear function of the flux over regions centred around $\Phi_Q = n\Phi_0$ (n integer), and will be dominated by the term Φ_{xI}, while the term $\Delta\varphi_Q$ will be very small. In these regions, the measured resistance oscillates with constant period. Around the points $\Phi_Q \approx (2m-1)\Phi_0/2$, where m is an integer, the reversal of the

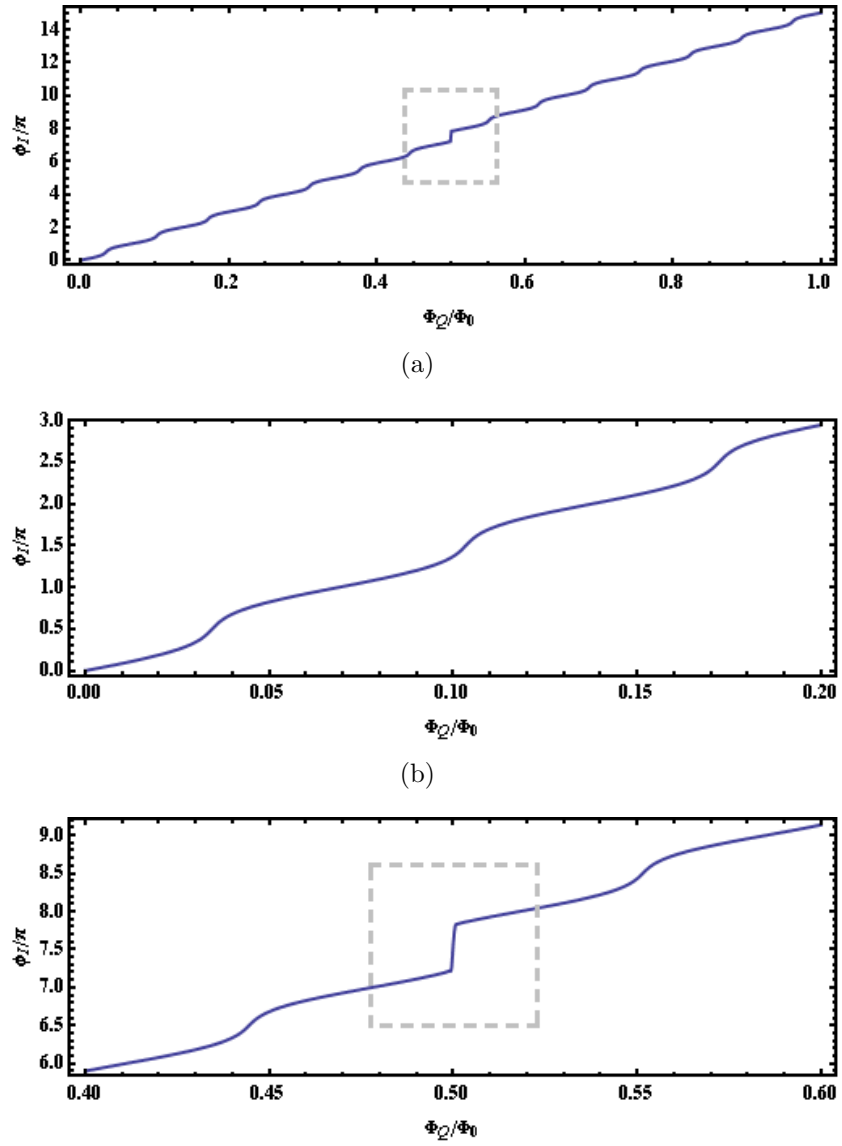

Figure 4.8: *Phase φ_I as a function of magnetic flux calculated using Eq. (4.14) with values β=0.5, I_0=500 nA and Δ=0.001E_J. (a) Overall picture and blow up of plots near (b) $\Phi_Q \approx 0$ and (c) $\Phi_Q \approx \Phi_0/2$. The current i_I circulating around the interferometer loop causes the periodic modulation of φ_I. An abrupt change in φ_I (dashed square) is caused by a reversal of the persistent current i_Q at $\Phi_Q \approx \Phi_0/2$.*

circulating current causes the term $\Delta\varphi_Q$ to vary abruptly over a small flux range. As a result, the measured resistance oscillations undergo a sudden phase change.

The following general trends in Fig. 4.8 can be used to analyse the experimental data:

1. The current-phase relation for φ_I (Eq. 4.4) ensures that when φ_I is an integer multiple of π, the supercurrent in the interferometer loop i_I is zero.

2. The flux dependence of $\Delta\varphi_Q$ described in Sec. 4.1.2 is retained in the combined device, and $i_Q = 0$ at $\Phi_Q = n\Phi_0/2$. In particular, this is true at $\Phi_Q = m\Phi_0$, when the phase φ_I assumes the value $\varphi_I = 2m\pi f$.

3. In the flux regions far away from $\Phi_Q \approx (2n-1)\Phi_0/2$, the phase φ_I is given by a sum of contributions that are linear in the flux Φ_Q, except for the oscillating term i_I which causes a periodic modulation.

4.2 Estimation of relaxation and decoherence

The description of a qubit in terms of superposition of macroscopic states given in Sec. 2.2 does not include the effect of the external environment on the qubit state. The qubit is indeed permanently coupled to the environment via several channels, whose effect has to be taken into account when designing an efficient measurement scheme. The possibility to manipulate and readout solid-state qubits using integrated nano-scale electronic devices is considered one of their most attractive features. On the other hand, this feature is also one of their major drawbacks, because the same electrical leads needed for qubit operation are paths through which environmental noise can reach the device.

Among the different noise sources, special attention deserves the measuring device used for qubit state detection, which has to be permanently coupled to the qubit in order to achieve an efficient measurement of its state. In our devices, the interferometer is in electrical contact with the qubit and thus strongly coupled to it. An understanding of the mechanisms in which the interferometer itself and the setup induce decoherence of the qubit state is needed in order to reduce the interaction between the readout and qubit devices to the minimum necessary for the state detection. In this section we will concentrate on relaxation and decoherence induced by the interferometer readout junction and measurement setup, and the results will be used in the next section when the device design will be treated.

4.2.1 Background theory

The effect of the environment can be determined in the framework of the so called spin-boson model [78, 79], in which the impedance $Z(\omega)$ associated with each noise source is described by an infinite set of LC oscillators which are coupled to a central spin-$\frac{1}{2}$. We will follow the treatment by Grifoni *et al.* [80], where the relaxation and decoherence rates Γ_r and Γ_φ are calculated for weak damping occurring via coupling to σ_z. The latter assumption is valid for degrees of freedom which couples to the qubit via magnetic flux and persistent current, producing fluctuations in the energy bias $\epsilon = i_Q(\Phi_Q - \Phi_0/2)$. The effect of the oscillator bath on the qubit is represented by an environment spectral function $J(\omega)$ describing the overall frequency dependent coupling strength between the oscillator bath and the central spin spin-$\frac{1}{2}$. Due to the large number of oscillators composing the environment, $J(\omega)$ can be treated as a continuous function and can be calculated from the spectral density of

the energy fluctuations $\langle \delta\epsilon\delta\epsilon \rangle$ as [81]

$$J(\omega) = \frac{\langle \delta\epsilon\delta\epsilon \rangle}{\hbar^2 \coth\left(\frac{\hbar\omega}{2k_B T}\right)}. \tag{4.15}$$

The relaxation rate Γ_r is determined by the spectral density $J(\omega)$ at the qubit resonant frequency $\omega_0 = \nu/\hbar$

$$\Gamma_r = \frac{1}{2}\left[\left(\frac{\Delta}{\hbar\omega}\right)^2 J(\omega) \coth\left(\frac{\hbar\omega}{2k_B T}\right)\right]_{\omega=\omega_0}, \tag{4.16}$$

where T is the temperature of the oscillator bath. On the contrary, decoherence is produced by low frequency fluctuations, which give the rate

$$\Gamma_\varphi = \frac{\Gamma_r}{2} + \left(\frac{\epsilon}{\nu}\right)^2 \alpha 2\pi \frac{k_B T}{\hbar}, \tag{4.17}$$

where α is a dimensionless parameter given by

$$\alpha \equiv \lim_{\omega\to 0} \frac{J(\omega)}{2\pi\omega} \approx \frac{1}{2\pi}\frac{\partial J(\omega)}{\partial\omega} \qquad at \quad \omega \approx 0. \tag{4.18}$$

The different frequency behaviour of relaxation and decoherence can be physically understood considering that relaxation involves the exchange of energy from the qubit to the environment, which occurs at the qubit resonant frequency. On the contrary, slow fluctuations in the energy bias cause dephasing of the qubit state during the time needed to collect the information on the state itself.

The values of the relaxation and decoherence times are calculated from the corresponding rates using Fermi's golden rule, which gives $\tau_r = 1/\Gamma_r$ and $\tau_\varphi = 1/\Gamma_\varphi$.

4.2.2 Estimation of rates

The main sources of noise which couple to qubit in our experimental setup (see Sec. 6.1) are schematically shown in Fig. 4.9. These are:

1. thermal fluctuations from the normal section of the SNS readout junction;
2. flux noise from the on-chip antenna;
3. flux noise from the superconducting magnet.

In the following, each contribution will be calculated separately. Due to the heavy filtering of the electrical leads (see Sec. 6.1.2), noise from measurement electronics and environmental interference which couple to the leads will not be considered.

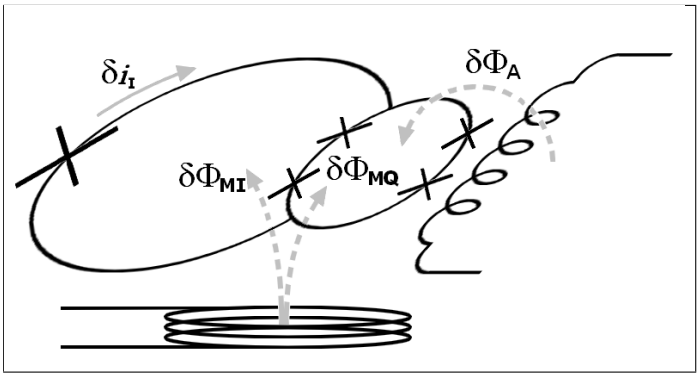

Figure 4.9: *Sources of decoherence for the interferometer-qubit devices. Noise in the magnetic flux due to the superconducting magnet (Φ_{MI} and Φ_{MQ}) and antenna (Φ_A) are shown with dashed arrows. Fluctuations in the interferometer current δi_I are represented by a solid arrow.*

Noise from the SNS readout junction

The noise induced by the SNS readout junction results from Johnson-Nyquist fluctuations δV of the voltage across the normal metal section, whose power spectral density $\langle \delta V \delta V \rangle$ is [82]

$$\langle \delta V \delta V \rangle = \hbar\omega \Re[Z_{SNS}(\omega)] \coth\left(\frac{\hbar\omega}{2k_B T}\right), \tag{4.19}$$

where $\Re[Z_{SNS}]$ is the real part of the equivalent impedance Z_{SNS} of the SNS junction. The voltage fluctuations produce a noise current $\delta i_I = \delta V / Z_{SNS}$ in the interferometer loop, which, in turn, induces fluctuations δi_Q in the current flowing around the qubit loop. Using Eqs. (4.8) and (4.9), the persistent current i_Q can be written as

$$i_Q = \frac{i_T - i_B}{2} + \frac{1-2\gamma}{2} i_I, \tag{4.20}$$

where the parameter $\gamma = L_B/L_Q$ is introduced to account for the asymmetry between the two qubit branches. Differentiating Eq. (4.20) with respect to i_I, we find the relation

$$\delta i_Q = \frac{1-2\gamma}{2} \delta i_I, \tag{4.21}$$

which expresses the fact that the sensitivity of i_Q to fluctuations in the current i_I can be reduced if symmetric qubit branches are used ($\gamma = 1/2$).

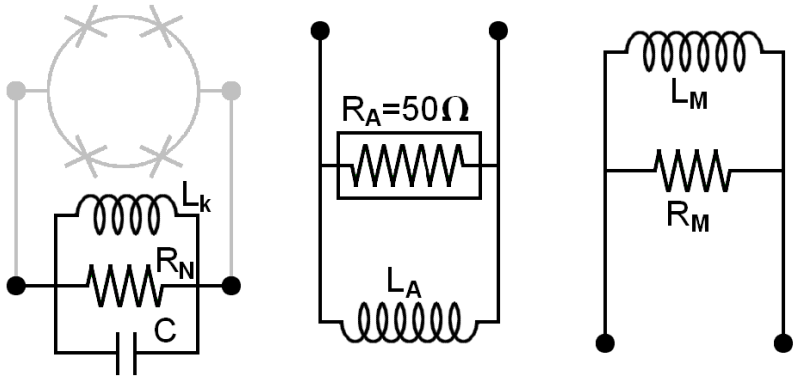

(a) (b) (c)

Figure 4.10: *Equivalent impedances of the fluctuation sources seen by the qubit. (a) SNS readout junction, showing the connection with the qubit loop (in grey); (b) Antenna; (c) Superconducting magnet.*

Inserting δi_I into Eq. (4.21) and differentiating in the frequency domain gives

$$\langle \delta i_Q \delta i_Q \rangle = \left(\frac{1-2\gamma}{2} \right)^2 \frac{1}{Z_{SNS}^2} \langle \delta V \delta V \rangle \,, \tag{4.22}$$

from which, using Eqs. (4.15) and (4.19), we find the noise spectral density

$$J_{eff}(\omega) = \frac{\omega}{\hbar} (\Phi_Q - \Phi_0/2)^2 \, (1-2\gamma)^2 \, \frac{\Re[Z_{SNS}]}{Z_{SNS}^2}. \tag{4.23}$$

The equivalent impedance of the readout junction can be modelled, by analogy to a Josephson junction, as the parallel combination of three lumped elements [19], as shown in Fig. 4.10(a):

- The resistance R_N of the normal metal section;
- The capacitance C between the S electrodes;
- The non-linear inductance $L_k(\varphi) = \frac{\hbar}{2ei_I(\varphi)}$ accounting for the Josephson effect;

The total impedance $Z_{SNS}(\omega)$ is then

$$Z_{SNS}(\omega) = \frac{j\omega L_k}{1 + j\omega \frac{L_k}{R_N} + (j\omega)^2 C L_k}, \tag{4.24}$$

and its real part can be approximated to

$$\Re[Z_{SNS}(\omega)] \approx \omega^2 L_k^2/R_N \qquad \omega \ll \omega_c = \frac{1}{\sqrt{L_k C}} \tag{4.25}$$

$$\approx \frac{1}{\omega^2 C^2 R_N} \qquad \omega \gg \omega_c = \frac{1}{\sqrt{L_k C}}. \tag{4.26}$$

The frequency $f_c = \omega_c/2\pi$ is of the order of several tens of GHz for typical values of $L_k \approx 10^{-10}$ H and $C \approx 10^{-11}$ F [17, 19], and is above the expected qubit resonant frequency $\omega_0/2\pi$=1-10 GHz. Therefore, Eq. (4.25) will be used in the calculations of both rates. Using Eq. (4.23) we obtain the relaxation and decoherence rates

$$\Gamma_r = \frac{1}{2}\frac{\Delta^2}{\hbar^3\omega_0}\frac{1}{R_N}\left(\Phi_Q - \frac{\Phi_0}{2}\right)^2 (1-2\gamma)^2 \coth\left(\frac{\hbar\omega_0}{2k_BT}\right), \tag{4.27}$$

$$\Gamma_\varphi = \frac{\Gamma_r}{2} + \frac{\epsilon^2}{\hbar^4\omega_0}\frac{1}{R_N}\left(\Phi_Q - \frac{\Phi_0}{2}\right)^2 (1-2\gamma)^2 k_BT. \tag{4.28}$$

From these results, one can see the importance of the normal resistance R_N in reducing the backaction of the readout junction on the qubit state. The dependence of the rates on $1/R_N$ reflects the relation between the noise voltage δV generated across the readout junction and the resulting fluctuating current δi_I causing decoherence. The backaction of the interferometer readout can be reduced by designing an interferometer with high resistance normal metal sections that suppress current fluctuations in the interferometer loop.

Noise from sources inductively coupled to qubit

The calculations of fluctuations due to sources inductively coupled to the qubit loop has been treated in Ref. [81]. We will follow their treatment for our devices considering two sources: the on-chip antenna and the superconducting magnet. These elements are coupled to the qubit via the mutual inductance M_i (i=A, M for antenna and magnet, respectively). Fluctuations δI in the current in these elements result in a change in the magnetic flux Φ_Q through the qubit $\delta\Phi_Q = M_i\delta I$, which in turn produces fluctuations $\delta\epsilon$ in the energy bias given by

$$\delta\epsilon = 2i_Q M_i \delta I. \tag{4.29}$$

The equivalent impedances for the on-chip antenna and the superconducting solenoid are shown in Figs. 4.10(b) and (c), respectively. In both cases, the impedances consist of an inductor L_i in parallel with a resistor R_i. For the on-chip antenna, the latter is the impedance of the RF coaxial lines

and attenuators, whereas R_M is the shunting resistor placed at 4.2 K. The equivalent impedance Z_i for these sources is then

$$Z_i(\omega) = \frac{j\omega L_i}{1 + j\omega L_i/R_i} \qquad i = A,\ M \tag{4.30}$$

and has a real part that can be approximated to

$$\Re[Z_i] \approx \omega^2 \frac{L_i^2}{R_i} \qquad \omega \ll \omega_{3dB} \tag{4.31}$$

$$\approx R_i \qquad \omega \gg \omega_{3dB}, \tag{4.32}$$

where $\omega_{3dB} = R_i/L_i$. The current fluctuations in the inductors are $\delta I = \frac{1}{j\omega L_i}\delta V$, where δV is the Johnson-Nyquist noise produced by the resistors R_i. Using Eqs. (4.29) and (4.19), the energy bias fluctuations are given by

$$\langle \delta\epsilon \delta\epsilon \rangle = 4\frac{\hbar}{\omega}\left(\frac{i_Q M_i}{L_i}\right)^2 \Re[Z_i] \coth\left(\frac{\hbar\omega}{2k_B T}\right). \tag{4.33}$$

which results in the power spectral density

$$J_{eff}(\omega) = \frac{4}{\hbar\omega}\left(\frac{i_Q M_i}{L_i}\right)^2 \Re[Z_i]. \tag{4.34}$$

Noise from antenna

Using the values R_A=50 Ω and the calculated inductance L_A=150 pH, the cut-off frequency is f_{3dB}=$\omega_{3dB}/(2\pi)$ ≈300 GHz, well above the expected qubit resonant frequency, and hence the equivalent impedance for the antenna can be approximated by Eq. (4.31). Using Eq. 4.34, the relaxation and decoherence rates for the coupling to the antenna are

$$\Gamma_r = \frac{2\Delta^2}{\hbar^3\omega_0}\frac{(i_Q M_A)^2}{R_A}\coth\left(\frac{\hbar\omega_0}{2k_B T}\right), \tag{4.35}$$

$$\Gamma_\varphi = \frac{\Gamma_r}{2} + 4\frac{\epsilon^2}{\hbar^4\omega^2}\frac{(i_Q M_A)^2}{R_A}k_B T. \tag{4.36}$$

In these results, the factor $(i_Q M_A)^2$ determines the strength of the decoherence induced by the antenna, and confirm that small rates can be achieved if an on-chip antenna with small coupling with the qubit loop is used. However, a lower limit for M_A is set by the need to provide sufficient RF power to excite the qubit.

Noise from the superconducting magnet

For the magnet impedance, a cut-off frequency f_{3dB} ≈5 kHz is obtained with R_M ≈3 Ω and L_M ≈100 μH. Thus, the equivalent impedance should be calculated with Eq. (4.32) for the relaxation rate, whereas Eq. (4.31) should be used to obtain the decoherence rate. Due to the high sensitivity of our device to magnetic fluctuations, we assumed a worst case scenario and used Eq. (4.31) for the calculation of both rates, obtaining

$$\Gamma_r = \frac{2\Delta^2}{\omega_0 \hbar^3} \frac{(i_Q M_M)^2}{R_M} \coth\left(\frac{\hbar\omega_0}{2k_B T}\right), \tag{4.37}$$

$$\Gamma_\varphi = \frac{\Gamma_r}{2} + 4\frac{\epsilon^2}{\hbar^4\omega^2} \frac{(i_Q M_M)^2}{R_M} k_B T. \tag{4.38}$$

As for the on-chip antenna, the rates obtained for the magnet contain the prefactor $(i_Q M_M)^2$ arising from the inductive coupling to the qubit loop. Small rates can be achieved making the mutual inductance M_M very small. In this case, the lower limit for how small M_M can be is set by the maximum current that can be driven in the superconducting magnet without dissipation.

The decoherence and relaxation times calculated for the three sources are summarised in Table 4.1. For the calculations, the parameters ω_0=2π×10 GHz and Δ=h×2 GHz from Ref. [24] were used, while the other parameters were calculated or measured. From these results, Nyquist fluctuations across the readout junction are expected to be the most severe contribution in limiting the coherence of our device. As described in Sec. 5.2.1, the relation between the times τ_r and τ_φ and the value of R_N was exploited in order to decrease the backaction of the readout.

Parameters				
ω_0=2π×10 GHz	γ=0.25	M_A=1 pH	R_A=50 Ω	L_A=150 pH
Δ=h×2 GHz		M_M=0.1 pH	R_M=3 Ω	L_M=100 μH

Decoherence sources		
Interferometer	$\tau_r \approx 1 \times R_N$ ps	$\tau_\varphi \approx 2 \times R_N$ ps
Antenna	τ_r ≈26 μs	τ_φ ≈7.23 ns
Magnet	τ_r ≈9 μs	τ_φ ≈350 ns

Table 4.1: *Calculated relaxation and decoherence times.*

Chapter 5

Device design and fabrication

This chapter describes the experimental implementation of interferometer/qubit devices. The results developed at the end of the last chapter are used in Sec. 5.2 to discuss the properties of the device and to design a readout scheme with low backaction. The fabrication steps are described in Sec. 5.3.

5.1 Device description

The devices investigated in this thesis are multi-layered hybrid normal metal-superconductor structures fabricated on a silicon substrate with an insulating native oxide layer on top. Two different types of devices were fabricated and investigated: Andreev interferometer and interferometer-qubit devices. The former device consists of a superconducting aluminium loop interrupted by a 3 μm long silver section, attached to the contact leads in a cross geometry. An on-chip aluminium antenna was used to launch RF radiation onto the chip. A *SEM* image of a typical sample (referred to as AgInt, *Ag*-normal part Andreev *Int*erferometer) is shown in Fig. 5.1(a).

One interferometer-qubit device (named SbQ) was produced with the layout shown in Fig. 5.1(b). This device consists of a large superconducting loop ("interferometer loop") interrupted by a 600 nm long normal metal section. A small superconducting loop containing four Josephson junctions ("qubit loop") is inserted in the interferometer loop. The normal metal section of the interferometer and part of the contact leads were fabricated using antimony. Aluminium was used to create the interferometer and qubit loops, the antenna, and a remaining contact connection to the normal part of the interferometer.

The parameters of the samples are summarised in Table 5.1. The lengths

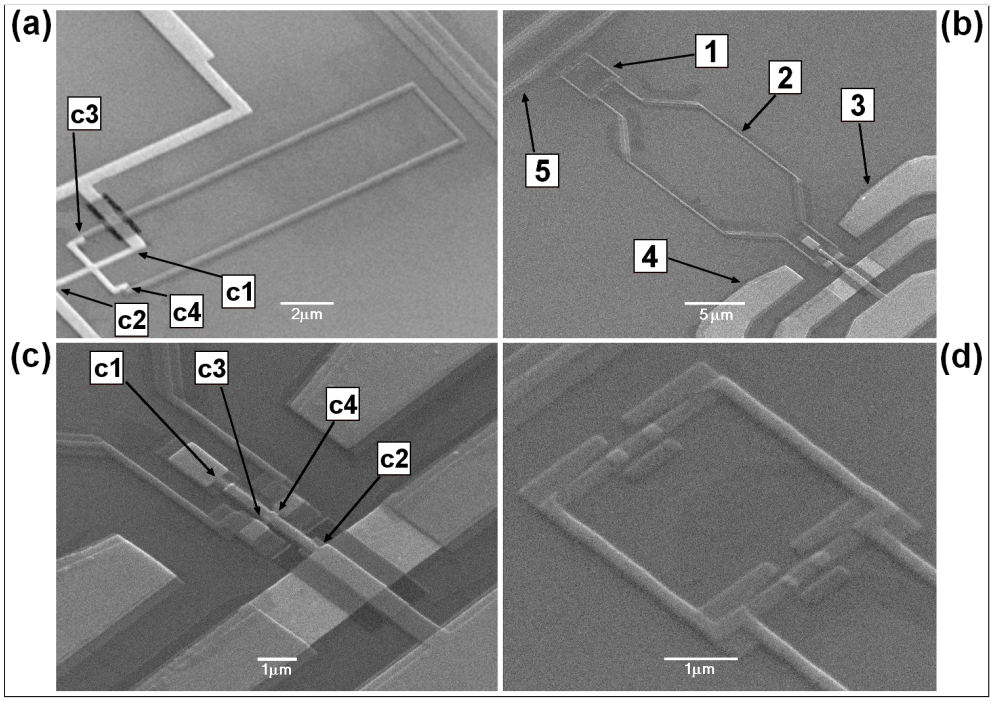

Figure 5.1: *SEM images of (a) the AgInt sample and (b) the SbQ sample. The labels in (b) indicate: (1) Qubit Loop; (2) interferometer loop; (3 and 4) ground planes; (5) antenna. (c) and (d) show enlarged views of the folded cross and the qubit loop containing the four Josephson junctions. Light and medium grey are the normal metal and aluminium layers, and the insulator layer is dark grey. The segments* $c1-c2$ *and* $c3-c4$ *have lengths* L_N *and* L_{SNS}*, respectively.*

L_N and L_{SNS} of the segments $c1-c2$ and $c3-c4$ (defined in Fig. 5.1) were obtained from SEM images, together with the ratio $f{=}A_I/A_Q$ of the interferometer (A_I) to qubit (A_Q) areas. The geometric inductance L_I of the interferometer loop was calculated with the modelling program FASTHENRY [83].

	$L_N(\mu m)$	$L_{SNS}(nm)$	f	L_I (pH)
AgInt	3	3000	-	24
SbQ	3.5	600	15	53

Table 5.1: *Interferometer design parameters.*

5.2 Device design

5.2.1 Material choice

Equations (4.27) and (4.28) in the previous chapter highlight the role of the interferometer normal resistance R_N in determining the backaction of the readout junction onto qubit dynamics. To reduce current fluctuations in the interferometer loop, which couple to the qubit and cause relaxation and decoherence, large values of R_N must be used. This can be achieved by fabricating the readout junction with a normal metal section of high resistance. Unfortunately, previous experimental studies of Andreev interferometers with metallic N sections have focused on low resistance materials such as silver [75, 15], gold [84, 85] or copper [86]. For our interferometer-qubit device, we used antimony as the normal metal for its high resistivity ($\rho \approx$50-60 $\mu\Omega$cm, see Sec. 7.1) would allow us to obtain easily large normal resistance $R_N \approx$100 Ω. Compared to typical Ag-based interferometer ($R_N \leq$10 Ω in Ref. [75]), an antimony SNS junction reduces the amplitude of current fluctuations by at least one order of magnitude.

Andreev interferometers with antimony normal section were investigated in Ref. [68] and a sizeable proximity induced correction of the magnetoresistance was measured. The magnitude of the effect, however, was rather small ($\Delta R/R_N \leq 10^{-3}$) compared to similar interferometer structures with silver normal section. This prompted us to use relatively short N sections ($L_{SNS} \approx$600 nm) to compensate for the small proximity amplitude expected from antimony. As shown in Sec. 7.1, amplitudes up to $\Delta R/R_N \approx$40 % were achieved in our samples.

5.2.2 Phase sensitivity

The dependence of the phase φ_I across the SNS junction on the device parameters expressed by Eq. (4.12) defines the sensitivity of the interferometer resistance to the variable $\Delta\varphi_Q$. Maximum sensitivity to $\Delta\varphi_Q$ is achieved when the terms linear in the interferometer and qubit currents i_I and i_Q can

be ignored. An over-estimate of the latter can be obtained using $i_Q = I_0$ and L_B from Table 5.2, giving $i_Q L_B/\Phi_* \approx 3 \times 10^{-4}$, which is much smaller than the other terms, and so can be ignored. The term linear in i_I is subject to a further constraint due to the need to avoid hysteretic behaviour in the dependence of φ_I on the externally applied flux, and must satisfy the condition

$$\beta = \frac{i_{0I}}{\Phi_*}\left(L_I + L_{eQ}\right) \ll 1. \tag{5.1}$$

The condition above can be satisfied by either minimising the geometric inductance L_I (fabricating small interferometer loops), or using a SNS readout junction whose length L_{SNS} exceeds the coherence length ξ_N in N (long-junction limit). The second strategy, which exploits the exponential decay of i_{0I} as a function of L_{SNS}/ξ_N, was followed in Ref. [15], where negligible supercurrent through the SNS junction was obtained using a 3 μm long silver normal metal section. We used a similar strategy in designing the sample AgInt described in Sec. 7.3.

Equation (5.1) may not be satisfied in our interferometer-qubit device, where the short antimony junction may cause a significant supercurrent to flow around the interferometer loop. In such device, the coherence length is estimated to be $\xi_N = \sqrt{(\hbar D)/(2\pi k_B T)} \approx 1$ μm at T=20 mK using the diffusion coefficient D determined in Sec. 7.1. The readout junctions are in the so called short-junction limit ($L_{SNS} \ll \xi_N$), where there is a strong Josephson coupling between the superconducting electrodes. For this interferometer-qubit device, the long-junction limit was achieved by increasing the electron temperature of the SNS junction. Using the Thouless energy $E_{TH} = D/L^2$, the condition for a small supercurrent becomes $k_B T \gg E_{TH}$, and can be fulfilled by either increasing the fridge temperature or increasing the electron temperature in the readout junction by means of the measurement current. Successful tuning of critical currents in SNS junction was first demonstrated in Ref. [58], where tuning of the critical current in a cross-shaped SNS junction was achieved by changing the current driven perpendicularly to the junction. The mechanism of supercurrent suppression is related to the finite voltage across the leads, which causes the injection of electrons at energies higher than those of the quasiparticles at equilibrium in the weak link. These electrons create a non-equilibrium distribution function of quasiparticles in the SNS junction, and tend to equilibrate the occupation of Andreev bound states carrying current in opposite directions.

As shown in Sec. 7.2.2, we were able to access both the short- ($E < E_{TH}$) and long-junction ($E > E_{TH}$) regime in our interferometer-qubit device by changing the pulse parameters of the measurement current.

5.2.3 Interferometer geometry

A novel multi-layered design was used for the normal part of the interferometer, named "folded cross", as shown in Fig. 5.2. The upper section of the contact leads is made of aluminium and overlays the normal part of the interferometer, and an insulating layer of SiO_x is interposed between the two to prevent shorts. The folded cross design is an improvement on the simple cross design previously investigated (see for instance Ref. [15] and references therein) and that was also used for the sample AgInt, which has the disadvantage of having asymmetric connections to the interferometer normal part. In the simple cross design, the current used for the measurement of the interferometer resistance will induce a magnetic flux through the interferometer and qubit loops, thus coupling the flux bias to the external circuitry used for the experiment. This flux acts on the device dynamics in two ways: it introduces a flux offset in the bias point of the qubit and causes a persistent current to flow in the interferometer loop and through the qubit junctions. Any fluctuation in the current is then transmitted to the qubit, and can lead to relaxation and decoherence. The folded cross design solves this problem by making symmetric connections to the interferometer. In this design, the same current flows in the bottom and top contact leads, and no net flux is induced in the interferometer loop.

5.2.4 On-chip leads

The superconducting antenna used for the interferometer sample AgInt, shown in Fig. 5.3(a), consists of a simple closed loop microfabricated at a distance of 500 nm from the qubit loop. Strong coupling between the antenna and the interferometer loop was experimentally observed for this sample, and the properties of the SNS junction were significantly affected by the RF field (see Sec. 7.3). This strong coupling prompted us to change the simple loop antenna layout in favour of a "quadrupole" design shown in Fig. 5.3(b) to diminish the amount of RF radiation reaching the interferometer loop.

The quadrupole design consists of three wires in a coplanar configuration, shorted at the end, and running parallel to the qubit edge. The difference between the two antenna designs can be understood by considering that the magnetic field generated by a current flowing in a straight wire has a x^{-1} dependence given by the Biot-Savart law, where x is the distance from the wire. In the simple loop scenario, the field at a distance x is given by the sum of two opposing contributions, one of which is weaker than the other due to the larger distance. With the quadrupole design, the third wire adds a further $1/x$ term, with the effect of an overall steeper decrease of the field as

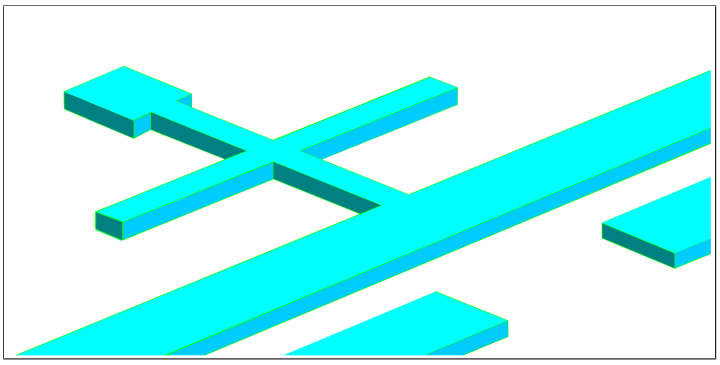

(a)

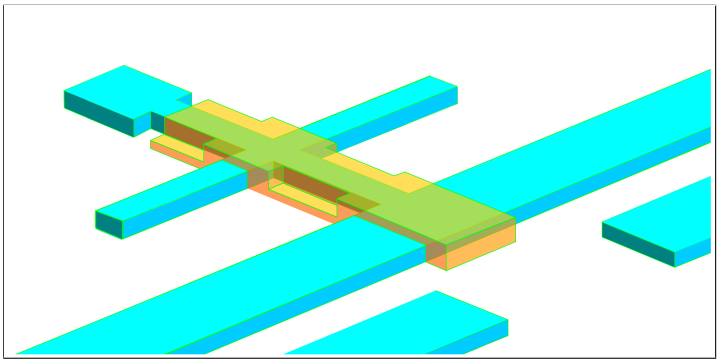

(b)

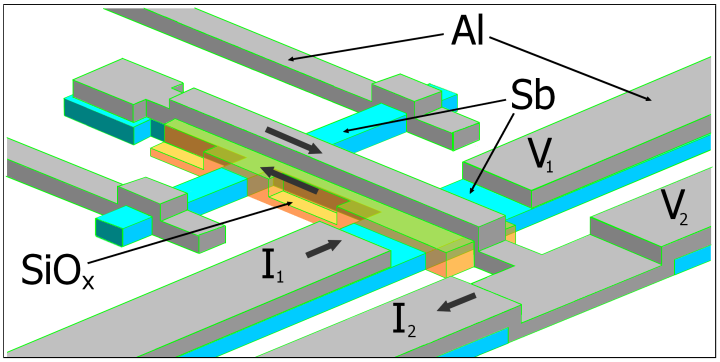

(c)

Figure 5.2: *Fabrication steps of the "folded cross" design, showing the different layers: (a) antimony interferometer N section; (b) SiO_x insulating layer; (c) aluminium top lead and interferometer loop. The labels in (b) show the configuration needed for the 4-point resistance measurement, where the lead I_2 was connected to earth. The arrows indicate the floww of the measurement current.*

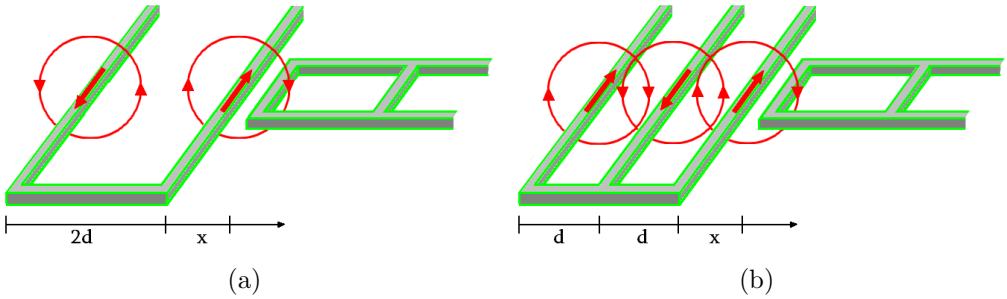

Figure 5.3: *Different antenna designs used in our device: (a) simple loop and (b) "quadrupole" design. The latter is composed of three wires separated by a distance d, and produces a magnetic field which decreases faster with increasing x than in the simple loop design.*

a function of the distance x. Performing the calculations for the structures shown in Figs. 5.3(a) and 5.3(b), where the inter-wire separation d and the length x are defined, the ratio B_S/B_Q between the fields in the "simple" and "quadrupole" designs is found to be

$$B_Q/B_S = \frac{d}{2(d+x)}. \tag{5.2}$$

As an example, at a distance $x = d$, Eq. (5.2) gives $B_Q = \frac{1}{4}B_S$.

The resistance of the measurement leads contacting the cross needs to be minimised to meet the frequency requirement imposed by the pulsed measurement (see Sec. 6.4.2). The lead resistance R_L creates an RC low-pass filter with the distributed capacitance $C \approx 100$ pF/m of the readout lines, which can narrow the bandwidth below the desired 1 MHz if $R_L > 100\ \Omega$. For this reason, the contacts to the N section of the folded cross were designed to be as wide as possible, and where fabricated using a Sb/Al bilayer to lower their resistance.

Extra ground planes, shown in Fig. 5.1, were fabricated to screen the qubit from the radiation produced by the pulsed current used to probe the interferometer SNS junction.

5.2.5 Qubit parameters

The Josephson circuit investigated in this thesis was designed to operate as a persistent current qubit, which requires the conditions $E_J/E_C \gg 1$ to be satisfied. Estimations of E_J and E_C for our device were obtained from test

Josephson junctions co-evaporated with the interferometer-qubit device and SEM imaging of the measured device. Typical critical currents I_0 ≈300 nA and capacitances C ≈2 fF were obtained for the large area (≈0.05 μm^2) junctions, giving E_J/E_C >15. The small area junctions were fabricated with area smaller by a factor α=0.66±0.05. A small geometric inductance of the qubit loop L_Q ≈13 pH was calculated with the modelling program FASTHENRY [83], which allows us to ignore flux screening in Eq. (4.12). A summary of the design parameters for the qubit device are given in Table 5.2.

	I_0 (nA)	C (fF)	E_J/E_C	L_Q (pH)	L_B (pH)
SbQ	300	2	>15	13	6

Table 5.2: *Qubit design parameters.*

5.3 Nanofabrication of devices

All the fabrication steps were carried out in the clean room at Royal Holloway. During fabrication, a lift-off technique employing a double layer of resist was used. In this technique, a ∼ 1 μm thick bottom layer of resist is first spun onto the substrate, followed by a thin (∼10 nm) layer of a different resist material. Both layers are exposed simultaneously and developed in a suitable solution. In the top layer, the pattern of the wanted structure is developed, thus creating a mask for a later film evaporation. The bottom layer resist is selected to develop slightly quicker than the top one, and an undercut is created. This technique is used to make the lift-off of excess material and unexposed resist easier and is the basis of the Dolan bridge technique [87] for the evaporation at different angles. For the last aluminium layer, a tri-layer technique was used, in which a thin germanium (≈20 nm) layer is interposed between the two PMMA layers [88]. The top PMMA layer acts as a mask for the germanium layer, which is etched, and then acts as a mask for the bottom PMMA layers. Tri-layers allow a better definition of small-size structures and an independent exposure of the undercut pattern.

5.3.1 Photolithography

Standard photolithography was used to create the contact pattern needed to connect the sample to the electrical lines of the measurement setup. The pattern containing 75 sample microchips is processed on a 5 mm thick 4”

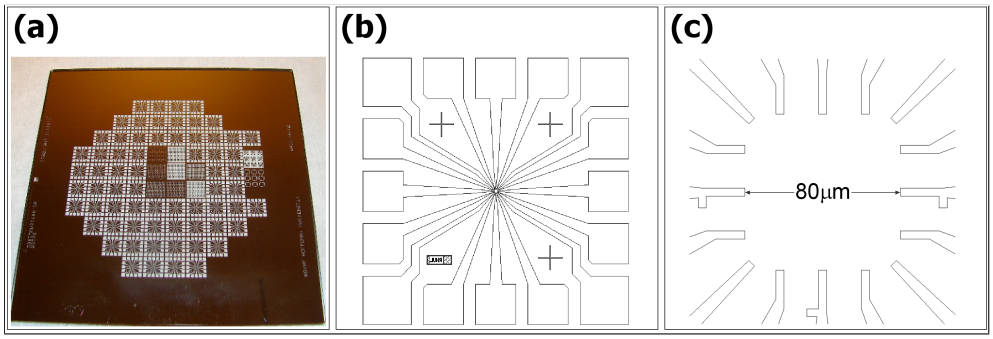

Figure 5.4: *Photolithography steps: (a) The NiCr-Au contact layer is fabricated on a 4" wafer by photolithography. (b) Further processing is carried out on individual 7 mm×7 mm chips obtained cutting the wafer. The layout of the contact layer containing the squares pads and the leads is shown. Three crosses and the RHUL logo (lower, left corner) are used to determine a unique chip orientation. (c) 80 μm×80μm blank area at the centre of the chip, where devices are drawn using electron-beam lithography.*

wafer, then cut into single 7 mm×7 mm chips for further processing, as described in Figs. 5.4(a)-(c). The chip pattern includes square pads used for bonding and the leads converging to the centre where a 80 μm×80μm area is left blank for electron-beam defined structures. After cleaning the wafer with Reactive Ion Etching (*RIE*) in an oxygen plasma, a 1200 nm thick LOR-5B and a 400 nm thick S1183 resist layers are separately spun onto the wafer and baked. The wafer is exposed using a custom-made UV system performing contact photolithography. After developing the pattern in MF69 developer, the wafer is moved to an Edwards E306A evaporator for the contact layer deposition. The evaporator is fitted with a double pumping system consisting of a rotary pump and a diffusion pump, and reaches a base pressure of $\sim 10^{-7}$ Torr in about 5 hours. When a pressure of $\approx 5\times10^{-6}$ Torr is reached in the evaporator chamber, 10 nm of NiCr and then 80 nm of Au are evaporated onto the wafer. The contact layer is created by immersing the wafer in Microposit remover 1165 and letting the excess metal be lifted-off. The wafer is cut into single chips that are separately processed.

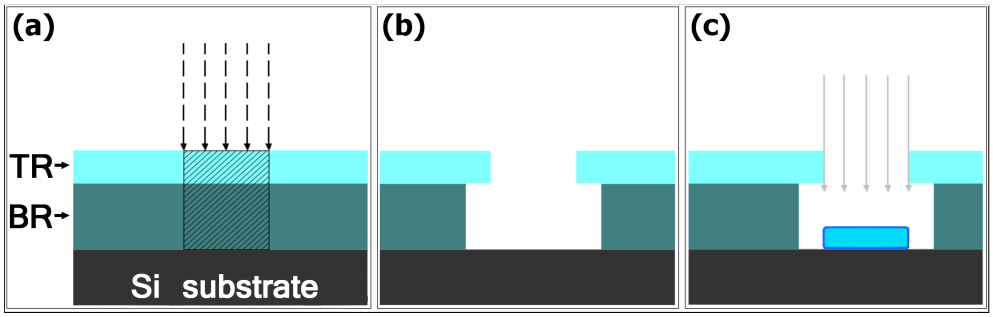

Figure 5.5: *Fabrication steps for the normal metal layer. The resist bi-layer is created by spinning a thick bottom layer (BR) and a thin top layer (TR). The bi-layer is (a) exposed and (b) developed. The latter step produces the undercut in the bottom layer. The normal metal is then evaporated (c).*

5.3.2 Electron-beam lithography

Normal metal layer

The normal metal layer defines the normal metal part of the interferometer as well as the wires that connect to the contact leads defined by photolithography. Two different normal metals were used for this layer, silver for the AgInt and antimony for the SbQ samples. The fabrication steps for metal deposition are described in Figs. 5.5(a)-(c). A layer of copolymer (1000 nm) and one of PMMA (80 nm) are separately spun onto the chip and baked. The pattern is defined by electron-beam lithography using a JEOL JSM-6460 Scanning Electron Microscope (*SEM*). Marker crosses were also written to allow the alignment of the subsequent electron-beam patterns. After development in a deionised water-isopropanol solution, the chip is loaded into the evaporator. When a pressure of less than 5×10^{-6} Torr is reached in the evaporator chamber, in-situ argon plasma etching is used to remove residuals of resist which could compromise the contact between the metal layer and the gold contact leads. After the pressure in the chamber comes back to $\approx5\times10^{-6}$ Torr, 50 nm of normal metal are evaporated onto the chip. The chip is then immersed in 1165 Microposit remover at 70 °C for the lift-off stage.

Insulator layer

An insulator patch is needed in the SbQ sample to isolate the normal metal layer from the aluminium layer. This is obtained by evaporating a

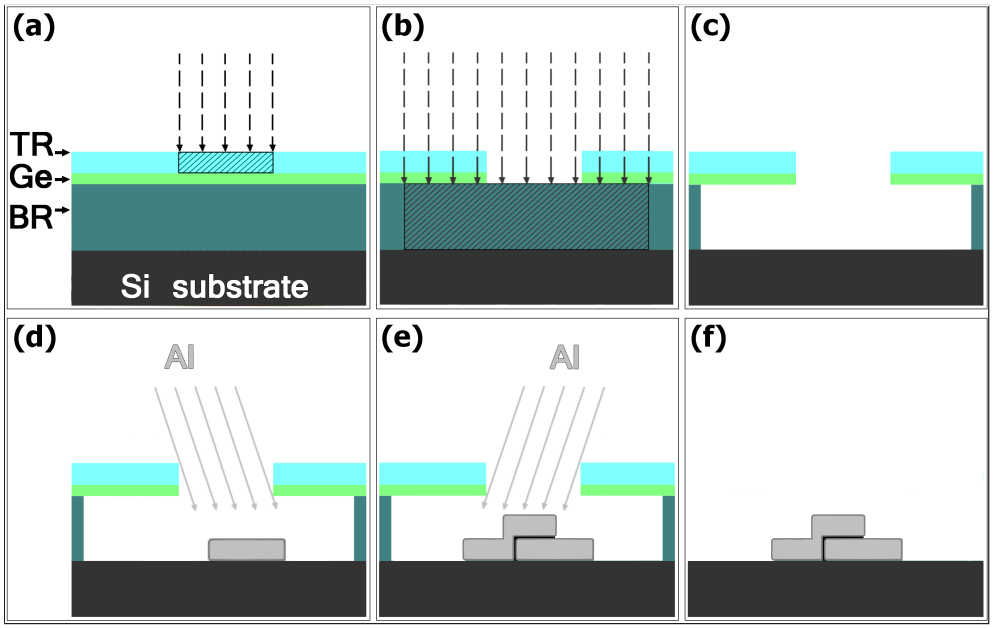

Figure 5.6: *Fabrication steps of the aluminium layer. (a) Exposure of the resist layer on top of the Ge layer. (b) Exposure of the undercut in the bottom resist layer after the Ge mask has been created by plasma etching. (c) Development of the undercut. (d) Angle evaporation of the first aluminium layer. (e) Angle evaporation of the second aluminium layer after the oxidation of the first aluminium layer. (f) Josephson junction created after lift-off.*

30 nm thick silicon oxide film, which covers the normal section of the interferometer and part of the leads. Due to the simple geometry of the patch, a single 80 nm thick layer of PMMA is used instead of the bi-layer. The exposure, development and evaporation stages are identical to those described in Sec. 5.3.2.

Aluminium Layer

Aluminium is the last metal deposited and completes the device creating the superconducting structures. In the interferometer device this consists of a single 50 nm layer which defines the interferometer loop and antenna. In the interferometer-qubit device, a shadow-evaporated Al/AlO_x/Al tri-layer of total thickness of 70 nm is used. In these device, this layer creates the interferometer and qubit loops, the antenna, and the remaining top connection to the folded cross. To create the mask for the shadow evaporation, 1000 nm

of PMMA resist is first spun onto the chip and baked. The sample is then loaded into the evaporator where 20 nm of germanium are deposited on top of the PMMA layer. A second PMMA layer (80 nm thick) is then spun onto the sample and baked. Electron-beam lithography is used to expose the upper PMMA layer, which is then developed. A SF_6-O_2 plasma is used to etch the germanium layer where it is not covered by the upper layer of PMMA, thus transferring the pattern to the germanium layer. The undercut is created exposing the bottom PMMA layer by electron-beam lithography through the germanium layer, using a pattern which is ≈300 nm wider than the structures in the germanium mask. The electron-beam is not affected by the thin germanium layer, and the dose after the germanium layer is enough to expose the bottom PMMA layer, which is then developed.

After defining the germanium-PMMA mask, the sample is loaded into the evaporator and the system is pumped to a pressure of about 1×10^{-6} Torr. During this stage, a heater mounted inside the chamber was used to remove any water residuals that could compromise the subsequent oxidation stage. In-situ argon plasma etching is used to ensure clean interfaces between the aluminium structures and the normal metal and the antenna pads. For the interferometer device, 50 nm of aluminium are evaporated onto the sample at 0°. For the interferometer-qubit device, the double-angle evaporation is needed to create the four Josephson junctions of the qubit without breaking the vacuum in the evaporation chamber. For this purpose, the evaporator has a sample holder which can be rotated around one of the horizontal axis, thus changing the angle of incidence of the evaporated material with respect to the sample surface. First, a 35 nm thick aluminium layer is evaporated at an incident angle of 10°, then the chip is exposed for 15 minutes to 2 mTorr of pure oxygen admitted into the chamber in a continuous flow. As a result, the aluminium surface is covered by a thin AlO_x insulating layer. Once the oxygen flow is stopped, the pressure in the chamber falls back to $\approx2\times10^{-6}$ Torr in a few seconds, and a second 35 nm thick aluminium layer is evaporated at an angle of -10°. The excess metal and the PMMA-germanium layers are lifted-off using Microposit remover 1165.

Chapter 6

Experimental Setup

This chapter describes the experimental setup used for the low temperatures measurements described in Chapters 7 and 8. Pulsed resistance measurements of our device were performed for the first time, and required the installation of filtered low frequency lines and RF coaxial lines, as well as the fabrication of a new sample holder and a printed circuit board. Magnetic screens were built to protect the devices from environmental magnetic fluctuations, and were used for the first time in these measurements.

This chapter is organised as follows. Section 6.1 gives a detailed description of the wiring and filtering, with emphasis on the issue of thermal noise. Then, the design of the sample holder, the printed circuit board and the magnetic screens are described in Secs. 6.2 and 6.3. Finally, the room temperature equipment used for the measurements on interferometer and interferometer-qubit device is described in Sec. 6.4.

6.1 Electrical Wiring

6.1.1 Thermal considerations

In designing an experimental setup for cryogenic temperatures, an important issue is the thermal load on cold parts due to the thermal conduction of the electric leads and elements linking parts of the setup at different temperatures. Special attention has to be put into the choice of materials and sizes, to ensure good thermalisation of all elements and avoid Joule heating by measurement currents. The total thermal load due to heat conduction and the Joule heating have to be smaller than the cooling power of the fridge.

The heat flow through a bar of length l and uniform cross-section A,

whose ends are at temperatures T_2 and T_1 is given by the Fourier law

$$\dot{Q} = \frac{A}{l} \int_{T_1}^{T_2} \lambda(T) dT, \tag{6.1}$$

where $\lambda(T)$ is the temperature-dependent thermal conductivity of the material. The mean thermal conductivity

$$\bar{\lambda} = \frac{1}{T_2 - T_1} \int_{T_1}^{T_2} \lambda(T) dT, \tag{6.2}$$

is found in literature (see for instance Ref. [89]) for a large variety of materials commonly used at cryogenic temperatures. Once the material is selected, the geometrical sizes (l and A) can be chosen to have an acceptable thermal load at the cold stages of the fridge.

A second contribution to the thermal load comes from Joule heating. The power P dissipated by an element of resistance R is equal to $P = R \cdot I^2$, where I is the current flowing through it. If large currents have to be fed into leads made of resistive materials, the dissipated power can even exceed the cooling power of the fridge and cause an increase of the sample temperature. Materials with low thermal conductance usually offer high electrical resistance, so that, in general, a compromise between thermal load and Joule heating has to be found.

The fridge used in the experiments is an Oxford Instrument Kelvinox 400 with a base temperature of 10 mK and nominal cooling power of 400 μW: by definition, this is the power that, if delivered to the mixing chamber stage, will set its temperature to 100 mK. The fridge already had 64 Manganin braided wires for thermometers, heaters and general purpose measurements. The implementation of the pulsed scheme used for the measurements described in Chapters 7 and 8 required the installation of four additional low frequency lines and two high frequency lines. The additional thermal load reaching the mixing chamber from room temperature, due to the additional wiring, is estimated to be less than 3 μW. The Joule heating in the resistive sections was minimised by using low resistance or superconducting wires for the lines carrying large currents, as described in Sec. 6.1.3. As a result, no increase in the base temperature of the fridge was noticed after these modifications were made.

6.1.2 Filtering

The presence of unwanted signals is inevitable in the laboratory. Several precautions can be taken to make sure that known sources of disturbances are

placed far away from the experiments, or a means of isolation is interposed between these and the sensitive parts of the experiment. The presence of interference in the measurement setup can compromise the detection of the experiment output, especially when dealing with low-level signals which can be overwhelmed. Moreover, the biasing of the sample can be significantly affected by interference, which can introduce fluctuations in the working point of the device and lead to decoherence of the qubit. The control over the dynamic of the qubit can be also compromised by spurious high frequency signals, which can randomly excite the qubit to the upper level.

In the following, the thermal noise is assumed to be the main noise source. Then, the characterisation of the filtering elements and a description of the electrical lines in the experiment setup are given. Finally, the thermal noise reaching the sample is estimated.

Thermal noise

An inevitable source of noise in cryogenics is thermal noise (known as Johnson-Nyquist noise), which originates from the agitation of carriers contained in a conductor as a result of temperature. In general, a metal at the temperature T_0 can be seen as composed by two subsystems: the electrons, characterised by the temperature T_e, and the phonons, at the temperature $T_{ph} = T_0$. When excited to a temperature $T_e > T_0$, the electrons can relax either by exchanging energy with other electrons or by emitting phonons. The latter mechanism depends on the electron-phonon coupling, which is so strong at room temperature to ensure $T_e = T_{ph}$. At low temperatures, the cooling rate due to phonons has a dependence $\propto T_0^n$, with $4 < n < 5$, and is very small for $T < 1$ K [90]. As a result, while travelling from hotter parts to colder parts of the lines, the electron system can be at a temperature T_e significantly larger than T_{ph}.

The (one-sided) noise spectral density associated with the resistance R at temperature T is described by Planck's formula [82]:

$$S_{v,n}(\nu, T) = 4R\frac{h\nu}{e^{h\nu/k_BT} - 1}, \tag{6.3}$$

where ν is the frequency, and k_B and h are Boltzmann's and Planck's constants. The spectrum $S_{v,n}(\nu, T)$ is essentially flat up to the temperature dependent frequency $\nu_c = k_BT/h$. At room temperature $\nu_c \approx 6$ THz, while at 10 mK this reduces to $\nu_c \approx 200$ MHz. For frequencies below ν_c, Eq. (6.3) can be approximated by the famous Nyquist formula $S_{v,n} = 4Rk_BT$. If two resistors R_1 and R_2 are connected in a circuit, the noise power density $S_{v,n}^{(2)}$

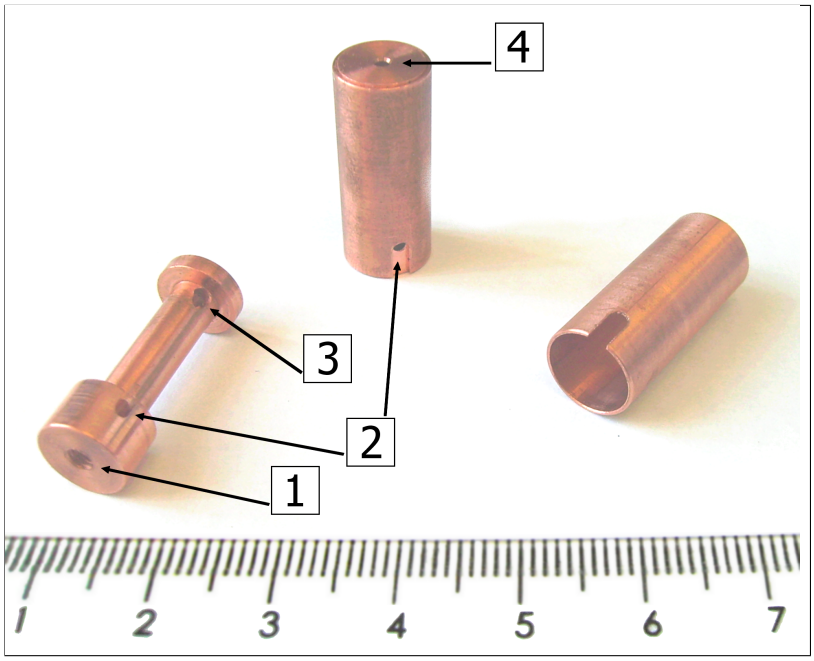

Figure 6.1: *Copper posts used for the thermalisation of the read-out and low-frequency magnetic bias lines. Shown are the central element (left), which is screwed onto a fridge plate through the threaded hole (1), and the outer shell (right), which fits tightly around the post. The assembled post is shown in the centre. The manganin wires enter the post through the hole (2), make several turns around the central element, and exit from the hole (3). The capillary tubes fit tightly into the holes (2) and (4), thus ensuring a continuous shielding of the wires. The graduate scale is in cm units.*

produced by R_1 and delivered to R_2 is given by:

$$S_{v,n}^{(2)} = S_{v,n}^{(1)} \left| H(\nu) \right|^2 , \tag{6.4}$$

where $S_{v,n}^{(1)}$ is produced by R_1 and $H(\nu)$ is the transfer function between R_2 and R_1. In general, several sources R_1^i are connected to R_2 through networks of transfer functions $H(\nu)^i$. In this case, the superposition principle applies, and the total noise power density reaching R_2 is the sum of the various contributions given by the Eq. (6.4).

Ideally, the electromagnetic environment surrounding the sample must be described by an equilibrium spectral density equal to that of black-body radiation at the sample temperature. This ensures that the electrons in the sample are in equilibrium with the phonon system at the fridge tempera-

ture. In our devices, the control of the electron temperature is extremely important, as it affects both the amplitude of the detected signal and the quantum dynamics of the qubit. First, hot electrons in the interferometer will decrease the resistance change induced by proximity effect (thermal effect), thus reducing the sensitivity of the measurement to the qubit phase. Secondly, hot electrons from the leads raise the equivalent temperature of the interferometer, increasing the noise spectral density across the qubit, and hence shortening its relaxation time. For these reasons, several copper posts, similar to the one shown in Fig. 6.1, were used in the setup to thermalise the wires at progressively colder stages on the fridge. Between the stages, low-pass filters were fitted to attenuate the high frequency spectrum of noise coming down from the hotter stages. Where large bandwidth was needed, broadband RF attenuators with flat attenuation were used with the double purpose of attenuating the thermal noise from room temperature and thermalising the inner conductor of the coaxial lines. Moreover, the wires were continuously shielded down the fridge by metallic (CuNi or Cu) capillary tubes to ensure that the electrons in the wires were not heated by photons emitted by higher temperature parts of the fridge, such as the walls. An estimation of the noise spectral density at the sample is given at the end of this chapter, after the description of the filters built into the wiring.

Characterisation of filtering elements

Commercial filters are usually not guaranteed at temperatures below -55 °C, and changes in their attenuation characteristics have to be expected below this temperature. At cryogenic temperatures, no standard way of filtering exists, and several different implementations and filtering elements have been proposed in the past. Among these are microfabricated thin films microwave filters [91]-[93], Philips Thermocoax filter [94], custom-made microcoaxes [95] and metal powder filters [96]-[100]. Useful comparisons between different filtering strategies can be found in Refs. [98] and [101]. Although each type of filter has different attenuation properties, the literature suggests that their performance can be made comparable, and the choice of a particular filtering scheme depends on other aspects, like available fridge space. In our experiments, we decided on metal powder filters as they are compact, relatively easy to fabricate, and offer minimal DC resistance. If properly built, they can also be used to enhance the thermalisation of the electrical leads.

In the following sections, the filters and attenuators in the setup are described. The attenuation properties of the filters and the impedance match-

ing of the attenuators were measured at room temperature and 4.2 K. The attenuation measurements were performed with two systems: an Agilent 33250A Arbitrary Waveform Generator (*AWG*) combined with an Anritsu MS2668C Spectrum Analyser (*SA*) was used for the low frequency range (0.4-60 MHz), while an Anritsu 37397C Vector Network Analyser (*VNA*) was used for the high frequency range (40 MHz-40 GHz). The attenuators were first tested at room temperature using the same instrument setup, and then at 4.2 K using a standard DC 4-point lock-in technique to detect changes in the characteristic impedance upon cooling. All devices were mounted on a dipstick fitted with 50 Ω coaxial lines, and the attenuation of the leads was measured and then subtracted from the filter characteristics. The measurements at 4.2 K were performed by dipping the dipstick into a liquid He dewar. In some cases, the procedure was repeated several times to check that the filters did not degrade on thermal cycling.

Metal Powder Filters

Metal powder filters were first proposed by Martinis *et al.* [96] and different variations have been developed by other groups [97, 98, 99, 100]. The basic metal powder filter consists of a thin insulated wire surrounded by fine grain metal powder, where the wire is usually shaped in a coil to maximise the wire length (up to few meters), while maintaining compact dimensions. The high frequency components of the signal carried by the wire induce eddy currents in the powder, which are dissipated via the skin-effect. The effective surface area of the powder is enormous, thus producing a considerable damping. The attenuation properties are dependent on the electrical conductivity and grain size of the powder, as well as the material and diameter of the wire. Detailed investigations on these aspects to achieve the strongest attenuation have been reported in several papers [99, 101], where wire diameters of about 100 μm and Cu powder with 50-100 nm nominal grain size have shown to give the best performances. In our experiments, powder filters with the design proposed in Ref. [100] were built. In comparison with previous designs, these contain 4 nF discoidal capacitors in a π configuration, which produce a well defined low frequency cut-off characteristics, while the attenuation at high frequencies is due to the dissipation in the powder. Using a mixture of epoxy and powder instead of powder alone improves the robustness of the filter and the thermalisation of the wires contained in the filters. Copper powder ([102]) with 50 μm nominal grain size was used, mixed with Stycast 1266 [103] in a 1:1 volume ratio. This epoxy was preferred to Stycast 2850, used in Ref. [100], because its low viscosity allowed a more homogeneous epoxy/metal mixture. Stainless steel powder [104] with 50 μm nominal grain

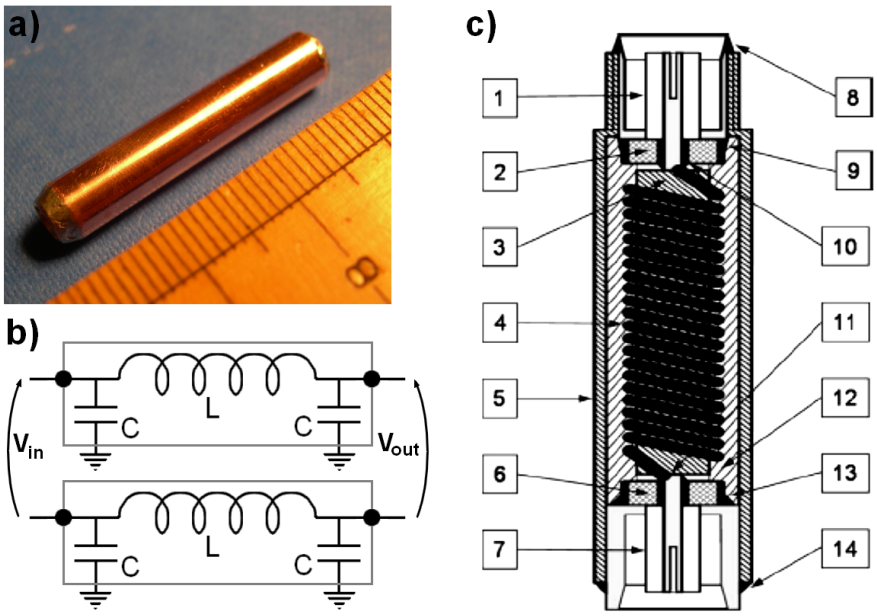

Figure 6.2: *(a) Metal powder π-filters fitted with MCX plug connectors. The ruler shows cm scale. (b) Circuit diagram of a section of twisted pair line employing one powder filter for each wire. (c) Schematic cutaway drawing of the assembled filter (reproduced from Ref. [100]). (1 and 7) MCX plug connectors; (2 and 6) discoidal capacitors; (3) metal powder/epoxy rod; (4) insulated copper wire; (5) outer copper shell; (8 and 14) low temperature solder joints; (9-11, 13) standard solder joints; (12) metal powder/epoxy filling.*

size was also investigated, showing a lower cut-off frequency and resonance free characteristics as in Refs. [97, 98, 100], but the strongly magnetic behaviour of the powder was not compatible with our experiments.

First, the metal powder/epoxy rods for the wire coil were prepared. Equal volumes of epoxy and powder were gently mixed together and poured into a large plastic box which was used as a mould. This procedure was carried out very slowly to avoid trapping air in the mixture. Following deairing in rough vacuum for 10-20 minutes, the mixture was left to cure for 16 hours. Additional baking at 100 °C for 2 hours was needed to solidify the inside. Once solid, the moulded piece was cut into several cylindrical rods which are 4 mm in diameter and 27 mm in length. For each filter about 1 m of 38 SWG ($\approx$ 150 μm in diameter) varnish insulated Cu wire was wound around each rod, being careful to maintain a regular pitch with no gaps between the turns.

The two halves of the coil were counterwound to reduce magnetic field pick up. The inner and outer terminals of the discoidal capacitors (3.3 nF measured at 4.2 K, supplied by Johanson Dielectrics) were soldered to the centre and ground connections of the miniature MCX plugs. The centre pins of the assembled connectors were then soldered to the ends of the coiled wires and then glued to the rod body with GE Varnish, giving a straight bar about 32 mm long. For the outer shell of the filters, sections of thin wall copper tubes (5 mm inner diameter $\times$ 26 mm length) were used. The bar fits into the shell with the MCX connectors partially sticking out of the tubes. The air gap between the centre coil and the tube walls was filled with the powder/epoxy mixture. To achieve this, the coil assembly was covered with the mixture and was slowly inserted into the copper tube. In our filters, the mixture was liquid enough to easily cover the surface of the coil, but thick enough to remain on the wire during insertion. For this purpose, a 50%-50% mixture was first prepared, then additional powder was added to thicken the mixture. It is essential to fill in the gap completely so that the wire is completely surrounded by the powder/epoxy mixture, to ensure an effective dissipation and thermal contact between the wire and the copper tube. After curing for 16 hours, the MCX connectors were soldered to the outer copper tube, thus providing a continuous ground for either side of the filter. Low temperature solder (Woods metal) was used, so that other joints are not damaged by high temperatures. Copper brackets were used to anchor the filters to the fridge stages. A picture of an assembled filter, as well as a schematic showing the various parts is shown in Fig. 6.2.

Figure 6.3(a) shows the measured transmission characteristics of a typical copper powder filter at room and liquid helium temperatures. The filter has a cutoff frequency of $\approx$2 MHz and the transmission rolls off at -60 dB/decade, reaching the noise floor of the VNA at about 300 MHz. A small resonance, previously reported in Ref. [100], occurs at $f \approx$35-50 MHz, and shifts to higher frequency at low temperatures. This resonance is not particularly significant, as the transmission at this frequency is very small (about -55 dB). In the high frequency range, the transmission is always less than the noise floor of the VNA. Figure 6.3(b) shows the low frequency characteristic of four identical copper powder filters measured at room and liquid helium temperatures. At both temperatures, the frequency response of all the filters is very reproducible and almost coincide. The transmission characteristics at 4.2 K are very similar to the room temperature ones. Our filters were thermally cycled several times and no significant difference was found in the measured transmission.

The transmission characteristics of the powder filters was modelled using

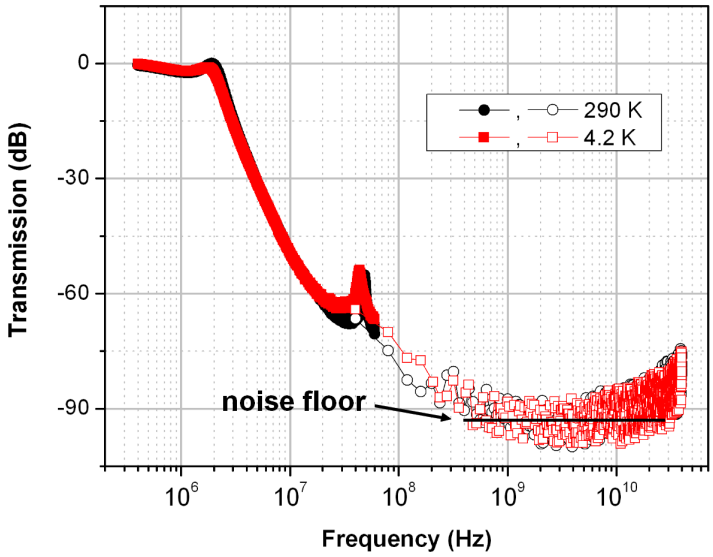

(a)

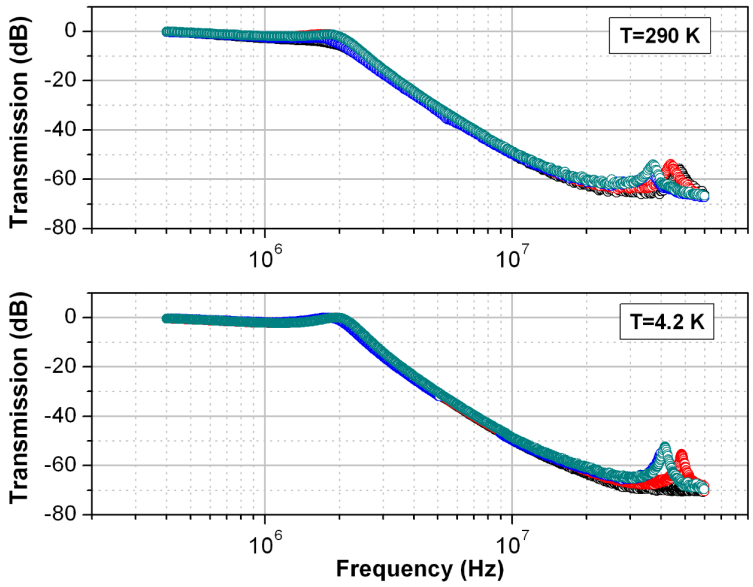

(b)

Figure 6.3: *(a) Transmission characteristics of a typical copper powder filter at room temperature and T=4.2 K. Full and open symbols refer to WFG+SA (0.4 MHz-60 MHz) and VNA (40 MHz-40 GHz) measurements, respectively. (b) Comparison of the low frequency transmission characteristics of four filters at room temperature (top) and T=4.2 K (bottom).*

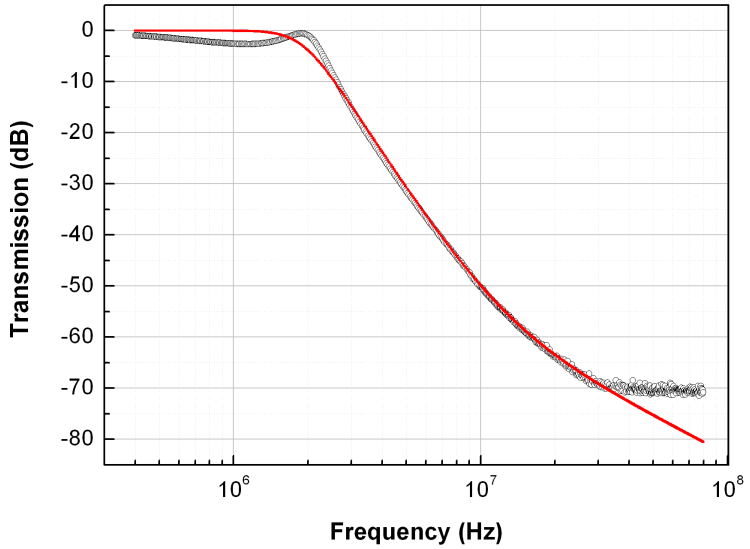

Figure 6.4: *Fit of the transmission characteristic of metal powder filters using Eq. 6.5.*

the general function describing a Butterworth filter [105]

$$\frac{(1+f/f_2)^{n_2}}{\sqrt{(1+f/f_1)^{n_1}}}, \tag{6.5}$$

where the frequencies f_1 and f_2 and the exponents n_1 and n_2 were used as fitting parameters. An example fit, obtained for one of the filters contributing to Fig. 6.3(b), is shown in Fig. 6.4, where f_1=1.9 MHz, f_2=12 MHz, n_1=7.5 and n_2=2.5 were used. The simple model of Eq. (6.5) does a reasonable job of simulating the overall transmission characteristic, but features like the small attenuation in the bandpass and the small resonance at $f \approx$35-50 MHz are not reproduced. Nevertheless, for the purpose of estimating the thermal noise reaching the sample (see Sec. 6.1.3) the description given by Eq. (6.5) is satisfactory.

In our experiments, a second design of filters was also used, where instead of tubes, the external shell was made of a rectangular shaped copper box in which two coiled assemblies could be placed. A lid bolted on a face allows the access to the interior of the box and ensures an optimal filling of the gap between the rod and the shell walls. This design was preferred for the filtering stage closest to the sample, as these were also used as thermalisation posts. The connections were made by MCX plugs at one end, while a female

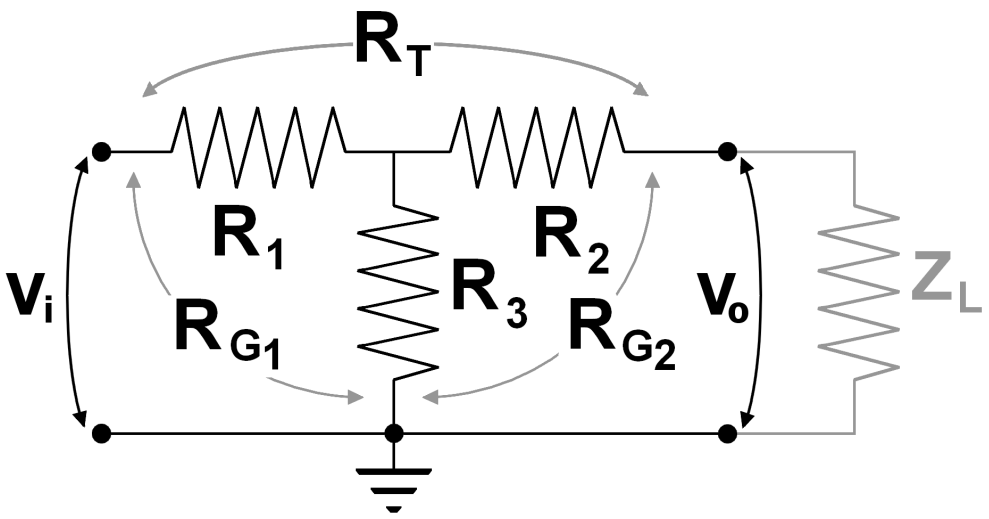

Figure 6.5: *Circuit schematic of a "T" attenuator.* R_i *(*$i = 1, 2, 3$*) are the resistors inside the attenuator;* R_{G_1}*,* R_{G_2} *and* R_T *are the measured resistances.* Z_L *is the impedance of the load (50* Ω*).*

5-way Cinch connector was used for the connection to the sample box.

RF Attenuators

Broadband attenuators are used when flat transmission is required over a large frequency range, and are used in systems employing high frequency coaxial lines. In these systems, the attenuators accomplish a twofold purpose: the thermalisation of the inner conductor and attenuation of noise coming from the higher and hotter stages of the fridge. Figure 6.5 shows the circuit schematic of the attenuators of the type used in our setup. These are composed of three resistor in a "T" configuration, with two nominally identical in-line resistances, R_1 and R_2, and a resistance R_3 to ground. The latter provides the link to the cold ground which is used to thermalise the inner conductor. The reactive part of the impedance, due to the capacitance and inductance of the attenuator, is negligible over the guaranteed bandwidth (2-20 GHz), and the total impedance is determined by the resistors alone. Applying Ohm's and Kirchoff's laws to the circuit shown in Fig. 6.5 gives the equivalent impedance of the attenuator Z_{Att}, when connected to a load impedance Z_L, to be

$$Z_{Att} = \frac{(Z_L + R_2)(R_1 + R_3) + R_1 R_3}{Z_L + R_2 + R_3}. \tag{6.6}$$

	T=4.2 K				
	$R_1(\Omega)$	$R_2(\Omega)$	$R_3(\Omega)$	$Z_{Att}(\Omega)$	A_{dB}
RF line					
20 dB	39.695	40.075	10.045	48.732	-19.748
6 dB	15.832	15.783	69.154	49.545	-5.727
3 dB	8.122	8.014	146.921	49.713	-2.841
3 dB	8.232	7.873	143.972	49.512	-2.850
3 dB	8.062	8.261	147.023	49.788	-2.863
3 dB	8.513	8.502	153.521	50.873	-2.955
Pulse line					
20 dB	38.045	38.015	34.335	62.745	-13.009
10 dB	34.475	34.105	49.555	65.657	-10.985
3 dB	8.011	8.164	147.523	49.727	-2.839
3 dB	7.986	8.142	143.972	49.402	-2.842
6 dB	15.795	16.175	68.195	49.380	-5.783

Table 6.1: *Measured resistances of the attenuators used in the setup.*

Zero reflection in the line is achieved in the case of perfect impedance matching, that is when Z_{Att}=Z_L=50 Ω in standard RF lines. In the same way, it is possible to calculate the linear attenuation $A_L = V_o/V_i$ which, assuming perfect impedance matching, is

$$A_L = \frac{Z_L}{Z_L + R_2} \frac{(Z_L + R_2)R_3}{Z_L + R_2 + R_3} \frac{1}{Z_{Att}}, \tag{6.7}$$

and is independent of frequency in the nominal bandwidth. Using Eq. (6.7), the attenuation in decibel is obtained by $A_{dB} = 20\log(A_L)$.

Commercially available attenuators are built for room temperature RF systems, and are usually not guaranteed at temperatures below −55 °C. At cryogenic temperatures, both the attenuation and the characteristic impedance can change drastically from the room temperature values as a result of the temperature dependence of the resistive elements inside the attenuators. In particular, the resistor R_3 could turn superconducting, thus shorting the RF lines to ground. Moreover, the low temperature behaviour of the attenuators is often batch dependent, so that each attenuators used in the setup needs to be tested at T=4.2 K. In our setup, we used Midwest Microwave SMA attenuators of different attenuations (part numbers ATT-0550-X-35M-02, where "X" is the attenuation). These were mounted on a dipstick and the resistances R_T, R_{G1} and R_{G2} were recorded by standard 4-point resistance measurements using a lock-in amplifier. From these measurements, the

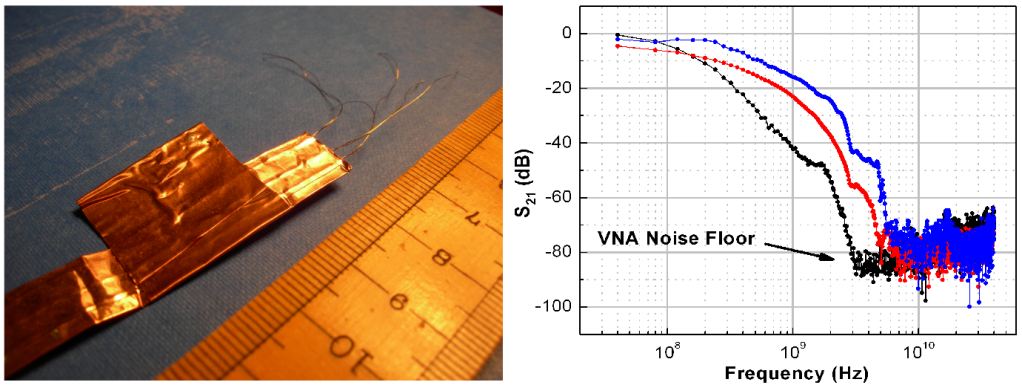

Figure 6.6: *Left: End of a twisted pair filter. Right: Attenuation characteristic for 40 cm (blue), 70 cm (red), and 140 cm (green) long tape filters, measured with a VNA.*

values of R_1, R_2 and R_3 were calculated giving the values shown in Table 6.1 for T=4.2 K. Most of the attenuators used in our experiments retain the room temperature properties, with impedance changes upon cooling of less than 2.4%. The cooling/measurement procedure was repeated several times and the characteristic impedances were found to remain within 0.5% between each cooldown test.

Twisted pairs tape filters

Custom-made distributed *R-C* tape filters were first proposed in by the Yale group [106], and consist of several manganin twisted pairs sandwiched between two layers of copper tape, which are then tightly squeezed together. The copper enclosure provides both RF screening and a large capacitative coupling to ground. The combination of the wire resistance and distributed capacitance (from the wires to ground and between the wires) creates a distributed *R-C* low-pass filter. We have tested tape filters of various lengths, and the transmission characteristics are shown in Fig. 6.6. The bandpass clearly depends on the length of the wires, and extends up to 1-3 GHz for lengths between 40 and 140 cm. Above 3 GHz, the measured transmission is below the noise floor of the VNA. In our experimental setup, a tape filter consisting of six 70 cm long twisted pairs, and fitted with 12-way Cinch connectors was connected to the Manganin braided line at the mixing chamber stage. The thermalisation of the wires was obtained by wrapping the tape several times around the mixing chamber.

6.1.3 Description of lines

In the following, the electrical lines in the experimental setup are described in details. A schematic summarising the wiring is shown in Fig. 6.7.

Manganin braided line

This line, which was installed by Oxford Instrument, is a general purpose line of Manganin wire braid running from a hermetically-sealed 24-way Fischer connector at the top of the cryostat to a 25-way Cinch connector mounted on the mixing chamber plate. The braid is heat sunk at each fridge stage by wrapping it around copper posts. At the mixing chamber stage, a 70 cm long tape filter makes a connection to the sample and attenuate the thermal noise from room temperature. This filter is wrapped around the mixing chamber body several times to thermalise the wires.

The braided line was used for the 4-terminal resistance measurements of the Andreev interferometer sample AgInt, while during the experiments of the interferometer/qubit device (SbQ), the lines described below were used instead, and the braided line was used to measure some test structures mounted on the top surface of the mixing chamber.

Pulse input line

This line was used to carry fast trapezoidal voltage pulses generated at room temperature down to the mixing chamber stage. These pulses have a typical rise time τ_r=5 ns, which gives a broad frequency spectrum extending up to a few $1/\pi\tau_r$, which is in the GHz range. A wide bandwidth coaxial line was used, and RF attenuators placed at each fridge stage provided heat sinking of the central conductor and attenuated the thermal noise coming down from the hotter stages. The line is made up of several sections of semirigid coaxial cables with certified 50 Ω impedances in the range 0-20 GHz, terminated at each end by 50 Ω SMA connectors. Due to the relatively large cross-section, the coaxial lines are the main contribution to the thermal load on the fridge, which was estimated using Eq. (6.1) for several materials. The following choice was made for the three temperature ranges:

- **Room temperature → 4.2 K:** Semirigid UT-141C cables (Micro-coax) were used, that have a silver-plated inner conductor and a copper outer jacket. This section of the fridge is always immersed in the liquid He of the bath, so that the large thermal conduction between room temperature and the 4.2 flange can be neglected.

- **4.2 K → Mixing chamber:** Lossy sections of UT-141-SS cables (Micro-coax) were used between the individual fridge stages. This ca-

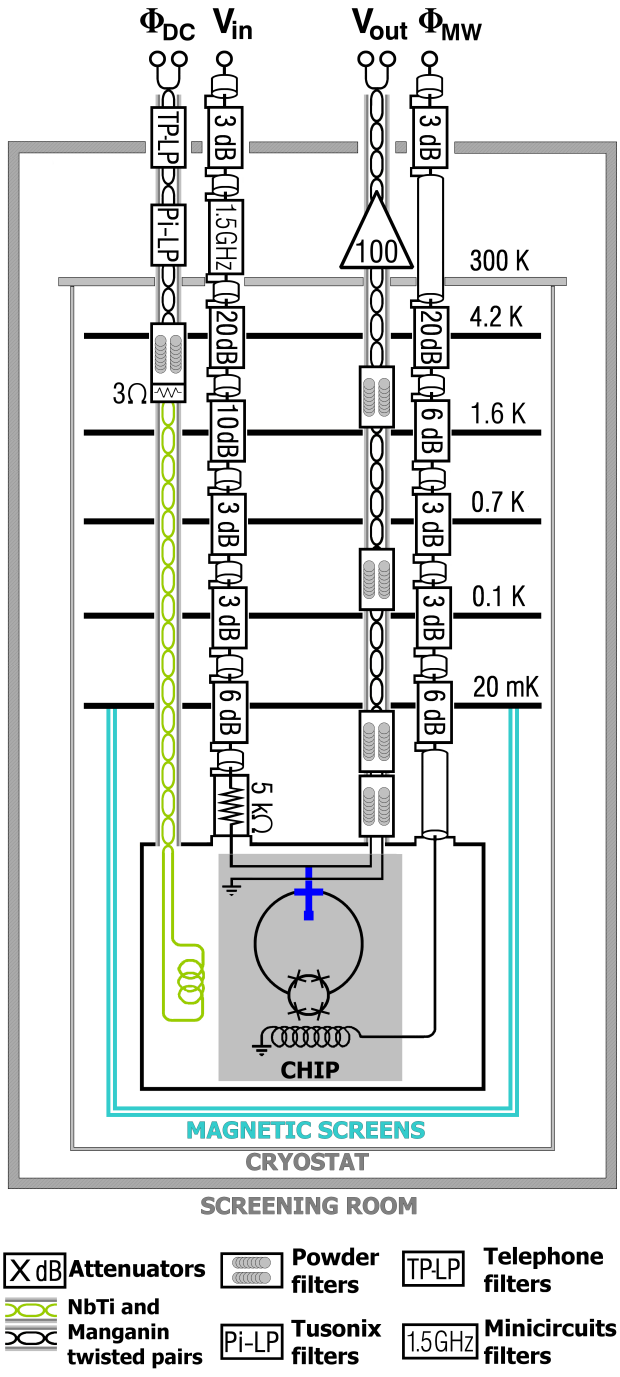

Figure 6.7: *Schematic of wiring and filtering used during the experiments.*

ble has an inner conductor of silver-plated copper and outer jacket of stainless steel, selected to minimise the heat conduction between the fridge stages.

- **Mixing chamber → sample holder:** Semirigid EZ-86-TP/M17 cables by Huber & Suhner were chosen for the last section. This coax has an inner conductor of silver-plated copper and an outer conductors of copper, thermally connecting the sample holder and the mixing chamber.

To choose the correct attenuators, thermal and noise considerations have to be taken into account. A resistive element at temperature T_{in} produces a noise spectral density $S^{in}_{v,n}$ according to Eq. (6.3). If this element is connected in series with an attenuator of linear attenuation A_L placed at temperature T_{Att}, the noise spectral density $S^{out}_{v,n}$ at the output of the attenuator is the sum of the attenuated spectral density $S^{in}_{v,n}$ plus the spectral density $S^{Att}_{v,n}$ produced by the attenuators itself, that is

$$S^{out}_{v,n} = \frac{1}{A_L} S^{in}_{v,n}(\nu, T_{in}) + S^{Att}_{v,n}(\nu, T_{Att}). \tag{6.8}$$

Ideally $\frac{1}{A_L} S^{in}_{v,n}(\nu, T_{in}) \ll S^{Att}_{v,n}(\nu, T_{Att})$ so that the spectral density $S^{out}_{v,n}$ is dominated by the attenuator at temperature T_{Att}. Assuming a flat attenuation over the whole bandwidth, the frequency dependence of $S_{v,n}$ can be neglected and the Nyquist version of the noise spectral density can be used, which gives the condition $T_{in}/T_{Att} \ll A_L$. For example, an attenuation much larger than 40 dB is needed to fully attenuate the thermal radiation going from room temperature to 30 mK.

Joule heating sets a limit on the maximum value of attenuation which can be used. The bigger the attenuation, the more current that is dumped to the ground, which is one of the fridge stages. In our system, a 20 dB attenuator is placed at 4.2 K in the He bath, followed by a 10 dB attenuator at the 1-K pot. Then 3 dB attenuators are placed at the still and cold stages. At the mixing chamber plate, a final 6 dB attenuator is placed before the bias resistor. The biggest temperature gradient is attenuated by the first 20 dB attenuator, where most of the power (about 99%) was also dumped. This does not affect the fridge performances as the power dumped only boiled off liquid He in the bath. At the other stages, no excessive heating has been noticed for the used range of pulse amplitudes. A total attenuation of 42 dB is used to eliminate the radiation from room temperature, giving the room temperature S_{21} scattering parameter in the 0-40 GHz range shown in

Fig. 6.8.

Very close to the sample holder, the voltage at the bottom end of this line is converted to current by means of a 5 kΩ resistor anchored at the mixing chamber plate. This is made of three NiCr metal film resistors connected in series, enclosed in a copper box and embedded in Stycast 1266 to ensure the thermalisation. Several resistors in series were used to increase the surface area in contact with the epoxy filling. Thick metal film resistors were chosen because they show small changes in resistance with temperature. Several 6 mm wide copper braids were bolted to the copper box, with the other ends bolted to the mixing chamber plate.

Readout line

The readout line was used to measure the voltage generated across the normal part of the interferometer. The line is made of a ≈2 m long twisted pair of Formvar insulated Manganin wire 0.1 mm in diameter going from a 5-way Cinch connector at the sample holder to a hermetically-sealed 16-way Fischer connector at the top of the fridge. The wires are thermalised at 4.2 K using the posts shown in Fig. 6.1. To protect the device from excessive noise, this line is heavily filtered at different stages with Copper powder filters. Single-stage powder filters are placed at T≈1.6 K and T≈0.1 K, while double-stage filters are used just before the wires entered the sample box. For the latter, the rectangular design was used, where the filter body is also used to thermalise the wires at the sample temperature. Between the stages, the twisted pair of manganin are continuously shielded by sections of thin CuNi capillary tubing, and PTFE sleeves are used to prevent shorts to ground. The shielding capillaries give the dominant contribution to the thermal conductance, and the calculation of the heat flow was necessary to determine the length between the sections. The resistance of the wires and the capacitance to ground provided by the capillary tubing creates a natural distributed $R-C$ filter which further attenuates high frequency noise; as a result, the measured bandwidth of the line is limited to approximately 1 MHz.

Magnetic biasing line

The magnetic field applied to the sample was provided by driving a DC current (up to 100 mA) through a small superconducting solenoid housed inside in the lid of the sample box. The measurements required that this current was either swept at a rate of less than 10 mA/hour or kept constant for periods of a few hours. The requirement on this line are particularly strict for two reasons: first, the quantum dynamics of the qubit will be

evident in a narrow flux range $\Delta\Phi$ around the bias point $\Phi_Q = \Phi_0/2$, where $\Delta\Phi \approx \pm 2$ %, thus precision to less than $\approx 10^{-4}\Phi_0$ over periods of several hours is required; second, fluctuations in the driving current can produce flux noise that change the bias point of the qubit during the measurement, thus causing the qubit to decohere. For these reasons, a careful filtering scheme including shielding of the line is required. To limit the Joule heating, copper wire twisted pairs (0.5 mm in diameter) are used from the top of the cryostat to the 4.2 K flange, and then a continuous twisted pair of multi-filamentary Nb/Ti wire in a Cu/Ni matrix is used to reach the solenoid in the sample holder cover. At 4.2 K, a thermalisation post and a copper powder filter in a rectangular box are used to attenuate the thermal radiation and environmental noise from room temperature. The box also houses a shunt resistor which allows the superconducting solenoid to be charged. This resistor is a 3 cm long Manganin wire ($\approx$3 Ω measured at 4.2 K) connected in parallel to the solenoid. Additional thermalisation posts are placed at 1.6 K and at the mixing chamber stage. Down the fridge, the wires are continuously shielded with a capillary tube. Additional filtering is provided by the capacitance between the wires and the capillary tube, while the self-inductance of the solenoid and the shunting resistor create a lowpass filter with a cutoff frequency of $\approx$5 kHz.

RF excitation line

This line was used to carry the RF radiation from room temperature to a small antenna patterned on chip. The same considerations already expressed for the fast pulse line apply and the two lines are indeed identical. Figure 6.8 shows the measured S_{21} scattering parameters for the assembled line in the frequency range DC-40 GHz. The transmission is essentially free of resonances up to 20 GHz, above which the components are not fully specified to work, and a sensible degradation of their properties occurs. The monotonic decrease in the transmission in the DC-20 GHz range is due to the attenuation of the lossy coaxial cables, which adds to the 38 dB provided by the attenuators. During the experiment, frequencies from DC to 30 GHz and RF amplitudes in the wide range 10μV-600 mV were used.

Estimate of thermal noise

An estimate of the thermal noise reaching the sample through the pulse input line and readout line was carried out using the formalism described in section 6.1.2. The calculations were used to guide the wiring of the cryostat, and employed several approximations described in the following. Only the pulse input line and the readout line were considered, and these were treated

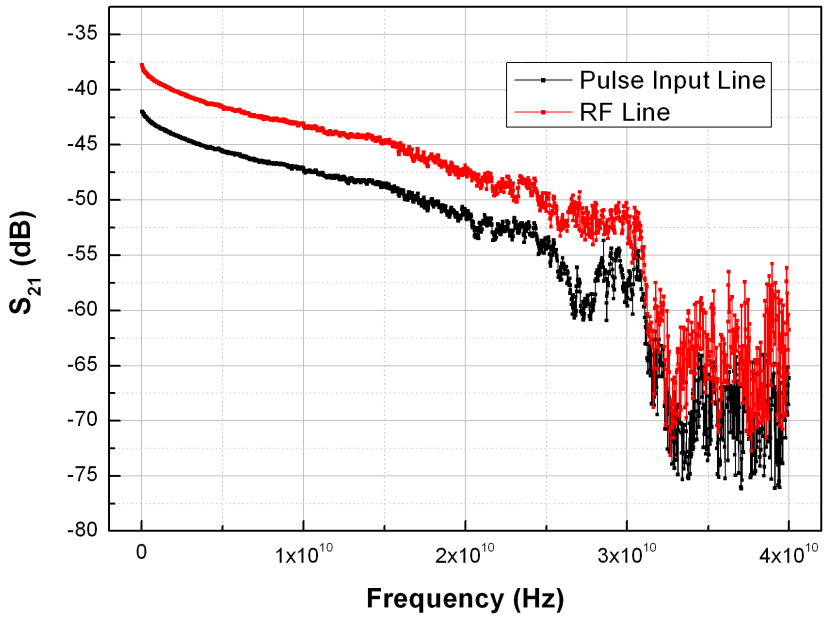

Figure 6.8: *Room temperature S_{21} scattering parameters of the pulse input line and RF line.*

separately using slightly different approaches.

For the pulse input line, the coaxial cables and the attenuators were modelled as systems with infinite bandwidth. The attenuators were modelled as 50 Ω elements with flat attenuation A_{dB} (measured at 4.2 K) over the entire bandwidth. The contribution to the noise due to the cables was not included in the calculations, an assumption that does not change the final result as the attenuators produce the dominant contribution. For the readout line, each section of the resistive twisted pair was divided into 100 subsections, and the contribution to the noise of each subsection was added to give the total noise spectral density of the section. The temperature of each subsection was calculated using a linear interpolation between the temperatures at which the ends of the total section are thermalised. In the calculations, the attenuation due to the capillary tubing was neglected. The transfer function of the powder filters was modelled using Eq. (6.5) with values f_1=1.9 MHz, f_2=12 MHz, n_1=7.5 and n_2=2.5 for the fitting parameters.

The results of the calculations are shown in Fig. 6.9(a) and (b) for the two lines. For the pulse input line, the noise spectral density at low frequencies is dominated by the sample, while the contributions from hotter parts are strongly attenuated by the attenuator stages and the cold bias resistor.

At higher frequencies, the thermal noise is several order of magnitude smaller than at low frequency, and further attenuation is expected from the coaxial lines, as their capacitance to ground (not included in the calculation) becomes relevant.

The noise spectrum due to the readout line shows different behaviour. At high frequencies, a much smaller noise spectral density is expected as a result of the heavy filtering of the line, and the noise spectrum is again dominated by the sample. On the other hand, a significant amount of thermal radiation from room temperature is present at frequencies below 10 MHz. This frequency range corresponds to the bandwidth used for the pulsed measurements, and cannot be further narrowed. Nevertheless, the frequency at which the noise contribution from the sample becomes dominant ($\approx$10 MHz) is well below the excitation frequency of the qubit, which is expected to be in the 1-5 GHz range.

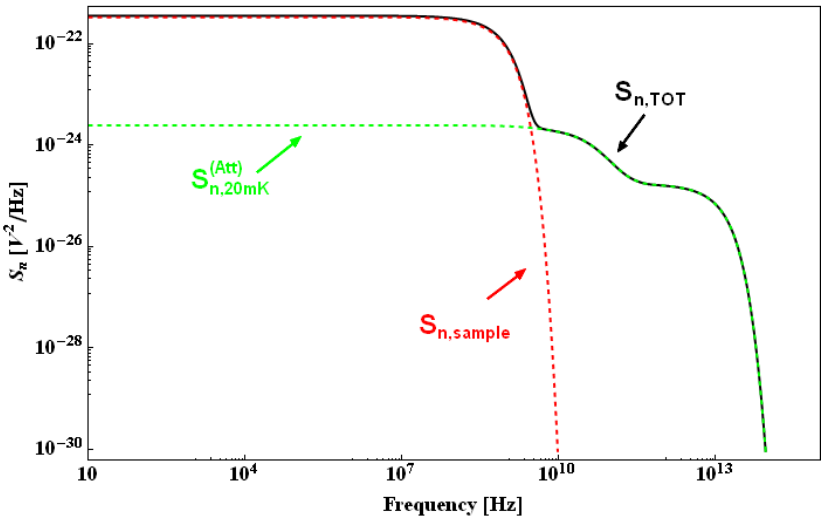

(a)

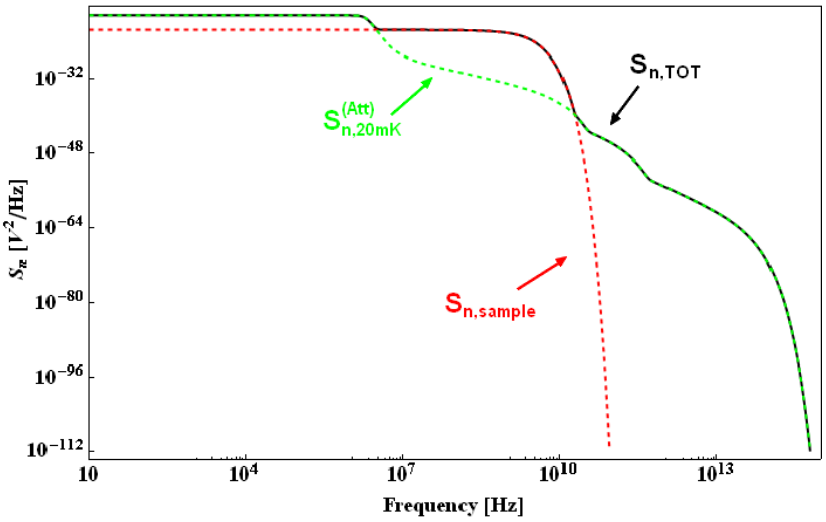

(b)

Figure 6.9: *Calculated noise spectral density across the sample for (a) the input and (b) the readout lines. Contributions to the total spectral density from the lines ($S^{(Att)}_{n,20mK}$) and the sample ($S_{n,sample}$) are shown for comparison. In the calculations, the interferometer was assumed to have a resistance of 300 Ω.*

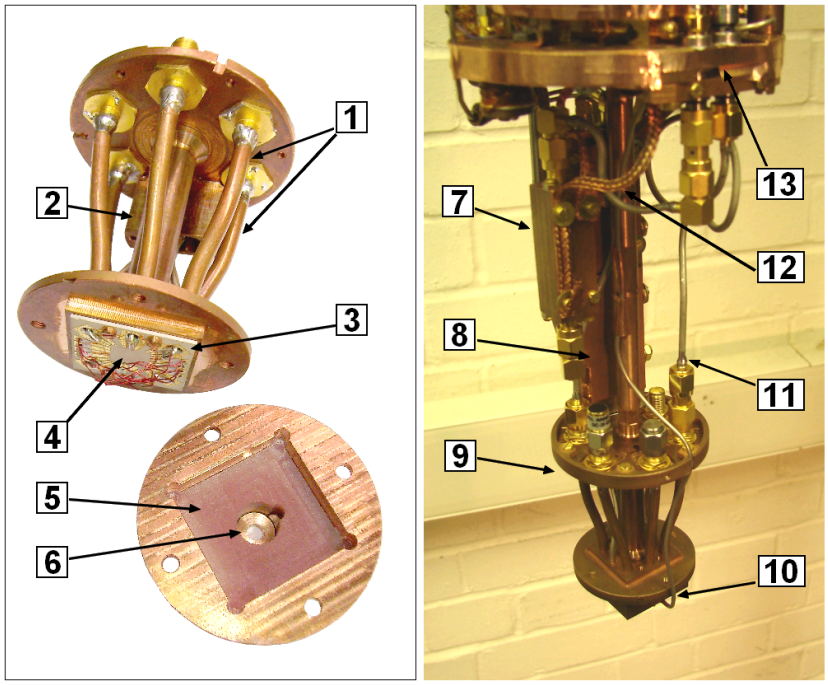

Figure 6.10: *Left: Sample holder before loading the sample. Right: Sample holder attached on the fridge. The labels indicate: (1) Coaxial lines; (2) DC lines; (3) PCB; (4) sample space; (5) copper powder/epoxy absorber; (6) magnet housing; (7) 5 kΩ bias resistor; (8) double-stage powder filter; (9) sample holder; (10) magnet line; (11) RF line; (12) thermalisation copper braids; (13) 6 dB attenuators.*

6.2 Sample holder

6.2.1 Sample holder and Printed Circuit Board

The sample holder shown in Fig. 6.10 was specifically designed to perform the pulsed measurements of our devices with 10 DC and 5 high frequency lines. For sample mounting and wire bonding, as well as for room temperature characterization of the devices, the holder was detached from the mixing chamber plate of the fridge. The body consists of two round plates connected by a central pillar. On the top plate five SMA connectors and one 15-way Cinch connector links the leads of the holder to the lines installed on the fridge. Five copper coaxial lines and five twisted pairs of copper wire in a Cu-Ni capillary tube were used between the top and the bottom plates.

On the bottom plate, a square plinth was machined onto which the Printed Circuit Board (PCB) was screwed facing down. A square cover screws to the plate from below to produce an RF tight chamber. Holes were drilled in the bottom plate, through which the electrical leads enter the chamber. The leads are retained by the tight fit of the holes, so that no solder joint was needed. All the electrical lines entered the chamber from the back of the PCB onto which the ends were soldered. The holder was made from Oxygen Free High Conductivity (*OFHC*) copper, and the amount of solder used was kept to a minimum. We also avoided any ferromagnetic material in the vicinity of the sample, and the magnetic properties of the materials involved in the construction of the box have been tested. A small superconducting solenoid was housed in the cover at about 2 mm from the sample. The bobbin was made of the copper powder/epoxy mixture used for the powder filters, and the remaining space in the cover was filled with the same mixture to suppress resonant modes in the cavity. For the measurements, the holder was attached to the mixing chamber plate by a threaded pillar made of OFHC copper. The superconducting screen surrounded the holder and was screwed at the upper plate.

6.2.2 Printed circuit board

The Printed Circuit Board (*PCB*) was designed to carry the pulsed voltage and RF signals to the sample. At these frequencies, the electric signal is treated as being composed of travelling waves whose wavelengths are comparable or smaller than the size of the system they are travelling in. The wavelength in the media defines a critical length below which a structure can be considered as a discrete element, and above which a distributed model has to be employed. As a general criterion, the critical length should be at least ten times smaller than the wavelength of the travelling wave: in our case, when dealing with frequency up to 30 GHz, the critical length is about 5 mm. Structures larger than this have to be designed according to standard RF design techniques [107].

Figure 6.11 shows the Autocad file of the PCB, which was manufactured by Printech Circuit Laboratories [108] on a TMM10I [109] ceramic substrate. TMM10I was chosen as substrate because of the stability of properties with temperature, and it also provides a tight control of dielectric constant and low loss. The pattern is defined with a 1 μm thick layer of gold over a 17.8 μm thick copper base. To avoid ferromagnetic materials, the PCB was produced by electro-deposition without the nickel layer that is normally used to improve the adhesion between gold and copper layers. The PCB was designed to accommodate five high frequency lines and ten low frequency lines. As a

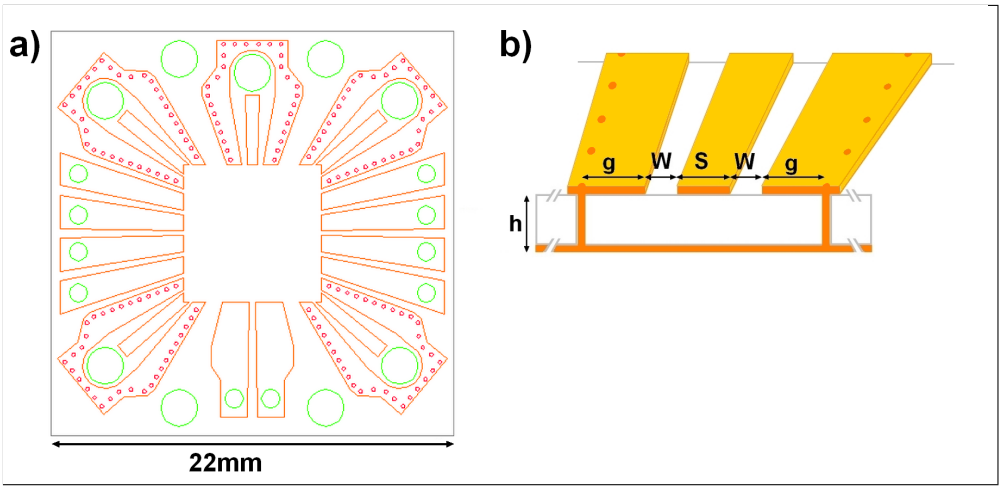

Figure 6.11: *(a) Autocad file of the PCB. The Au pattern is in orange, while vias connecting the top ground planes with the back metallization are in red. Holes for wiring and holding screws are shown in green. TMM10I substrate is in grey. (b) Section of the coplanar lines showing the parameters described in the text. The width g of the ground planes is defined at the outer edge by the vias row.*

general criterion, the lines have been designed to be as wide as possible, to guarantee good thermalization and allow multiple wire bonding to the chip. High frequency lines have to be matched to the characteristic impedance of the lines at which these will be connected (50 Ω) to guarantee low reflection. These lines are then designed as coplanar waveguides, with a central line carrying the signal and two lateral ground planes as the return path. On the contrary, the DC lines have a simple rectangular shape.

The need to provide good thermalization of the chip and leads imposes the use of a conductor backed configuration, connected to the top ground planes by means of a row of vias which are 0.2 mm in diameter and 0.53 mm apart. The ground back plane also ensures that excitations of spurious modes are eliminated. Following Ref. [107], the overall geometry of the high frequency lines can be modelled as a channelized coplanar waveguide (CCPW) with lateral walls formed by the via hole rows. In a CCPW, the characteristic impedance Z_{PCB} of the waveguide depends on the geometric quantities defined in Fig. 6.11(b): the width S of the central conductor, the gap W between this and the ground planes, the width g of the ground planes, and the thickness h of the substrate. For the calculations of Z_{PCB}, the formulae given in Appendix A were used. The values for S, W and g were calcu-

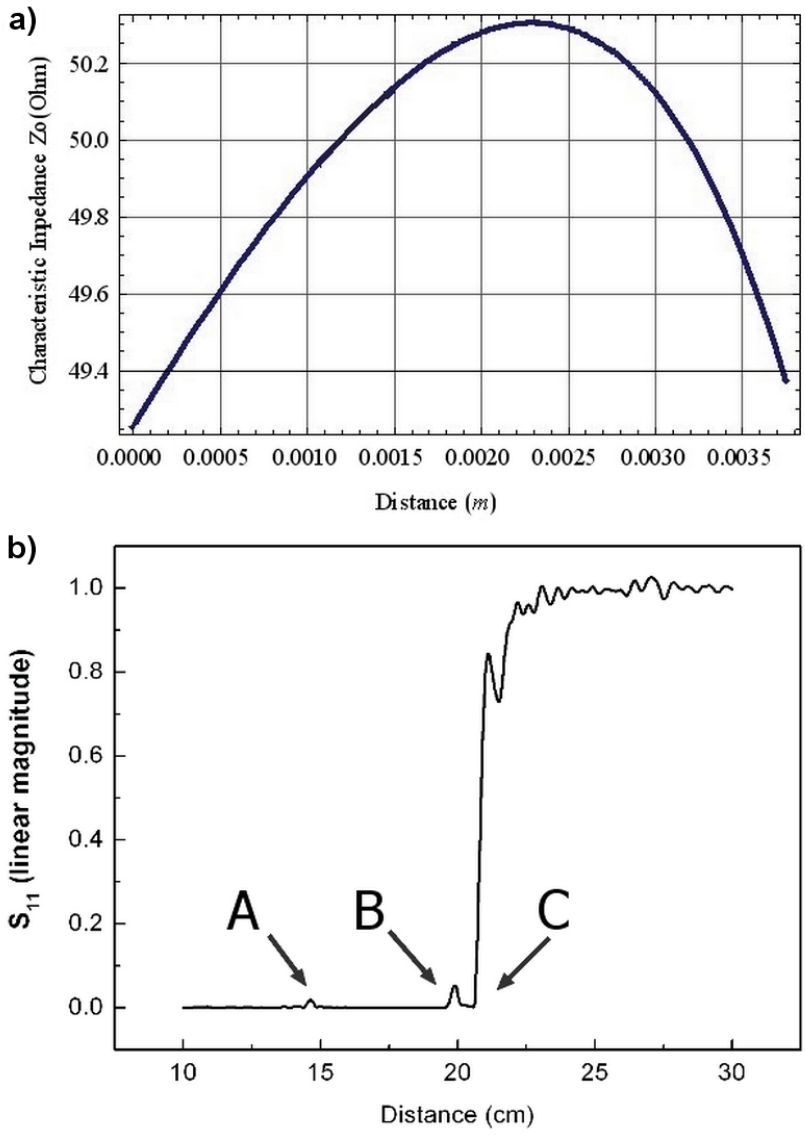

Figure 6.12: *(a) Calculated characteristic impedance of the CCPW along the length of the line. The axis direction is from the cable side to the chip side. (b) Time-domain measurement of the scattering parameter S_{11} (linear magnitude). The points A, B and C correspond to the input SMA connector, the solder joint at the cable/waveguide transition, and the end of the waveguide, respectively.*

lated at the edge and at the centre of the PCB, and a linear interpolation of the two sets was used along the line. Since the formulae are not linear in the geometric parameters, deviations from 50 Ω impedance are expected. Figure 6.12(a) shows the calculated impedance along the length of one coplanar waveguide. Linear tapering causes the characteristic impedance to vary from 50 Ω in the centre, but the variations are less than 2%. Figure 6.12(b) shows the time domain S_{11} parameter measured with the PCB mounted on the sample holder. The central contact of the coaxial line was soldered onto the central contact of the waveguide, while the other end was fitted with a standard SMA connector. The continuity of the return path from the PCB was provided by mechanical contact of the coaxial cables with the copper slab. The small reflection (≈5%) occurring at point B corresponds to the joint between the coaxial cable and PCB (point B), and it is probably due to the bend in the cable. Total reflection at point C marks the end of the waveguide. Between the points B and C, the reflection is negligible, which confirms the validity of the model used for the PCB design.

6.3 Magnetic screens

Qubit flux biasing and detection requires an extremely clean magnetic background. Any slow drift in the magnetic flux Φ_Q through the qubit can move the working point of the device, and becomes particularly important in long measurements, e.g., during the acquisition of time switching events described in Chapter 8. The signature of the macroscopic quantum states occurs within a few percent of the qubit degeneracy point $\Phi_Q = \Phi_0/2$. For a typical qubit area $A_Q \approx 10\ \mu\text{m}^2$, the fluctuations in the external magnetic field have to be $\ll 1\ \mu$T. Moreover, low frequency fluctuations cause the qubit quantum state to decohere, shortening the time over which quantum operation can be performed. For this reason, extremely stable magnetic field must be provided at the sample location, and any undesired fluctuation must be suppressed.

The conventional approach at cryogenic temperature is to screen the sensitive parts of the experiment using superconducting enclosures. This is usually achieved using hollow cylinders with either one or both ends left open, to allow leads to reach the sample in the screened inner region. After undergoing the superconducting transition, any change in the magnetic field will cause persistent currents to flow around the enclosure. These set up a magnetic field that opposes any additional field (perfect diamagnetism). Additional shields made of soft ferromagnetic materials usually surround the superconducting shield to minimise the external magnetic field before the normal-

superconducting transition is reached. The ferromagnetic screens are made of materials with high relative magnetic permeability, specially processed to have increasing permeability at cryogenic temperatures. Compared to superconducting shields, high permeability materials offer a low reluctance region for the magnetic field, which is deflected and concentrated inside the wall of the screen.

In the next sections, the design of a magnetic shield composed of a superconducting cylinder surrounded by a high-μ cylindrical screen is presented, with the configuration shown in Figure 6.13. Calculations were performed to study the dependence of the magnetic field attenuation on geometry and size, in order to obtain the optimum design for the setup. In the following, the attenuation is defined as the ratio $S = H_{ext}/H_{int}$, where H_{int} is the magnetic field inside the screen and H_{ext} is the external field in the absence of the screen. Because the attenuation of magnetic fields transverse to the axis is always greater than the longitudinal one, only the latter is considered.

6.3.1 Superconducting screen

The superconducting screen built into the setup consists of a hollow cylinder (12 cm long $\times$ 5.2 cm inner diameter) made of copper and closed at one end. The inner surface is covered with a thin layer ($\approx$300 μm) of Sn-Pb solder, which is superconducting with a critical temperature between 4 K and 7 K [110]. The thickness of this layer is much smaller than the cylinder radius, and a zero wall thickness was assumed in the following calculations.

In a cylindrical geometry, the fundamental parameter is the length-to-diameter ratio, L_{SC}/D_{SC}. The attenuation is an exponential function of this parameter, and high attenuation is achieved when $L_{SC}/D_{SC} \gg 1$. In our experiment, this was limited by the available space in the cryostat to a value of ≈ 2.2, but nevertheless, the attenuation can be still modelled using the asymptotic form which is strictly valid for an infinitely long cylinder, if the regions within one radius from the openings are avoided. Within this assumption, an approximate formula for the longitudinal attenuation of a superconducting cylinder with one open end is given by [111]

$$S \approx 1.3\,[J_0(\beta r_{SC})\sinh(\beta z)\widehat{z} - J_1(\beta r_{SC})\cosh(\beta z)\widehat{r}]\,e^{-\beta L_{SC}}, \tag{6.9}$$

where L_{SC} and $r_{SC} = D_{SC}/2$ are the length and radius of the cylinder, $\beta = 3.83171/r_{SC}$, J_i is the Bessel function of i^{th} order, and the origin of the z-axis is taken at the closed end. Figure 6.14 shows a plot of the on-axis attenuation calculated using Eq. (6.9) for various values of L_{SC}/D_{SC}. The exponential term in Eq.(6.9) causes orders of magnitude changes in

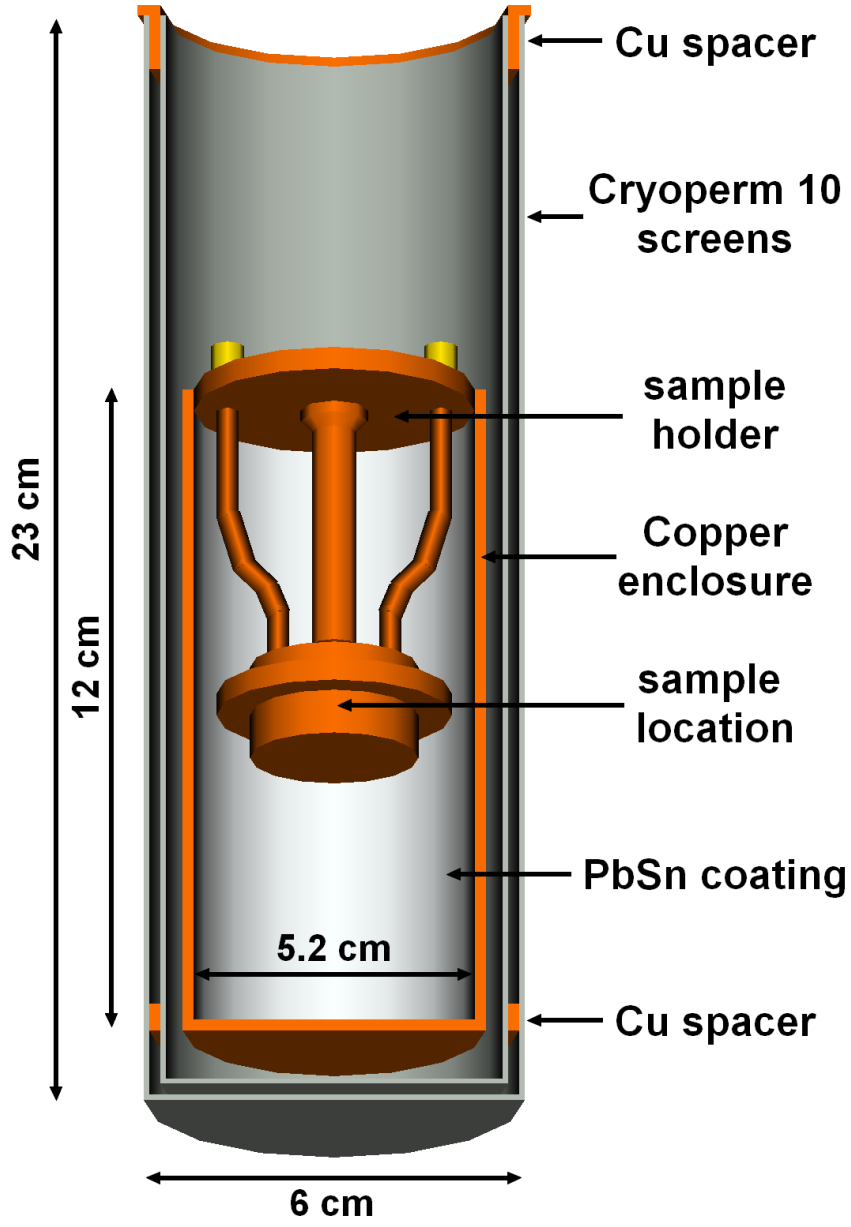

Figure 6.13: *Geometry of the magnetic shields. One cylinder of solder-coated copper is surrounded by two longer cylinders of Cryoperm 10. The origin of the z-axis is taken at the closed end. Also shown is the position of the sample box inside the shields.*

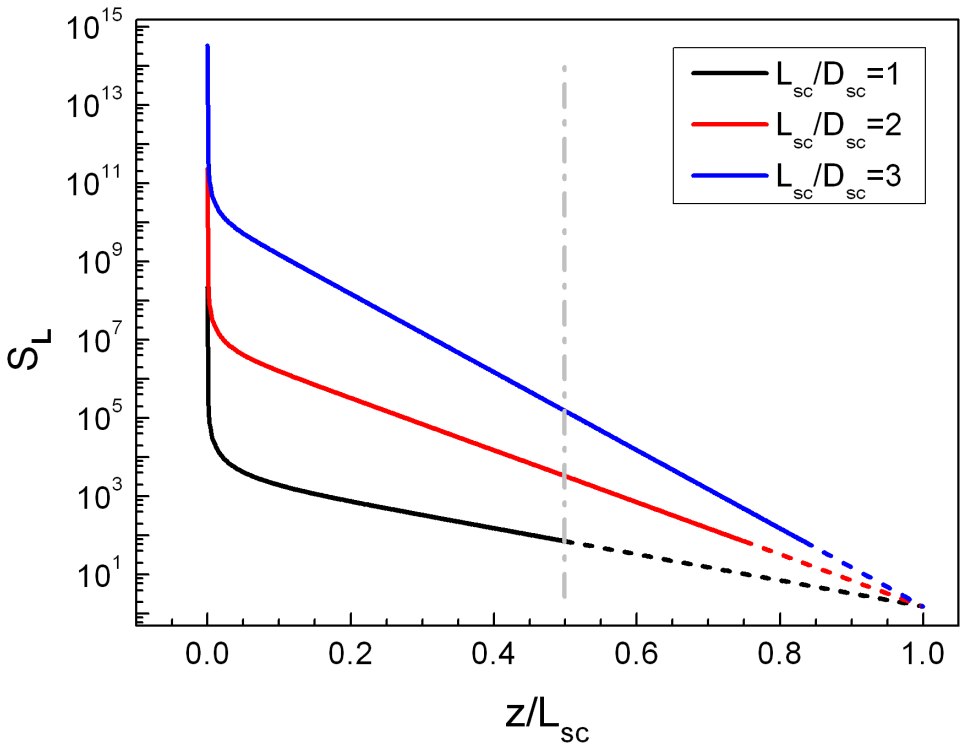

Figure 6.14: *On-axis longitudinal attenuation versus distance from the closed end, calculated using Eq. 6.9, for superconducting cylinders of various length to diameter ratios L_{SC}/D_{SC}. In the regions within one radius from the open end, where Eq. 6.9 is not a valid approximation, dashed lines are used. The position of the sample is marked by the dash-dotted line.*

the attenuation for small changes in the ratio L_{SC}/D_{SC}. According to this model, a value of $L_{SC}/D_{SC} = 2.2$ should guarantee an attenuation ≈7000 at the centre of the screen. The use of a screen surrounding the solenoid could distort the magnetic field in the inner region. For this reason, the superconducting solenoid was positioned at a distance of 2 mm from the chip and at the centre of the screen. Given the small fields used in the experiments, and the distance between the solenoid and the superconducting walls, the distortion of the field due to the presence of the screen is expected to be minimal. The screen was mounted on the top plate of the sample holder, which provide it with grounding and a thermal link to the mixing chamber. The copper enclosure also gives further protection against high frequency EM noise.

6.3.2 High permeability screen

The superconducting screen is surrounded by a two-layer cylindrical screen of Cryoperm 10 in a coaxial configuration. Cryoperm 10 is a nickel-iron alloy (77% Ni, 15.1% Fe, 4.5% Cu, 2.5% Mo, in weight) specially processed to provide high permeabilities at cryogenic temperatures. In comparison with other high permeability materials (Mumetal, Conetic) Cryoperm 10 has the highest magnetic permeability at cryogenic temperature ($\mu \approx 65000$ at 4 K from Ref. [112]).

During the design of the high permeability screens, several aspects were considered. First, the maximum flux density inside the screen walls must be smaller than the saturation field of the material. To test this, it is possible to estimate the averaged flux density inside the material, taking into account that the shield collects flux lines from a region much wider than the shield region. Different regions have to be considered depending on the direction of the external field, and the exact formulae for the calculations are described in Appendix B. The averaged flux density can be compared with the saturation magnetisation of the material and a condition for the minimum thickness to be used is obtained. In our experiments, the main contribution was the earth's magnetic field ($\approx 5 \times 10^{-5}$ T). This value is much smaller than the saturation field of Cryoperm 10 (≈ 0.9 T [113]), and a thickness much smaller than the minimum available on the market (0.1 mm) would have sufficed.

A further constraint on the thickness comes from the shielding factor S_T in the transverse direction. For an infinite cylinder in a uniform transverse field, S_T can be approximated by the following expression valid for $t \ll D$ and $\mu \gg 1$ [114]:

$$S_T = \frac{\mu_r \cdot t}{D} + 1, \tag{6.10}$$

where $D = \frac{1}{2}(D_o + D_i)$, $t = \frac{1}{2}(D_o - D_i)$ is the wall thickness, D_o and D_i are the inner and outer diameter of the shield, and μ_r is the relative permeability of the material. The transverse shielding factor is linear in the shield thickness, but inversely proportional to the shield diameter. Practically, the maximum value of t is limited by the cost of the shield, and thicknesses between 0.5 and 2 mm are usually used. On the contrary, to maximise S_T, D has to be the minimum allowed by the experiment. For our setup, values of $t = 0.5$ mm and $D = 5.6$ cm have been used.

The longitudinal attenuation of a cylindrical screen of finite length L, diameter D, wall thickness t and magnetisation μ_r, closed at both ends, can be approximated using an ellipsoid of revolution with the same length to

diameter ratio $p = L/D$. This gives

$$S_L = \frac{4 \cdot N(p) \cdot S_T + 1}{1 + 1/2p}, \tag{6.11}$$

where S_T is given by Eq. (6.10) and $N(p)$ is the demagnetising factor of an ellipsoid with length-to-diameter ratio p (see Appendix B).

The unavoidable presence of holes in the screen let the external field penetrate. This has an exponential decay, extending inside the cylinder for about one diameter. Experimentally tested formulae [115] for the corrections due to the openings to shielding factor are

$$S_{T,op} = 3\exp[k_T(2z/D)], \tag{6.12}$$

$$S_{L,op} = \frac{1}{1.3(L/D)^{1/2}}\exp[k_L(2z/D)], \tag{6.13}$$

where $k_T = 3.832$ and $k_L = 2.405$ are the first zeros of the Bessel functions J_1 and J_0 respectively, and the coordinate z runs along the axis perpendicular to the opening, with the origin at the opening. The total shielding factor is made up of the contributions of the jacket and the opening. For both directions, this is

$$1/S_{eff} = 1/S + 1/S_{op}, \tag{6.14}$$

with S equal to either S_T or S_L.

Figure 6.15(a) shows the calculated longitudinal attenuation along the cylinder axis as function of the length of the screen, at a distance from the closed end corresponding to the upper edge of the superconducting screen as a function of the length of the screen. The non-monotonic behaviour results from the sum of two contributions in Eq. (6.14): for short screens, the field fully penetrates the shield, whereas very long screens have poor shielding factors as can be seen from Eq. (6.11). A maximum occur for L =23 cm, which is almost twice the length of the superconducting screen. Figure 6.15(b) shows the attenuation along the axis of the screen for L = 23 cm. In the region hosting the superconducting screen, the attenuation is always greater than 300.

A large increase in the shielding factors can be achieved using a multilayer configuration. Combining multiple shields has a multiplicative effect on the shielding factor, thus producing very high attenuations. For a double-layer shield, Eqs. (6.10) and (6.11) becomes [115]

$$S_T^{dl} = S_{T,i} \cdot S_{T,o} \cdot (4\Delta/D_o)(D_m/D_o) + S_{T,i} + S_{T,o} + 1, \tag{6.15}$$

$$S_L^{dl} = 4 \cdot N_o \cdot S_{T,o}\frac{D_m}{L_o + 0.5D_m} \cdot S_{T,i} \cdot \frac{4\Delta}{D_o}\frac{D_m}{D_o}, \tag{6.16}$$

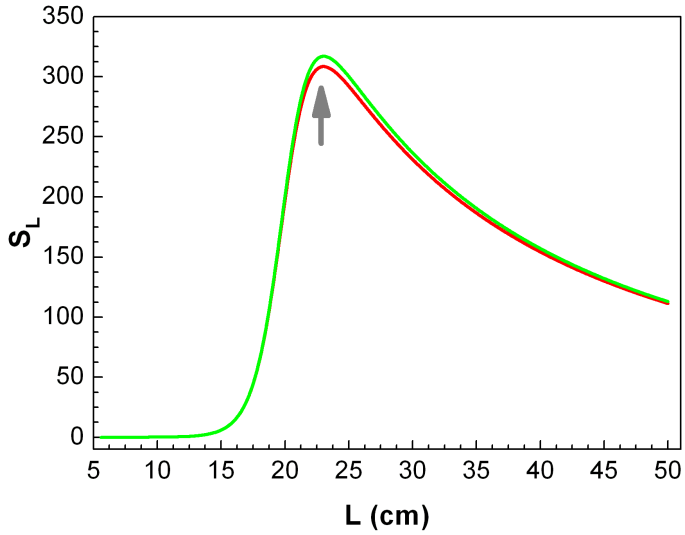

(a)

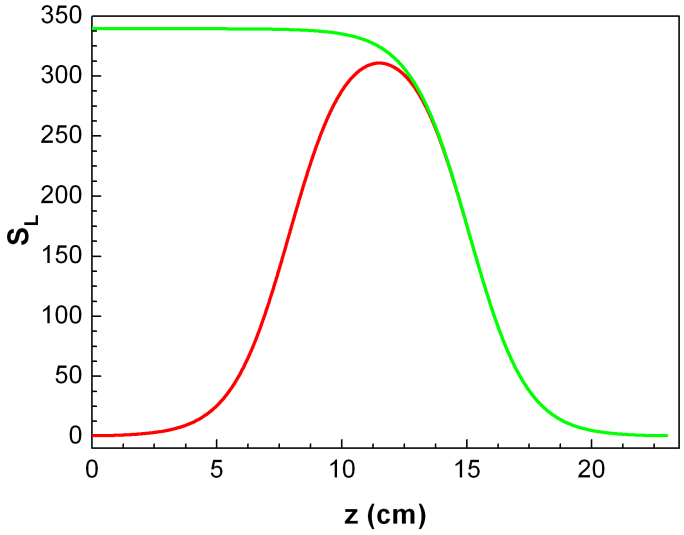

(b)

Figure 6.15: *Calculated on-axis longitudinal attenuation S_L for a single-layer cylinder with one end open (green) and both ends open (red). (a) Attenuation at a distance of 12 cm from the closed end, for a diameter D=5.6 cm and wall thickness t=1 mm, as a function of cylinder length L. The grey arrow indicates the length L^* at which the attenuation has a maximum. (b) Attenuation inside a cylinder with the same parameters above and length L=23 cm, versus distance from the closed end.*

where $S_{T,i}$ and $S_{T,o}$ are given by Eq. (6.10) for the inner and outer layers, D_i and D_o are the inside and outside diameters of the space between the layers, $\Delta = \frac{1}{2}(D_o - D_i)$ is the air gap and $D_m = \frac{1}{2}(D_o + D_i)$ is the mean diameter.

Figure 6.16(a) shows the axial attenuation at the upper edge of the superconducting screen due to a double-layer screen of identical lengths and wall thicknesses as a function of screen length, with an inner diameter $D_{IN} = 5.6$ cm, and different outer diameters D_{OUT}. As before, a maximum in the attenuation appears at a particular length L^*. With increasing outer diameter, L^* moves to a higher value, and the corresponding attenuation increases. With $D_{OUT} = 6$ cm, then $L^* \approx 25$ cm. To minimize the screen length, $L = 23$ cm was been chosen. Figure 6.16(b) shows the attenuation along the axis for the double-layer configuration. The attenuation in the region occupied by the superconducting screen is always >1200. Due to the small volume available and the high cost of Cryoperm 10, the double-layer configuration with $D_{IN} = 5.6$ cm, $D_{OUT} = 6$ cm, thickness $t = 0.5$ mm and length $L = 23$ cm was chosen.

6.4 Measurement equipment

The Kelvinox fridge used for the experiments is housed inside a steel shielded room fitted with a dedicated mains supply, which was isolated from the common mains via a centre-tapped transformer. The measurement equipment was powered using this mains to avoid ground loops, except the preamplifier stages which were battery powered. Multiple ground connections were avoided using a single common ground point for the equipment chassis and the cryostat body. The instrumentation was interfaced by standard GPIB connections and the data were acquired using custom-made Labview software.

The experiments described in this thesis where performed using two different room temperature measurement setups, described in Sec. 6.4.1 and Sec. 6.4.2 respectively. For the measurements of interferometer device in high RF field (sample *AgInt*), the measurement equipment was placed inside the shielded room. During the other experiment (sample SbQ), all the instrumentation was moved outside the shielded room, except the voltage preamplifiers which were kept at short distance from the fridge connections. The low frequency signals used for the magnetic biasing of the device entered the shielded room through a telephone filter stack, while feedthrough connections were used for all the other signals. The computer used for the data acquisition was outside this room and connected to the instrumentation via a fibre optic link.

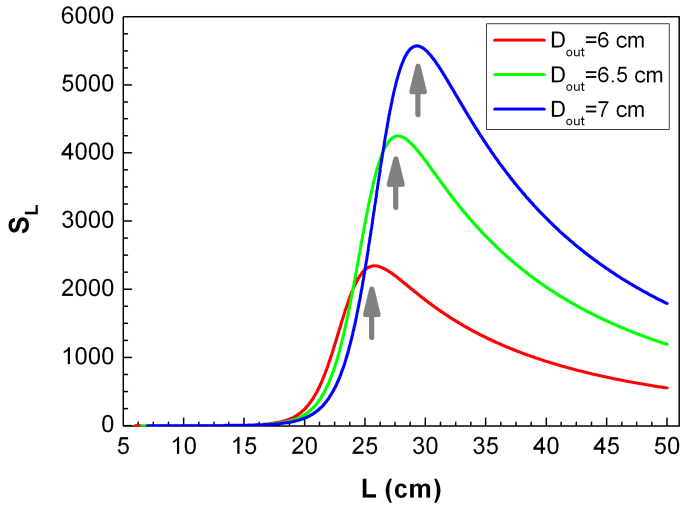

(a)

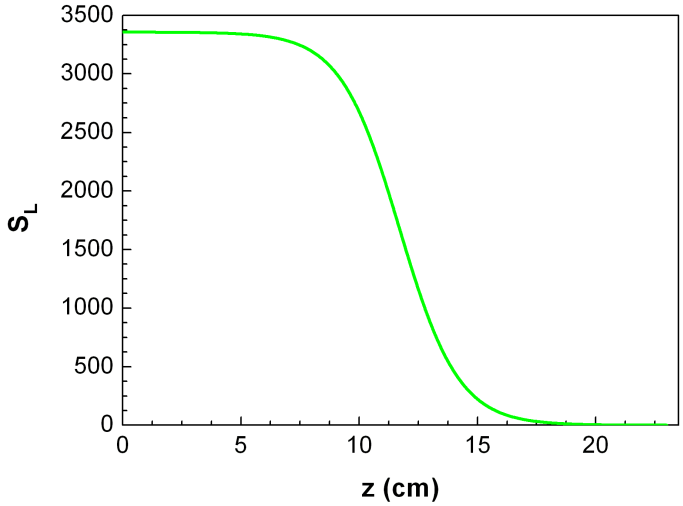

(b)

Figure 6.16: *Calculated on-axis longitudinal attenuation S_L for a double-layer cylinder with one open end. (a) Attenuation at the upper edge of the superconducting screen as a function of the cylinder length L, for an inner diameter D_{IN} = 5.6 cm, wall thickness t = 0.5 mm and various outer diameter D_{OUT} given on the figure. The grey arrows indicate the length L^* at which the attenuation is maximum. (b) Attenuation inside the double-layer screen with the same parameters in (a), D_{out} = 6 cm and L = 23 cm.*

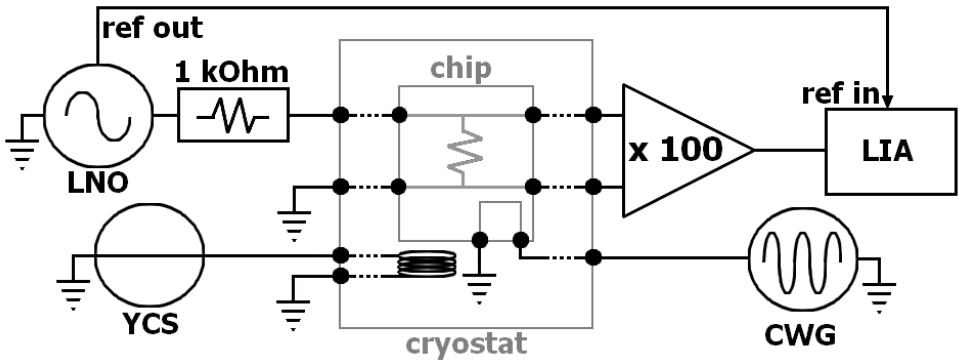

Figure 6.17: *Schematic of the room temperature equipment used for the measurements of sample AgInt, showing the connections between the instruments: LNO (Low Noise Oscillator); YCS (Yokogawa Current Source); CWG (Continuous Wave Generator); LIA (Lock-in Amplifier). Additional room temperature filters (not shown) were fitted on all the input lines at the top of the cryostat. The lines inside the fridge, described in Sec. 6.1.3, are shown as dotted lines.*

6.4.1 Sinusoidal current measurements

For the resistance measurements of sample *AgInt*, a standard 4-terminal lock-in technique was used. The room temperature measurement equipment and the connections are shown in Fig. 6.17. A Krohn-Hite 4402-B low noise oscillator and a Signal Recovery 7465 Lock-In Amplifier (*LIA*) were used to measure the resistance of the SNS junction. A large bias resistor (1 MΩ) at room temperature was connected on the input line to drive a current in the μA range through the sample. The voltage across the sample was amplified by a custom-made voltage preamplifier with 30 dB gain, and then phase detected with the lock-in amplifier. Reference frequencies below 100 Hz were selected after searching for a proper low noise windows in the background spectrum. A Yokogawa 7651 DC Current Source (*YCS*) was used to drive a current up to ≈50 mA through the small superconducting solenoid. Commercial *L-C* lowpass filters (part number 4209-053LF, supplied by Tusonix) with 20 dB attenuation at 10 MHz were connected on the magnet line before entering the fridge. Electromagnetic radiation in the 1-20 GHz range was applied to the device antenna by an Anritsu MGS69A Continuous Wave Generator (*CWG*) connected to the RF-input line.

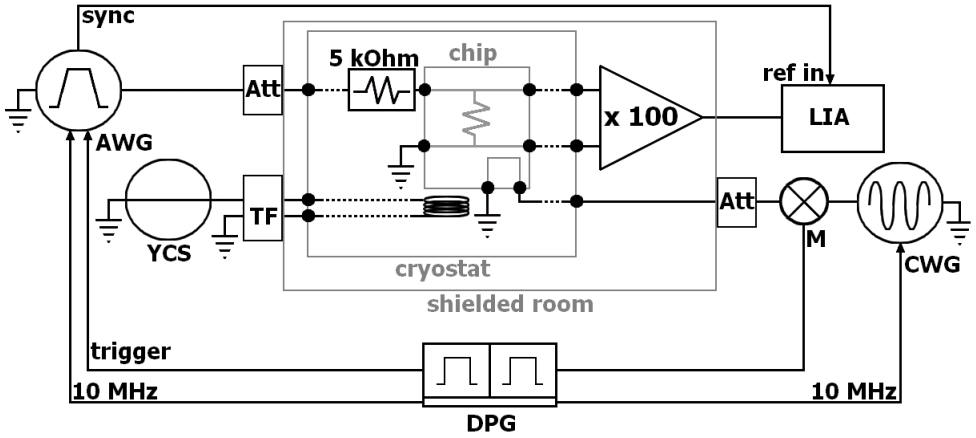

Figure 6.18: *Schematic of the experimental setup used for the pulsed measurements of sample SbQ. The instruments shown are: AWG (Arbitrary Waveform Generator); YCS (Yokogawa Current Source); DPG (Delay Pulse Generator); CWG (Continuous Wave Generator); LIA (Lock-in Amplifier). Telephone Filters (TF) and 3 dB Attenuators (Att) were used to attenuate the noise in the lines before entering the shielded room. A system of broadband Mixers (M) was used to generate RF pulses. The lines inside the fridge, described in Sec. 6.1.3, are shown as dotted lines.*

6.4.2 Pulsed current measurements

For measurements of sample SbQ, high frequency input and readout lines were used. Figure 6.18 shows a schematic of the room temperature equipment used for these experiments. The measurement is still a 4-terminal type, but a pulsed current is used to probe the resistance of the sample. An Agilent 33250A Waveform Generator (AWG) was used to apply trapezoidal voltage pulses to the input line. The voltage produced across the SNS junction reaches the amplification stage at room temperature via a filtered twisted pair return line. The voltage preamplifier is a battery powered LI 75A ultralow-noise preamplifier from NF-Electronics with 40 dB gain, 1.2 nV/$\sqrt{Hz}$ voltage noise and 1 MHz bandwidth. The pulse repetition frequencies used during the experiments are in the 100-800 kHz range, which is out of the range of most lock-in amplifiers. The SR844 lock-in amplifier with large bandwidth (25 kHz to 200 MHz) was used for the signal detection.

To implement a pulsed scheme which allows the use of NMR protocols, a precise control on the timing of the pulses is mandatory. For this purpose, a

4-channel Stanford Research DG645 digital pulse generator (*DPG*) was used as the time base for all the instruments. The 10 MHz clock reference output of the DPG was distributed to all AC measurement equipment for synchronisation. One channel of the DPG was connected at the trigger input of the WFG, while the second channel was used to modulate the continuous RF radiation, as described in the next section. The synchronised square wave produced at the *Sync* output of the *AWG* was sent to the lock-in amplifier as a reference signal. Broadband attenuators of 2 dB and 3 dB were fitted on the input and RF lines where these enter the shielded room. The magnetic bias to the sample was provided by a DC current source (YCS) connected to the magnetic bias line, which was then passed through a Telephone Filter (*TF*) stack before entering the shielded room.

Pulsed RF modulation

To manipulate the qubit state, short RF pulses at the qubit resonant frequency are needed. These consist of a RF carrier with typical frequencies in the 1-20 GHz range, modulated by DC pulses with lengths between 5 ns and a few hundred ns. The CWG can directly produce RF pulses using internal modulation, although the minimum pulse length is limited to 20 ns. Excitation pulses for qubit experiments are usually generated combining the continuous signal from a CWG with the signal from a pulsed source. In our experiments, the second channel of the DPG was used to provide the pulsed signal, thus setting the lower limit of the pulse length to the DPG resolution (1 ns).

The instrument setup used to provide the pulsed RF modulation in our experiments is shown in Fig. 6.19. The pulsed signal from the DPG was equally splitted by a broadband Minicircuits ZX10R-14+ power splitter. Two Marki M8 0420 mixers were used to multiply the incoming CW RF with the pulse reference, and the output was sent to the RF line. To increase the isolation between CW source and the output, two mixers were used and 1 or 2 dB attenuators were fitted between the elements to suppress reflections arising from small impedance mismatches. The parameters of the measurement and excitation pulses (pulse length and amplitude) could be set independently. The relative synchronisation could be finely adjusted by setting the appropriate delay between the channels of the DPG, to compensate for the idle time of the instruments.

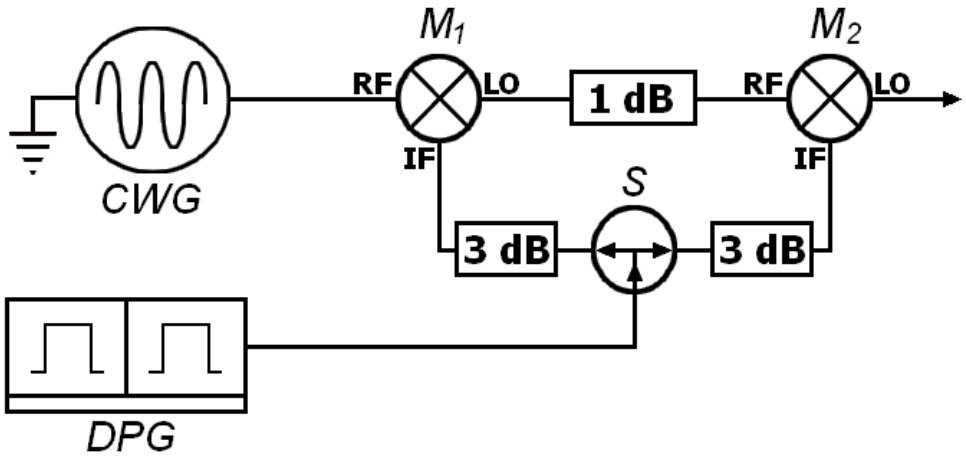

Figure 6.19: *Mixer combination used for RF pulse modulation. Two broadband mixers (M_1 and M_2) multiply the continuous RF signal from the CWG with the pulsed modulating signal from the DPG. In-phase pulsed signals are obtained using a broadband splitter (S) and symmetric connections to the mixers. Attenuators (1 and 3 dB) were used to suppress any impedance mismatch.*

Pulsed lock-in technique

Pulsed current measurements of the interferometer resistance are in general harder to perform than standard low-frequency measurements using a lock-in amplifier. The exact lineshape of the signal introduces new parameters that need to be taken into account when evaluating the device resistance. Figure 6.20 shows the time and frequency representation of the pulses. In the time domain, the train of trapezoidal pulses is characterised by the pulse duration τ_p, the rise time τ_r, and the repetition period T_p. In the frequency domain, the signal is represented by an infinite series of delta functions at integer multiples of the fundamental frequency $f_p = 1/T_p$, and the overall spectrum is modulated by the Fourier transform of the single trapezoidal pulse, which shows two knees at frequencies $1/\pi\tau_p$ and $1/\pi\tau_r$. The frequency spectrum of such a signal is very broad, since signal components at frequencies of several times $1/\pi\tau_p$ can still have sizeable amplitude. If the transmission of the line is not constant up to frequencies $f \approx 1/\pi\tau_r$, i.e. some peaks or dips are present in the transmission characteristic, the harmonics are subject to uneven attenuations and the shape of the signal in time-domain is significantly distorted.

In our setup, due to the large bandwidth of the input line, the fast pulsed signal can travel to the sample with an amplitude which is progressively reduced by the attenuators. After the cold bias resistor, the fast current pulses are driven into the sample, which develops a pulsed voltage signal at its output terminals. The current signal at the end of the input line, after the bias resistor, was analysed using an Agilent DSA80000B oscilloscope with 12 GHz bandwidth and it was found that the line smoothed the pulse, changing its rise time from $\approx$5 ns to $\approx$5.7 ns.

After the sample, the heavy filtering of the readout line limited its response time, and the signal at the top of the fridge showed an exponential modulation with a time constant of $\approx$1 μs. In the frequency domain, the spectrum was modified from the original one, since the components of the signal at frequencies larger than the cutoff frequency of the line were heavily attenuated. In our setup, the total attenuation of the line in the passband was $\approx$1 dB, and the measured signal was not affected by the filtering as long as the reference frequency was selected in this frequency range. During the experiments, the voltage signal detected by the lockin amplifier was typically 1-100s μV, depending on the value of the harmonic at the reference frequency, which was a function of the pulse parameters.

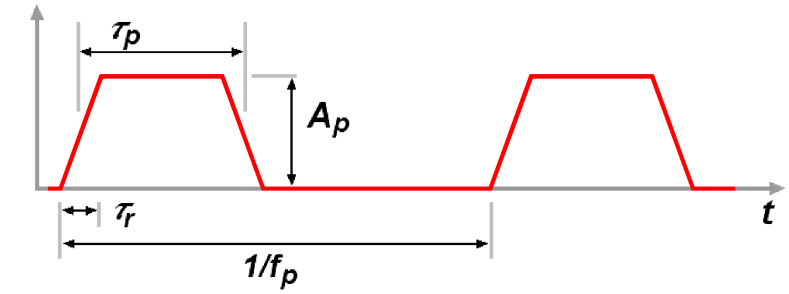

(a)

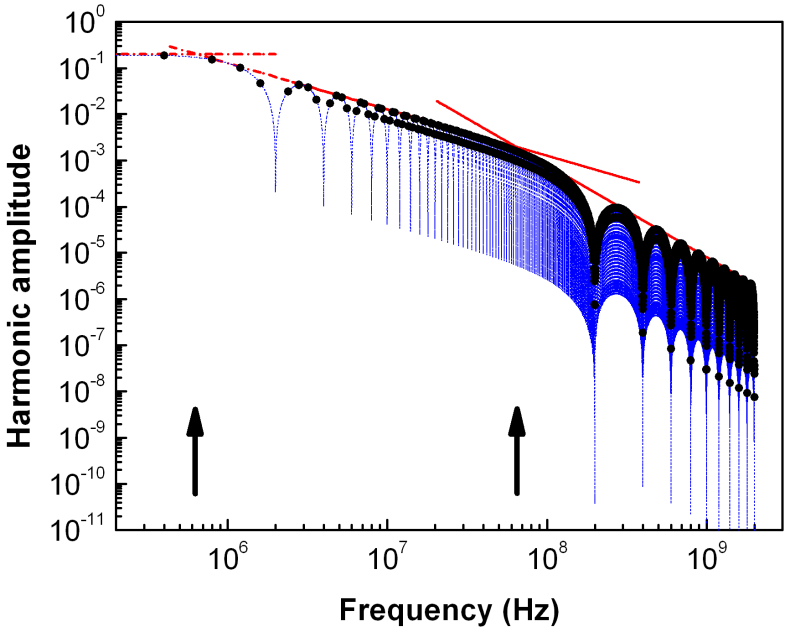

(b)

Figure 6.20: *Time (a) and (b) frequency representation of the measurement pulses. The frequency spectrum is calculated for f_p=400 kHz, τ_p=500 ns, τ_r=5 ns and A_p=1, and is made up of an infinite number of harmonics (black circles) at frequencies $f=nf_p$, where n is an integer, whose amplitude decreases with n. The spectrum is modulated by the Fourier transform of a single trapezoidal pulse (blue dotted line) and can be approximated by the asymptotic envelopes (red dash-dotted lines) in the regions far away from the frequencies $1/\pi\tau_p$ and $1/\pi\tau_r$ (marked by the arrows). Within these regions, the spectrum has a slope of 0 dB/decade ($f < 1/\pi\tau_p$), -20 dB/decade ($1/\pi\tau_p < f < 1/\pi\tau_r$) and -40 dB/decade ($f > 1/\pi\tau_r$), respectively.*

Chapter 7

Investigation of the interferometer properties

In the combined interferometer/qubit device, the magneto-resistance in flux intervals far away from the qubit degeneracy points, i. e., at $\Phi_Q \approx n\Phi_0$ (n=0, 1, 2 ...), is nearly insensitive to the qubit dynamics, as described in Sec. 4.1.3. In these flux intervals, the magneto-resistance provides useful information about the physics of the readout device independently of the properties of the qubit. This allows to characterise the interferometer response to the experimental controls and to define suitable parameters to describe the interferometer readout. The dependence of the resistance oscillations of the interferometer/qubit device on temperature and input current is described in Secs. 7.2.1 and 7.2.2, and a value for the effective temperature of the quasiparticles in the interferometer is presented in Sec. 7.2. The effect of a strong continuous RF field on the properties of an SNS junction was investigated in a third sample, comprising an Andreev interferometer with the normal part made of silver, and the results are described in Sec. 7.3.

7.1 Magneto-resistance at $\Phi_Q \approx 0$

In the flux region around $\Phi_Q \approx 0$, the qubit contribution to the phase difference φ_I across the interferometer readout junction is a small linear term, and the magneto-resistance can be described by the formula [75]

$$R = R_N - \Delta R = R_N - \gamma \left(1 + \cos(\varphi_I)\right), \tag{7.1}$$

where R_N is the resistance of the normal-metal section in the normal state and ΔR is the correction due to the proximity effect; the parameter γ defining the amplitude of the oscillations, depends on the temperature, the diffusion

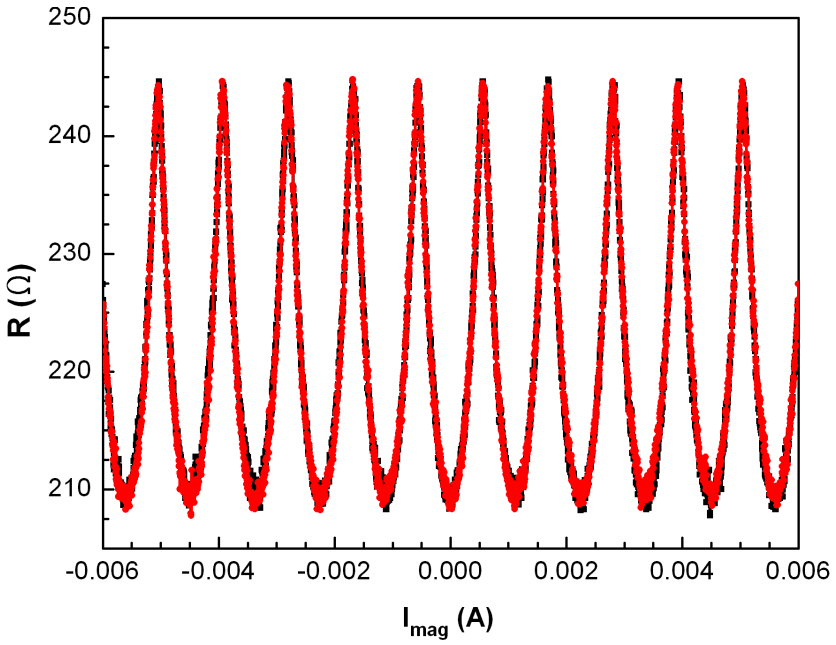

Figure 7.1: *Normalised magneto-resistance of sample SbQ as a function of current I_{mag} measured at T=20 mK over an interval corresponding to $\Phi_Q \approx 0$.*

properties of the junction and the quality of N-S interfaces.

The magneto-resistance of the sample SbQ was measured using the four-probe pulsed technique discussed in Sec. 6, and the magnetic field was produced by driving a current I_{mag} through the small superconducting magnet enclosed in the sample holder.

The investigated device displayed the expected magneto-resistance oscillations described by Eq. (7.1), as shown in Fig. 7.1. The values of the parameters extracted from the data are listed listed in Table 7.1. For the calculations, the value of $\rho\ell = 2.5 \times 10^{-10}$ Ωcm^2 from Ref. [116] was used, where ρ and ℓ are the resistivity and mean free path in an antimony wire. First, the value of ℓ was calculated using the resistivity obtained from R_N, then the diffusion coefficient $D = \ell v_F/3$ was calculated using the Fermi velocity $v_F = 1.2 \times 10^6$ m/s [39].

	R_N (Ω)	ρ ($\mu\Omega cm$)	ℓ (nm)	D (cm^2/s)	γ_{MAX}/R_N
SbQ1	244.5	53	48	159	0.41

Table 7.1: *Calculated and measured parameters for samples SbQ.*

7.2 Thermal effect

The flux region around $\Phi_Q \approx 0$ was used to investigate the thermal properties of the SNS junction. This investigation includes the dependence of the resistance correction ΔR on temperature and applied voltage. The latter is of particular interest since the pulsed probing of the SNS junction is a new type of measurement. The pulsing introduces a set of four parameters: pulse repetition frequency (f_p), pulse length (τ_p), rise time (τ_r) and current pulse amplitude (I_p)), whose effect was characterised introducing an effective electron temperature.

7.2.1 Dependence on temperature

Changes of the electron temperature in an Andreev interferometer is expected to produce two effects:

- a change in the resistance correction ΔR.
- a change in the shape of the oscillations.

The dependence of ΔR on temperature is known to follow a non-monotonic behaviour below the critical temperature T_c of the superconductor. In the limit when $T \ll E_{TH}/k_B$ and $T \gg E_{TH}/k_B$, E_{TH} being the Thouless energy, the resistance R is expected to approach the normal-value R_N, giving $\Delta R \approx 0$ ("reentrance"). For intermediate temperatures, ΔR is finite with a maximum amplitude at a temperature $T^* \approx T_{TH} = E_{TH}/k_B$.

The shape of the resistance oscillations is expected to deviate from Eq. (7.1) as a result of the temperature dependent supercurrent flowing through the SNS junction induced by external magnetic the flux Φ_I. As described in Sec. 4.1.1, the perfect sinusoidal oscillations at $T \gg T_{TH}$ become "cusp" shaped as T approaches $T \approx T_{TH}$, and the feature becomes more pronounced as T is further decreased below T_{TH}. This effect can be accounted for by fitting the measured resistance oscillations far away from the degeneracy points with a modified version of Eq. (4.14), where the terms $2\pi\Phi_{xI}/\Phi_0$ and $\Delta\varphi_Q$, which are linearly dependent on I_{mag} in this flux region, are grouped together using a coefficient M_{tot}:

$$\varphi_I = M_{tot} I_{mag} - \beta \sin(\varphi_I). \tag{7.2}$$

In our experiments, we observed both a temperature dependent resistance correction ΔR and a change in the shape of the oscillations. The magnetoresistance of our device was measured at several fridge temperatures using fixed f_p and τ_r, and different pulse lengths τ_p. The peak current I_p=1.5 nA

was used for all the measurements; this is the minimum current allowing to observe clear oscillations and corresponds to a peak voltage across the normal part of the interferometer of $\approx$0.3 μV$\ll (1/e)k_BT \approx$ 26 μV at T =30 mK. As a result, negligible self-heating is expected from the used current. Figure 7.2(a) shows the resistance oscillations of sample SbQ at different temperatures between 40 mK and 300 mK, measured with f_p=400 kHz, τ_p=100 ns and τ_r=5 ns. For this particular set of pulse parameters, the temperature range correspond to $E > E_{TH}$ and the resistance decreases monotonically with T. At the same time, the shape of the oscillations evolves from being "cusp-like" at T=40 mK to sinusoidal at T=300 mK. Figure 7.2(b) shows the temperature dependence of the normalised resistance correction $\Delta R/R_N$ for pulse lengths τ_p=40 ns, 100 ns and 500 ns. As expected, ΔR exhibits reentrant behaviour, with a maximum amplitude at $T^* \approx$ 40 mK, and decreases at both higher and lower temperatures.

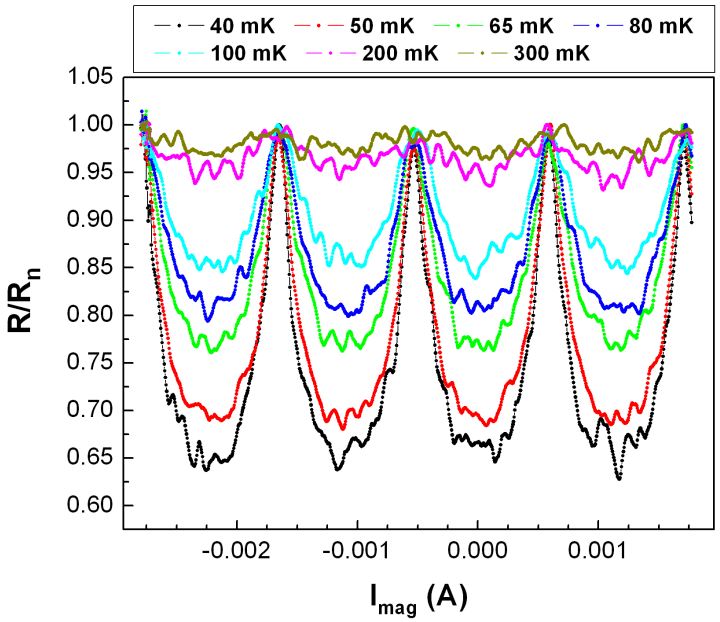

(a)

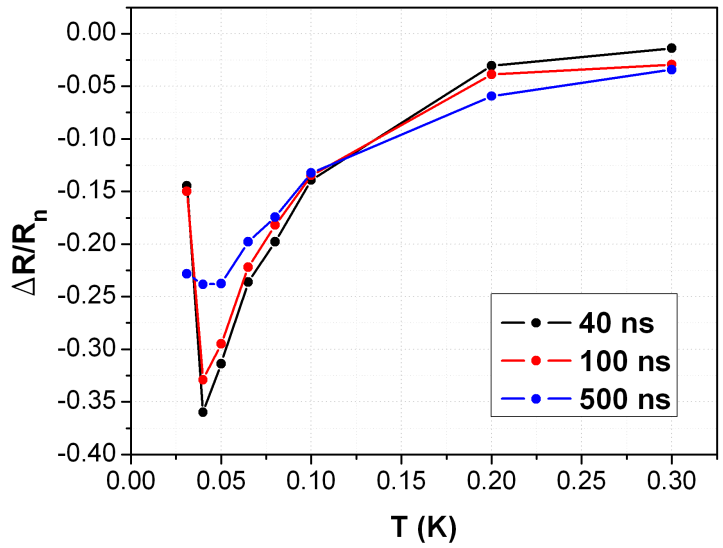

(b)

Figure 7.2: *(a) Normalised resistance of sample SbQ as a function of current through the magnet measured at temperatures between 40 mK and 300 mK. The curves shown are the average of at least 6 flux sweeps. (b) Percentage resistance change $\Delta R/R_N$ of sample SbQ as a function of temperature for different lengths of the measurement pulses τ_p.*

7.2.2 Dependence on pulsed measurement current

The resistance of an SNS junction exhibits reentrant behaviour not only as a function of temperature, but also as a function of the voltage across the normal metal. Similar to temperature, the voltage V^* at which ΔR has a maximum is related to the Thouless energy E_{TH}, and is given by $V^* \approx E_{TH}/e$. As a result, the same qualitative features of the temperature dependence are expected as a function of the measurement current.

In our experiments, the magneto-resistance at base temperature T≈30 mK was recorded as function of flux for different measurement pulse parameters. The variation ΔR of the resistance was extracted from the measured resistance oscillations, and its dependence on pulse length τ_p and pulse amplitude I_p was investigated. Typical magneto-resistance oscillations measured using fixed f_p, τ_r and τ_p and several pulse amplitudes I_p is shown in Figs. 7.3(a) and (b). The two figures correspond to the two different thermal regimes $E < E_{TH}$ and $E > E_{TH}$ as can be seen from the opposite behaviour of the resistance correction on peak current: as I_p is increased, ΔR increases in Fig. 7.3(a) and decreases in Fig. 7.3(b). At the same time, the shape of the oscillations evolves from cusp-like at low current to almost sinusoidal at high current.

Figure 7.4 shows the dependence of ΔR on I_p determined from the resistance oscillations shown in Figs. 7.3(a) and (b). At large pulse amplitudes, ΔR is vanishingly small and the interferometer resistance is almost equal to the normal value. As the pulse amplitude decreases, ΔR decreases quickly reaching a minimum at a value I_p^{min} which depends on the pulse parameters. For smaller amplitudes, ΔR has a steeper increase till the resistance recovers the normal value R_N.

To account for the contribution of the pulse parameters on the thermal effect, the energy associated with the pulsed waveform has to be considered. The amount of energy dissipated by an AC signal is defined by its rms value, i.e. the DC current that would dissipate the same amount of energy on the same resistive load. For a train of trapezoidal pulses, the rms value can be calculated to be:

$$I_{p,rms} = I_p \sqrt{f_p \left(\tau_p - \frac{\tau_r}{3}\right)}. \tag{7.3}$$

A plot of $\Delta R/R_N$ as a function of $I_{p,rms}$ is shown in Fig. 7.5(a) and (b) for different values of the pulse length. After scaling to rms values, the minima positions coincide at a value $I^*_{p,rms}$, showing that the dependence of $\Delta R/R_N$ on the pulse parameters can be characterised by the rms current $I_{p,rms}$. The measured value of $I^*_{p,rms}$ ≈5.5 nA gives an equivalent temperature

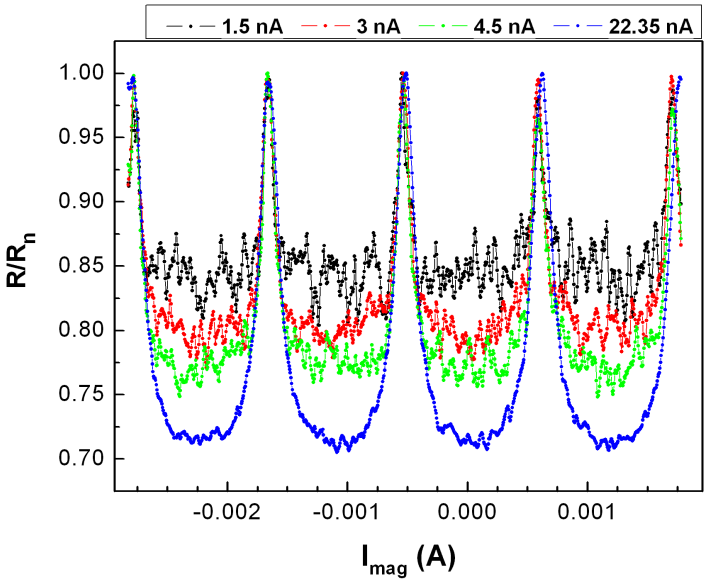

(a)

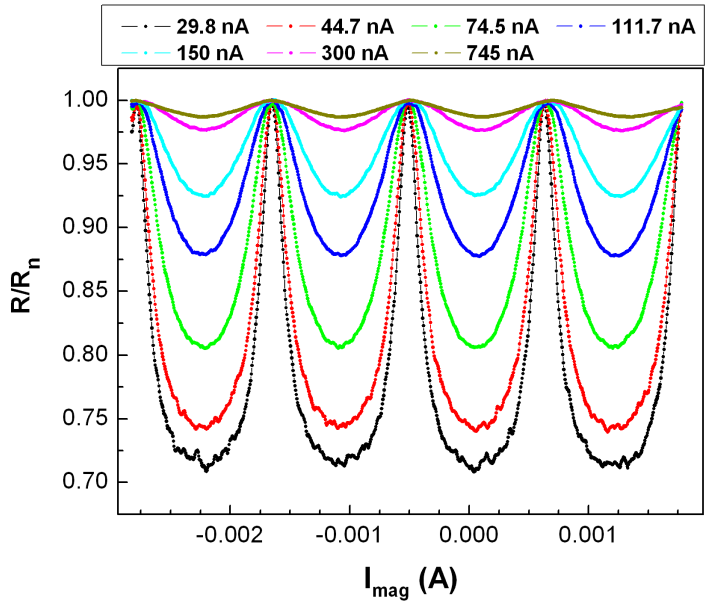

(b)

Figure 7.3: *Normalised resistance of sample SbQ as a function of current through the magnet, measured with f_p=400 kHz, τ_r=5 ns, τ_p=100 ns and input pulse amplitudes I_p corresponding to (a) $E < E_{TH}$ and (b) $E > E_{TH}$. In the two ranges of I_p, ΔR (a) increases and (b) decreases monotonously with I_p. Each curve shown is the average of at least 6 flux sweeps.*

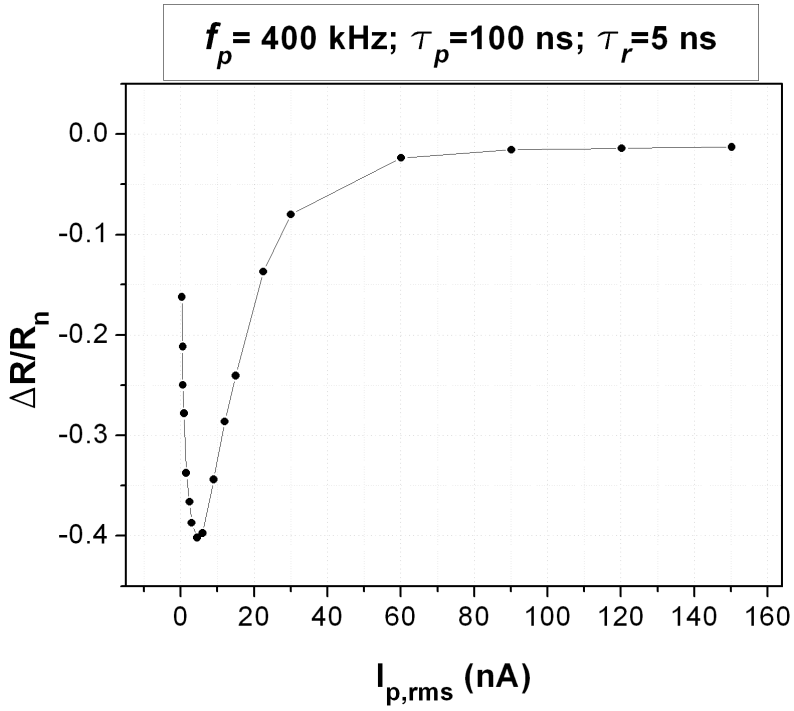

Figure 7.4: *Percentage resistance change of sample SbQ as a function of rms current, extracted from the data in Figs. 7.3(a) and (b).*

$T = eI^*_{p,rms}\ R_N/k_B$ ≈30.4 mK, in rough agreement with the T^*=40 mK obtained from the temperature dependence. The dependence of $\Delta R/R_N$ on the pulse length exhibits two further features:

- for $I_{p,rms} > I^*_{p,rms}$, the slope of the curves increases with τ_p, and consequently the region of $I_{p,rms}$ where a strong resistance change is detected becomes narrower;
- the maximum resistance correction as a function of the pulse length shows non-monotonic behaviour, which resembles the reentrant behaviour of $\Delta R/R_N$ on voltage and temperature (see Fig. 7.5(b)).

A more complete model accounting for the role of pulse length on the resistance correction in needed.

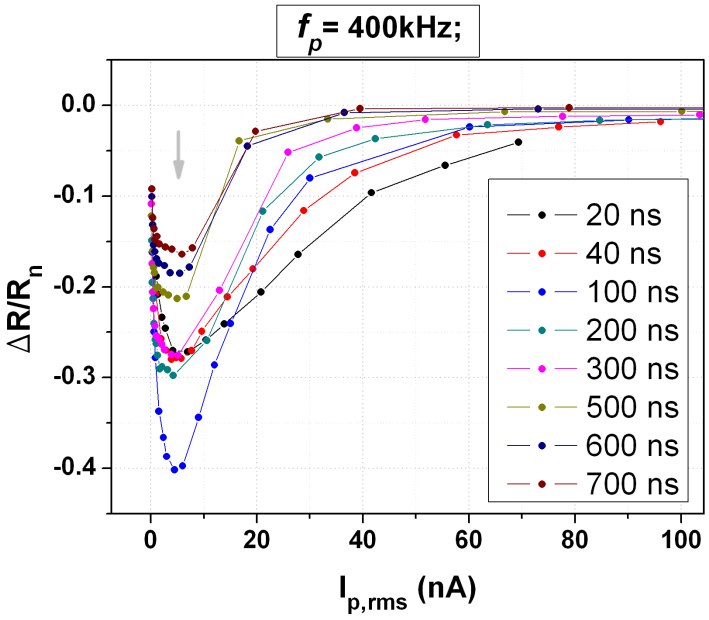

(a)

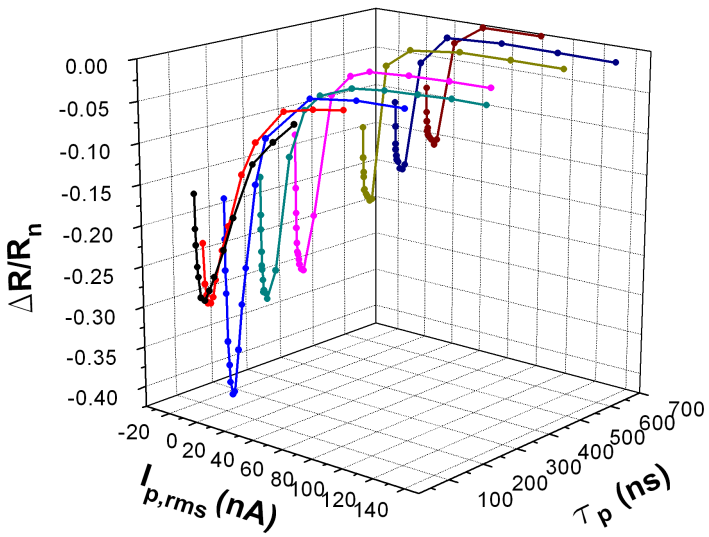

(b)

Figure 7.5: *Percentage resistance change of sample SbQ as a function of $I_{p,rms}$, measured using f_p=400 kHz and pulse lengths 20-700 ns. (a) All curve scaled using rms current, and the minima coincide at a value $I^*_{p,rms}$ (marked by the arrow) for all τ_p. (b) The maximum amplitude of $\Delta R/R_N$ exhibits non-monotonic behaviour as a function of τ_p.*

7.2.3 Equivalent temperature

The problem of Joule heating of metallic films by the measurement current at cryogenic temperatures has been addressed theoretically and experimentally by several groups (for a good review see Ref. [117]). At low temperature, the interaction between electrons and the lattice is usually very weak in mesoscopic metallic wires, where the electron-phonon interaction length is of the order, or smaller than, the sample size [118]. As a result, the electron temperature T_e can be greater than the temperature T_0 at which the device is heat sunk. The spatial profile of the electron temperature in a metallic film can be obtained by solving the heat flow equation

$$P_e = -P_J + P_{e-ph}, \tag{7.4}$$

which expresses the balance between the power P_J dissipated by Joule effect due to the current, and the cooling powers P_e and P_{e-ph} associated with electron diffusion to the contacts and electron-phonon interaction. Explicit forms for the different contributions can be found in literature, and approximate solutions of Eq. (7.4) were used to analyse experimental results. The effect of a pulsed current was investigated in Ref. [119] by adding to Eq. (7.4) a time-dependent term accounting for the response of the electron system to the application of a pulsed voltage.

In principle, it is possible to solve the complete heat flow equation for the geometry of our device, so as to calculate the temperature in the normal-metal section of the interferometer. However, this requires the knowledge of the electron-electron and electron-phonon interactions and the use of assumptions which do not guarantee a reliable result. Exploiting the strong current dependence of ΔR, it is possible to quantify experimentally the heating of the electron system due to the current in terms of an effective temperature of the quasiparticles. The method described in this thesis was previously used in Ref. [85], where the use of SNS structures as thermometers was investigated. The technique consists of correlating the measured $\Delta R/R_N(T)$ and $\Delta R/R_N(I)$ to associate the temperature and the current through their effect on the resistance correction. To explain the method used, the data in Figs. 7.2(b) and 7.4, measured with f_p=400 kHz and τ_p=100 ns, will be considered. The measured dependencies $\Delta R/R_N(T)$ and $\Delta R/R_N(I)$ in the regions corresponding to $E > E_{TH}$ were fit to a fourth order polynomial

$$\Delta R/R_N(x) = \sum_{i=0}^{4} a_i (\log x)^i, \tag{7.5}$$

where x is either temperature T or current I, and the results are shown in Fig. 7.6. The particular form of the fitting function is arbitrary, as long as

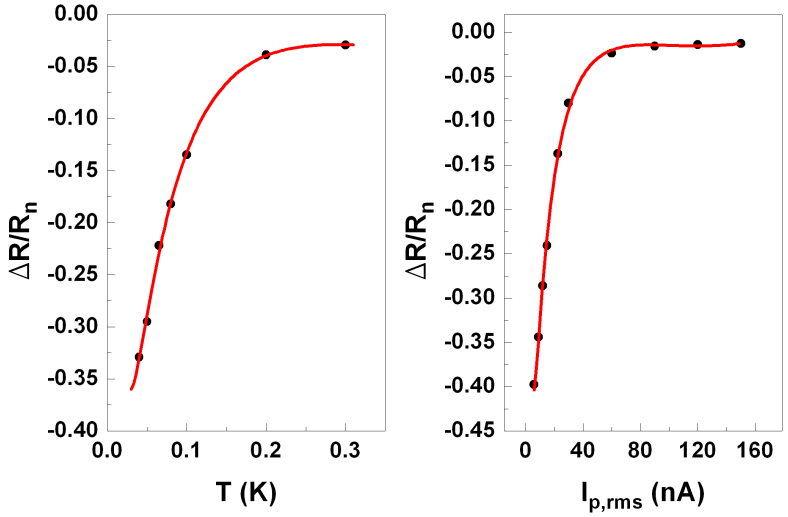

Figure 7.6: *Fits of the temperature (Left) and current (Right) dependences of* $\Delta R/R_N$ *for* f_p*=400 kHz and* τ_p*=100 ns.*

an accurate fit is achieved. First, a vector $\Delta R/R_N$ was generated containing equally spaced values in the range where the fits $\Delta R/R_N(T)$ and $\Delta R/R_N(I)$ overlap. Then, for each value $\Delta R/R_N(i)$, the equations

$$\Delta R/R_N(x) = \Delta R/R_N, \quad x = T, I \tag{7.6}$$

were solved for the pairs (T_{eff}, I), where T_{eff} is now used to denote the electron temperature. The effective temperature $T_{eff}(I)$ obtained from the calculations is shown in Fig. 7.2.3 for sample SbQ measured with pulse lengths τ_p=40, 100 and 500 ns. A number of conclusions can be drawn from these results:

- Small currents, even in the pulsing regime, can produce significant self-heating of the sample. For example, the increase in electron temperature observed in sample SbQ upon increasing the measurement current from 10 to 15 nA is ≈15 mK for τ_p=40 ns, but becomes ≈155 mK if τ_p=500 ns.

- Though the pulsed current was scaled to its rms value, $T_{eff}(I)$ is clearly a function of the pulse length: different $T_{eff}(I)$ are reached even if an identical power is dissipated in the device. As investigated in Ref. [119], the average dissipated power gives a good approximation to the average temperature in the wire only for high current values. For low

currents, the instantaneous electron temperature changes exponentially in a time scale given by the diffusion time $\tau_D = L^2/D$, where L is the length of the metal wire and D is the diffusion constant. If the time T_p between the pulses is $T_p \gg \tau_D$, the electrons in the wire thermalise at the lattice temperature before the next pulse arrives, and the average temperature is not reached. Using the values of T^* and V^* obtained in the previous sections, the values τ_D=1.2-1.6 ns was obtained. This is much smaller than the typical repetition periods $T_p = 1/f_p$=2.5-10 μs used during the experiments.

- For using the interferometer as readout of a qubit state, the electron temperatures in the readout junction must be as low as possible to satisfy the twofold purpose of good sensitivity to phase and low backaction. Maximum sensitivity to the phase across the SNS junction is achieved when $T_{eff} = T^* \approx$40 mK. At typical repetition periods $T_p = 1/f_p$=2.5-10 μs and currents $I_{p,rms}$ <10 nA, this condition is satisfied using pulse lengths τ_p <50 ns.

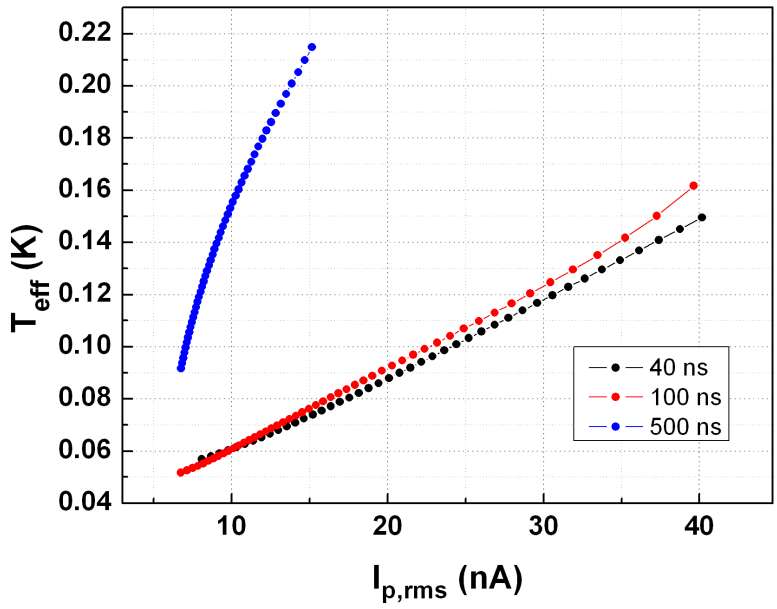

Figure 7.7: *Effective temperature of the quasipartcles as a function of applied voltage for (a) sample SbQ measured at a fridge base temperature T = 37 mK.*

7.3 Andreev interferometer in a strong RF field

This Section describes the experimental investigation of the influence of strong continuous RF field on the resistance of an Andreev interferometer. The experimental work was carried out in collaboration with Chris Checkley [19] and led to the publication of a paper [120].

A sample (AgInt) was fabricated with the normal metal part made of silver in a simple cross design and an aluminium superconducting loop, as shown in Fig. 5.1. The interferometer resistance was measured using a standard low-frequency technique employing the setup described in Sec. 6.4.1. The device was exposed to continuous RF radiation in the frequency range 1-40 GHz produced by an on-chip superconducting loop ("antenna"), which was connected to the Anritsu CWG at room temperature through the RF excitation line.

The device resistance showed the expected resistance oscillations as a function of applied magnetic flux Φ_{xI}, which are described by Eq. (4.1), with period $\Delta\Phi_{xI} = \Phi_0$. A summary of the parameters of the sample AgInt are shown in Table 7.2. The resistivity $\rho \approx 0.7\ \mu\Omega cm$, obtained from the measured normal state resistance R_N, and the value $\rho\ell = 5.36\times10^{-12}\ \Omega\text{cm}^2$ for Ag [121] give the mean free path $\ell \approx 77$ nm. From this, the diffusion coefficient $D = (1/3)v_F\ell \approx 400\ \text{cm}^2/\text{s}$ is obtained using the Fermi velocity of Ag $v_F = 1.39 \times 10^6$ m/s [39].

Figure 7.8(a) shows the resistance as a function of magnetic flux measured at different fridge base temperatures T between 22 and 600 mK, and Fig. 7.8(b) shows the resulting normalised resistance correction $\Delta R/R_N$ as a function of T. The resistance change $\Delta R/R_N$ decreases monotonously with increasing temperature and no "re-entrance" is observed, indicating that for this sample $E_{TH}/k_B < 22$ mK.

Irradiation of the device at RF frequencies produced two combined effects on the magneto-resistance:

- Oscillations of the resistance $R(\overline{\varphi}_I)$ at fixed phase $\overline{\varphi}_I$ as a function of the amplitude of the RF field. For some frequencies, a π-shift of the resistance oscillations was observed at large amplitudes.

	R_N (Ω)	ρ ($\mu\Omega cm$)	ℓ (nm)	D (cm^2/s)	$\Delta R_{MAX}/R_N$
AgInt	6.383	0.7	77	400	3.8%

Table 7.2: *Measured parameters of sample AgInt.*

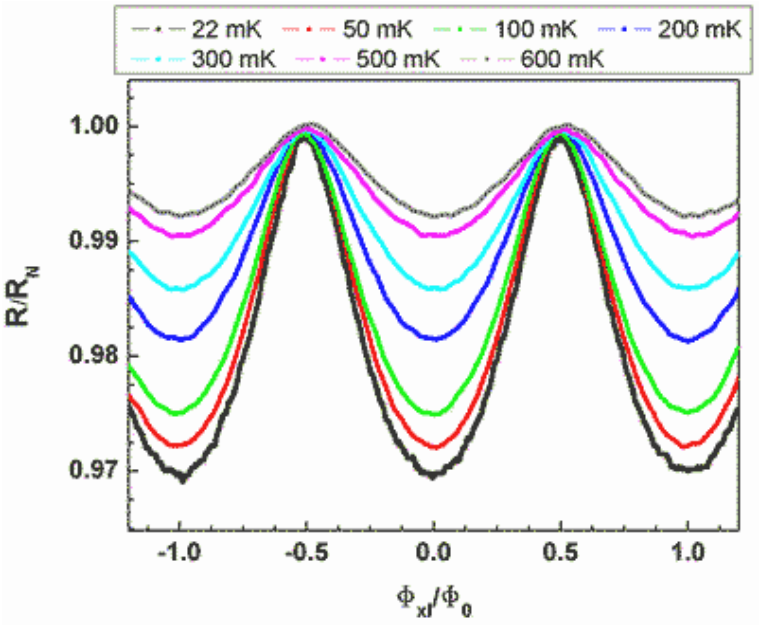

(a)

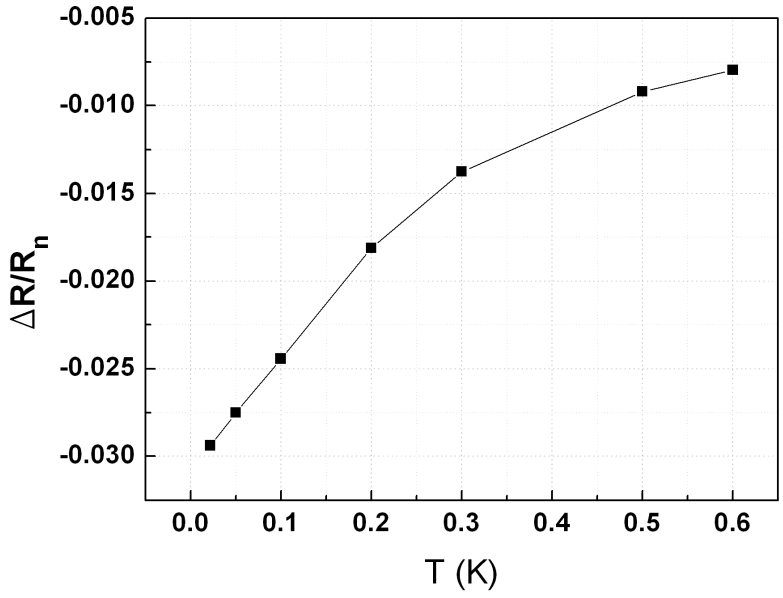

(b)

Figure 7.8: *(a) Normalised resistance of sample AgInt as function of normalised flux Φ_{xI}/Φ_0, measured at different fridge base temperature between 22 and 600 mK. The curves shown are obtained by averaging at least 6 flux sweeps. (b) Resistance correction $\Delta R/R_N$ as a function of temperature.*

- A suppression of the resistance correction ΔR with increasing amplitude of RF field.

Both effects were frequency dependent, with one prevailing on the other depending on the RF frequency. The oscillating behaviour of $R(\overline{\varphi}_I)$ is displayed in Fig. 7.9(a), which shows the interferometer resistance as a function of magnetic flux under radiation at frequency f_{RF}=8.1 GHz and amplitude s_{CWG} at the CWG output between 0 and 220.5 mV. The resistance change ΔR decreases with increasing s_{CWG}, and at s_{CWG}=220.5 mV the oscillations are π-shifted. Figure 7.9(b) shows $R(\overline{\varphi}_I)$ as a function of s_{CWG} measured at f_{RF}=8.1 GHz at different fixed phases $\overline{\varphi}_I$. Oscillations are clearly visible in $R(\overline{\varphi}_I)$, and beyond s^*_{CWG} ≈200 mV, $R(\pi)$ goes below $R(0)$, producing the flip in the magneto-resistance oscillations shown in Fig. 7.9(a).

The RF induced suppression of ΔR is clearly visible in Fig. 7.10(a), which shows the magneto-resistance oscillations measured at f_{RF}=5 GHz with s_{CWG} between 50 and 410 mV. At this frequency, radiation up to relatively large RF amplitudes produces a monotonic decrease in ΔR. This behaviour is more evident in Fig. 7.10(b), which shows $R(\overline{\varphi}_I)$ as a function of s_{CWG} for the same frequency at four different phases $\overline{\varphi}_I$. Compared to the behaviour at f_{RF}=8.1 GHz, the oscillations in $R(\overline{\varphi}_I)$ at f_{RF}=5 GHz are less pronounced and no π-shift is observed, and the main effect of the radiation is a suppression of ΔR due to the increase of $R(0)$. The dependence of $R(0)$ on radiation amplitude resembles the thermal effect discussed in Sec. 7.2 as a function of temperature and voltage, and it is thought to be due to an increase of the effective electron temperature caused by the RF field.

7.3.1 Magnetic flux modulation by the RF field

The behaviour shown in Figs. 7.9(a) and 7.9(b) can be explained in terms of modulation of the phase φ_I due to the fast oscillating RF field. When radiation at frequency f_{RF} is applied, the total magnetic flux threading the interferometer loop is the sum of the static flux bias Φ_{xI} and the RF induced flux $\Phi_{RF}(t)$, and the phase φ_I is given by

$$\varphi_I(t) = \frac{2\pi\Phi_{xI}}{\Phi_0} + \frac{2\pi\Phi_{RF}(t)}{\Phi_0} = \varphi_{DC} + 2\pi\mu\sin(2\pi f_{RF}t), \tag{7.7}$$

where $\varphi_{DC} = 2\pi\Phi_{xI}/\Phi_0$ and μ is the amplitude of the AC magnetic flux in units of Φ_0. The relation between μ and s_{CWG} is assumed to be linear and can be described as $\mu = k(f)s_{CWG}$, where $k(f)$ is a frequency dependent parameter accounting for the attenuation of the transmission lines and the

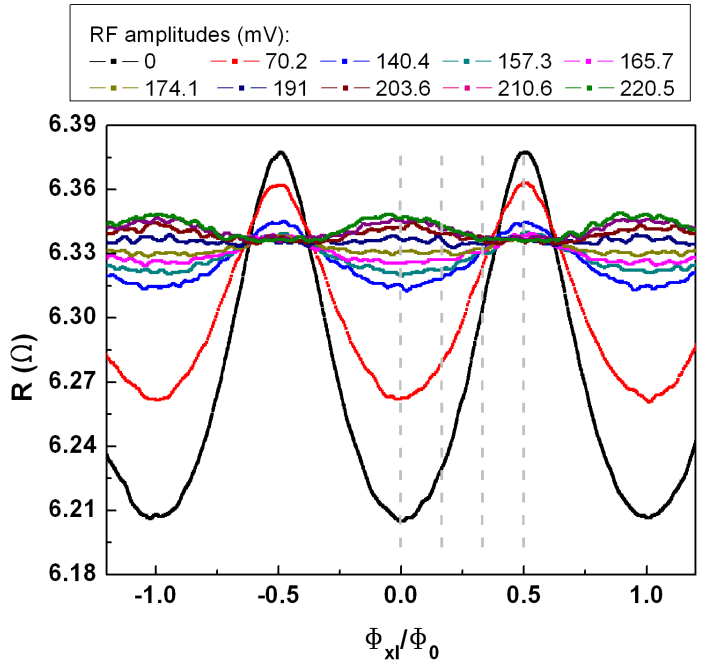

(a)

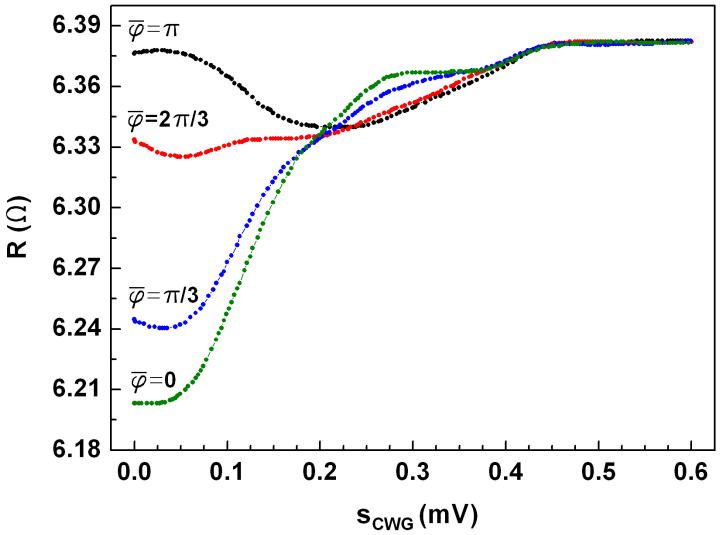

(b)

Figure 7.9: *(a) Magneto-resistance of sample AgInt measured at f_{RF}=8.1 GHz and RF amplitudes between 0 mV and 220.5 mV. (b) Resistance $R(\overline{\varphi}_I)$ as a function of RF amplitude, measured at the same RF frequency and $\overline{\varphi_I}$=0, π/3, 2π/3 and π (marked by dashed lines in (a)).*

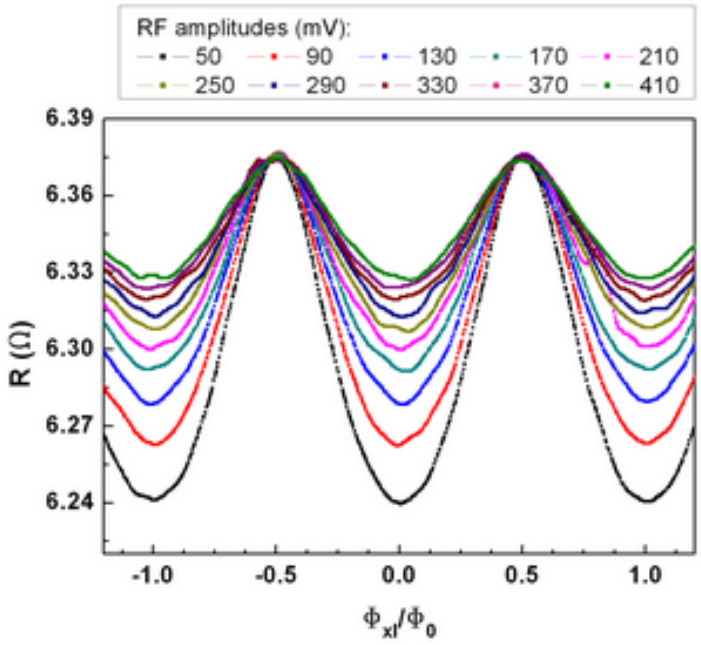

(a)

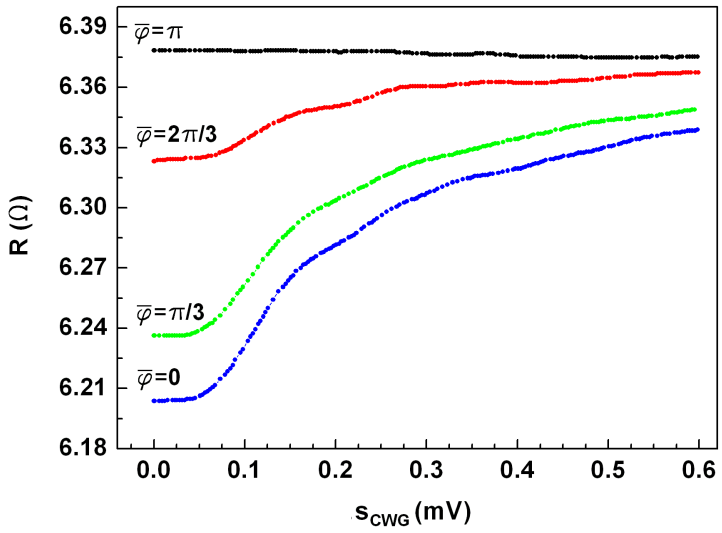

(b)

Figure 7.10: *(a) Magneto-resistance of sample AgInt measured at f_{RF}=5 GHz and RF amplitudes between 50 mV and 410 mV. (b) Resistance $R(\overline{\varphi}_I)$ as a function of RF amplitude measured at the same RF frequency and $\overline{\varphi}_I$=0, $\pi/3$, $2\pi/3$ and π (marked by dashed lines in (a)).*

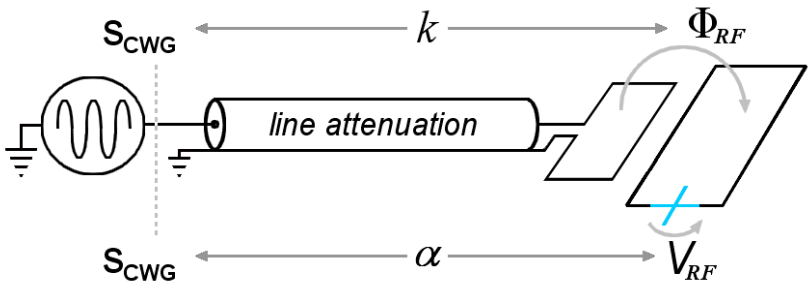

Figure 7.11: *Schematic showing the link between the RF amplitude s_{CWG} generated at room temperature and the quantities Φ_{RF} and V_{RF} at the device locations.*

coupling between the interferometer and antenna loops, as depicted in Fig. 7.11. If the interferometer follows adiabatically the fast phase changes, the instantaneous resistance Eq. (7.1) can be written as

$$R(t) = R_N - \gamma \left\{1 + \cos\left[\varphi_{DC} + 2\pi\mu \sin(2\pi f_{RF} t)\right]\right\}. \tag{7.8}$$

The measurement system detects the time-average of $R(t)$, which is

$$R_{av} = f_{RF} \int_{-1/2f_{RF}}^{1/2f_{RF}} R(t)dt. \tag{7.9}$$

Calculating R_{av} with Eqs. (7.9) and (7.8), one finds the resistance change

$$\Delta R_{av} = \gamma A(\varphi_I) \left(\frac{1}{2} + J_0(2\pi\mu)\right), \tag{7.10}$$

where $J_0(2\pi\mu)$ is the Bessel function of the first kind, and the factor $A(\varphi_I)$ contains trigonometric functions of the phase φ_I. Figure 7.12(a) shows R_{av} as a function of the RF induced magnetic flux μ calculated from Eq. (7.9) with $k(f)$=1 for four different values of φ_I. The resulting magneto-resistance oscillations are shown in Fig. 7.12(b) at μ=0, 0.15, 0.3 and 0.4, and display the decrease in ΔR with increasing μ and the oscillation flip occurring at large RF amplitude. The model above predicts multiple π-shifts of the magneto-resistance oscillations, occurring periodically at

$$\mu^* = \frac{j^*}{2\pi}, \tag{7.11}$$

where j^* are the zeroes of $J_0(j)$. The parameter $k(f)$ can be determined at each RF frequency by inserting into Eq. (7.11) the experimental RF

amplitudes $s^*_{CWG} = k(f)\mu^*$ at which π-shifts are observed, thus obtaining a calibration of the on-chip RF field. Unfortunately, the "Bessel" effect was displayed only in some frequency windows where the RF induced heating of the SNS junction (see Sec. 7.3.2) was weak enough for the π-shift to be observed.

7.3.2 RF induced thermal effect

The effect of radiation on the critical current of SNS junctions in the long junction limit (eV, $k_BT > E_{TH}$) was recently addressed both theoretically [122] and experimentally [52]. In these papers, suppression of the junction supercurrent was obtained by RF irradiation, whose effect is to increase the effective temperature of the quasiparticles in the normal metal. The RF radiation induces an oscillating voltage V_{RF} across the SNS junction, which modifies the distribution function of the quasiparticles in the normal metal by increasing their total energy.

We include the RF induced heating effect in the model of Eq. 7.8 using the experimental temperature dependence of ΔR (see Fig. 7.8(b)), which was interpolated as described in Sec. 7.2 to obtain the function $\gamma(T)$. The RF induced thermal effect is thus modelled introducing an effective electron temperature T_e which is a function of the RF induced voltage V_{RF}. The detailed form of T_e depends on the cooling mechanism in the normal section, that is quasiparticle diffusion to the contacts and energy exchange with the lattice. The latter is usually very small at low temperatures [119], as was the case in Ref. [123], where a device very similar to ours was investigated. If electron-phonon cooling is neglected, the electron temperature T_e at the centre of a metallic wire is [124]

$$T_e = \sqrt{T_L^2 + \frac{3}{4\pi^2}\frac{e^2}{k_B^2}V_{RF}^2}, \tag{7.12}$$

where the lattice temperature T_L is assumed to be the same as the fridge temperature. The RF induced voltage V_{RF} is assumed to be linearly dependent on s_{CWG} and given by $V_{RF} = \alpha(f)s_{CWG}$, where $\alpha(f)$ is the transfer function between the RF amplitude generated at room temperature and the induced voltage V_{RF}, schematically shown in Fig. 7.11. Inserting the effective temperature obtained from Eq. (7.12) into the prefactor $\gamma(T)$ in Eq. (7.8) allows us to model the RF induced heating using $\alpha(f)$ as a fitting parameter.

The averaged resistance R_{av} as a function of s_{CWG} is shown in Fig. 7.13(a) for α=52.6$\times(k_B/e)^2$ ($\approx$-64 dB) and k=1.9, together with the experimental

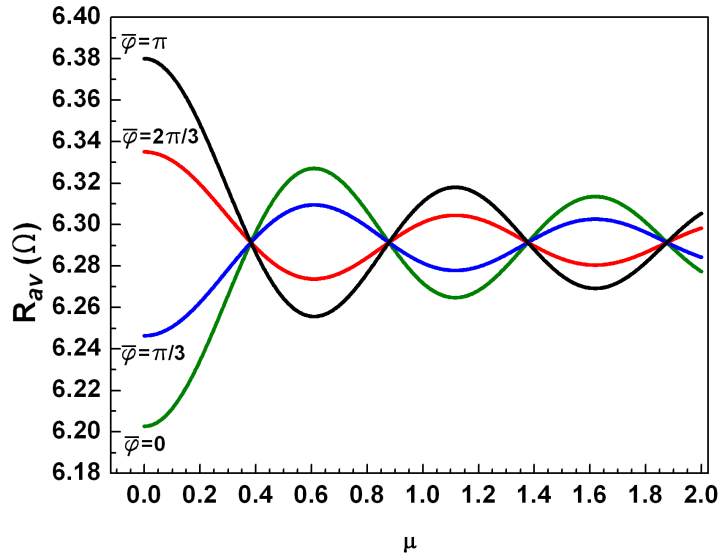

(a)

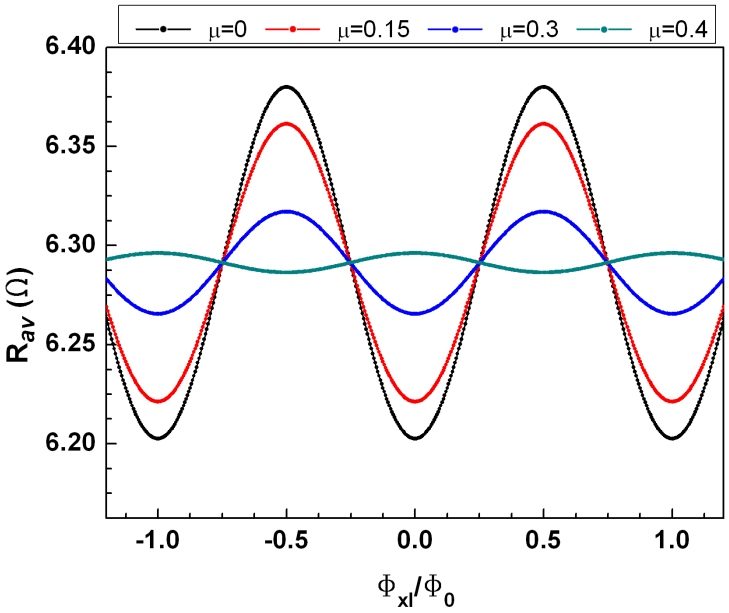

(b)

Figure 7.12: *(a) Calculated averaged resistance R_{av} as a function of RF induced flux μ at fixed phases φ_I=0, $\pi/3$, $2\pi/3$ and π. All curves intersect at $\mu^*=j^*/(2\pi)$, where j^* are the zeroes of the Bessel function of the first kind $J_0(j)$. (b) Averaged resistance R_{av} as a function of normalised flux Φ_{xI}/Φ_0 for μ=0, 0.15, 0.3 and 0.4.*

data at f_{RF}=8.1 GHz. Figure 7.13(b) shows R_{av} as a function of flux for the same the parameters and four different amplitudes s_{CWG}. Calculations of R_{av} of the calculations for f_{RF}=5 GHz are shown in Figs. 7.13(c) and (d) for α=17.1$\times(k_B/e)^2$ ($\approx$-69 dB) and k=0.3. From Figs 7.13(a) and 7.13(c), it can be seen that while the measured resistance $R(0)$ at small amplitudes is insensitive to s_{CWG}, the increase in the electron temperature expected from Eq. (7.12) is steeper than the observed one. At large s_{CWG}, the experimental resistances $R(0)$ and $R(\pi)$ both reach the normal value R_N much faster than predicted by the above model. The inclusion of the phonon contribution in Eq. (7.12) is not expected to produce a better match because, whether it would lower the electron temperature at small s_{CWG}, it would also increase the discrepancy at large s_{CWG}. The simple model of RF induced heating, though describes qualitatively the suppression of the resistance change ΔR with increasing s_{CWG}, fails to reproduce the behaviour of $R(\overline{\varphi}_I)$ at both small and large s_{CWG}, which suggests that proper calculations of the proximity induced resistance change in the presence of RF radiation are needed. As for the oscillatory dependence of $R(\overline{\varphi}_I)$ on s_{CWG} and the π-shift occurring at high RF amplitudes, the proposed model of "Bessel" effect is believed to successfully account for both features.

7.3.3 RF frequency dependence

The dependence of both the "Bessel" effect and RF induced heating on RF frequency can be determined from the measured resistance $R(\pi)$. For a perfectly symmetric cross-like interferometer, theory predicts complete destructive interference of the Andreev reflected quasiparticles at $\varphi_I = \pi$ [49, 75], which gives $R(\pi) = R_N$. As can be seen from the temperature dependence in Fig. 7.8(a), this is indeed the case for our device, and we believe the only explanation for the decrease of $R(\pi)$ below R_N is the "Bessel" effect. Figure 7.14 shows the measured resistance $R(\pi)$ as a function of RF frequency in the range 0-20 GHz and RF amplitudes s_{CWG} 50-600 mV. A large decrease in $R(\pi)$ is observed between f_{RF} $\approx$5 GHz and f_{RF} $\approx$13 GHz, which coincides with the frequency interval in which there is on oscillatory dependence of $R(\overline{\varphi}_I)$ on s_{CWG}. We attribute the resonant-like dips to resonances in the coaxial lines and sample holder box, which modulate the strength of both the "Bessel" effect and RF induced heating producing the frequency dependence incorporated into the parameters $\alpha(f)$ and $k(f)$. For f_{RF} <5 GHz and f_{RF} >13 GHz, the "Bessel" effect is suppressed and no π-shifts are observed, and the decrease in ΔR is explained by RF heating. Currently, we can not explain the presence of a window of transparency (5-13 GHz) where heating

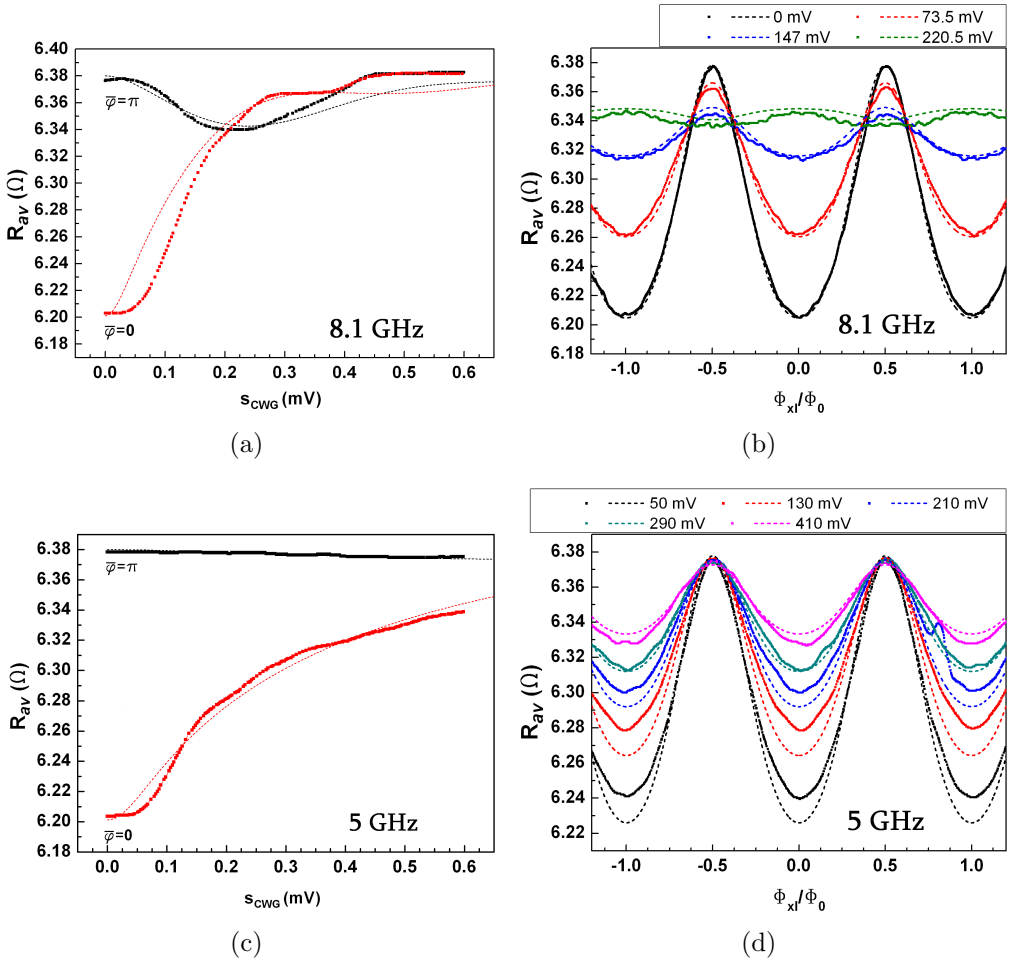

Figure 7.13: *Comparison between measured resistance and average resistance R_{av} calculated using Eqs. 7.9 and 7.12 for f_{RF}=8.1 GHz and 5 GHz. The left panel shows the resistance $R(\overline{\varphi}_I)$ as a function of the RF amplitude s_{CWG} for fixed phases $\overline{\varphi}_I$=0 and π. The right panel shows the averaged resistance as a function of normalised flux Φ_{xI}/Φ_0 for different RF amplitudes. The values α=52.6×$(k_B/e)^2$ and k=1.9 were used for f_{RF}=8.1 GHz, whereas α=17.1×$(k_B/e)^2$ and k=0.3 for f_{RF}=5 GHz.*

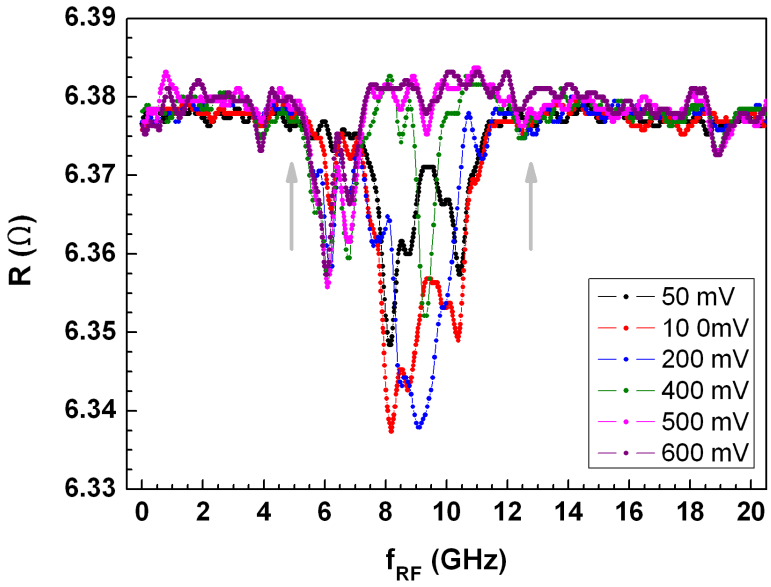

Figure 7.14: *Measured resistance as a function of RF frequency f_{RF} at RF amplitudes s_{CWG} between 50 and 600 mV. The grey arrows mark the frequency window in which the "Bessel" effect is observed.*

effects are weak enough to allow for the "Bessel" effect.

The model of "Bessel" effect described in this section is valid as long as the interferometer resistance can to follow adiabatically the fast phase changes and Eq. (7.8) is valid. Defining a response time of the interferometer τ_I to be the time the device takes to react to changes in φ_I, the observation of the "Bessel" effect requires that $\tau_I \ll 1/2f_{RF}$. An upper estimation of τ_I can be obtained by using the largest frequency at which we observe the Bessel effect, f_{MAX}=13 GHz, which gives a response time $\tau_I \ll 1/2f_{MAX} \approx$40 ps.

Chapter 8

Quantum state probing using an Andreev interferometer

Macroscopic tunnelling of the system between the two classical persistent current states is expected to occur over a narrow flux region centred around $\Phi_Q = \Phi_0/2$. Changes of the phase across the qubit are reflected on the shape of the interferometer magneto-resistance, and information about the qubit state can be inferred. In this Chapter we describe the experimental investigation of an interferometer/qubit device where the interferometer is used as a readout meter of the qubit state. The overall phase dependence of the interferometer resistance is presented in Sec. 8.1, where the information about the classical persistent current states is determined. The interferometer resistance when the qubit was biased to $\Phi_Q \approx \Phi_0/2$ showed evidence of tunnelling between two metastable states, and it is described in Sec. 8.2.

8.1 Detection of the classical dynamics

The interferometer magneto-resistance was measured using the four-probe pulsed technique discussed in Sec. 6 while sweeping the magnetic flux through the device. The magnetic field was produced by driving a current I_{mag} through the small superconducting solenoid housed in the sample holder. Typical magneto-resistance oscillations of sample SbQ measured at T=20 mK are shown in Fig. 8.1 over a wide flux range. The behaviour of the magneto-resistance R can be divided into wide regions in which the resistance oscillates periodically, separated by narrow regions where I_{mag} correspond to $\Phi_Q \approx (2n-1)\Phi_0/2$, where R deviates significantly from the periodic oscillating pattern. Figure 8.2 shows details of Fig. 8.1 at $\Phi_Q \approx 0$ (Fig. 8.2(a)), and at the first degeneracy points at $\Phi_Q = \pm\Phi_0/2$ (Fig. 8.2(b) and (c)).

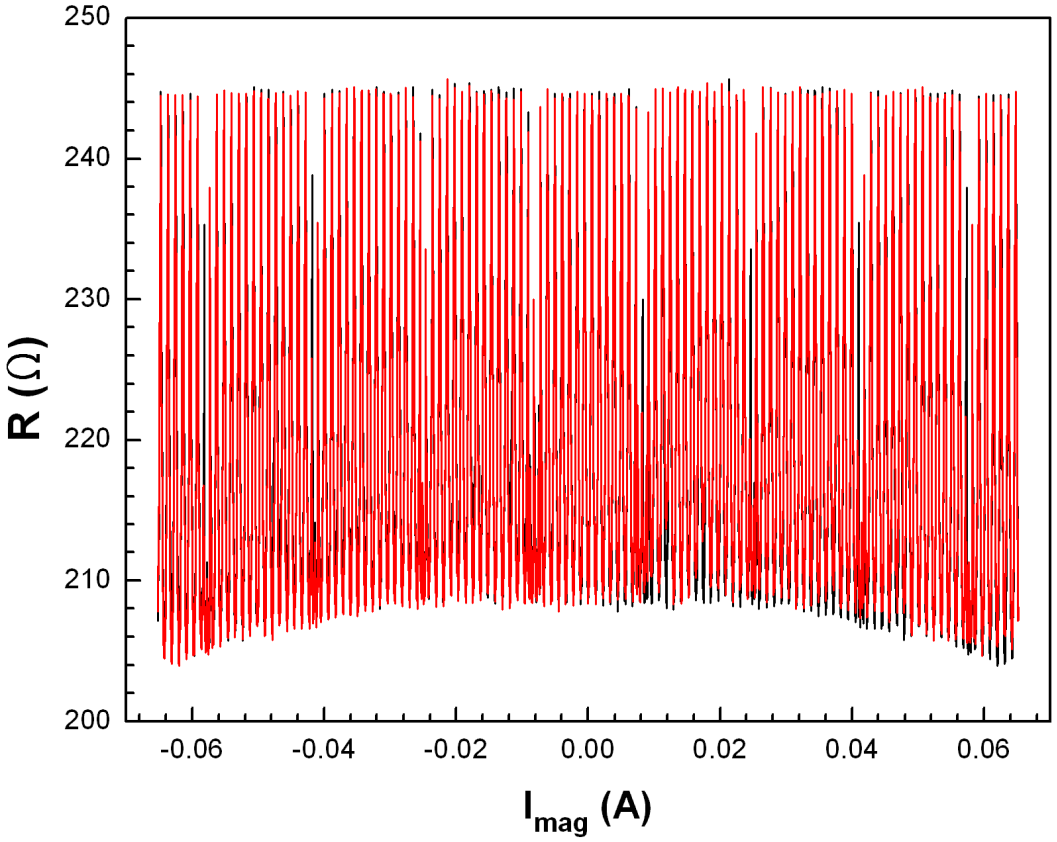

Figure 8.1: *Resistance of sample SbQ as a function the current I_{mag} through the magnet. Black and red curves correspond to left-to-right and right-to-left sweeps of the current, respectively.*

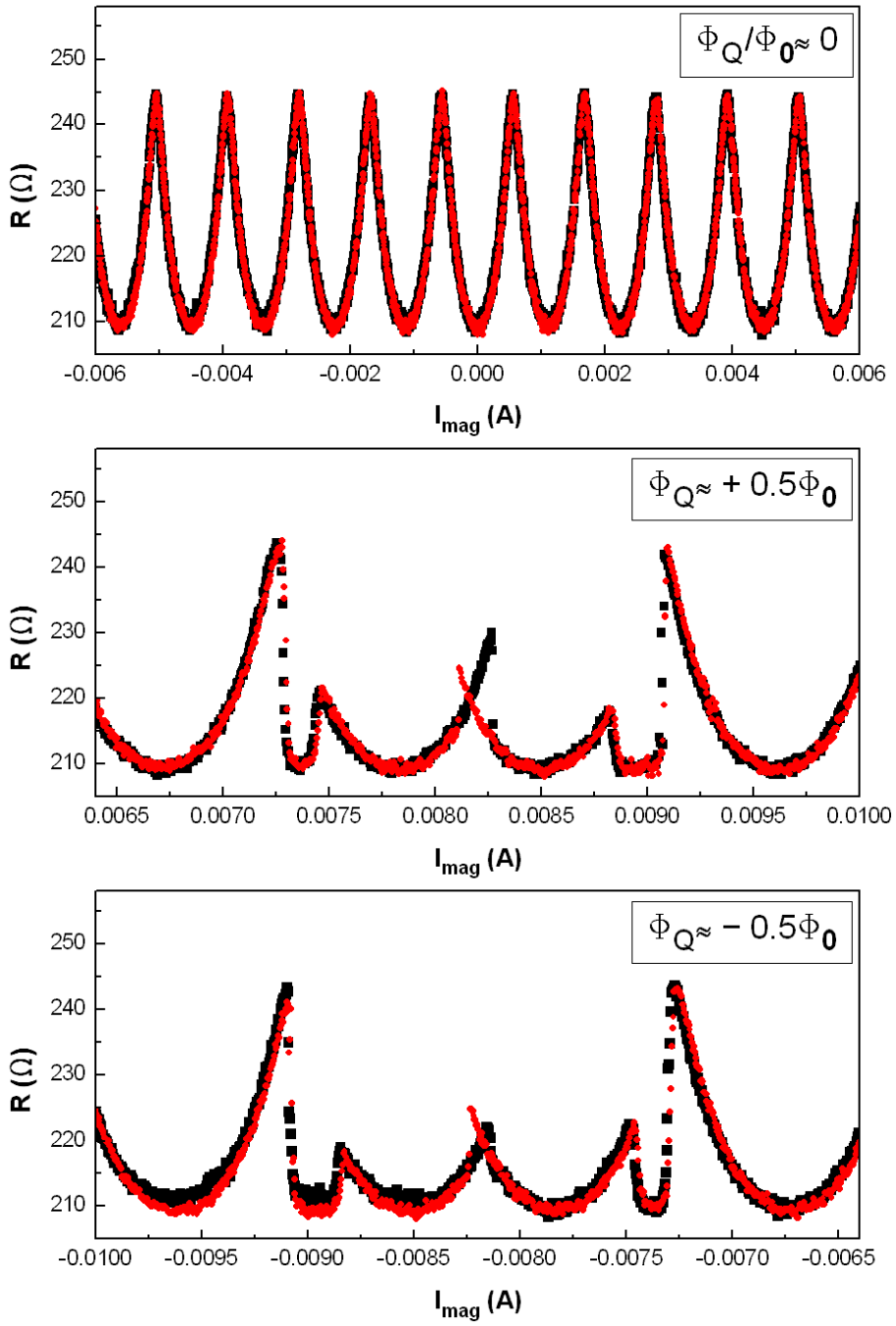

Figure 8.2: *Enlarged views of Fig. 8.1 showing the resistance at (a)* $\Phi_Q = 0$ *and (b), (c)* $\Phi_Q = \pm\Phi_0/2$.

As described in Sec. 4.1.3, the overall flux dependence of the phase φ_I is given by

$$\varphi_I = \frac{2\pi\Phi_I}{\Phi_0} + \Delta\varphi_Q, \tag{8.1}$$

where Φ_I is the flux through the interferometer loop, $\Delta\varphi_Q$ is the phase change due to the qubit, and $\Phi_0 = h/2e$ is the flux quantum. The phase $\Delta\varphi_Q$ has a saw-tooth behaviour as a function of Φ_Q, with linear regions separated by sudden phase changes at the "degeneracy points" $\Phi_Q \approx (2n-1)\Phi_0/2$, where n is an integer.

The dependence of $\Delta\varphi_Q$ on magnetic flux far away from $\Phi_Q \approx (2n-1)\Phi_0/2$ can be extracted from the measured magneto-resistance using the procedure described below based on the considerations expressed in Sec. 4.1.3. This procedure also provides a calibration of the current I_{mag} driven into the superconducting magnet and gives the value of the ratio f between the loop areas.

P1: An index i is associated to each oscillation minimum in ascending order, with i=0 for the minimum occurring at I_{mag}=0. For each minimum, the current $I_{mag}(i)$ is determined.

P2: A 2D vector $\overline{\varphi_I}$ is constructed with the currents $I_{mag}(i)$ in the first column and the values $\varphi_I = i2\pi$ in the second column.

P3: A straight line $\varphi_{I,xI} = M_I I_{mag}$ corresponding to the linear term Φ_{xI} is found, which, when subtracted from the vector $\overline{\varphi_I}$, leaves a sawtooth-like term $\Delta\varphi_Q$. The linear term $\varphi_{I,xI}$ is found by choosing the coefficient M_I that gives, after subtraction, a sawtooth curve with zero mean. This step gives the calibration coefficient between I_{mag} and Φ_{xI}.

P4: The current axis is converted to magnetic flux exploiting the fact that i_Q=0 at $\Phi_Q = \Phi_0$. Thus, the sawtooth curve intersects the horizontal axis at currents $I^*_{mag}(j)$ corresponding to $\Phi_Q = j\Phi_0$, where j is the index of the intersection. The conversion is carried out by associating each intersection point to the corresponding flux values, that is, using $M_Q I^*_{mag}(j) = j\Phi_0/2$. This step allows to obtain the calibration coefficient M_Q for Φ_Q.

P5: The parameter f is obtained as $f = M_I/M_Q$.

The phase $\Delta\varphi_Q$ extracted with this procedure allows to determine the classical persistent current associated to the states $\{|0\rangle, |1\rangle\}$ localised in each well. Using the extracted $\Delta\varphi_Q$, the persistent current i_Q as a function of flux can

be obtained by solving Eq. (4.13) for i_Q. Figure 8.3 shows the behaviour of the phases φ_I and $\Delta\varphi_Q$ as a function of Φ_Q extracted from the data shown in Fig. 8.1. As expected, $\Delta\varphi_Q$ shows the sawtooth behaviour with period $\Delta\Phi_Q = \Phi_0$, reversing its sign at multiples of $\Phi_Q = \Phi_0/2$. At this fluxes, a phase drop of $\Delta\varphi_{Q,MAX} \approx 0.8\pi$ is observed. The resulting persistent current i_Q, obtained solving Eq. (4.14), is shown in Fig. 8.4 in units of the critical current I_0 of the Josephson junctions. As the magnetic flux is swept across $\Phi_Q = \Phi_0/2$, the persistent current reverses its sign and undergoes a total change $\Delta i_Q \approx 0.73 I_0$.

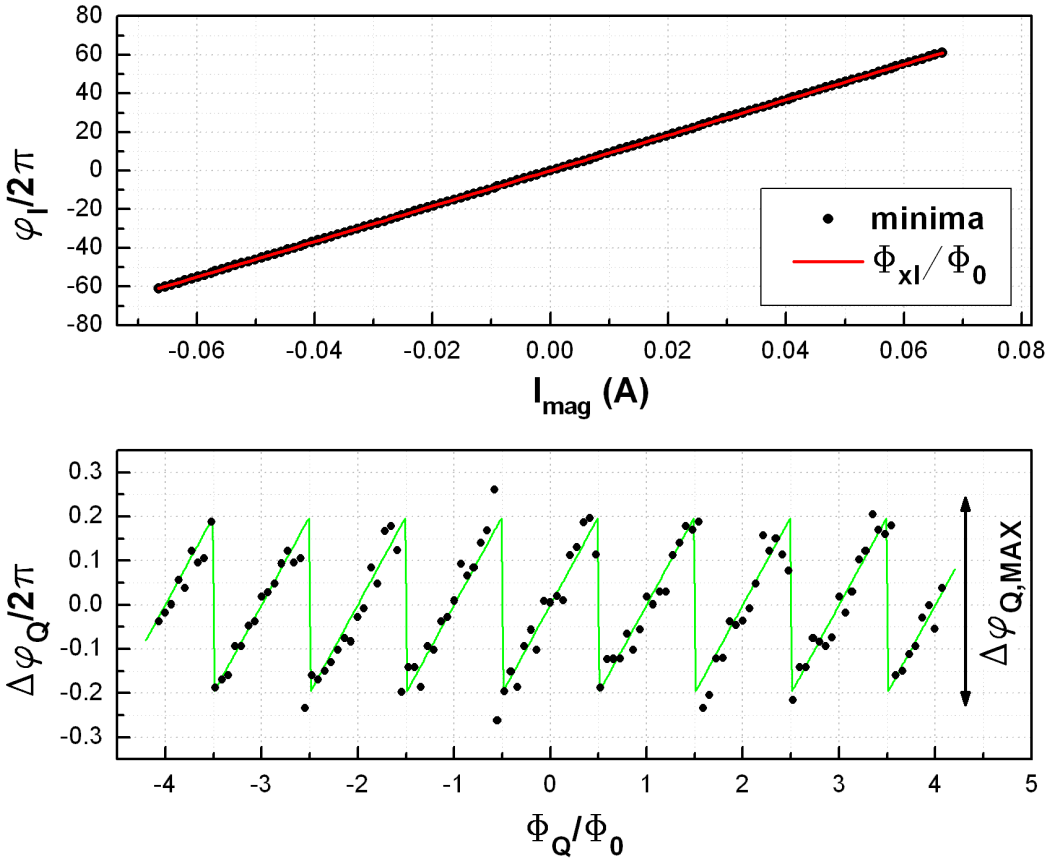

Figure 8.3: *Phase extracted from the magneto-resistance of sample SbQ. Upper: phase φ_I obtained from step (P2) as a function of the current I_{mag} through the magnet. The red line is the linear term $\varphi_{I,xI} = \Phi_{xI}/\Phi_0$. A small modulation of φ_I (not resolved in this scale) is due to the qubit contribution $\Delta\varphi_Q$, which is superimposed on the linear dependence. Lower: phase $\Delta\varphi_Q$ after the step (P4) as a function of magnetic flux Φ_Q. The green line is the sawtooth function used for the I_{mag}-Φ_Q conversion.*

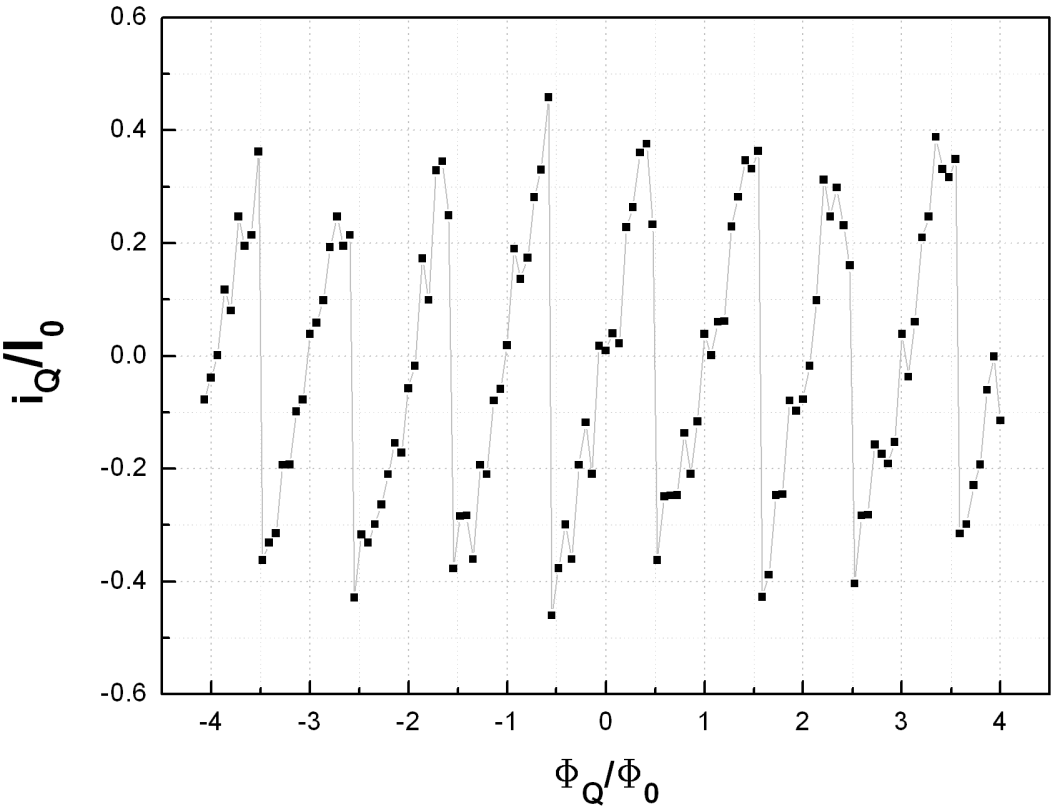

Figure 8.4: *Flux dependent persistent current of sample SbQ, calculated from the phase $\Delta\varphi_Q$ shown in Fig. 8.3.*

8.2 Degeneracy point of Sample SbQ

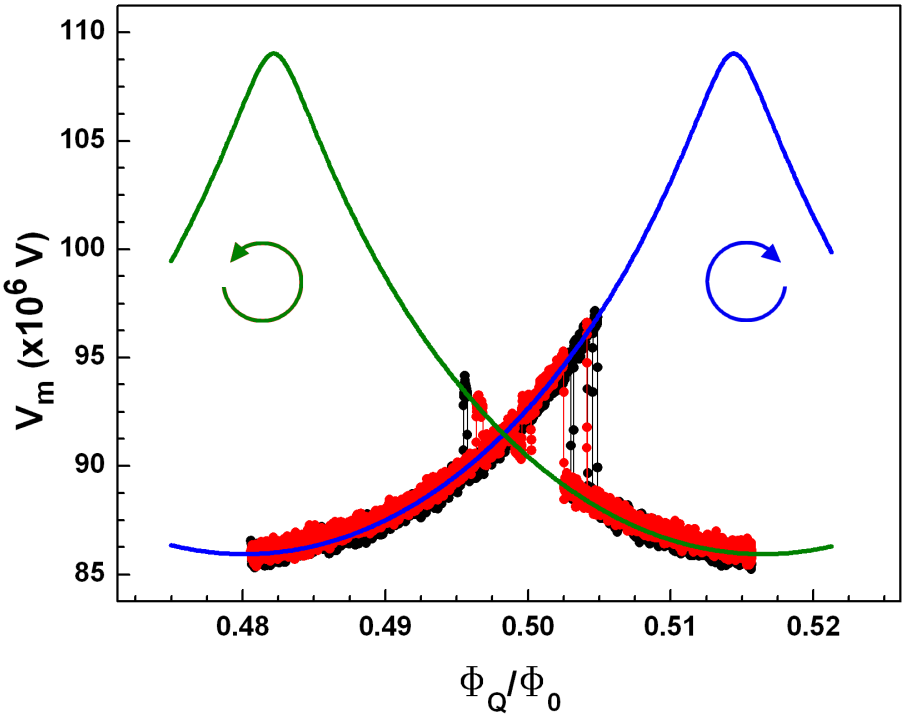

Figure 8.5: *Voltage V_m as a function of flux for the sample SbQ, in the flux range around the first degeneracy point $\Phi_Q = \Phi_0/2$. Two experimental datasets measured under identical conditions are shown in green and black, whereas the solid curves calculated using Eqs. 8.3 and 8.4 are shown in blue and red, respectively. There are vertical transitions, where the persistent current circulating in the qubit loop flips its direction.*

The interferometer resistance measured while sweeping the magnetic flux around the region $\Phi_Q \approx \Phi_0/2$ showed vertical jumps between curves corresponding to resistance oscillations shifted by an amount $\Delta\varphi_I$. Figure. 8.5 shows typical voltage records as a function of magnetic flux, where the two datasets were measured in identical conditions and using opposite sweeping directions. As Φ_Q approaches Φ_0, the voltages clearly switches between two levels. This transitions were observed for all magnetic fluxes Φ_Q multiple of $\Phi_0/2$ (qubit degeneracy points), and were present in flux intervals $\pm$ 1% wide, whereas away from these regions, the measured voltage showed the stable behaviour described in Sec. 7.1. The switching of the resistance between two oscillating patterns has been already observed in the past in

similar interferometer-qubit devices [18] with silver as the normal metal, but the mechanism of the transitions was not put forward.

The data shown in Fig. 8.5 were fitted to

$$R = R_N - \gamma\left(1 + \cos(\varphi_I)\right), \tag{8.2}$$

with the phase φ_I given by

$$\varphi_I = \frac{2\pi\Phi_I}{\Phi_0} - \Delta\varphi_Q/2, \qquad for \;\; \Phi_Q < \Phi_0/2 \tag{8.3}$$

$$\varphi_I = \frac{2\pi\Phi_I}{\Phi_0} + \Delta\varphi_Q/2, \qquad for \;\; \Phi_Q > \Phi_0/2 \tag{8.4}$$

where $\Delta\varphi_Q$ is the phase change produced by the qubit. The screening parameter β was obtained using Eq. (7.2) in the flux region $\Phi_Q \approx 0$, which gave $\beta = 0.1$. The fits are shown in Fig. 8.5 with the raw data, and gave a value $\Delta\varphi_Q$=-0.83π. With the aid of Fig. 8.4, one can see that this phase change $\Delta\varphi_Q$ corresponds to a total change in the persistent current $\Delta i_Q = i_{Q,R} - i_{Q,L}$=-0.79$I_0$, and the current has opposite signs at either sides of the degeneracy point. This results allowed us to interpret the jumps in the measured voltage as produced by the switching of the measured phase $\Delta\varphi_Q$ between the two states localised in the left and right well of the double-well potential, and described by the flux basis $\{|0\rangle, |1\rangle\}$.

In the next sections, the statistical properties of the switching events are investigated in the time domain, and the dependence on temperature, flux bias point, pulse measurement current and RF radiation are reported.

8.2.1 Time-domain analysis of qubit dynamic

Random telegraph signals have been observed in the time-domain measurements of a large variety of physical systems including semiconductor MOS devices [125, 126], superconducting interference devices [127], and tunnel junctions [128]. In these systems, charging and discharging of individual two-level fluctuators (TLF) localised in insulating layers create a fluctuating Coulomb field that affect the device parameters by partially blocking the current flow. Recently, coupling between such defects and either charge-phase [129], phase [130]-[132] and flux [133]-[135] qubits was reported. In particular, in Ref. [135], the coupling was connected to the phenomenon of quantum jumps, first developed in atomic systems [136]-[138] where the fluorescence signal produced by isolated two- and three-level atoms was observed to produce RTS.

More generally, RTS signals are usually associated with two-level systems

(TLS) whose potential can be described by two energy wells separated by a barrier. The system undergoes thermally activated or tunnel transitions between the states $|0\rangle$ and $|1\rangle$ localised in the wells which produce a random switching of the measured observable with characteristic rates $\Gamma_0 = \tau_0^{-1}$ and $\Gamma_1 = \tau_1^{-1}$, where τ_0 and τ_1 are the dwell times in the respective states.

The two-level random telegraph process is generally considered as a discrete two-state Markov process obeying Poisson statistics [138]. In this hypothesis, the probability density of recording a number k of $|0\rangle \rightarrow |1\rangle$ transitions in a given time interval Δt is [138]

$$P(k, \lambda) = \frac{\lambda^k}{k!} e^{-\lambda}, \tag{8.5}$$

where λ is the expected number of events.

From the functional form given in Eq. (8.5), the distribution of the dwell times in the $|0\rangle$ and $|1\rangle$ RTS levels is predicted to follow an exponential decay, with probability density function $P(\tau)$ given by [136]

$$P(\tau) = e^{-\tau/\overline{\tau}}, \tag{8.6}$$

where $\overline{\tau}$ is the average dwell time in either the $|0\rangle$ or $|1\rangle$ RTS levels.
Finally, the Power Spectral Density $S_V(f)$ of the RTS signal is described by a Lorentzian spectrum [137]

$$S_V(f) = \frac{\Gamma_0 \Gamma_1}{\Gamma_0 + \Gamma_1} \frac{\alpha^2}{(2\pi f)^2 + (\Gamma_0 + \Gamma_1)^2}, \tag{8.7}$$

with half-width $\Delta \mathrm{f} = (1/2\pi)(\Gamma_0 + \Gamma_1)$, where Γ_0 and Γ_1 are the $|0\rangle \rightarrow |1\rangle$ and $|1\rangle \rightarrow |0\rangle$ transition rates, respectively, and α is a constant with dimension of voltage.

As will be described in the next sections, the distribution of switching events between the two resistance patterns was indeed found to follow a Poisson distribution, and Eqs. (8.6) and (8.7) provided a good quantitative description of the measured rates. Though the presence of a single TLF in one of the tunnel junctions of our devices could in principle give RTS fluctuation in the interferometer resistance, the observed phase displacement $\Delta\varphi_Q$ seems to be much bigger than what would be produced by a single TLF, and would require the TLF to reverse the sign of the persistent current i_Q circulating in the qubit loop. The percentage change in the critical current induced by a TLF can be estimated using the data from Ref. [128], where Al/Ox/Al submicron Josephson junctions were investigated: using their estimated effective area δA of a TLF and the total area A of the junction, the percentage fluctuation in the critical current I_0 is $\delta I_0/I_0 = \delta A/A \approx 12 \times 10^{-6}$.

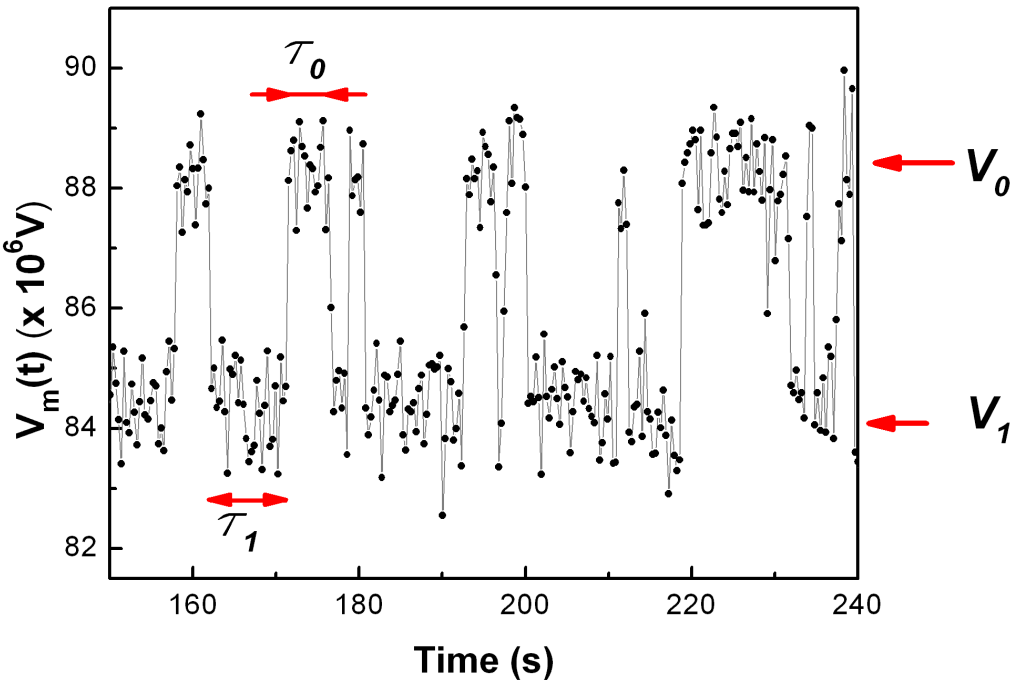

Figure 8.6: *Measured voltage trace $V_m(t)$ taken at T=20 mK as a function of time for a particular flux $\Phi_Q^* > \Phi_0/2$ and . The measurements shown are taken from a 2 hour long record consisting of N=4500 data points.*

The RTS signal observed in our system requires a percentage change in the critical current of $\delta I_0/I_0 \approx 0.80$, which is much bigger than the estimated value for a TLF. Thus, TLFs as the origin of the observed RTS signal is very unlikely, and the hypothesis that the switching is produced by transitions of the system between the states localised in the left and right well of the potential will be used here.

The statistical properties of the switching of φ_Q were investigated using the dependence on time of the voltage signal $V_m(t)$. The flux bias was ramped to a flux value $\Phi_Q^* \approx \Phi_0/2$, and held at Φ_Q^* while the resistance of the interferometer was measured using the pulsed lock-in technique described in Sec. 6.4.2. The voltage signal $V_m(t)$ as a function of time was recorded for typically 2 hours, producing datasets containing N=3000-6000 points. An example of $V_m(t)$ measured at $\Phi_Q^* > \Phi_0/2$ is shown in Fig. 8.6. The results look like random telegraph signal (RTS), with the voltage switching randomly between the levels $\overline{V}_0$ and $\overline{V}_1$, corresponding to the states $|0\rangle$ and $|1\rangle$ localised in the left and right wells, respectively. The characteristic parameters needed to describe the time traces $V_m(t)$ are the number of points

N_0 and N_1 in the $|0\rangle$ and $|1\rangle$ levels, and the corresponding dwell times τ_0 and τ_1. All these parameters were found to depend strongly on temperature, flux bias point, and pulse measurement current. In particular, very long dwell times (in the range 0.1-100 s) were measured. To check that transitions between the levels were not missed, the time constant of the lock-in amplifier was changed down to 10 ms, and no change in the statistical properties of the time traces were measured. Nevertheless, such short time constants drastically increased the noise in $V_m(t)$, and a time constant of 100 ms was used throughout all the measurements on the switching behaviour.

The amplitude of the pulsed current used to measure the interferometer resistance was chosen using the measurements described in Sec. 7.2.3. To ensure that the qubit was not affected by the pulsed current used for the resistance measurements, the pulse parameters were chosen to have a minimum spectral content at frequencies in the GHz range, where the qubit resonant frequency was expected. With the typical parameters f_p=100 kHz, τ_r=5 ns and τ_p=500 ns, the power spectral density of the pulsed current at 1 GHz was $S(1\ GHz) \approx 10^{-17} \times S(0)$, thus ensuring that no spurious excitation of the qubit would occur due to the pulsed current. For this set of pulse parameters, the current amplitude $A_p \approx$7 nA was chosen to minimise heating of the SNS junction, thus reducing the Nyquist noise induced by the interferometer on the qubit. This current amplitude corresponds to a quasi-particle energiy $E \approx E_{TH}$, thus ensuring that a considerable supercurrent flows through the SNS junction, which further protects the qubit from voltage fluctuations across the interferometer.

Occupation probability

The probability P_0 and P_1 that a particular point in $V_m(t)$ belongs to the $|0\rangle$ or $|1\rangle$ state was determined from the amplitude histogram of $V_m(t)$. For each dataset, the histogram was constructed using the standard procedure, with a bin size chosen to contain at least one data point. Figure 8.7 shows the histogram built from the time trace in Fig. 8.6. The result has been modelled as a sum of two Gaussian distributions $G_0(V)$ and $G_1(V)$

$$G(V) = G_0(V)+G_1(V) = \frac{A_0}{\sigma_0\sqrt{2\pi}}e^{-(V-\overline{V}_0)^2/2\sigma_0^2}+\frac{A_1}{\sigma_1\sqrt{2\pi}}e^{-(V-\overline{V}_1)^2/2\sigma_1^2}, \quad (8.8)$$

where $\overline{V}_0$ and $\overline{V}_1$ (average RTS voltages), A_0 and A_1 (areas), σ_0 and σ_1 (widths) were the fitting parameters. From the fit, the probabilities P_0 and P_1 were calculated as P_0=$A_0/(A_0 + A_1)$ and P_1=$A_1/(A_0 + A_1)$, respectively. The procedure described above was straightforward for the datasets in which the background noise was smaller than the separation of the RTS voltages

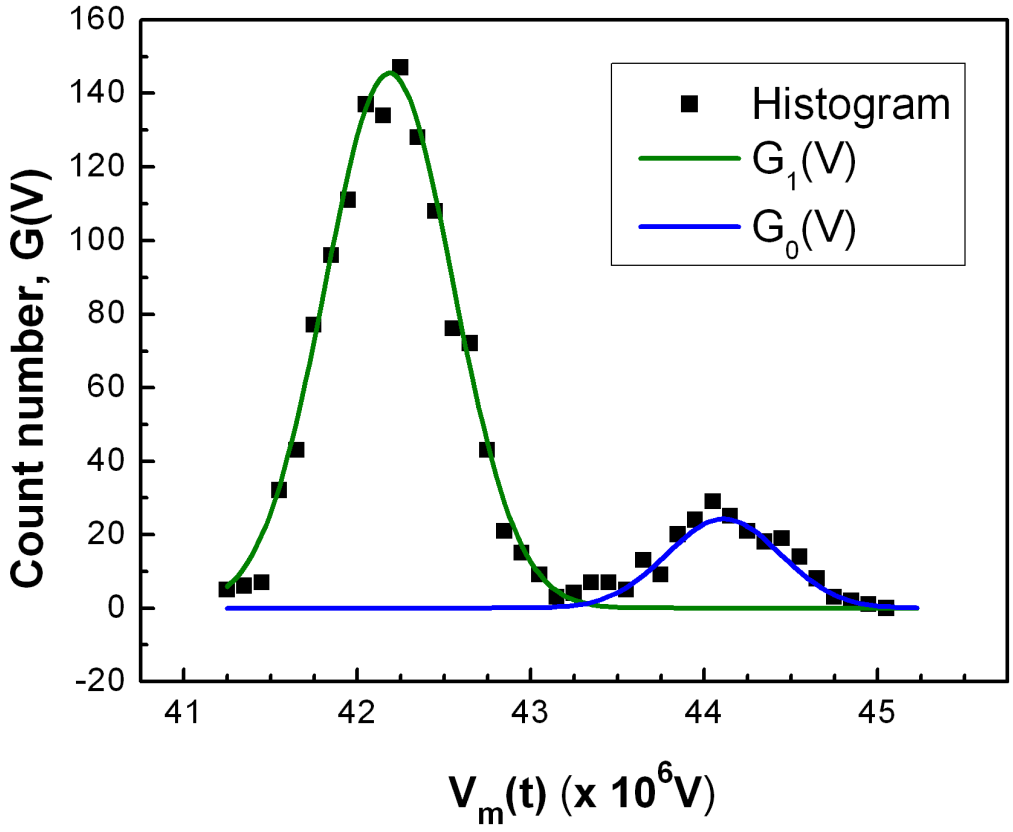

Figure 8.7: *Amplitude histogram of the time traces in Fig. 8.6. The solid lines are the least-square fit to Eq. (8.8).*

$\Delta V = \overline{V}_1 - \overline{V}_2$, i.e., $\Delta V > \overline{\sigma} = (\sigma_0 + \sigma_1)/2$, as in Fig. 8.7. In our device, ΔV is clearly a function of the applied flux, and becomes comparable to $\overline{\sigma}$ when the flux approaches the degeneracy point of the qubit $\Phi_Q = \Phi_0/2$. In these cases, the measured signal $V_m(t)$ was first regenerated using the iterative procedure described in Ref. [139], which creates a noiseless time trace $V_r(t)$ and yields the averaged dwell times $\overline{\tau}_0$ and $\overline{\tau}_1$. The calculations were carried out using Mathematica with the code in Appendix C.

Analysis of the dwell times

The probability distributions $P_{\tau_0}(t)$ and $P_{\tau_1}(t)$ of the dwell times were determined from the measured time trace $V_m(t)$. Practically, the series of individual times τ_0 and τ_1 were extracted from the time trace, and the respective histograms were built. The results were modelled using Eq. (8.6)

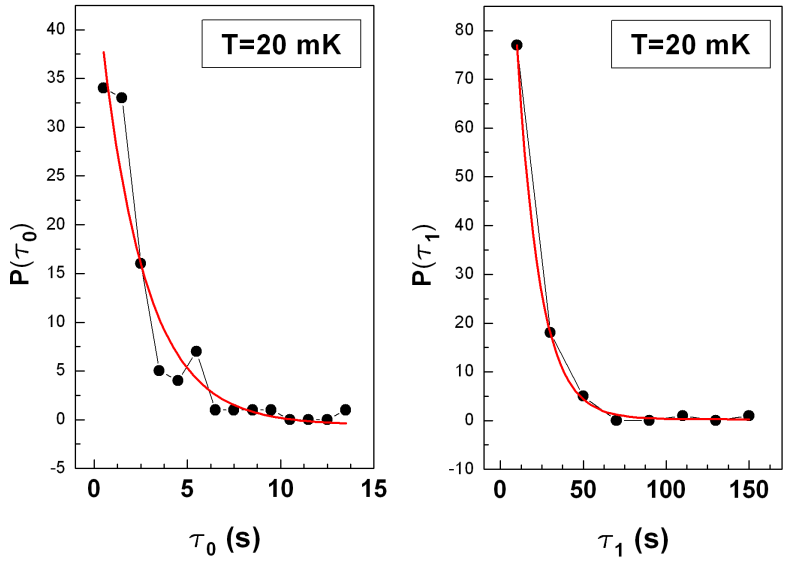

Figure 8.8: *Distribution of the dwell times in the* $|0\rangle$ *(left) and* $|1\rangle$ *(right) states at* T*=20 mK, obtained from the time trace in Fig. 8.6. The solid lines are least-squares fits to Eq. (8.6).*

with the average dwell times $\overline{\tau}_0$ and $\overline{\tau}_1$ as fitting parameters.

The histograms obtained from the time trace of Fig. 8.6 are shown in Fig. 8.8 together with the least-squares fits to Eq. (8.6). As can be seen, the experimental results are well described by an exponential dependence. The values $\overline{\tau}_0$=13.69 s and $\overline{\tau}_1$=2.40 s obtained from the fits are in good agreement with $\overline{\tau}_0$=16.13 s and $\overline{\tau}_1$=2.20 s calculated directly from the measured time trace $V_m(t)$ as the mean of the individual τ_0 and τ_1. A better agreement was expected if longer time records $V_m(t)$ were acquired, but the maximum measurement length was limited to about 3 hours by slow drifts in the measurement equipment. The same procedure was performed on all the measured datasets in which the number N of transitions between the RTS levels was large enough to have a good statistical representation. To check that N was sufficiently large for a given dataset, the analysis was also performed on the reduced dataset containing $N-1$ transitions, and the output values $\overline{\tau}_0$ and $\overline{\tau}_1$ from the two analysis were compared: the dataset was considered representative if the difference between the times obtained from the original and reduced sets was much smaller than 5%. For all the accepted datasets, the average dwell times obtained by the fits to Eq. (8.8) and those determined directly from the time traces agreed to within 15%.

As a consistency check, the power spectral density (PSD) $S_s(f)$ of the

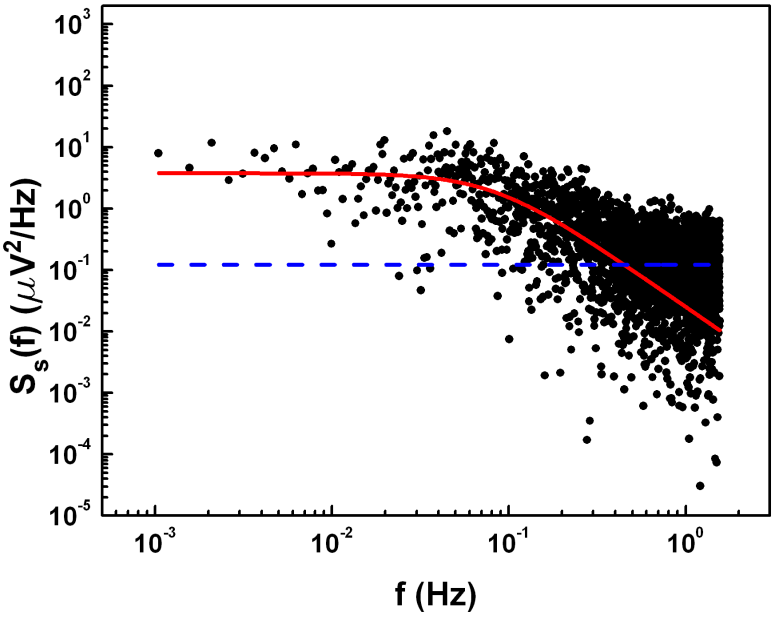

Figure 8.9: *Power spectral density of the time trace in Fig. 8.6. The red solid line is the Lorentzian spectrum calculated using Eq. (8.7) with* $\alpha=(\overline{V}_0 + \overline{V}_1)/2$*, and* $\overline{\tau}_0$ *and* $\overline{\tau}_1$ *obtained from the fits shown in Fig. 8.8. The blue dashed line is the background noise level* $S_n(f) = (\overline{\sigma}/2)^2$*.*

measured time traces was calculated and compared to the Lorentzian shape expected from Eq. (8.7). The PSD of voltages was obtained by applying the Fast Fourier Transform to the measured time traces $V_m(t)$ and squaring the result. Figure 8.9 shows $S_s(f)$ for the complete time trace shown in Fig. 8.6 together with the Lorentzian function (Eq. (8.7)) with $\alpha = (\overline{V}_0 + \overline{V}_1)/2$, $\overline{\tau}_0$ and $\overline{\tau}_1$ obtained from the experimental data. The results are in reasonable agreement with the predicted behaviour, except for frequencies f >0.3 Hz, where $S_s(f)$ deviates from the Lorentzian shape and seems to flatten. Unfortunately, the investigation of $S_s(f)$ above f =0.3 Hz was not possible because of the limited sampling rate used during the acquisition of the time trace. Nevertheless, the deviation is probably due to background noise, which can be estimated from the average width $\overline{\sigma}$ of the Gaussian fits obtained in Sec. 8.2.1, obtaining $S_n(f) = (\overline{\sigma}/2)^2$=1.21×10^{-13} V^2/Hz.

Transition probability

The probability distribution of the $|1\rangle \rightarrow |0\rangle$ transitions was obtained from the measured time traces $V_m(t)$ by dividing the time axis into intervals of length Δt, and counting the number of $|1\rangle \rightarrow |0\rangle$ transitions within each interval. The histogram constructed with this procedure is the probability distribution $P(k)$ that k transition have occurred in the time interval Δt.

As a typical example, the results obtained from the time trace of Fig. 8.6 are shown in Fig. 8.10 for Δt=23 s, 33 s and 43 s, together with the best fits to Eq. (8.5) where λ is the fitting parameter. The fits obtained are in reasonable agreement with the experimental data, considering the small number of points in the histograms: this is due to the finite number N_{tr} of transitions contained in the time trace $V_m(t)$ (N_{tr}=270), which was limited by the maximum measurement length allowed by drifts in the measurement setup.

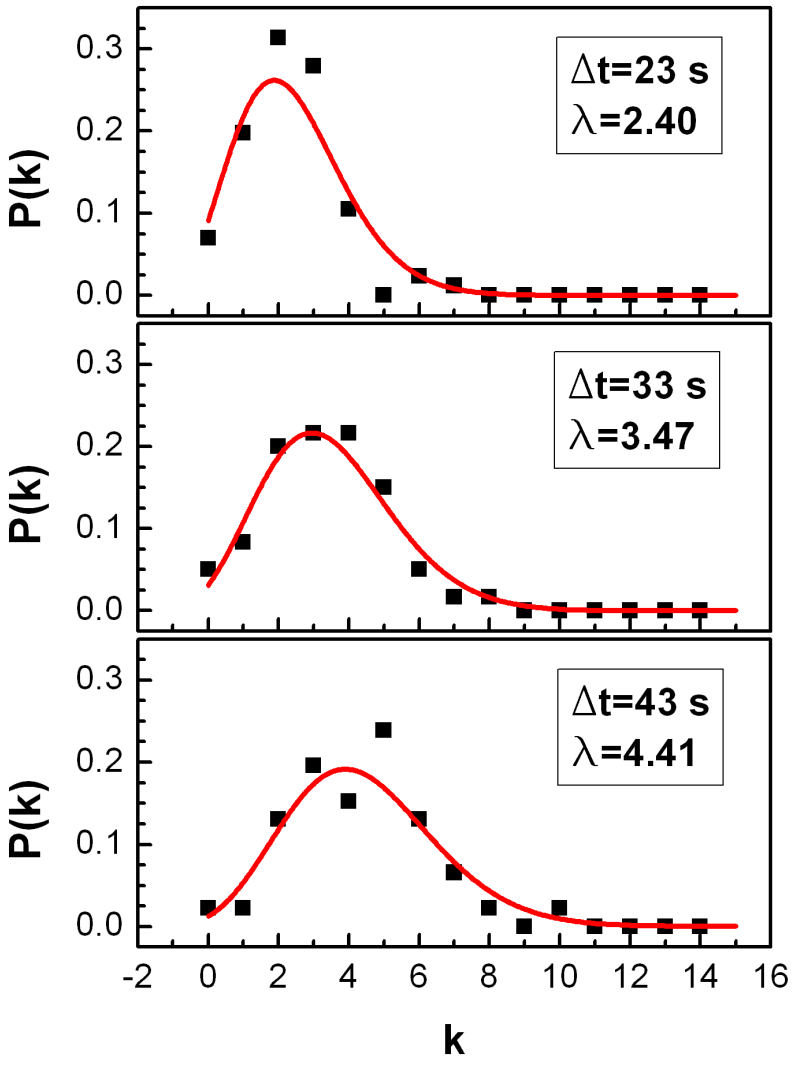

Figure 8.10: *Distribution of* $|1\rangle \rightarrow |0\rangle$ *transitions obtained from the time trace in Fig. 8.6, and best fits to Eq. (8.5). The time intervals* Δ *used to construct the histogram and the mean values* λ *obtained from the fits are shown.*

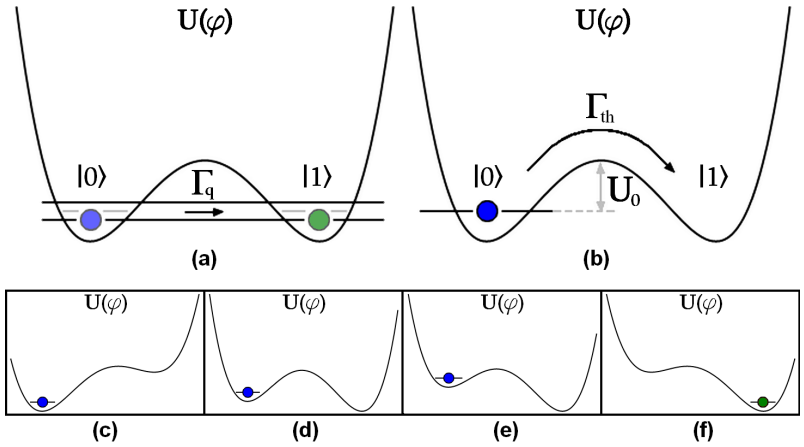

Figure 8.11: *Upper: Schematic representation of the escape mechanisms responsible for the switching of the system state: (a) quantum tunnelling occurring for* $T \ll U_0/k_B$ *and (b) thermal activation above the potential barrier for* $T > U_0/k_B$*. Lower panels (c)-(f): thermal activation regime at different fluxes* $\Phi_Q > \Phi_0/2$*.*

8.2.2 Switching mechanisms

Possible mechanisms responsible for the switching behaviour are thermal activation over the potential barrier and tunnelling through the barrier, and are schematically shown in Figs. 8.11(a) and (b). The transition rates for thermal activation are expected to obey an Arrhenius-type law [140]

$$\Gamma_{i,th} = A \exp(-U_i^*/k_B T) \qquad (i = 0, 1), \tag{8.9}$$

where U_0^* (U_1^*) is the height of the potential barrier separating the wells seen by the $|0\rangle$ ($|1\rangle$) energy level. The prefactor A depends on the exact shape of the potential and the strength of interaction with the environment. For small damping, it coincides with the so called "attempt frequency" f_a, which is taken to be the frequency of small oscillations at the bottom of the wells. Equation (8.9) expresses the increase in the probability of escaping from one well as the temperature is increased beyond the height of the potential barrier. The values of f_a and U_i^* can be obtained by plotting Eq. (8.9) in logarithmic scale versus $1/T$: the resulting graph is a straight line of intercept $\ln(f_a)$ and slope $-U_{0,i}/k_B$.

The dynamics of the thermal activation mechanism at different fluxes is schematically depicted in Figs. 8.11(c)-(f). In (c), the system is initially localised in the left well when $\Phi_Q < \Phi_0/2$, and the barrier is so high that

the probability to escape from the left well is zero. As the flux is increased to $\Phi_Q > \Phi_0/2$ (panels (d) and (e)), the reduction of the barrier increases the escape probability, until the system will escape to the right well (panel f). The system is in a condition similar to (c), i.e., the barrier seen from the right well is so high that the system is effectively trapped. In the case the thermal energy from the bath is not sufficient to cause the escape from the initial well when $\Phi_Q > \Phi_0/2$, an hysteretic behaviour of the system is expected when the magnetic flux is swept across $\Phi_Q = \Phi_0/2$ in both directions.

At sufficiently low temperature, the dominant mechanism is quantum tunnelling through the barrier, and the transition rate deviates from Eq. (8.9). Recent theoretical [142] and experimental [143] works investigated macroscopic resonant tunnelling (MRT) of flux in a SQUID system, whose potential is described by a double well. In these works, the flux dependence of the tunnelling rates was found to be sensitive to the shape of the spectral density $S(\omega)$ of flux noise, showing qualitatively different features in the case of "classical" and "quantum" noise [144]. In the presence of classical white noise, they predict the rates Γ_0 and Γ_1 to coincide and have the form [142]

$$\Gamma = \frac{1}{2}\frac{\Delta^2 W}{\epsilon^2 + W^2}, \qquad W = \pi S(0), \tag{8.10}$$

where Δ is the qubit energy gap and $\epsilon = i_Q \Phi_0 \phi$ is written using the magnetic flux bias $\phi = \Phi_Q/\Phi_0 - 1/2$. Equation 8.10 describes a Lorentzian flux dependence, as shown in Fig. 8.12(a), with maximum at ϕ =0 and width W. If the noise has a strong low frequency component, the rates are described by a Gaussian form [143]

$$\Gamma_i = \sqrt{\frac{\pi}{8}}\frac{\Delta^2}{W}\exp\left[-\frac{(\epsilon \mp \epsilon_p)^2}{2W^2}\right], \tag{8.11}$$

where $i = 0, 1$, and the "+" ("-") sign holds for $i = 1$ (0). For a classical noise source, ϵ_p=0 [142], and $\Gamma_0 = \Gamma_1$. For a quantum noise, Eq. 8.11 produces two distinct Gaussian peaks symmetrically shifted with respect to ϕ=0 by an amount $\phi_p = \epsilon_p/(i_Q\Phi_0)$, as shown in Fig. 8.12(b). In this regime, the width W of the Gaussians is [143]

$$W^2 = 2k_B T_{eff}\epsilon_p, \tag{8.12}$$

where T_{eff} is the effective equilibrium temperature of the source producing the low frequency noise. Using Eqs. 8.11 and 8.12, we obtain

$$\Gamma_0/\Gamma_1 = e^{\epsilon/k_B T_{eff}}, \tag{8.13}$$

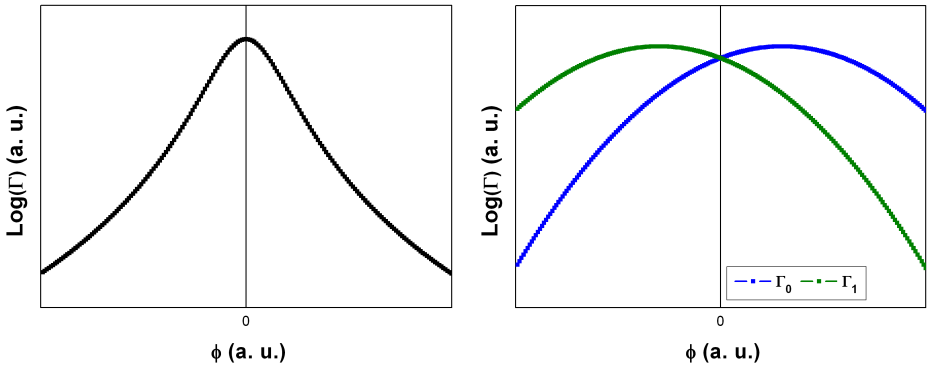

(a) (b)

Figure 8.12: *(a) Lorentzian rate produced by Eq. 8.10. (b) Distinct Gaussian rates obtained from Eq. 8.11. The rates are plotted in logarithmic scale*

which, if plotted in logarithmic scale as a function of the magnetic flux bias ϕ, gives a straight line with slope $i_Q\Phi_0/k_BT_{eff}$.

The occupation probabilities are linked to transition rates by a detailed balance equation

$$dP_0/dt = \Gamma_1 P_1 - \Gamma_0 P_0 \tag{8.14}$$

The probability P_0 at equilibrium can be obtained by setting $dP_0/dt = 0$, and using Eq. (8.13) and the fact that $P_0 + P_1 = 1$, which gives

$$P_0 = \frac{1}{2}\left[1 - \tanh\left(\epsilon/2T_{eff}\right)\right]. \tag{8.15}$$

8.2.3 Flux Dependence

The switching behaviour of φ_I was investigated at several fluxes around $\Phi_Q = \Phi_0/2$ at the fridge base temperature (T≈20 mK). For the purpose, the magnetic flux was ramped to the desired value, and then kept constant while the time trace $V_m(t)$ was acquired. The procedure was repeated for several magnetic fluxes, and the statistical analysis described in the preceding sections was performed on all recorded time traces.

The average escape rates are shown in Fig. 8.13(a) as function of the magnetic flux bias ϕ. The behaviour is symmetric with respect to $\phi = 0$, with increasing (decreasing) rates in the $|0\rangle$ ($|1\rangle$) state as the magnetic flux is changed across ϕ=0,with a total change 0.03-3 s^{-1} in the investigated range. This measured flux dependence is not accounted for by the single-peak Lorentzian in Eq. 8.14, whereby the tunnelling rates would exhibit a maximum when the energy levels $|0\rangle$ and $|1\rangle$ are resonant at $\phi = 0$, and then decrease as the magnetic flux is moved away from $\phi = 0$ and the energy difference between the levels is increased. On the other hand, from Fig. 8.13(a) one can see the similarity of the behaviour predicted by Eq. (8.11) for $|\phi| < \phi_p$ and the measured dependence.

Figure 8.13(b) shows the fit of the ratio $\ln(\Gamma_0/\Gamma_1)$ using Eq. 8.13. Using $i_Q = 0.4I_0$ and I_0=500 nA obtained from the analysis of the classical dynamics in Sec. 8.1, we find the value T_{eff} ≈21 mK, in excellent agreement with the fridge base temperature of T ≈20 mK at which the measurements were acquired.

Equation 8.11 has two further free parameters, Δ and ϵ_p, and a match with the measured rates can be found with a non-unique combination of them. Nevertheless, minimal values can be found for the parameters assuming that the maxima of the Gaussian peaks lie outside of our investigated flux range $\Delta\phi$=0-0.003. Thus, assuming $\phi_p > 0.003$, we obtain the condition for the shift ϵ_p >0.1 K. Using this value, a minimal value for the gap Δ can be found by plotting Eq. 8.11, and adjusting the parameter Δ to match the measured tunnelling rates. The result of this procedure is also shown in Fig. 8.13(a), and returned the value Δ=0.23 K. This value implies a qubit energy gap Δ >4.8 GHz, which lies in the expected range.

With the aid of Eq. 8.12, we also find W >65 mK, which, in units of frequency, corresponds to W >1.4 GHz. This results imply $W \approx \Delta$, i.e., the noise-induced broadening of the localised energy levels $|0\rangle$ and $|1\rangle$ is comparable to the energy level splitting. In this situation, a very low quality factor $Q = \Delta/W$ ∼1 is expected, which produces dephasing times [143] $\tau_\varphi = \sqrt{\epsilon^2 + \Delta^2}/(W|\epsilon|)$ ≈1 ns.

Figure 8.14 shows the probabilities P_0 and P_1 as a function of ϕ in the

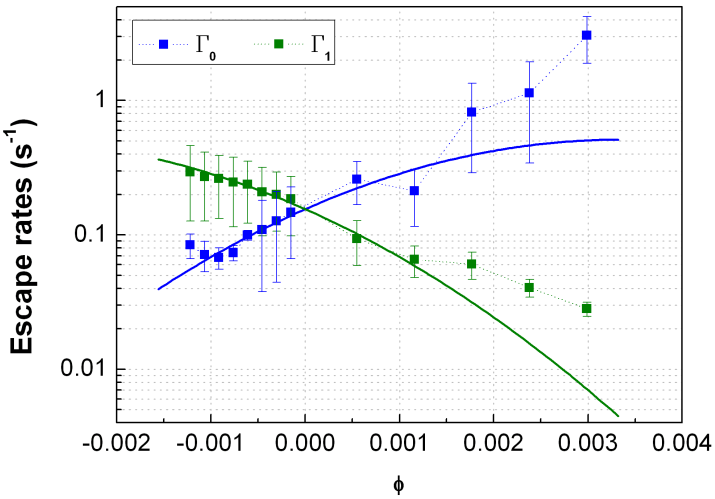

(a)

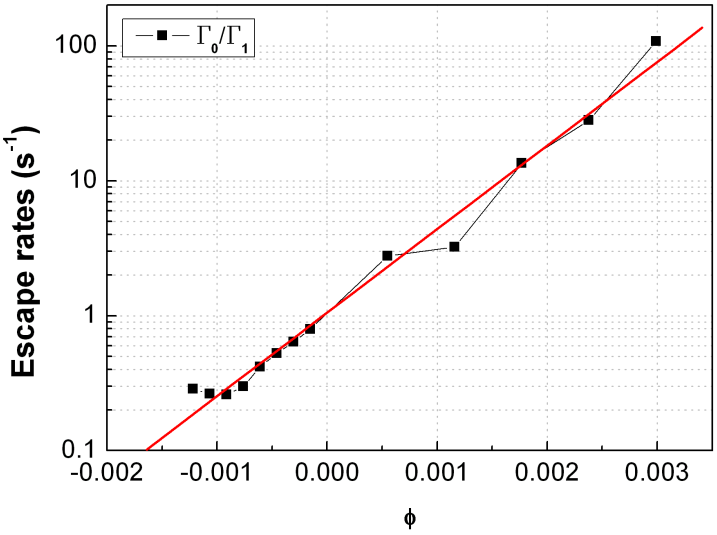

(b)

Figure 8.13: *(a) Measured tunnelling rates* Γ_0 *and* Γ_1 *as a function of* ϕ *(squares) and plot of Eq. 8.11 (solid lines) using* T_{eff}*=21 mK,* ϵ_p*=0.1 K, and adjusting the parameter* Δ *to match the measured rates. The value obtained is* Δ*=0.23 K. (b) Rate ratio* Γ_0/Γ_1 *in logarithmic scale as a function of magnetic flux bias* ϕ*. Fitting the data with a straight line gives an effective temperature* T_{eff}*=21 mK.*

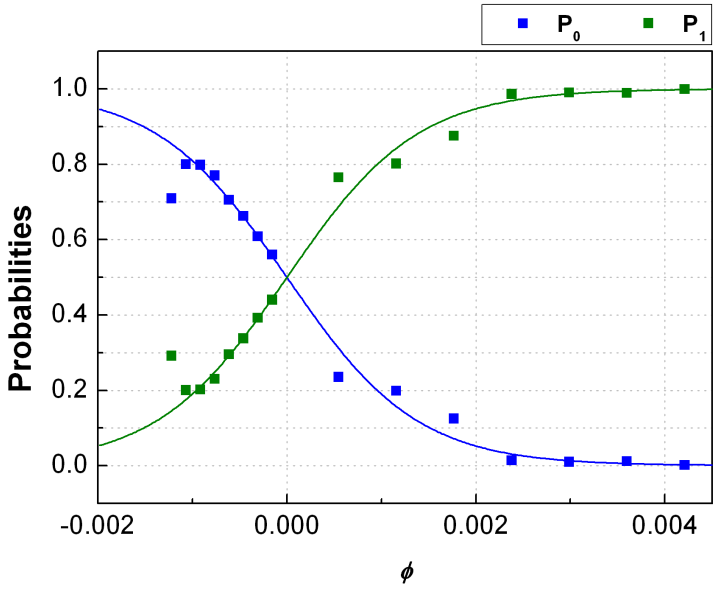

Figure 8.14: *Probabilities P_0 and P_1 as a function of ϕ. The continuous lines are the theoretical probabilities obtained from Eq. 8.15 using I_0=500 nA and T_{eff}=21 mK.*

same range around $\phi = 0$. As for the rates, the probabilities behave symmetrically around $\phi = 0$, at which point they cross. On either side of $\phi = 0$, one of the probabilities increases while the other decreases such that, away from $\phi = 0$, the system is found to be predominantly in the $|0\rangle$ ($|1\rangle$) state to the left (right) of $\phi = 0$. In the same figure we compare our data with Eq. (8.15) using I_0=500 nA and T_{eff}=21 mK, and we find that the experimental probabilities are well described by the model of MRT described in Sec. 8.2.2.

If the transitions between the $|0\rangle$ and $|1\rangle$ states occur by quantum tunnelling, the probabilities P_0 and P_1 can be used to construct the total persistent current i_Q in the qubit ground state

$$i_Q = P_0 i_{Q,0} + P_1 i_{Q,1}, \tag{8.16}$$

where P_0 and P_1 are the experimental occupation probabilities, and $i_{Q,0}$ and $i_{Q,1}$ are the classical persistent currents in the left and right well, respectively. For the currents $i_{Q,0}$ and $i_{Q,1}$, the experimental classical currents obtained in Sec. 8.1 were fit to straight lines $\bar{i}_{Q,0}$ and $\bar{i}_{Q,1}$ for $\Phi_Q < \Phi_0/2$ and $\Phi_Q > \Phi_0/2$, respectively. For each flux point, Eq. (8.16) was used to obtain i_Q at $\Phi_Q \approx \Phi_0/2$, and the result is shown in Fig. 8.15(a). Also

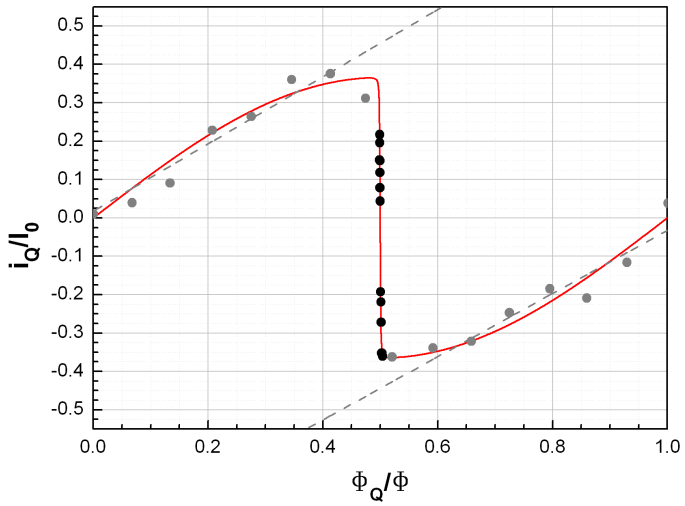

(a)

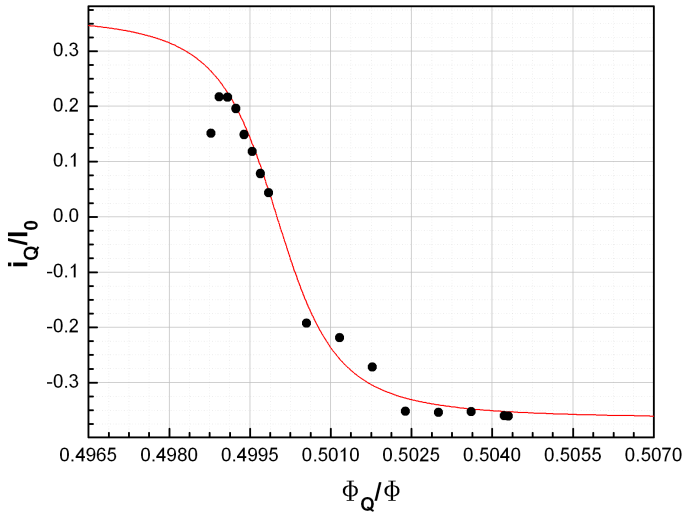

(b)

Figure 8.15: *(a) Persistent current i_Q in the qubit ground state normalised to the junction critical current I_0 as a function of flux. The black dots are the current calculated weighing the classical persistent currents with the probabilities P_0 and P_1. The grey dots are the classical persistent current obtained in Sec. 8.1, which were fit to straight lines $\bar{i}_{Q,0}$ and $\bar{i}_{Q,1}$ (grey dashed lines). The red solid line is a plot of the persistent current obtained from Eq. (4.5) with the values I_0=504 nA and Δ=0.00043E_J. (b) Detail of Fig. 8.15(a) close to $\Phi_Q \approx \Phi_0/2$.*

shown are the experimental classical persistent currents $i_{Q,0}$ and $i_{Q,1}$, and the linear fits $\bar{i}_{Q,0}$ and $\bar{i}_{Q,1}$. The total persistent current was fit to the model described in Sec. 4.1.3 using the junction critical current I_0 and the qubit gap Δ as free parameters, and the results are shown in Figs. 8.15(a) and 8.15(b) in different flux ranges. The values returned by the fits were I_0=504 nA and Δ=0.00043E_J. This value of the critical current, though larger than the expected I_0 ≈300 nA measured using test structures (see Sec. 5.2), is realistic for our fabrication technology. On the other hand, using I_0=504 nA, an energy gap amplitude $2\Delta/h$ ≈100 MHz is obtained, which is at least one order of magnitude smaller than the values ∼1-10 GHz [24] expected in our system, and the value Δ >4.8 GHz obtained fitting the transition rates. We believe this discrepancy is due to the simple model used to simulate the qubit dynamics, which provides only a qualitative description of the energy spectrum based on a two junction approximation, which is not accurate for our more complex system.

8.2.4 Temperature Dependence

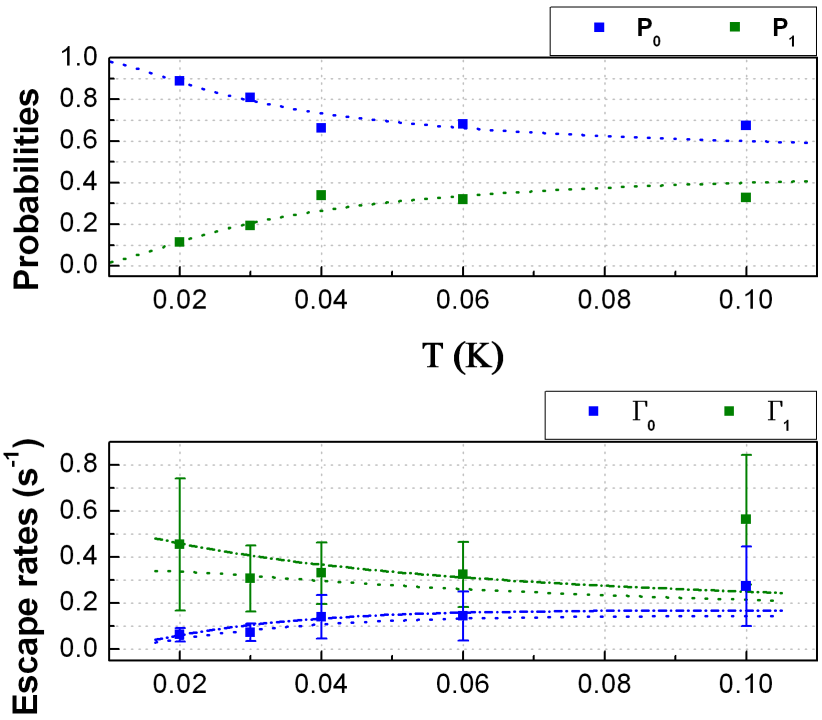

Figure 8.16: *Occupation probabilities (upper panel) and average escape rates (lower) as a function of temperature at ϕ=0.0014. The dotted lines are plots of Eqs. 8.11 and 8.15 with T_{eff}=21 mK, Δ=0.23 K, ϵ_p =0.1 K. The dash-dotted line is obtained for ϵ_p =0.08 K.*

The influence of bath temperature on the phase switching was investigated to understand the mechanism responsible for the switching. For the purpose, the switching events were recorded at fixed flux points near $\phi = 0$ as a function of the fridge temperature. The resulting occupation probabilities for ϕ=0.0014 are shown in Fig. 8.16(a) for temperatures T=20-100 mK. While at T=20 mK the system is predominantly in the $|1\rangle$ state with probability $P_1 \approx 0.9$, the probabilities P_0 and P_1 seem to converge at the middle value $P_0 = P_1$=0.5 as the temperature is increased. For T$\geq$40 mK, the probabilities remain almost constant at $P_0 \approx 0.32$ and $P_1 \approx 0.65$. The sensitivity to temperature of the probabilities at T$\leq$40 mK implies that the noise from environmental sources (e.g. on chip leads) is the dominant contribution, and the device is at an effective temperature $T_{eff} \approx T_L$, where the substrate temperature T_L is equal to the fridge temperature.

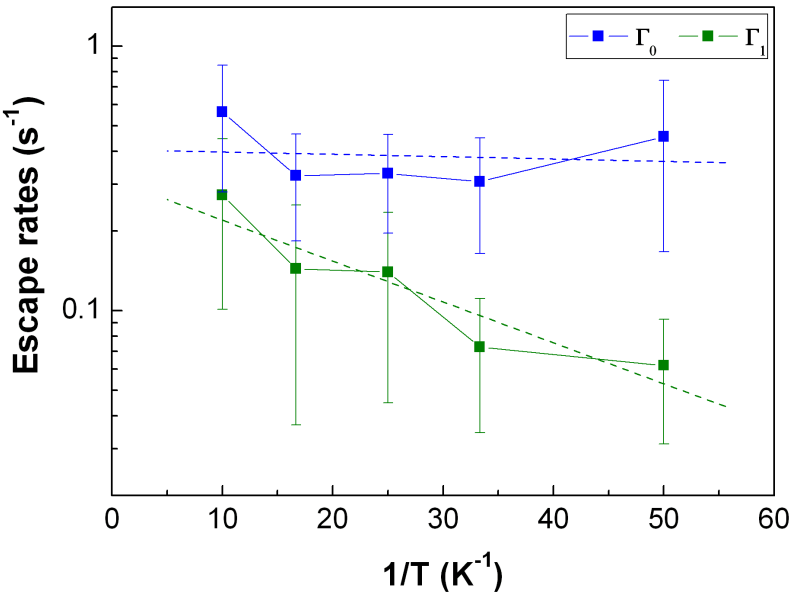

Figure 8.17: *Average escape rates* Γ_0 *and* Γ_1 *plotted as a function of* $1/T$ *at* $\Phi_Q = 0.5014\Phi_0$. *The grey dashed lines are linear best fits to the data, whose slope gives the barrier height respect to the* $|0\rangle$ *(*U_0^**) and* $|1\rangle$ *(*U_1^**) levels:* U_0^**=2.03 K and* U_1^**=18.9 K.*

The theoretical probabilities obtained from Eq. 8.15 with T_{eff}=21 mK, Δ=0.23 K and ϵ_p =0.1 K are shown in Fig. 8.16(a) as solid lines, and well reproduce the measured behaviour for T<60 mK. The average rates Γ_0 and Γ_1 at the same flux point ϕ=0.0014 are shown in Fig. 8.16(b), together with the prediction from Eq. 8.11 using T_{eff}=21 mK, Δ=0.23 K, ϵ_p =0.1 K (dotted line); although these value of the parameters give a qualitative description of the measured rates, a better fit is obtained using ϵ_p =0.08 K (dash-dotted line). At T>60 mK, the experimental rates differ substantially from the one predicted by the MRT model.

In order to investigate the escape mechanism, the rates are plotted in logarithmic scale as a function of $1/T$, together with the best fits to a straight line. The barriers heights obtained from the fits are U_0^*=2.03 K and U_1^*=18.9 K, much larger than the fridge temperature at which the measurements were acquired (20 mK). The values of the attempt frequency obtained from the intercepts were $f_{a,0}$=0.065 Hz and $f_{a,1}$=0.036 Hz, which are several order of magnitude smaller than the values f_a ~10 GHz [24] expected in our system. The investigation of the transition rates at higher temperatures, where thermal activation is expected to dominate with rates determined by Eq. (8.9),

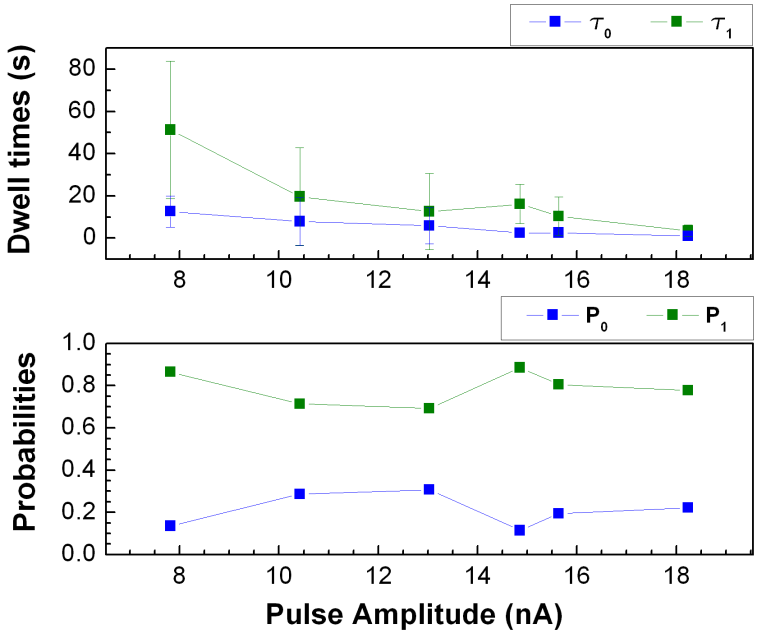

Figure 8.18: *Dwell times τ_0 and τ_1 as a function of current pulse amplitudes I_p at Φ_Q =0.5014Φ_0 and T=20 mK.*

would provide more evidence about the escape mechanism. Unfortunately, it was not possible to characterise the switching behaviour for T>100 mK, because the separation of the RTS voltages ΔV becomes comparable to the width of the Gaussian peaks, which merge together, and the voltage levels are no longer distinguishable. However, the hypothesis of quantum tunnelling as the main escape mechanism seem the most probable.

8.2.5 Pulse Amplitude Dependence

The influence of measurement current on the switching properties was investigated at T ≈20 mK by fixing the magnetic flux and recording the time traces with different current pulse amplitudes I_p. Figure 8.18 shows the occupation probabilities and dwell times measured at Φ_Q =0.5014Φ_0. The occupation probabilities do not display a clear dependence on I_p, and assume the values P_0=0.2±0.1 and P_1=0.8±0.1. On the contrary, the dwell times show a clear monotonic decrease as I_p is increased, and change about one order of magnitude in the 8-18 nA range.

A logarithmic plot of the escape rates as a function of the effective

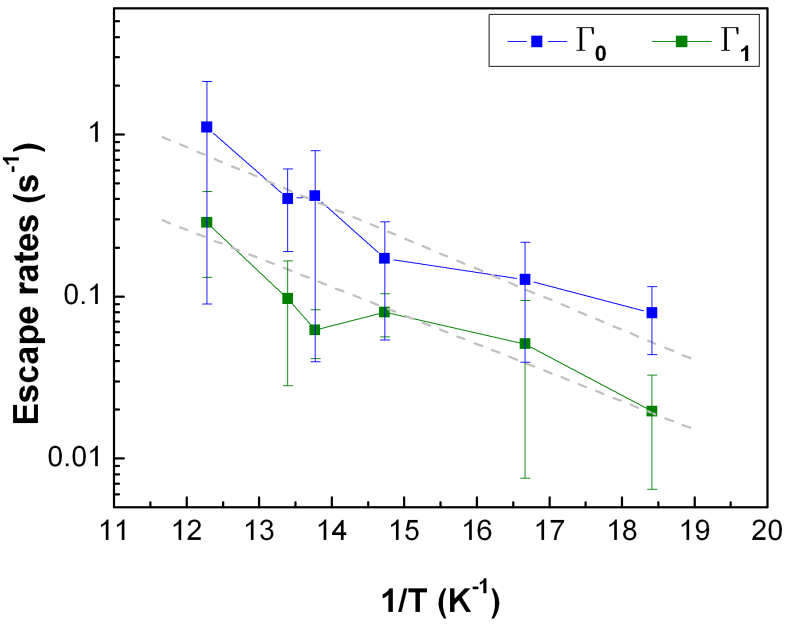

Figure 8.19: *Average escape rates* Γ_0 *and* Γ_1 *plotted as a function of inverse electron temperature* T_{eff}^{-1} *at* $\Phi_Q = 0.5014\Phi_0$. *The grey dashed lines are linear best fits to the data, giving the barrier heights respect to the* $|0\rangle$ *(*U_0^**) and* $|1\rangle$ *(*U_1^**) levels:* $U_0^* = 1.5$ *K and* $U_1^* = 2.2$ *K.*

electron temperature T_{eff} calculated in Sec. 7.2.3 is shown in Fig. 8.19. The rates exhibit a bigger change compared to the temperature dependence shown in Fig. 8.17 and a clear monotonic decrease with increasing T_{eff}. Fitting the rates with Eq. (8.9) gives the barrier heights U_0^*=1.5 K and U_1^*=2.2 K, and attempt frequencies $f_{a,0}$= 0.106 Hz and $f_{a,1}$= 0.103 Hz. The values of the barrier heights are two orders of magnitude larger than the fridge temperature $T \approx$20 mK at which the measurement were acquired, and about 20 times the maximum effective temperature $T_{eff} \approx$80 mK reached in the SNS junction. The attempt frequencies, though a factor of $\approx$ 10 larger than the values obtained in Sec. 8.2.4, are several order of magnitude smaller than expected for a flux qubit. However, the rough dependence $\ln(\Gamma) \propto 1/T_{eff}$ exhibited by the rates could suggest that the data shown in Fig. 8.19 were acquired in an intermediate regime where both quantum tunnelling and thermally assisted escape were present.

8.2.6 RF irradiation

The influence of RF irradiation on the switching properties was investigated by applying RF pulses of length τ_{RF}=50 ns-1 μs and frequencies f_{RF}=1-20 GHz to the on-chip superconducting antenna. The radiation produces a reduction of the resistance change ΔR, see Sec. 7.3, which decrease the sensitivity of the readout junction to the phase φ_I. This effect is more pronounced when large RF amplitudes were used, especially in continuous irradiation, while in the pulsed regime, the effect of irradiation on ΔR was weak.

Typical occupation probabilities as a function of magnetic flux for f_{RF}=10 GHz and 15.6 GHz are shown in Fig. 8.20, which show a symmetric dependence on magnetic flux about $\Phi_Q = \Phi_0/2$. The general effect of RF irradiation is to decrease the difference $P_1 - P_0$, an effect which is more pronounced when the flux is close to $\Phi_Q = \Phi_0/2$. The average transition rates $\Gamma_0 = 1/\tau_0$ and $\Gamma_1 = 1/\tau_1$ as a function of magnetic flux for the same RF frequencies are shown in Fig. 8.21. As for the probabilities, the rates under radiation retain the symmetry about $\Phi_Q = \Phi_0/2$, but are increased by one or two order of magnitudes compared to when no RF is applied. Both a decrease of $P_1 - P_0$ and an increase of the transition rates were observed for several RF frequencies in the 1-20 GHz range and for several pulse lengths τ_{RF}, and seem to be general properties of the measured samples under Rf irradiation. The fact that the probabilities do not show resonance peaks can be explained by considering the results described in Sec. 8.2.3, where a quality factor $Q \sim 1$ was obtained. The resonance peaks are expected to be have a width in flux $\Delta\Phi \approx \Phi_0\epsilon_p$, which covers the entire flux range in which we observe the switching between the levels $|0\rangle$ and $|1\rangle$.

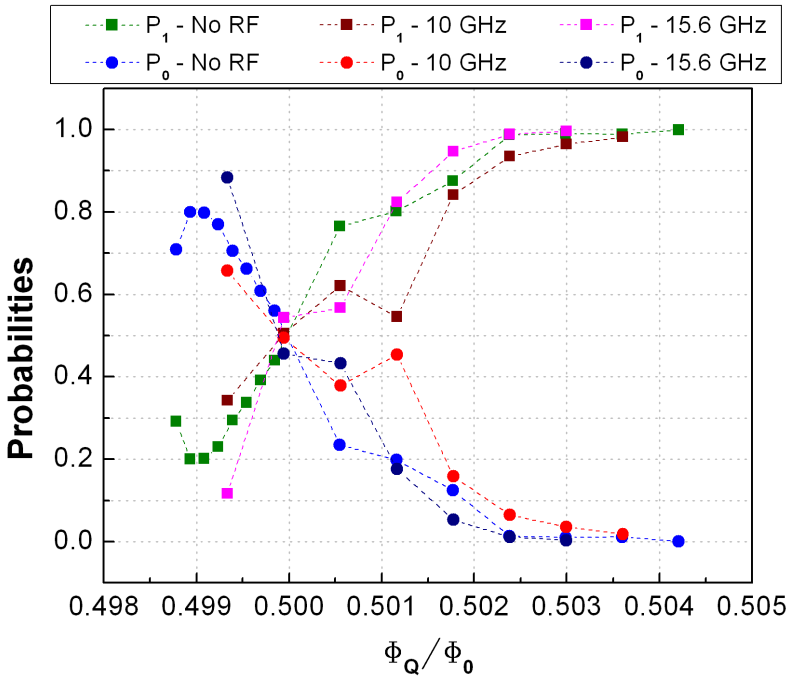

Figure 8.20: *Probabilities P_0 and P_1 as a function of flux about $\Phi_Q \approx \Phi_0/2$ under irradiation with RF pulses at f_{RF}=10 GHz and 15.6 GHz. The pulse length was τ_{RF}=600 ns.*

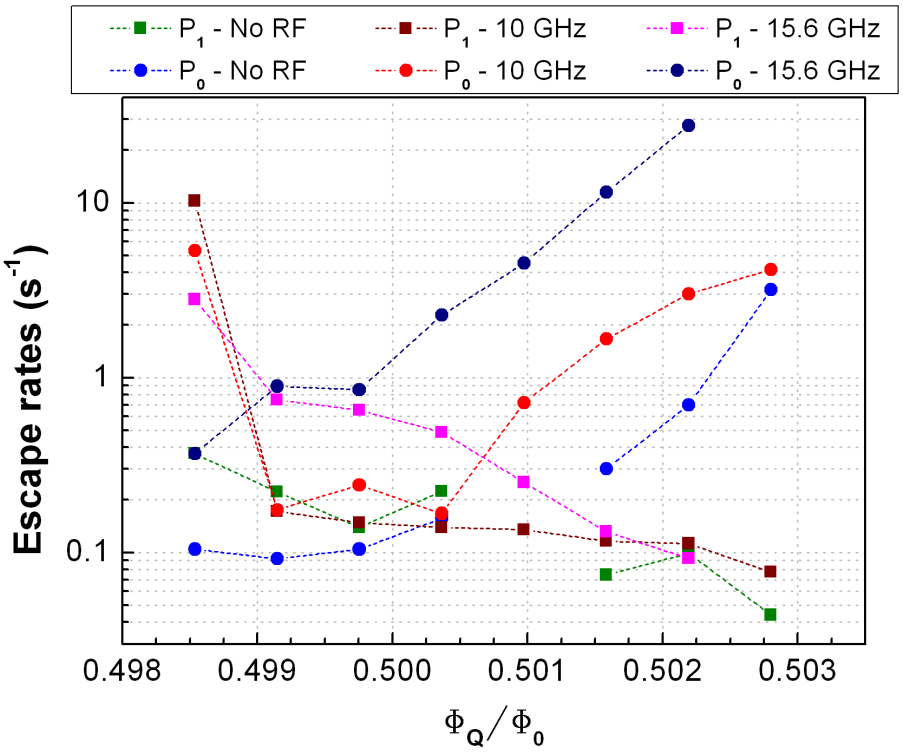

Figure 8.21: *Average transition rates* Γ_0 *and* Γ_1 *as a function of flux at* $\Phi_Q \approx \Phi_0/2$ *under irradiation with RF pulses at* f_{RF}*=10 GHz and 15.6 GHz. The pulse length was* τ_{RF}*=600 ns.*

Chapter 9

Conclusions and future developments

9.1 Conclusions

In this thesis we investigated the possibility of using Andreev interferometers as a readout probe for Josephson circuits designed to operate as persistent current qubits. Compared to previous experiments, several innovations to diminish the backaction of the SNS readout junction on the qubit were introduced. These include the "folded cross" geometry to minimise the inductive coupling of the qubit-interferometer system to the measurement circuit and the use of antimony as the normal metal, with one of the reservoirs made of a superconductor to minimize the Nyquist-Johnson noise. An important novelty for Andreev interferometry was the introduction of a pulsed lock-in measurement technique with pulse lengths down to 10 ns and repetition frequencies up to 1 MHz, which allowed control on the quasiparticle energy and temperature in the interferometer.

To optimize the readout method, the properties of the Andreev interferometers were investigated as a function of temperatures and measurement pulse parameters. Investigations of the effects of Radio Frequency radiation on the interference oscillations allowed us to measure the interferometer response time to be less than 40 ns. The qubit studied using Andreev interferometry showed a more complex dynamics than expected. Two metastable qubit states with extremely slow transitions rates in the range 0.01-10 Hz were observed. The results were interpreted as due to macroscopic resonant quantum tunnelling between the states. To our knowledge this is the first evidence of real time detection of macroscopic quantum tunnelling in persistent current qubits. The state dynamics was characterised by statistical analysis

in the framework of two-level systems. We explained the flux dependence of the tunnelling rates as due to low frequency "asymmetric" quantum noise. We argue that in our system such noise is the main source of decoherence, which prevents the observation of coherent dynamics of the qubit, while the Nyquist-Johnson thermal noise was reduced as a result of the modifications described above.

The experimental results show that an Andreev interferometer is a promising candidate as readout for persistent current qubits, in that, if suitably designed, it can perform detection of the qubit states with a simple and fast measurement of resistance. The system shows high sensitivity to the nature of noise and this property can be used to identify the mechanisms by which the environment induces decoherence.

9.2 Future developments

The sensitivity to low frequency noise demonstrated by our device rises the problem of reducing further the coupling with the environment. As the origin of noise has not yet been identified, we propose two methods of minimising the coupling of the qubit with two possible sources of noise: the measurement setup and the SNS interferometer junction.

The backaction of the interferometer on the qubit could be further reduced by decreasing the coupling of the SNS readout junction to the electrical contacts. As shown in literature (see for instance Ref. [57]), in an SNS junction with weak coupling with the normal reservoirs, a perfect minigap of amplitude $E_g \approx E_{TH}$ exists in the density of states of the N section. This gap prevents that quasiparticles at energy $E < E_g$ to enter the SNS junction from the contact leads, thus reducing the low-frequency contribution of the measurement setup. Practically, weak coupling can be achieved making contact with the readout SNS junction through tunnel barriers, using a design schematically shown in Fig. 9.1. This change requires to develop a more complex fabrication technology involving the deposition of a further material to produce the tunnel barriers (e.g. AlO_x). Moreover, to achieve a reliable control of the barrier resistance, both tunnel barriers should be created in the same fabrication step as the normal metal of the SNS junction, i.e., without breaking the vacuum in the evaporator. Thus, substantial modifications of the device design and fabrication would be needed to implement this change.

Further decrease in the backaction of the interferometer on the qubit could be achieved by coupling the two devices inductively. In this design, schematically shown in Fig. 9.2, an Andreev interferometer would be used as a magnetometer to detect changes in flux induced by the reversal of the

persistent current flowing in the qubit. The coupling between the two devices, occurring through the small mutual inductance (~ 10 pH), would lead to a decrease of the decoherence rate of several orders of magnitude. However, also the sensitivity of the interferometer to the qubit state would be greatly reduced compared to the actual design, and would probably require to average several measurements to achieve a sufficient signal-to-noise ratio.

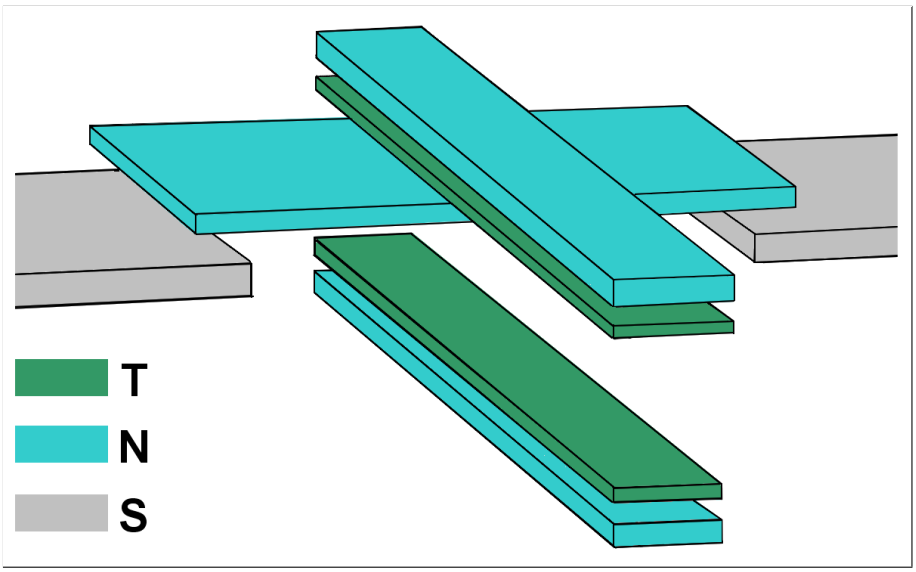

Figure 9.1: *Exploded view of an SNS readout junction coupled to the contact leads via tunnel junctions. "S" and "N" are the normal conductor and the superconductor, respectively, "T" is the material used to form the tunnel barrier.*

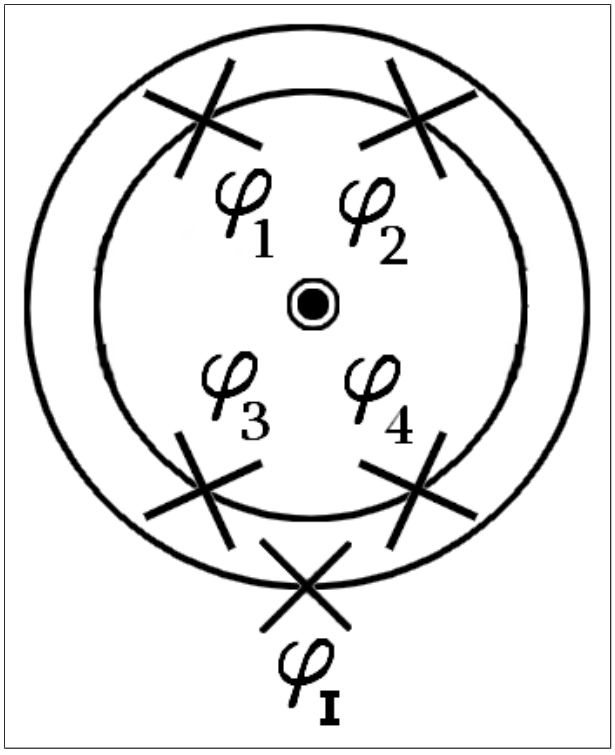

Figure 9.2: *Schematic of an Andreev interferometer inductively coupled to a flux qubit.*

Appendix A

PCB formulae

The impedance of a channelized coplanar waveguide ($CCPW$) is a function of the geometrical dimensions described in Fig. 6.11. For $g = S/2 + W$ and $S/(S + 2W) \leq 0.8$, the characteristic impedance can be approximated [107] with an accuracy of 2.2% by the formula

$$Z_0 = \left[\frac{5q}{1+5q} \cdot \frac{1}{Z_m} + \frac{1}{1+q} \cdot \frac{1}{Z_c} \right]^{-1},$$

where the following quantities are:

$$q = \frac{S}{h} \left(\frac{S+2W}{S} - 1 \right) \left\{ 3.6 - 2 \cdot \exp\left[-\frac{\epsilon_r + 1}{4} \right] \right\},$$

$$Z_m = \frac{60}{\sqrt{\epsilon_{effm}}} \cdot \ln\left[\frac{8h}{S} + 0.25\frac{S}{h} \right],$$

$$Z_c = \frac{30\pi}{\sqrt{\epsilon_{effc}}} \frac{K(k')}{K(k)}$$

$$k = \frac{S}{S+2W}, \qquad k' = \sqrt{1-k^2},$$

$$\epsilon_{effm} = \frac{\epsilon_r + 1}{2} + \frac{\epsilon_r - 1}{2} \left(1 + \frac{10h}{S} \right)^{-\frac{1}{2}},$$

$$\epsilon_{effc} = \frac{\epsilon_r + 1}{2} \left\{ \tan\left[0.775 \cdot \ln(h/W) + 1.75 \right] + \frac{kW}{h} \left[0.04 - 0.7k + 0.01(1 - 0.1\epsilon_r)(0.25 + k) \right] \right\},$$

and $K(k)$ is the complete elliptic integral of the first kind.

Appendix B

High permeability screen formulae

Wall thickness

A cylinder of high permeability material subject to a transverse external magnetic field collects flux from a circular area of twice its diameter [115]. The relationship between the field B_i inside the cylinder walls and the external field B_e is approximately

$$2 \cdot D \cdot B_e \approx 2 \cdot t \cdot B_i, \tag{B.1}$$

where D and t are the diameter and the wall thickness of the cylinder, respectively. Equation B.1 gives a condition for the minimum thickness t_{min} if the saturation value for the field B_i is used. For our screen, using B_i =0.9 T [113], B_e =5·10^{-5} T (earth's magnetic field) and D =5.6 cm, the minimum thickness results t_{min} ≈3 μm.

Similar considerations apply for the longitudinal direction, and the analogous equation to Eq. B.1 is [114]

$$t \cdot B_i \approx 0.5 \cdot B_e \sqrt{\frac{2L^3}{D}}. \tag{B.2}$$

Using the same values for B_e, B_i and D, and the screen length L =22 cm, the thickness t_{min} =17 μm is obtained. For both directions, the value of t_{min} is orders of magnitude smaller than commercially available thicknesses (≈1 mm).

Demagnetising factor

The demagnetising factor used in Eq. (6.11) is that of an ellipsoid of revolution with length-to-diameter ratio $p = L/D$; this factor is given by [114]:

$$N = \frac{1}{p^2 - 1} \left\{ \frac{p}{(p^2 - 1)^{1/2}} \cdot ln \left[p + (p^2 - 1)^{1/2} \right] - 1 \right\}.$$

Appendix C

Mathematica code

```
Analysis[TreshDN_, ThreshUP_, first_] := (
   DataRedistrib = Table[Data[[i, 1]], 0, i, DataLength];
   DataRedistrib[[1, 2]] = first;
   Testdn[n_, Uthdn_] := If[Data[[n, 2]] <= Uthdn, 0, 1];
   Testup[n_, Uthup_] := If[Data[[n, 2]] >= Uthup, 1, 0];
   For[i = 2, i != DataLength, i++,
    Switch[DataRedistrib[[i - 1, 2]], 0,
   DataRedistrib[[i, 2]] = Evaluate[Testdn[i, TreshDN]], 1,
   DataRedistrib[[i, 2]] = Evaluate[Testup[i, ThreshUP]]];
   ];
   tr = 0; updn = 0; dtr = 0; q = 0; dq = 0;
    For[i = 2, i != DataLength, i++,
   dtr =
   If[DataRedistrib[[i, 2]] == DataRedistrib[[i - 1, 2]], 0, 1];
    q = If[DataRedistrib[[i - 1, 2]] == 0, 0, 1];
   dq = If[dtr == 0, 0, q];
   tr = tr + dtr;
   updn = updn + dq;
];
dnup = tr - updn;
tot0 = Count[DataRedistrib[[All, 2]], 0];
tot1 = Count[DataRedistrib[[All, 2]], 1];
tauDN = (2/tr) ((tot0*BinSize)/BinSize)*Deltat;
tauUP = (2/tr) ((tot1*BinSize)/BinSize)*Deltat;
{tr, updn, dnup, tot0, tot1, tot0*BinSize, tot1*BinSize, tauDN, tauUP}
);

Cycle[ThDN_, ThUP_, first_] := (
```

```
   Outp = Evaluate[Analysis[ThDN, ThUP, first]];
   NewThresholds = Evaluate[Threshold[Outp[[8]], Outp[[9]]]];
   Join[NewThresholds, first, Outp]
);

AllOutputs = NestList[Cycle[#[[1]], #[[2]], #[[3]]] &, UthdnRough,
UthupRough, firstvalue, Cycles]
```

Bibliography

[1] R. P. Feynman, Int. J. Theor. Phys. 21, 467 (1982).

[2] P. Neumann, N. Mizuochi, F. Rempp, P. Hemmer, H. Watanabe, S. Yamasaki, V. Jacques, T. Gaebel, F. Jelezko, and J. Wrachtrup, Science **320**, 1326 (2008).

[3] H. Haffner, W. Hansel1, C. F. Roos, J. Benhelm, D. Chek-al-kar, M. Chwalla, T. Korber, U. D. Rapol1, M. Riebe, P. O. Schmidt, C. Becher, O. Guhne, W. Dur and R. Blatt, Nature **438**, 643 (2005).

[4] Wei-Bo Gao, Chao-Yang Lu, Xing-Can Yao, Ping Xu, Otfried Gühne, Alexander Goebel, Yu-Ao Chen, Cheng-Zhi Peng, Zeng-Bing Chen, Jian-Wei Pan, Nature Phys. **6**, 331 (2010).

[5] Q. A. Turchette, C. J. Hood, W. Lange, H. Mabuchi, H. J. Kimble, Phys. Rev. Lett. **75**, 4710 (1995).

[6] C. Monroe, D. M. Meekhof, B. E. King, W. M. Itano, D. J. Wineland, Phys. Rev. Lett. **75**, 4714 (1995).

[7] N. A. Gershenfeld and I. L. Chuang, Science **275**, 350 (1997).

[8] Y. Nakamura, C. D. Chen, and J. S. Tsai, Phys. Rev. Lett. **79**, 2328 (1997).

[9] J. R. Friedman, V. Patel, W. Chen, S. K. Tolpygo, and J. E. Lukens, Nature **406**, 43 (2000).

[10] C. H. van der Wal, A. C. J. ter Haar, F. K. Wilhelm, R. N. Schouten, C. J. P. M. Harmans, T. P. Orlando, S. Lloyd, and J. E. Mooij, Science **290**, 773 (2000).

[11] D. Vion, A. Aassime, A. Cottet, P. Joyez, H. Pothier, C. Urbina, D. Esteve and M. H. Devoret, Science **296**, 886 (2002).

[12] J. M. Martinis, S. Nam, J. Aumentado, C. Urbina, Phys. Rev. Lett. **89**, 117901 (2002).

[13] J. Clarke, Nature **453**, 1031 (2008).

[14] A. O. Niskanen, K. Harrabi, F. Yoshihara, Y. Nakamura, S. Lloyd, and J. S. Tsai, Science **316**, 273 (2007).

[15] V. T. Petrashov, K. G. Chua, K. M. Marshall, R. Sh. Shaikhaidarov, and J. T. Nicholls, Phys. Rev Lett. **95**, 147001 (2005).

[16] F. Yoshihara, K. Harrabi, A. O. Niskanen, Y. Nakamura, and J. S. Tsai, Phys. Rev. Lett. **97**, 167001 (2006).

[17] K. G. Chua, *Andreev Interferometry with Superconducting Persistent Current Qubits*, Ph.D. thesis, Royal Holloway University of London, London (2005).

[18] K. Marshall, *An Andreev Probe of Superconducting Quantum Circuits*, Ph.D. thesis, Royal Holloway University of London, London (2007).

[19] C. Checkley, *Andreev Interferometry of Flux Qubits Driven By Radio Frequency Field*, Ph.D. thesis, Royal Holloway University of London, London (2009).

[20] B. D. Josephson, Phys. Lett., **1**, 251 (1962)

[21] R. P. Feynman, R.B.Leighton, and M.Sands, *The Feynman lectures on physics*, vol 3, Chapter 21, (Addison-Wesley, second edition, 1966).

[22] P. W. Anderson, *Lectures on the Manybody Problem*, 113 (E. R. Caianiello Academic press, New York, 1964).

[23] T. P. Orlando, J. E. Mooij, L. Tian, C. H. van der Wal, L. S. Levitov, S. Lloyd, and J. J. Mazo, Phys, Rev. B **60**, 15398 (1999).

[24] J. E. Mooij, T. P. Orlando, L. Levitov, L. Tian, C. H. van der Wal, and S. Lloyd, Science **285**, 1036 (1999).

[25] S. Saito M. Thorwart, H. Tanaka, M. Ueda, H. Nakano, K. Semba, and H. Takayanagi1, Phys. Rew. Lett **93**, 037001 (2004).

[26] I. Chiorescu, Y. Nakamura, C. J. P. M. Harmans, J. E. Mooij1, Science **299**, 1869 (2003).

[27] D. Vion, A. Aassime, A. Cottet, P. Joyez, H. Pothier,C. Urbina, D. Esteve, and M.H. Devoret, Fortschr. Phys. **51**, 462 (2003).

[28] P. Bertet, I. Chiorescu, G. Burkard, K. Semba, C. J. P. M. Harmans,D. P. DiVincenzo, and J. E. Mooij, Phys. Rew. Lett. **95**, 257002 (2005).

[29] J. B. Majer, F. G. Paauw, A. C. J. ter Haar, C. J. P. M. Harmans, and J. E. Mooij, Phys. Rev. Lett. **94**, 090501 (2005).

[30] J. H. Plantenberg, P. C. de Groot, C. J. P. M. Harmans, and J. E. Mooij, Nature **447**, 836 (2007).

[31] E. Il'ichev, N. Oukhanski, A. Izmalkov, T. Wagner, M. Grajcar, H.-G Meyer, A. Y. Smirnov, A. Maassen van den Brink, M. H. S. Amin, and A. M. Zagoskin, Phys. Rev. Lett. **91**, 097906 (2003).

[32] A. Izmalkov, S. H. W. van der Ploeg, S. N. Shevchenko, M. Grajcar, E. Il'ichev, U. Hubner, A. N. Omelyanchouk, and H.-G. Meyer, Phys. Rew. Lett. **101**, 017003 (2008).

[33] A. Lupascu, E. F. C. Driessen, L. Roschier, C. J. P. M. Harmans, and J. E. Mooij, Phys. Rew. Lett. **96**, 127003 (2006).

[34] A. Lupascu, S. Saito, T. Picot, P. C. De Groot, C. J. P. M. Harmans and J. E. Mooij, Nat. Phys. **3**, 119 (2007).

[35] J. C. Lee, W. D. Oliver, K. K. Berggren, and T. P. Orlando, Phys. Rew. B **75**, 144505 (2007).

[36] V.L. Ginzburg and L.D. Landau, Zh. Eksperim. i. Teor, Fiz., **20**, 1064, (1950).

[37] M. Tinkham, *Introduction to superconductivity*, 2nd Ed., (McGraw Hill, New York, 1996).

[38] J. Bardeen, L. N. Cooper, and J. R. Schrieffer, Phys. Rev. B **108**, 1175 (1957).

[39] C. Kittel, *Introduction to Solid State Physics*, 7th Ed., (Wiley, New York, 1996).

[40] A. F. Andreev, Sov. Phys. JETP **19**, 1228 (1964).

[41] B. Pannetier, H. Courtois, J. Low Temp. Phys., **118**, 599 (2000).

[42] P. Mohanty, E. M. Q. Jariwala, and R. A. Webb, Phys. Rev. Lett. **78**, 3366 (1997).

[43] K. K. Likharev, Rev. Mod. Phys. **51**, 101 (1979).

[44] S. Guéron, H. Pothier, N. O. Birge, D. Esteve, and M. H. Devoret, Phys. Rev. Lett. **77**, 3025 (1996).

[45] W. Belzig, C. Bruder, and G. Schon, Phys. Rev. B **54**, 9443 (1996)

[46] F. Zhou, P. Charlat, B. Spivak, and B. Pannetier, J. Low Temp. Phys. **110**, 841 (1998).

[47] C. W. J. Beenakker, Phys. Rev. Lett. **67**, 3836 (1991).

[48] S.K. Yip, Phys. Rev. B **58**, 5803 (1998).

[49] A. F. Volkov, N. Allsopp, and C. J. Lambert, J. Phys.: Condens. Matter **8**, L45 (1996).

[50] A. A. Golubov, M. Yu. Kupriyanov, E. Il'ichev, Rev. Mod. Phys. **76**, 411 (2004).

[51] C. J. Lambert, and R. Raimondi, J. Phys.: Condens. Matter **10**, 901 (1998).

[52] M. Fuechsle, J. Bentner, D.A. Ryndyk, M. Reinwald, W. Wegscheider, and C. Strunk, Phys. Rev. Lett. **102**, 127001 (2009).

[53] P. G. de Gennes, Rev. Mod. Phys. **36**, 225 (1964).

[54] H. Courtois, Ph. Gandit, and B. Pannetier, Phys. Rev. B **52**, 1162 (1995).

[55] F. K. Wilhelm, A. D. Zaikin, and G. Schon, J. Low Temp. Phys., 106, 305, (1997)

[56] P.Dubos, H. Courtois, B. Pannetier, F.K. Wilhelm, A.D. Zaikin and G. Schön, Phys. Rev. B. 63 064502-1 (2001).

[57] T. T. Heikkila, J. Sarkka, and F. K. Wilhelm, Phys. Rev. B **66**, 184513-1 (2002).

[58] A. F. Morpurgo, T. M. Klapwijk, and B. J. van Wees, Appl. Phys. Lett. **72**, 966 (1998).

[59] J. J. A. Baselmans, A. F. Morpurgo, B. J. van Wees, and T. M. Klapwijk, Nature **397**, 43, (1999).

[60] R. Shaikhaidarov, A.F. Volkov, H. Takayanagi, V.T. Petrashov, and P. Delsing, Phys. Rev. B **62**, R14 649 (2000).

[61] B. Z. Spivak, and D. E. Khmel'nitskii, JETP Lett. **35**, 413 (1982).

[62] H. Nakano and H. Takayanagi, Solid State Commun. **80** (1991).

[63] S. Takagi, Solid State Commun. **81**, 579 (1992).

[64] C. J. Lambert, J. Phys.: Condens. Matter **5**, 707 (1993).

[65] V. T. Petrashov, V. N. Antonov, P. Delsing, and T. Claeson, Phys. Rev. Lett. **70**, 347 (1993).

[66] P. G. N. de Vegvar , T. A. Fulton, W. H. Mallison and R. E. Miller, Phys. Rev. Lett. **73** 1416 (1994).

[67] H. Pothier, S. Guéron, D. Esteve, and M. H. Devoret, Phys. Rev. Lett. **73**, 2488 (1994).

[68] V. T. Petrashov, V. N. Antonov, P. Delsing, and T. Claeson, JETP Lett. **60**, 606 (1994).

[69] V. T. Petrashov, V. N. Antonov, P. Delsing, and T. Claeson, Phys. Rev. Lett. **74**, 5268 (1995).

[70] J. van Wees, S. G. den Hartog, and A. F. Morpurgo, Phys. Rev. Lett. **76**, 1402 (1996).

[71] A. F. Volkov and V. P. Pavlovsky, *Proceedings of the Moriond International Symposium on Correlated Fermions and Transport in Mesoscopic Systems*, (Les Arcs, France, 1996).

[72] A. F. Volkov, R. Seviour, and V. P. Pavlovsky, Superlatt. Microstruct. **25**, 647 (1999).

[73] Yu. V. Nazarov, and T. H. Stoof, Phys. Rev. Lett. **76**, 823 (1996).

[74] V. T. Petrashov, R. Sh. Shaikhaidarov, I. A. Sosnin, I. JETP Lett. **64**, 839 (1996).

[75] V. T. Petrashov, R. Sh. Shaikhaidarov, I. A. Sosnin, P. Delsing, T. Claeson, and A. Volkov, Phys. Rev. B **58**, 15 088 (1998).

[76] S.H. Courtois, Ph. Grandit, D. Mailly, and B. Pannetier, Phys. Rev. Lett. **76**, 130 (1996).

[77] A. F. Volkov, and H. Takayanagi, Phys. Rev. B **56**, 11184 (1997).

[78] A.J. Leggett, S. Chakravarty, A. T. Dorsey, M. P. A. Fisher, A. Garg, W. Zwerger, Rev. Mod. Phys. **59**, 1 (1987).

[79] U. Weiss, *Quantum Dissipative Systems*, (World Scientific Publishing, London, 1999).

[80] M. Grifoni, E. Paladino, U. Weiss, Eur. Phys. J. B **10**, 719 (1999).

[81] C.H. van der Wal, F.K. Wilhelm, C.J.P.M. Harmans, and J.E. Mooij, Eur. Phys. J. B **31**, 111 (2003).

[82] H. Nyquist, Phys. Rev. **32**, 110 (1928).

[83] M. Kamon, M. J. Tsuk, and J. K. White, IEEE Trans. Microwave Theory Tech., **40**, 1496 (1992); the software can be downloaded at: http://www.fastfieldsolvers.com/.

[84] J. Eom, C. J. Chien, and V. Chandrasekhar, Phys. Rev. Lett. **81**, 437 (1998).

[85] J. Aumentado and V. Chandrasekhar, J. Eom, P. M. Baldo and L. E. Rehn, Appl. Phys. Lett. **75**, 3554 (1999).

[86] H. Courtois, Ph. Grandit, D. Mailly, and B. Pannetier, Phys. Rev. Lett. **76**, 130 (1996).

[87] G. J. Dolan, Appl. Phys. Lett. **31**, 337 (1977).

[88] B. Cord, C. Dames, K. K. Berggren, and J. Aumentado, J. Vac. Sci. Technol. B **24**, 3139 (2006).

[89] G.K. White and P. J. Meeson, *Experimental Techniques in Low-Temperature Physics*, 4th eds, (Oxford University Press, USA, 2002).

[90] F. C. Wellstood, C. Urbina, and J. Clarke, Phys. Rev. B **49**, 5942 (1994).

[91] D. Vion, P. F. Orfila, P. Joyez, D. Esteve, M. H. Devoret, J. App. Phys. **77**, 2519, (1995).

[92] H. le Sueur and P. Joyez, Rev. Sci. Instrum. **77**, 115102 (2006).

[93] I. Jin, A. Amar, and F. C. Wellstood, Appl. Phys. Lett. **70**, 2186 (1997).

[94] A. V. Zorin, Rev. Sci. Instrum. **66**, 4296 (1995).

[95] D. C. Glattli, P. Jacques, A. Kumar, P. Pari, and L. Saminadayar, J. Appl. Phys. **81**, 7350 (1997).

[96] J. M. Martinis, M. H. Devoret, and J. Clarke, Phys. Rev. B **35**, 4682 (1987).

[97] A. Fukushima, A. Sato, A. Iwasa, Y. Nakamura, T. Komatsuzaki, and Y. Sakamoto, IEEE Trans. Instrum. Meas. **46**, 289 (1997).

[98] K. Bladh, D. Gunnarsson, E. Hurfeld, S. Devi, C. Kristoffersson, B. Smalander, S. Pehrson, T. Claeson, and P. Delsing, Rev. Sci. Instrum. **74**,1323 (2003).

[99] F. P. Milliken, J. R Rozen, G. A. Keefe, and R. H. Koch, Rev. Sci. Instrum. **78**, 024701 (2007).

[100] A. Lukashenko and A. V. Ustinov, Rev. Sci. Instrum. **79**, 014701 (2008).

[101] M. Hashisaka, Y. Yamauchi, K. Chida, S. Nakamura, K. Kobayashi, and T. Ono, Rev. Sci. Instrum. **80**,096105 (2009).

[102] Emerson and Cumming Inc., Canton, MA, 02021, USA.

[103] Goodfellow Cambridge Ltd., Huntingdon, PE29 6WR, England.

[104] Kremer Pigmente GmbH & Co. KG, Hauptstr. 41–47, DE 88317, Aichstetten, Germany.

[105] P. Horowitz and W. Hill, *The Art Of Electronics*, (Cambridge University Press, New York, 1989).

[106] L. Spietz, J. Teufel, R. J. Schoelkopf, e-print cond-mat/1316 (2006)

[107] R. N. Simons, *Coplanar Waveguide Circuits, Components, and Systems*, (Wiley, New York, 2001).

[108] Printech Circuit Laboratories, Chelmsford, CM3 5ZA, England.

[109] Rogers Corporation, Chandler, AZ 85226, USA.

[110] Y. Hariharan, M. P. Janawadkar, and T. S. Radhakrishnan, Pramana **13**, 117, (1979).

[111] T. I. Smith, J. Appl. Phys. **44**, 852 (1973).

[112] Amuneal Manufacturing Corporation, Philadelphia, PA 19124, USA.

[113] Amuneal Manufacturing Corporation application note, *Custom Magnetic Shielding for Low Temperature Applications*, available at: http://www.amuneal.com/sites/default/files/AmunealDataSheet2.pdf.

[114] A. Mager, J. Appl. Phys. **39**, 1914 (1968).

[115] A. J. Mager, IEEE Trans. Magn. **6**, 67 (1970).

[116] J. Liu and N. Giordano, Phys, Rev. B **43**, 3928 (1991).

[117] F. Giazotto, T. T. Heikkil*ä*, A. Luukanen, A. M. Savin, J. P. Pekola, Rev. Mod. Phys. **78**, 217 (2006).

[118] A. H. Steinbach, J. M. Martinis, and M. H. Devoret, Phys. Rev. Lett. **76**, 3806 (1996).

[119] B. Huard, H. Pothier, D. Esteve, and K. E. Nagaev,, Phys, Rev. B **76**, 165426 (2007).

[120] C. Checkley *et al.*, J. Phys.: Condens. Matter **23**, 135301 (2011).

[121] S. Wind, M. J. Rooks, V. Chandrasekhar, and D. E. Prober, Phys. Rev. Lett. **57**, 633 (1986).

[122] P. Virtanen, T. T. Heikkila, F. Sebastian Bergeret, and J. C. Cuevas, Phys. Rev. Lett. **104**, 247003 (2010).

[123] V. T. Petrashov, R. Sh. Shaikhaidarov, P. Delsing, and T. Claeson, JETP Lett. **67**, 513 (1998).

[124] K. E. Nagaev, Phys, Rev. B **52**, 4741 (1995).

[125] T. M. Buehler, D. J. Reilly, R. P. Starrett, V. C. Chan, A. R. Hamilton, A. S. Dzurak, and R. G. Clark, J. Appl. Phys. **96**, 6827 (2004).

[126] M. J. Uren, D. J. Day, and M. J. Kirton, Appl. Phys. Lett. **47**, 1195 (1985).

[127] F. C. Wellstood, C. Urbina, and J. Clarke, Appl. Phys. Lett. **85**, 5296 (2004).

[128] J. Eroms, L. C. van Schaarenburg, E. F. C. Driessen, J. H. Plantenberg, C. M. Huizinga, R. N. Schouten, A. H. Verbruggen, C. J. P. M. Harmans, and J. E. Mooij, Appl. Phys. Lett. **89**, 122516 (2006).

[129] G. Ithier, *Manipulation, readout and analysis of the decoherence of a superconducting quantum bit*, Ph.D. thesis, CEA, Saclay (2005).

[130] R. W. Simmonds, K. M. Lang, D. A. Hite, S. Nam, D. P. Pappas, and John M. Martinis, Phys. Rev. Lett. **93**, 077003 (2004).

[131] B. Cooper *et al.*, Phys. Rev. Lett. **93**, 180401 (2004).

[132] K. B. Cooper, Matthias Steffen, R. McDermott, R. W. Simmonds, Seongshik Oh, D. A. Hite, D. P. Pappas, and John M. Martinis, Phys. Rev. Lett. **95**, 210503 (2005).

[133] A. Lupascu, P. Bertet, E. F. C. Driessen, C. J. P. M. Harmans, and J. E. Mooij, Phys. Rev. B **80**, 172506 (2009).

[134] F. Deppe, M. Mariantoni, E. P. Menzel, S. Saito, K. Kakuyanagi, H. Tanaka, T. Meno, K. Semba, H. Takayanagi, and R. Gross, Phys. Rev. B **76**, 214503 (2007).

[135] Yang Yu, Shi-Liang Zhu, Guozhu Sun, Xueda Wen, Ning Dong, Jian Chen, Peiheng Wu, and Siyuan Han, Phys. Rev. Lett. **101**, 157001 (2008).

[136] R. Blatt and P. Zoller, Eur. J. Phys. **9**, 250 (1988).

[137] R. J. Cook and H. J. Kimble, Phys. Rev. Lett. **54**, 1023 (1985).

[138] A. Schenzle and R. G. Brewer, Phys, Rev. A **34**, 3127 (1986).

[139] Y. Yuzhelevski, M. Yuzhelevski, and G. Jung, Rev. Sci. Instrum. **71**, 1681 (2000).

[140] P. Hanggi, J. Stat. Phys. **42**, 105 (1986).

[142] M. H. S. Amin, and D. V. Averin, Phys. Rev. Lett. **100**, 197001 (2008).

[143] R. Harris,M.W. Johnson, S. Han, A. J. Berkley, J. Johansson, P. Bunyk, E. Ladizinsky, S. Govorkov, M. C. Thom, S. Uchaikin, B. Bumble, A. Fung, A. Kaul, A. Kleinsasser, M. H. S. Amin, and D.V. Averin, Phys. Rev. Lett. **101**, 117003 (2008).

[144] Yu.V. Nazarov and Ya.M. Blanter, *Quantum transport, Introduction to nanoscience*, (Cambridge University Press, 2010).